A thesis entitled

A CALORIMETRIC STUDY OF SOME SOLID SOLUTION ALLOYS UNDERGOING TRANSITIONS TO MAGNETIC ORDER

submitted for the

Degree of Doctor of Philosophy of the University of London

and for the Diploma of Imperial College

by

DAVID GLYN DAWES

January 1980

The Blackett Laboratory
Imperial College
Prince Consort Road
London SW7 2BZ

ABSTRACT

The transition from a disordered spin glass regime to a long-range ordered regime in Au Fe, Cu Mn and Y Gd alloys was investigated calorimetrically, using a novel steady-state AC technique. Data is presented between 1.5 and 18K for the nominal composition ranges : Au 14 - 28 at% Fe, Cu 30 - 70 at% Mn, Y 2 at% Gd, and Y 3.4 at% Gd.

The low constant-temperature total specific heat of the Au Fe alloys exhibited a broad peak as a function of concentration close to the critical concentration for ferromagnetism ~16 at% Fe, and almost diminished to the equivalent non-magnetic value, as measured with a Au 22 at% Ni alloy, at ~28 at% Fe. The low temperature-dependent specific heat exhibited slight non-linear downward curvatures in plots of C/T vs. T^2 which were particularly noticeable in the 18, 20 and 22 at% Fe alloys.

The low-temperature specific heat of Au Fe alloys was considered to be due due to the excitations of a frozen configuration of finite-clusters.

A fairly sharp rise of the low constant - temperature total specific heat of the Cu Mn alloys was observed in the concentration regime between 50 and 70 at% Mn, leading up to the emergence of long range antiferromagnetic order at ~72 at% Mn. A slight non-linear upward curvature, which increased with higher Mn concentration, was evident in plots of C/T vs. T^2 of the low temperature-dependent specific heat.

The rather rapid rise of specific heat in the regime leading up to the critical concentration is discussed in connection with the extensive magnetic short range order and the developing itinerant character of the Mn d-electrons.

The specific heat of the Y 2 at% Gd spin glass alloy peaked at 6.4 ± 0.15K, whereas a much broader peak was observed at 12.8 ± 0.6K in the long-range helically ordered Y 3.4 at% Gd alloy.

ACKNOWLEDGEMENTS

I would like to express my deepest gratitude to Professor Bryan Coles for his invaluable guidance, indefatigable interest and encouragement as supervisor of my research project.

It gives me great pleasure to thank Drs. A.D. Caplin, J.R. Davis, C.N. Guy, N. Rivier and B.V.B. Sarkissian for many fruitful discussions and for helpful advice during the course of the research work and the preparation of this thesis.

My special thanks go to Dr. Kay Nicholson for initiating me in the dark art of calorimetry and to Dr. H.E.N. Stone for providing the samples and for invaluable advice on metallurgical topics.

My warmest regards go to my fellow research students for their friendship and for providing an amicable working atmosphere.

My final thanks go to Miss Deanne Eastwood for the efficiency with which she typed the thesis.

I gratefully acknowledge the SRC for its financial support during the tenure of my research studentship.

CONTENTS

CHAPTER 1

THEORETICAL BACKGROUND

1.1 Introduction

The theoretical understanding of transition metal - noble metal alloys is at present limited to the very dilute regime. The localisation and indirect exchange interactions between moments in the very dilute alloys like AuFe and CuMn are reasonably well understood, although theories fail to predict the correct low-temperature properties of these alloys. In moderately concentrated alloys the comparative importance of indirect interactions diminishes with respect to direct first-neighbour exchange interactions. A percolation theory description will be useful to some extent in understanding this change in character of the exchange interactions.

This first chapter of the thesis briefly outlines the development of some of the theoretical concepts and models of spin glasses and the percolation process. The chapter is subdivided into three sections on the theory of specific heat, spin glasses and the percolation process. The first section on specific heat theory concentrates mainly on the topic of magnetic contributions which arise at low temperatures from single particle or collective excitations in noble-transition metal alloys.

The second section surveys the principal theories of spin glasses with some brief discussion on the proposed models of the ground state and the approaches to their solution. The final section on percolation theory discusses the basic principles of the concept of percolation and the methods employed to derive critical concentrations.

1.2 Theory of Specific Heat

The low-temperature specific heat of a metallic system is usually separated into three relatively independent contributions from the electron, phonon and spin systems : C_E, C_L and C_M respectively.

$$C = C_E + C_L + C_M \qquad 1.1$$

The derivation of the lattice and electronic contributions for simple metallic systems is well established. An excellent review of the theoretical development of the subject may be found in an article by DeLaunay (1). A brief summary of these well known results will be given in the following section.

Magnetic contribitons to the specific heat arising from excitations or ordering of the spin system are diverse in character. A small treatise on the subject of low-temperature specific heat by Gopal (2) includes a useful introduction to the various forms of magnetic specific heat contributions.

1.2.1 Lattice and electronic contributions

A quantum statistical treatment of lattice vibrations, principally by Debye, established the simple "Debye T^3- law" expression for the molar specific heat contribution C_L.

$$C_L = \beta T^3 = 12/5\ \pi^4 N k_B (T/\Theta_D)^3 \qquad 1.2$$

k_B is the Boltzmann constant and Θ_D is the characteristic Debye temperature. The Debye model treats the lattice as a dispersionless continuum ($\omega = ck$, where c is the isotropic sound velocity) for which the density of phonon states $g(\omega) \propto \omega^2$ is cut-off at frequency $\omega = \omega_D = k_B \Theta_D / \hbar$ chosen to limit the number of states to 3N, the total number of normal modes of an N-particle system.

Expression 1.2 is only strictly valid in the low-temperature limit $\Theta_D/T \gg 1$,

for most metallic systems this is experimentally found to be $T \lesssim \Theta_D/50$. Deviations from this simple expression at higher temperatures can be seen in normalised plots of $\Theta_D(T)/\Theta_D(0)$ vs. T; they are usually negative (i.e. $1/\Theta_D . d\Theta_D/dT < 0$ but gold is exceptional.

A more realistic representation of the phonon density of states spectra was given by the Born-von Kármán model. In this model the lattice dynamics are calculated from first principles using equations of coupled atomic motion based on the assumption that the lattice is a set of point masses coupled by harmonic restoring forces. Some of the finer details, such as singularities in the density of states at certain symmetry points and gaps in the phonon dispersion curves of diatomic lattices are reproduced by this model.

Sommerfeld used Fermi-Dirac statistics to evaluate the molar specific heat contribution from the conduction electron system C_E.

$$C_E = \gamma T = \tfrac{2}{3} \pi^2 N_A k_B^2 n(E_F) . T \qquad 1.3$$

where $n(E_F)$ is the total density of electronic states per atom at the fermi energy level $E_F = k_B T_F$, N_A is Avogadro's number. Expression 1.2 is the first term of the Sommerfeld expansion, at low temperatures $T \ll T_F \sim 10^5$K the higher order terms are negligible. In the free electron model the density of states $n(E_F) = \frac{3}{4} z/E_F$ where z is the number of free electrons per atom participating in conduction.

$$C_E = \tfrac{1}{2} \pi^2 z N_A k_B (T/T_F) = \gamma_0 T \qquad 1.4$$

Electron many-body effects are usually included by defining an effective electron mass $m^*/m = \gamma/\gamma_0$.

1.2.2 Magnetic Schottky anomaly

Single or small groups of paramagnetic spins thermally fluctuating in local fields

give rise to a Schottky specific heat anomaly at low temperatures. A local field B splits the ground state of a system of spin - J particles into (2J + 1) energy levels, the thermal population of these levels follows Maxwell-Boltzmann statistics. The molar Schottky specific heat C_{SCH} can be evaluated from the partition function Z of the system

$$C_{SCH}/R = -\beta^2 \cdot \frac{\partial^2 \ln Z}{\partial \beta^2} \qquad 1.5$$

where $R = N_A k_B$ and $\beta = 1/k_B T$.

The simplest form of Schottky anomaly is for a system of spin - $\frac{1}{2}$ particles for which the ground state splits into two levels separated in energy by $\Delta = g \mu_B B$ in the presence of a magnetic field B. The Schottky specific heat C_{SCH} of such a system is given below (see also fig. 1.2.1)

$$C_{SCH}/R = x^2 \operatorname{sech}^2 x \qquad 1.6$$

where $x = \beta\Delta$

At low temperatures ($x \gg 1$) the specific heat rises exponentially to a broad peak, then falls again to zero as $\sim 1/T^2$ at higher temperatures ($x \ll 1$). Schottky anomalies are characteristic features of the very low-temperature specific heat of nuclear moments of rare earth elements fluctuating in their local hyperfine fields. In the limit of infinite spin value ($J \gg 1$) the form of the specific heat approaches Einstein's result for a classical one dimensional harmonic oscillator, i.e. above the characteristic Einstein temperature $T_E = \Delta/k_B$ the specific heat tends to a constant value of $C_{SCH}/R = 1$ whilst below T_E it falls exponentially to zero.

1.2.3 Mean-field models

Some early attempts to explain the large, essentially concentration independent,

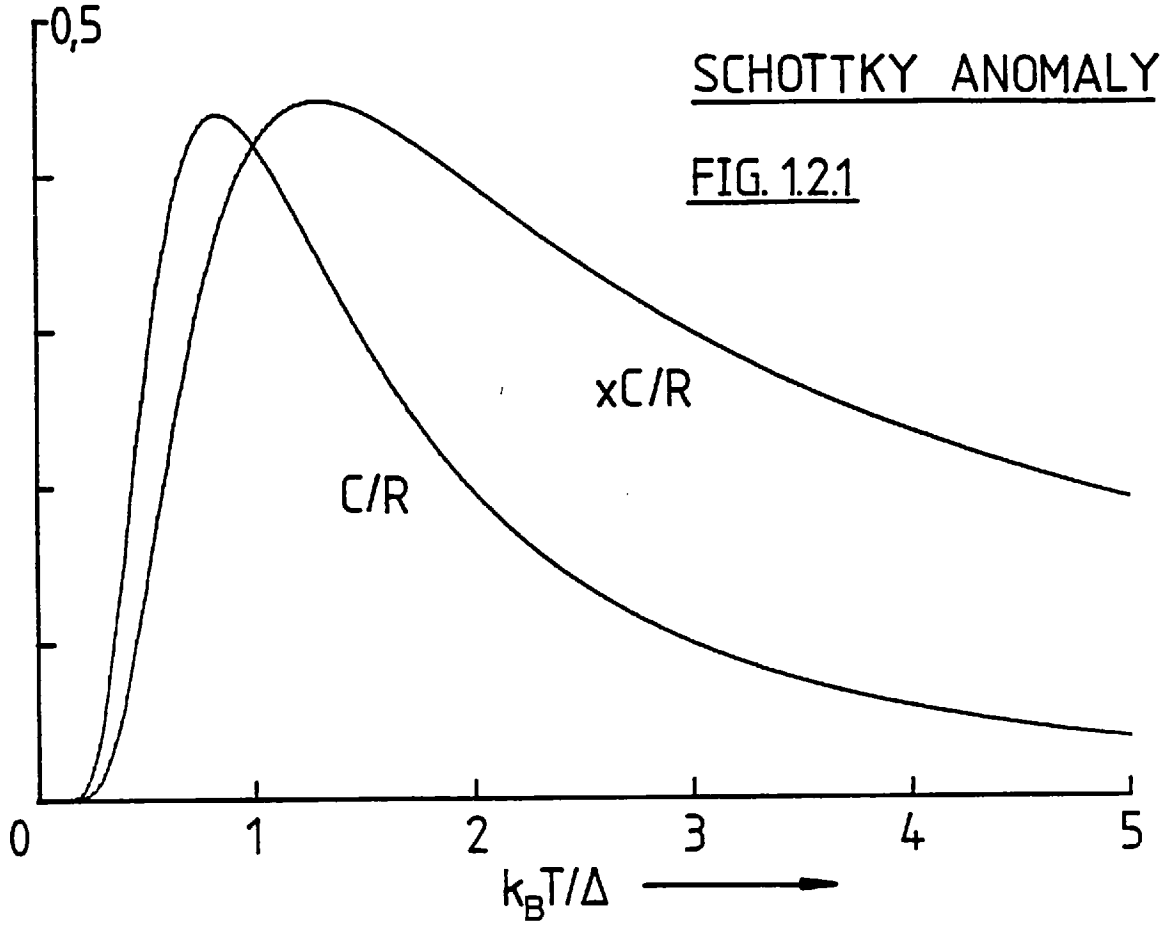

SCHOTTKY ANOMALY

FIG. 1.2.1

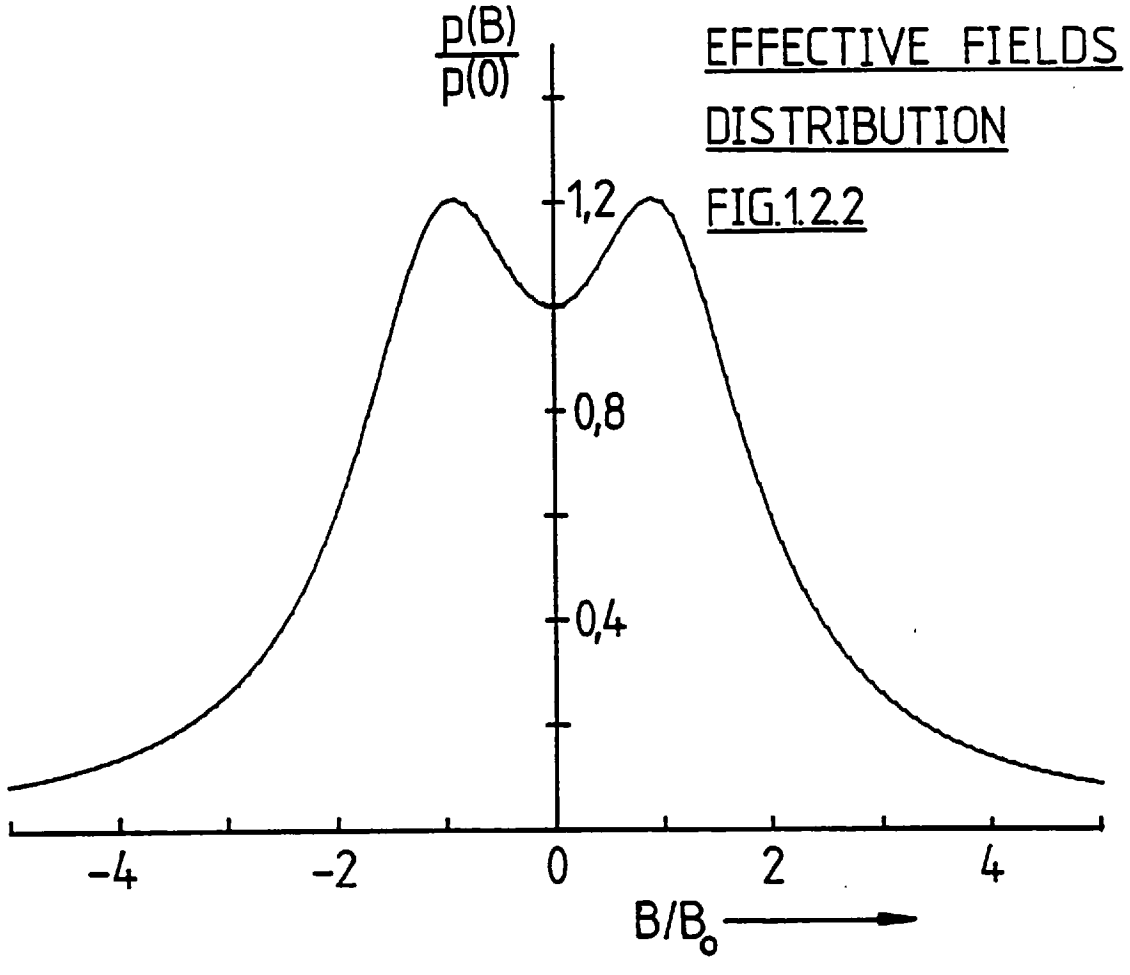

EFFECTIVE FIELDS DISTRIBUTION

FIG. 1.2.2

low temperature linear specific heat of dilute alloys of transition metal impurities in noble metal hosts by Marshall, Klein and Brout were based on mean field concepts.

Marshall (3) proposed that at low temperatures the low lying excitations of localised spins in small effective local fields could account for the observed specific heat behaviour of dilute Cu Mn alloys. His model was based on an Ising approximation to the random RKKY spin interaction in which a distribution of effective local fields $p(B, T)$, acting along a unique quantisation axis at spin sites, incorporates the details of the complex RKKY hamiltonian.

He reasoned that most spins would be rigidly aligned in large effective local fields $B \gg k_B T/\mu$ at low temperatures and could not contribute significantly to the specific heat. The most significant contribution arose from the low lying Schottky-like excitations of the few spins in relatively small effective local fields $B \sim k_B T/\mu$.

He proposed that the distribution curve $p(B, T)$ was of Lorentzian form with width $\sim \langle B \rangle$, the average effective field, (see fig. 1.2.2) by generalising concepts of the Bethe-Peierls theory of order-disorder transitions to the dilute alloy problem. A series of qualitative arguments were given to justify that $p(0, 0) \propto 1/c$, since the amplitude of the RKKY interaction from which the distribution was derived is proportional to the impurity concentration c. At low temperatures the leading term in the magnetic specific heat was shown to be proportional to $Tc\,p(0, 0)$, thus arriving at the low temperature - linear, concentration independent magnetic specific heat term observed experimentally.

Klein and Brout (4) adopted a more fundamental approach in which statistical mechanical arguments were used to derive the distribution of effective fields experienced by a small cluster of spins arising from interactions with all other spins. Their model was also based on the Ising approximation but was corrected for local spin correlations. The clusters were the result of highly correlated interactions with 2 - 3

closely neighbouring spins, but uncorrelated with spins beyond. The range of the correlation r was such that the cluster spin density $\sim 1/r^3$ was proportional to concentration and the number of spins in a cluster was independent of concentration. The shape of the distribution of effective fields derived by this procedure resembled the curve proposed by Marshall. This model was only strictly valid in the limit of $T \rightarrow 0$, Klein (5) generalised the model to higher temperatures and derived the universal expression $C_m/c = f(T/c)$, but the validity of some of the assumptions on which his reasoning was based were questionable. More recently, Klein (6) extended these early ideas to account for the weak concentration dependence of the temperature-linear specific heat coefficient of dilute Cu Mn and Au Fe up to solute concentrations $\sim 5\%$.

An alternative approach was adopted by Overhauser (7), who emphasised the importance of exchange interactions between the impurity moments and the conduction electrons. The premise of his model was that under certain conditions it was possible for exchange interactions to stabilise an excited state of the conduction electron gas in which the electron spin density varied sinusoidally in space but the charge density remained uniform. The spin density wave amplitude was determined by the minimum in the free energy of the system, the latter being composed of kinetic and exchange energy terms. The effective field distribution of Overhauser's model depended on the spin density wave amplitude, which at low temperatures was proportional to concentration c, implying that $p(0, 0) \propto 1/c$. The form of the specific heat expression thus derived was qualitatively very similar to the one obtained by Marshall.

A possible disadvantage with Overhauser's theory was that it predicted a fairly sharp break up of the spin density wave above some critical temperature T_c, proportional to concentration, which would have given rise to a sharp specific heat anomaly at T_c. This aspect of the theory, however, depended on basic assumptions

about the range of the sd-exchange interaction which may be modified by competing indirect solute-solute interactions.

1.2.4 Cluster mean-field models

The Coherent Potential Approximation (CPA) method of evaluating electronic and magnetic properties of more concentrated binary alloys involves a configurational averaging which would make it unsuitable for calculating properties sensitive to the degree of local inhomogeneity which may be present in some alloys. Levin and Mills (8) proposed a model of such alloys based on giant spin clusters, employing Cu Ni alloys with compositions close to the critical concentration as examples. Their approach was uniquely different from earlier cluster models in that they stressed the internal spin dynamics of the clusters rather than assuming a rigid parallel alignment of spins in all clusters. The strength of a cluster's internal spin correlations was characterised by an intracluster exchange constant $J^{dd} \sim k_B T_c^{Ni}$, taken to be of the same order as the exchange constant of pure nickel. Although a localised spin description was not entirely appropriate for nickel alloys, since in the dilute limit nickel atoms do not possess moments, it was nevertheless used as a first approximation to extract some qualitative results as a Hartree-Fock calculation based on an itinerant electron model would have been unable to take account of the internal spin dynamics of clusters. Unlike the Klein and Brout cluster theories, a clear distinction was made between exchange interactions of spins in the same cluster and of spins in separate clusters, the latter being weaker RKKY-like interactions which could be replaced by an effective mean field distribution as in previous treatments of the dilute alloys by Marshall, Klein and Brout.

Local environment effects were considered to be an important factor in establishing local moments at nickel atom sites. In a close-packed FCC structure the nickel atoms were assumed to possess local moments if at least 8 out of the 12

possible near neighbours were also nickel atoms. A cluster concentration of c p(c)/N was obtained for an alloy of solute concentration c, composed entirely of uniform N-spin clusters, where p(c) was the concentration dependent probability that a Ni atom has 8 or more near neighbours.

Hamiltonians for small clusters of 2-4 spins were solved exactly, the specific heat per cluster as a function of reduced temperature $k_B T/J^{dd}$ exhibited a broad peak, increasing in amplitude and positioned at temperatures increasing with the number of spins per cluster. For the larger sized clusters of Cu Ni alloys (N = 50 spins experimentally) tractable results could only be obtained at low temperatures $k_B T \sim \mu_B B \ll J^{dd}$. In this low temperature regime spins were rigidly aligned parallel to each other by the relatively strong intracluster exchange interactions. Thermal fluctuations of the giant effective cluster moments in a uniform mean-field B gave rise to the familiar Schottky type specific heat contributions. In the paramagnetic alloys the effective field B was assumed to be equal to the anisotropy field of pure iron with a characteristic energy $\mu_B B \sim 0.05 k_B$. In the ferromagnetic alloys ($c > c_{CRIT} \sim 43\%$) the effective field was derived from the molecular field theory expression 1.7, valid for $T < T_c \ll J^{dd}/k_B$.

$$\mu_B B = \frac{6 k_B T_c}{(N+2)} \cdot \left[1 - (T/T_c)^2\right] \qquad 1.7$$

No account was taken of fluctuation effects.

In the paramagnetic alloys where $k_B T/\mu_B B \sim 40$ at 2 K the specific heat per cluster was predicted to increase as $\sim 1/T^2$ and to reach a peak at some temperature below 1 K before falling to zero. In the ferromagnetic alloys where $k_B T/\mu_B B \sim 1$ at 2 K the specific heat per cluster was predicted to be weakly temperature dependent or perhaps to fall with the decrease of temperature. These theoretical predictions were

in remarkable qualitative accord with the experimentally observed behaviour considering the simplicity of the model's basic assumptions.

Soukoulis and Levin (9, 10) developed the cluster mean field model into a model of a spin glass based on the Edwards-Anderson mean-field treatment (see section 1.3). Their work was motivated by the failure of the Edwards-Anderson model to predict the rounded maximum in the specific heat which was observed experimentally to occur between T_f and $2T_f$. Their calculations based on uniformly sized clusters of 3 and 6 spins revealed for antiferromagnetic intracluster spin interactions a very broad specific heat maximum occurring between T_f and $2T_f$ and a smaller feature at T_f (see fig. 1.2.3). For ferromagnetic intracluster spin interactions the specific heat exhibited a cusp as in the original Edwards-Anderson theory, the intercluster specific heat contribution dominating such systems of small clusters. Exact solutions of the Heisenberg hamiltonian for the intracluster interactions of clusters of more than 6 spins were prohibitively long; Soukoulis (11) obtained Ising approximation solutions for these larger clusters. The specific heat evaluated for such clusters (N = 15) exhibited a rounded peak above T_f, but somewhat less broad than that observed for the systems of small clusters with antiferromagnetic intracluster spin couplings, though this was considered to be an artifact of the Ising approximation. A further attempt to crudely approximate the oscillatory RKKY spin interaction by considering an antiferromagnetic second neighbour coupling in addition to the ferromagnetic first neighbour coupling, resulted in a similarly shaped peak, but shifted closer to T_f. Only compact cluster spin configurations were considered in their analyses, whereas percolation theories predicted that clusters in alloys close to the percolation concentration (not necessarily the critical concentration) were rather ramified in shape (see section 1.4). Riess (12) took account of fluctuations in his mean-field approach and predicted

Fig. 1.2.3 Soukoulis and Levin, Ref. 10

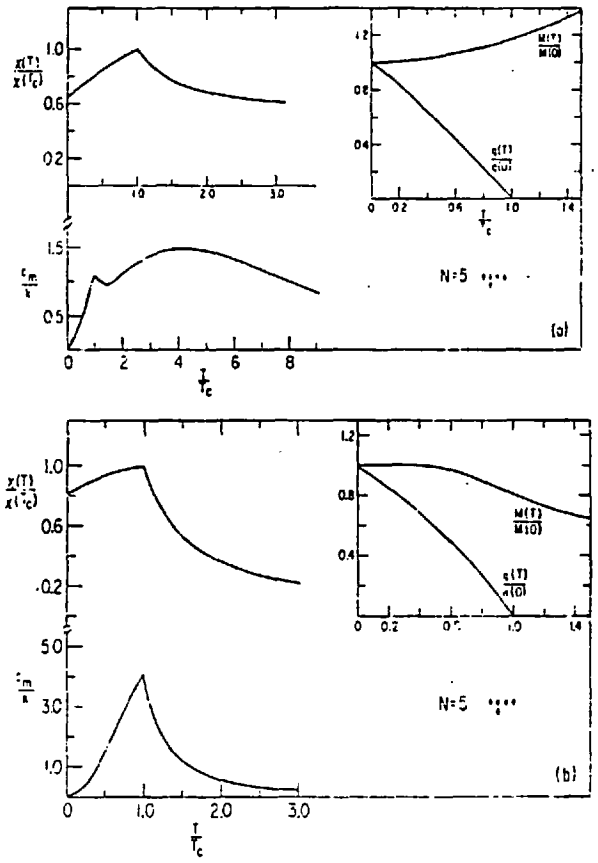

FIG. 2. Temperature dependences of the static susceptibility and specific heat per cluster for $N = 5$ spins in an (a) antiferromagnetically and (b) ferromagnetically coupled cluster. The inset plots the temperature dependences of the normalized cluster moment and order parameter. The ground-state spin configuration is also shown.

Fig. 1.2.6 a) Robinson and Friedberg , Ref. 20

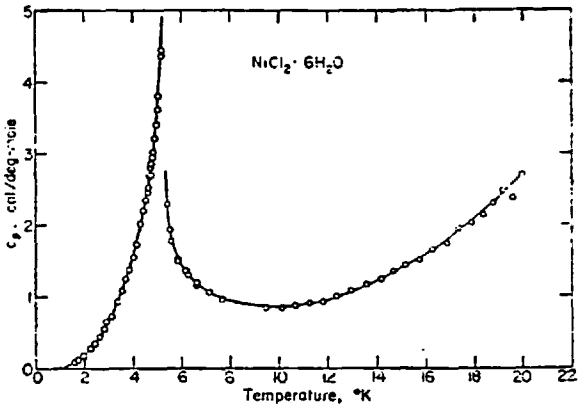

FIG. 1. Molar specific heat of $NiCl_2 \cdot 6H_2O$ as a function of temperature.

b) Kornblit et al., Ref. 19

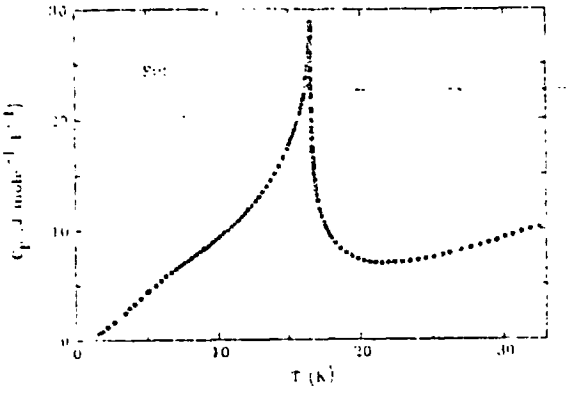

IG. 1. Specific heat of EuS-I as a function of the temperatu

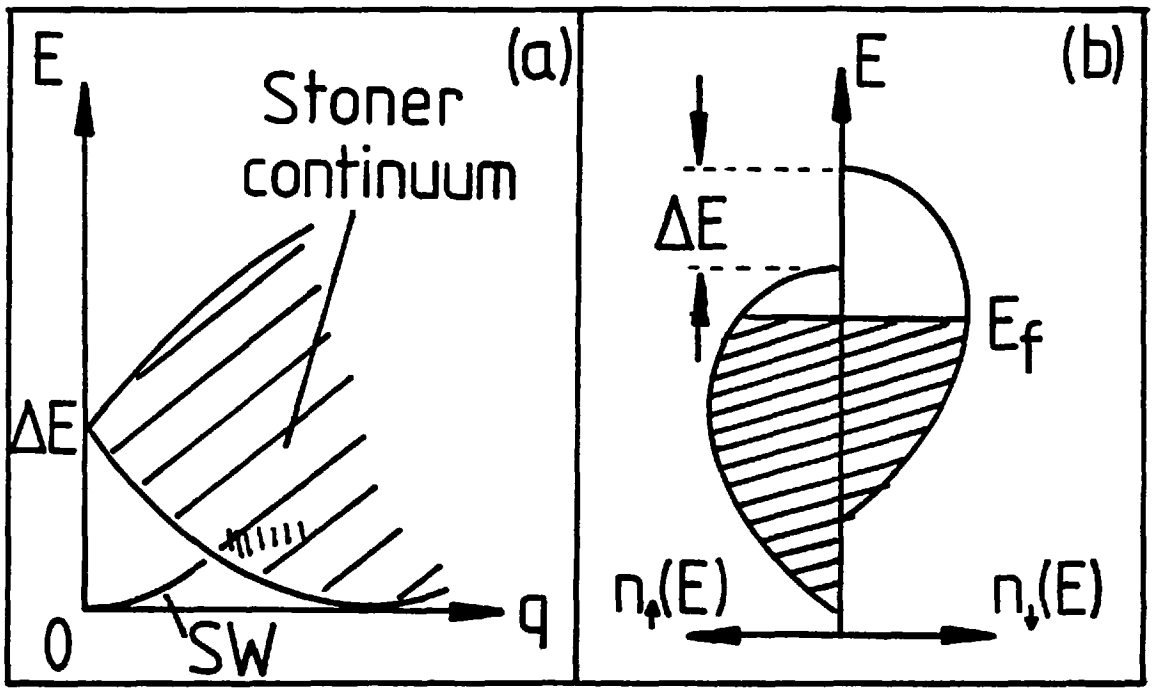

FIG.1.25

specific heat behaviour very similar to that shown in fig. 1.2.3 for antiferromagnetic intracluster spin interactions.

An interesting experimental observation of this type of specific heat behaviour has been reported by de Jongh (13) and Algra et al (14) for the pyridine nitroxide complex of cobalt chlorate, site diluted with non-magnetic Zn. The pure cobalt salt exhibits a sharp λ-type critical specific heat anomaly (see fig. 1.2.4) which becomes weakened by the increasing dilution and gradually obscured by the growth of a Schottky-type anomaly due to the extensive regions of short range order resulting from the break up of the long range order. The critical specific heat anomaly becomes too small to observe well before the percolation concentration $c_{CRIT} \sim 31\%$ is reached. In the language of percolation theory, the importance of groups of spins in finite-sized clusters, responsible for the Schottky-type specific heat contribution, grows with increasing dilution at the expense of the infinite cluster response for the critical specific heat feature. Algra et al (14) argued that the predicted number of finite clusters at a cobalt concentration of $\sim 50\%$ would be too small to account for the size of the remaining Schottky-type contribution. They speculated that the infinite cluster being rather ramified just above the percolation concentration would also contribute a Schottky-type specific heat term due to excitations of its many chain-like branches.

1.2.5 Collective spin excitations

An elementary excitation mode of a magnetically ordered system involves the propagation of a collective spin displacement as a quantised spin wave or magnon. The Heisenberg hamiltonian is the most appropriate hamiltonian to represent a system of localised spins with first neighbour interactions.

$$\mathcal{H} = -J \sum_{ij} \underline{S}_i \cdot \underline{S}_j \qquad 1.8$$

SPECIFIC HEAT OF

$(Co_{1-x}Zn_x)(C_5H_5NO)_6(ClO_4)_2$

FIG. 1.2.4

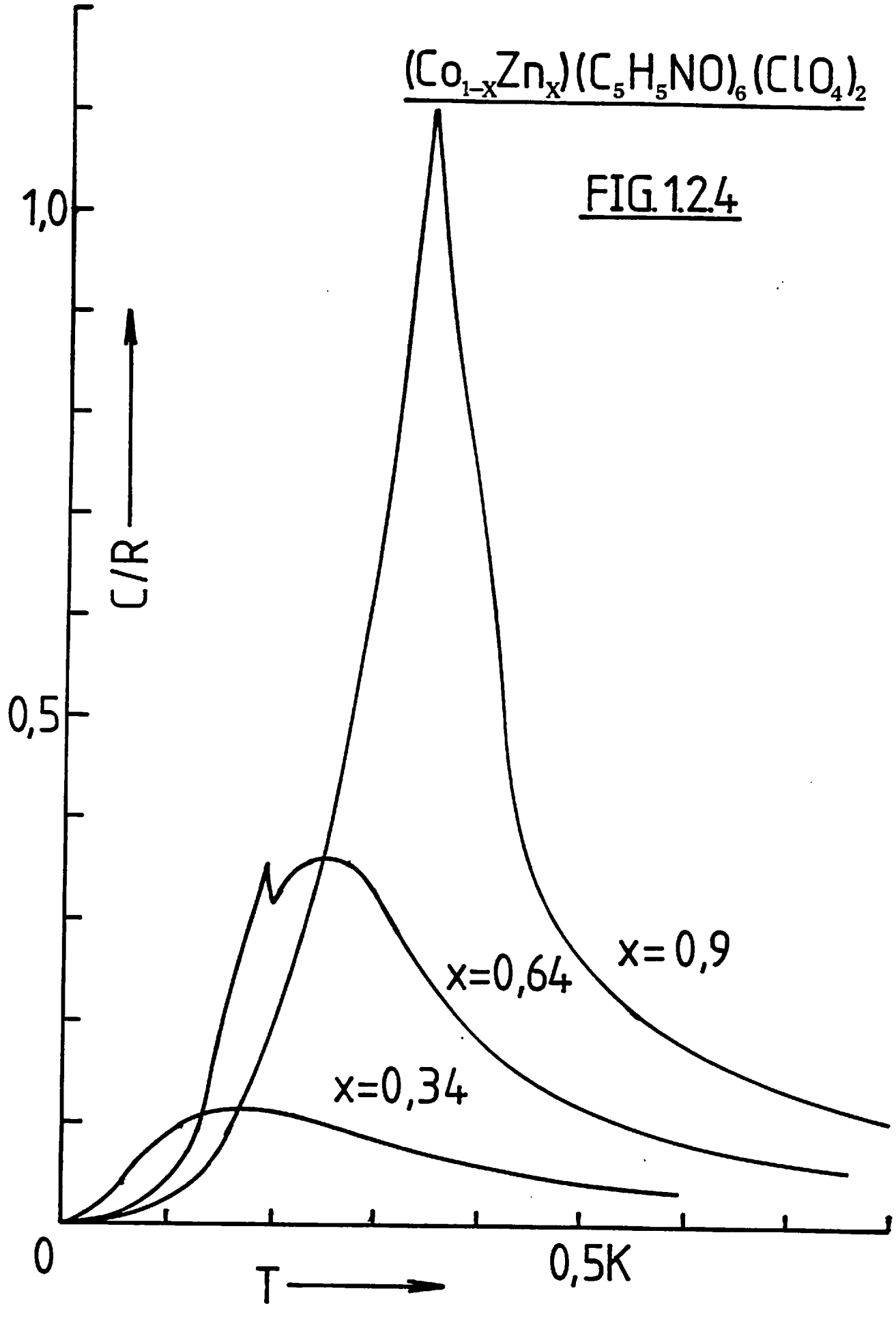

To derive the spin wave dispersion relationship the hamiltonian is usually rewritten in terms of the magnon creation and annihilation operators, S^+ and S^- respectively.

$$S^+ = S^x + iS^y$$
$$S^- = S^x - iS^y \qquad 1.9$$

This operator transformation is formally known as the Holstein-Primkoff transformation. The dispersion relations derived for a cubic ferromagnet and antiferromagnet are $\omega = D_F q^2$ and $\omega = D_{AF} q$ respectively in the long wavelength limit as q the spin wave-vector tends to zero. The spin wave stiffness constant D is proportional to T_c or T_N, the respective spin ordering temperature of a ferromagnet or antiferromagnet. Magnons obey Bose-Einstein statistics and their contributions to the specific heat may be evaluated from their total energy.

$$C_M = \frac{\partial}{\partial T} \int d\omega \hbar\omega g(\omega)\, n(\omega) \qquad 1.10$$

where the density of magnon states $g(\omega) \propto \omega^{\frac{1}{2}}$ for ferromagnets and ω^2 for antiferromagnets is evaluated from their respective dispersion relationships; $n(\omega) = 1/(e^{-\beta\hbar\omega} - 1)$ is the Bose-Einstein distribution. Evaluating the integral 1.10 leads to a spin-wave specific heat contribution of $C_m \propto (T/T_c)^{3/2}$ for ferromagnets and $C_m \propto (T/T_N)^3$ for antiferromagnets at low temperatures. In some antiferromagnets anisotropy leads to a gap in the spin-wave spectrum which can further complicate the specific heat behaviour.

The preceding discussion refers mainly to ionic compounds (typically MnF_2 and Eu S) with well defined localised moments whose low-temperature dynamics are well represented by a Heisenberg hamiltonian. In such insulating systems, devoid of electronic specific heat terms, the magnon term is usually dominant at low

temperatures, and easily observable experimentally. The situation in metallic ferromagnets is complicated by the presence of other elementary excitations, such as Stoner single-particle excitations, which involve the excitation of an electron from a majority-spin band state to a minority-spin band state. It is well established that magnons do exist in the long wavelength limit with a $C_m \propto (T/T_c)^{3/2}$ specific heat term (see Herring and Kittel, ref. 15), but further out in q-space they become critically damped in the region where the magnon branch meets the Stoner excitation continuum (see fig. 1.2.5a) and can decay into Stoner excitations. At low temperatures Stoner excitations lead to a temperature-linear specific heat of the form given in expression 1.3, where $n(E_F)$ now refers to the total density of states at the fermi level from both sub-bands. The topology of a d-band may be such that $\frac{dn(E)}{dE}$ and higher derivatives near the fermi level become important at finite temperature (due to the broadening of the fermi distribution), leading to additional temperature-linear specific heat terms arising from the greater significance of higher order terms in the Sommerfeld expansion (see Wohlfarth, ref. 16).

The relative importance at low temperatures of Stoner and spin wave excitations in an itinerant electron ferromagnet depends on the size of the exchange splitting ΔE (i.e. the relative energy shift between the two sub-bands which occurs when the electron correlation energy is sufficiently large and results in a redistribution of electrons between the subbands and hence a spontaneous magnetisation at $T = 0$; see fig. 1.2.5b). In weak itinerant electron ferromagnets, where the exchange splitting is small, Stoner excitations will dominate the low energy regime of the elementary excitation spectrum. Conversely, in strong itinerant ferromagnets spin waves dominate at low energies. The general question of low-lying elementary excitations of itinerant electron systems is reviewed in connection with their influence on the low-

temperature resistivity by Rivier and Mensah (17).

In spin glass systems the absence of long range order has been shown by Spalek and Rivier (18) to lead to both non-propagating spin diffusive modes ($q > q_c$) and damped propagating spin wave modes ($q < q_c$) which in the long wavelength limit (where the details of the disorder are unimportant) exhibit a linear dispersion relation $\omega \sim q$ similar to an ordered antiferromagnet.

1.2.6 Critical specific heat anomalies

Specific heat anomalies are characteristically associated with spin ordering in magnetic systems which can either be of a non-cooperative type, as in paramagnetic salts (e.g. $Ni\,SO_4 \cdot 6H_2O$) or of a cooperative type (phase transition) as observed in ferromagnets like EuS, $Gd\,Cl_3$ and antiferromagnets like $Ni\,Cl_2 \cdot 6\,H_2O$. In the former case a Schottky-type anomaly is usually observed in the low temperature specific heat. In magnetic systems undergoing cooperative phase transitions to long range order a λ-type singularity is often observed in the specific heat at the ordering temperature (see figs. 1.2.6a and b) which usually exhibits close to the singularity an inverse power law or logarithmic temperature dependence or $\ln \epsilon$ where $\epsilon = \left|\frac{T-T_c}{T_c}\right|$ is the reduced temperature. Such singularities are not well described by conventional Landau mean field theory, which predicts a discontinuous change in specific heat at the ordering temperature and a linear temperature dependence below it. The specific heat of a magnetically ordered system well below its ordering temperature is due mainly to spin waves which cannot be treated in mean field theory. Short range magnetic order often persists well above the ordering temperature, as is evidenced by the presence of magnetic specific heat contributions. Close to the singularity critical fluctuations of the order parameter (usually the spontaneous magnetisation) are observable by the

critical scattering of neutrons when the size of the fluctuations diverges.

Geometrical critical behaviour, in analogy with the thermal critical behaviour just described, is observable as a function of concentration in a number of magnetic properties near some critical concentration at which long range magnetic order is established from a disordered regime (see section 2.4.4). Mathon (21) employed simple Landau mean-field theory to deduce the qualitative concentration dependence of the low-temperature specific heat and electrical resistivity close to the critical concentration c_{CRIT}. The theory was generally applicable to any weakly ferromagnetic alloy with spatially unifarm magnetisation. The theory assumed that close to the critical concentration the relative magnetisation ζ was small ($\zeta = 0$ at $c = c_{CRIT}$) and therefore, following Landau's theory, the free energy was expanded as a power series in the magnetisation. Neglecting fluctuations in the magnetisation, the free energy (see expression 1.11) was minimised with respect to the magnetisation M.

$$F = F_o + \tfrac{1}{2}A(T,c)M^2 + \tfrac{1}{2}B(T,c)M^4 \ldots \qquad 1.11$$

Two solutions were obtained, the first $M = 0$ corresponds to $A > 0$ in the paramagnetic state ($c < c_{CRIT}$) and the second $M = \left(\frac{-A}{B}\right)^{\frac{1}{2}}$ corresponds to $A < 0$ in the ferromagnetic state ($c > c_{CRIT}$). It was therefore argued that the simplest formulation of $A(T, c)$ would be $A(T, c) = a(T)(c_{CRIT} - c)$. The temperature dependence of the magnetisation was taken to be of the usual mean-field theory form.

$$\frac{M(T,c)}{M(0,c)} = \left[1-(T/T_c)^2\right]^{\frac{1}{2}} \qquad 1.12$$

Assuming that the low temperature dependence of B was negligible such that $B(T) \simeq B$ and by differentiating the free energy the low-temperature linear specific

heat coefficient was shown to change by $\Delta\gamma$ close to the critical concentration.

$$\Delta\gamma = \gamma_{FERRO} - \gamma_{PARA} \simeq D(c_{CRIT}-c) \qquad 1.13$$

where $D = a(0)(M(0,c)/T_c)^2$ is independent of concentration. The theory was valid, provided the fluctuations in the magnetisation were small compared to the magnetisation, i.e. at sufficiently low temperatures (except for a region very close to c_{CRIT}). The theory was not considered to be applicable to alloys forming localised moments as their magnetisation may be spatially non-uniform.

1.3 Spin Glass Theories

1.3.1. Introduction

The concept of a spin glass was a natural development of theoretical work on the indirect exchange interactions between localised moments on transition metal impurities in noble metal hosts. The early work of Friedel (22) and Anderson (23) had established the condition for the localisation of moments on impurity sites. The essence of the localisation process was in the polarisation of virtual bound states (VBS) which occur near the fermi surface due to resonant scattering of conduction electrons by the impurity ion potentials. The condition for the formation of localised moments was that the width of the VBS should be less than the on-site electron correlation energy.

The theory of indirect exchange interactions of nuclear moments mediated by the conduction electrons was originally proposed by Ruderman and Kittel (24) to account for nuclear spin resonance phenomena. The basic concept was extended to indirect exchange interactions between local moments in dilute alloys (Cu Mn in particular) by Yosida (25) who derived an expression (1.12) for the now familiar Ruderman-Kittel-Kasuya-Yosida (RKKY) oscillatory exchange interaction.

$$J(r) = A(x\cos x - \sin x)/x^4 \qquad 1.12$$

$$x = 2k_F r$$

where r is the distance between moments, k_F the k-space fermi radius and A is related to the s-d interaction strength. In the asymptotic limit $x \gg 1$ expression 1.12 simplifies to :

$$J(r) = A\cos x / x^3 \qquad 1.13$$

The random phase of the exchange interaction results from the random distribution of moments in solid solution alloys through the cosine dependence on r, the distance between moments. The $1/r^3$ dependence of the interaction strength results in concentration scaling of many spin glass properties as discussed by Souletie and Tournier (26).

Early spin glass theories were based on a mean-field distribution p(B) representing the random phase of the exchange interaction between moments. The work of Marshall, Klein and Brout in connection with the low-temperature specific heat behaviour has already been discussed (see section 1.2.3). The main resurgence of theoretical interest in spin glasses did not occur until after the publication of AC susceptibility measurements on several spin glass alloys by Cannella and Mydosh (see Chapter 2) which exhibited characteristic cusp-like peaks strongly suggestive of a cooperative spin ordering. Some of the theories which followed this striking experimental observation are outlined in the following sections.

1.3.2 Mean-field theories

Adkins and Rivier (27) were the first to attempt to extend the early mean-field concepts to account for the cusp-like AC susceptibility peaks of spin glasses.

In their model the mean-field distribution p (B) was calculated from first principles, employing the formalism of the random-walk problem. A short range order parameter, the local magnetisation m (T), evolved naturally from this treatment. The collective behaviour originated from the long range of the RKKY interaction (limited to the electron mean free path in real alloys) with respect to the coherence length of the short range order. A susceptibility cusp was predicted to occur at a temperature T_o above which the short range order disappeared.

Edwards and Anderson (28) adopted a different approach in which they assumed the ground state of the spin glass could be described by a classical spin interaction hamiltonian (expression 1.14) in which the first-neighbour exchange interactions were distributed Gaussian fashion $P(J_{ij}) \sim \exp\left\{-J_{ij}^2/2J^2\right\}$.

$$\mathcal{H} = -\sum_{\langle ij \rangle} J_{ij} S_i S_j \qquad 1.14$$

Employing a statistical mechanical method they derived the free energy of the system from the partition function $Z = \mathrm{Tr} \exp -\beta\mathcal{H}$ using the now controversial replica method to evaluate the average of the ln Z term in the free energy.

$$\langle \ln Z \rangle_c = \lim_{n \to 0} \frac{1}{n}\left\{\langle Z^n \rangle_c - 1\right\} \qquad 1.15$$

where $\langle Z^n \rangle_c$ is the bond configurational average over the partition function of the n identical replicas of the original system. An order parameter q defined the correlation between spins in different replicas.

$$q = \langle S_i^{\alpha} S_i^{\beta} \rangle_c \qquad 1.16$$

Above temperature T_o the order parameter was zero, whereas just below T_o it could be expanded as a power series in $t = \frac{(T_o - T)}{T}$ the reduced temperature.

The theory predicted a cusp in the susceptibility and specific heat at T_o, and that the specific heat tends to a constant value as T approaches zero. This latter result is a feature of the classical approach of the Edwards-Anderson theory. A quantum mechanical treatment by Fischer (29) in which a Heisenberg spin interaction hamiltonian was employed gave the correct low-temperature linear specific heat behaviour. In a later paper Edwards and Anderson (30) consider the dynamics of their model spin glass through the time dependence of the order parameter $q(t) = \langle S_i(t)\, S_i(0) \rangle$. They argued that the low temperature specific heat could contain terms both linear and cubic in temperature, due respectively to the finite density of spin "tunneling" states near zero energy (see also Anderson et al (31) for further discussion) of the highly degenerate ground state and to low-lying antiferromagnetic spin wave - like excitations.

Sherrington and Southern (32) and Sherrington and Kirkpatrick (33) proposed a spin glass model with infinite-ranged interactions, suggesting that it should be solvable in analogy with the exact mean-field theory for a ferromagnet. Fluctuations of the mean-field parameter J_o were distributed according to Gaussian statistics with probability $P(J_{ij}) \sim \exp - \left\{ (J_{ij} - J_o)^2 / 2J^2 \right\}$. Two order parameters were defined : $m = \langle\langle Si \rangle\rangle_c$ and $q = \langle\langle S_i \rangle^2 \rangle_c$ (the inner $\langle\rangle$ - bracket represents a thermal average and the outer $\langle\rangle$ - bracket a bound configurational average). The free energy was then derived using the same replica procedure as was employed by Edwards and Anderson. A magnetic phase diagram was established with ferromagnetic ($m = q = 0$) regimes. The theory predicted a cusp in both the susceptibility and specific heat at temperature T_o but gave unphysical results near $T = 0$.

Thouless et al (34) obtained an approximate solution near $T = 0$ to the Sherrington and Kirkpatrick infinite-ranged model by avoiding the use of the replica method. A high-temperature series expansion of the free energy gave

similar results to the original model. A mean-field theory treatment which took account of both the mean $\langle S_i \rangle$ and variance $\langle S_i^2 \rangle$ of the local magnetisation was employed to obtain low-temperature solutions. The specific heat was predicted to have a quadratic temperature dependence near $T = 0$, although they suggested that this unusual result may be an artifact of the infinite-ranged model (employed to obtain an tractable solution) and should therefore not be taken too literally.

1.3.3 Other models and simulation experiments

An alternative model proposed by Smith (35 - 6) was based on the concept of finite-sized regions or clusters in which spins were highly correlated in a predominately collinear fashion, and outside which thermal fluctuations disrupted the spin correlations. A temperature dependent cluster radius r_c could thus be defined by the relation $S\,|J(r_c)| \sim kT$, where $S\,|J(r)|$ is a measure of the spin correlation energy. Using an early percolation theory result due to Domb and Dalton (51) for a 3D Bethe lattice, he derived the critical cluster radius and hence the critical temperature T_o for percolation of the long-ranged RKKY interactions which stabilise an infinite-sized spin cluster below T_o. At low concentrations T_o was linearly dependent on concentration. He speculated that the experimentally observed $\sim c^{0.6}$ concentration dependence at higher concentrations (e.g. AuFe 5 - 12% Fe) may be due to a pre-asymptotic $J \sim 1/r^2$ dependence of the RKKY interaction strength. A superpara-magnetic blocking of the infinite cluster was considered to be responsible for the sharp cusp in the susceptibility at T_o. This cluster model leads to the familiar low-temperature linear specific heat behaviour by the same arguments given in the theories of Marshall, Klein and Brout. However, in contrast to these earlier works and most other cluster models, the high-temperature ($T > T_o$) specific heat behaviour was argued to be $\sim T_o/T$ due to residual magnetic correlations rather than the $(T_o/T)^2$

dependence usually expected from the tail of a Schottky anomaly.

In cases where analytical methods become too difficult to apply, some researchers have advocated the use of Monte Carlo computer experiments to simulate the behaviour of spin glass models. The simulation method is based on the Monte Carlo method of evaluation of many-dimensional integrals. The free energy of a finite-sized sample of spins ($\sim 10^3 - 10^4$ spins) is averaged over a number of the more probable configurations (probability $\sim \exp -\beta E$) of the system selected at random. The method is, however, limited by both the finite size of the sample and the periodic boundary conditions usually imposed to overcome the complications of surface effects. This size limitation implies that the method is not strictly suitable for simulating true critical behaviour which, by nature, involves the divergence of spin correlations to macroscopic dimensions. Binder and Schroder (37) simulated the Edwards-Anderson (EA) spin glass model in an attempt to clarify the validity of mean-field approximations used in this model. They chose to simulate a square lattice ($N \times N$, $24 \leq N \leq 160$) of $S = \frac{1}{2}$ Ising spins with random (Gaussian distribution) first-neighbour exchange interactions as in the original EA-model. Although time restrictions implied that their simulated systems could never reach a true equilibrium state, they argued that their results were sufficiently close to be representative of that state. A sharp peak was observed in the susceptibility at T_o which became rounded in the presence of finite external fields, although this model like the original model was less sensitive to external fields than a real spin glass. A rounded peak was observed in the specific heat which had a maximum just above T_o, there was no detectable anomaly at T_o. These results were apparently independent of the size of the simulated system.

Walker and Walstedt (38) investigated the distribution of internal fields and the low-temperature specific heat of a system of RKKY coupled spins randomly

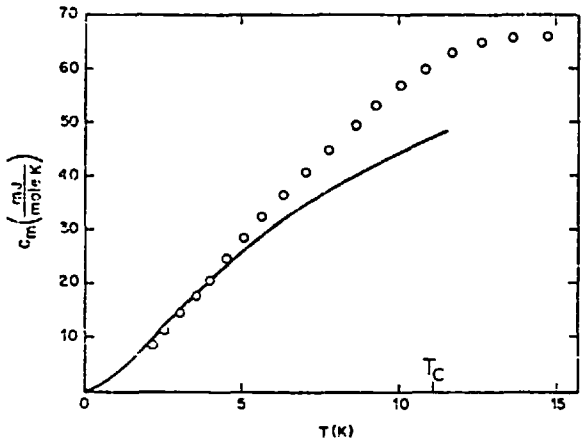

FIG. 3. Solid curve, molar specific heat from model calculated as described in text. Circles, data for 1.2% Mn in Cu from Wenger and Keesom (Ref. 2).

Fig. 1.3.1

Walker and Walstedt, Ref. 38

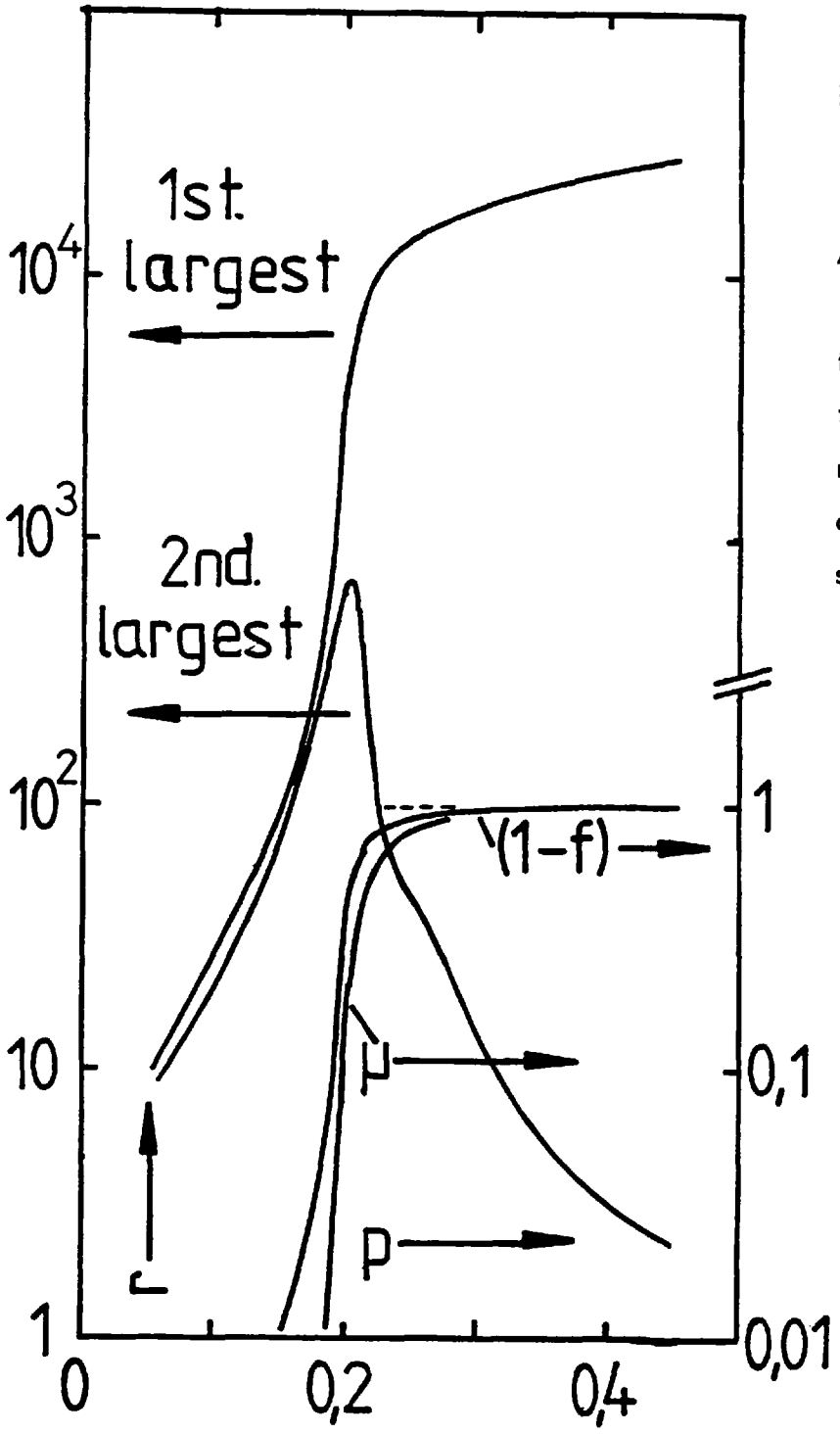

Fig. 1.4.1

Dean and Bird, Ref. 50

A plot of the size r of the 1st. and 2nd. largest clusters, the fraction of spins (1-f) in the infinite cluster and μ the modified second moment of cluster size, as a function of site occupation probability p.

embedded at low concentration in an FCC lattice to simulate the dilute spin glass Cu Mn. The purpose of their simulation was in part to attempt to resolve the controversy centred on the low temperature - linear specific heat obtained in the older mean-field treatments by Marshall, Klein and Brout (3 - 5). These employed an Ising model for which there was argued to be a finite probability for a spin to be in a zero mean field. In contrast, a self-consistent derivation (see comment, ref. 39) of the mean-field probability distribution which fully took into account the spin correlations of vector spins led to a probability distribution which vanished as $p(\underline{B})\, d^3B \sim B^2 dB$ at low fields. Such a distribution has been shown to lead to a low-temperature specific heat of the form $C \sim T^3$ contrary to experimental observations. Rivier (39) argued that this was not necessarily so, and pointed out that the relevant probability distribution for calculating the specific heat was $p(B_z)$ not $p(|\underline{B}|)$ where B_z was defined by the direction of the local magnetisation. Since $p(B_z)$ was finite at $B_z = 0$ a low temperature - linear specific heat was obtained in the same manner as in the older derivations.

In their simulation experiment, Walker and Walstedt considered systems of 96 and 324 spins in total, distributed in the FCC lattice at average concentrations of 0.3 and 0.9%. The spin interaction was assumed to follow the asymptotic form of the RKKY interaction, truncated to avoid double interactions resulting from the periodic boundary conditions. Spin configurations were varied iteratively to minimise the total free energy of the system. The approach to equilibrium involved initially a very rapid phase followed by a much slower phase in which spins underwent remarkably large changes of orientation which was considered to reflect the weakness of the exchange stiffness (near equilibrium configuration) but could also be interpreted as evidence for a high ground state degeneracy (as first proposed by Anderson et al., ref. 31). The

computer generated mean-field probability distribution p(B) was shown to have the same form as calculated by a self-consistent analytical method (see ref. 39).

$$p(B) \sim \frac{B^2 \Delta_B}{(B^2+\Delta B^2)^2} \qquad 1.17$$

The spectrum of elementary excitations was also calculated from linearised classical equations of motion of the spins in their equilibrium configurations. The low-lying modes were shown to be the most extended. The low-temperature magnetic specific heat results (see fig. 1.3.1) compared favourably with measurements by Wenger and Keesom on a Cu 1.2% Mn alloy (see Chapter 2). A small departure from linearity at temperatures below $\sim$ 1K was ascribed to the possible presence of a small gap in the excitation spectrum at $\omega = 0$, concluding that it could have resulted from the neglect of some small anisotropy in their model.

1.3.4 Concluding remarks

At the time of writing this thesis there exists no satisfactory solution of mean-field spin glass model; there are certainly no exact treatments and the approximate solutions suffer from many problems (e.g. negative entropy). Some of the controversy concerning the lower critical dimensionality (below which no phase transition exists) of spin glass models and the replica method have been indicated in the introductory comments of recent communications by Anderson and Pond (40) and Bray and Moore (41).

1.4 Percolation Theory

Percolation theory is a statistical theory of random systems consisting of many elements, in which adjacent elements may or may not be linked. In general there exists no unbroken path through the entire system below some critical concentration of links, which depends on the dimensionality and coordination of the system. The theory has many applications ranging from the propagation of a viral infection to the

conduction properties of a resistor network (see de Gennes's article, ref. 42, for a general introduction).

The specific application of the theory relevant to this work concerns the emergence of long range magnetic order in random solid solution binary alloys. Direct exchange interactions between adjacent magnetic solute atoms, randomly substituted for non-magnetic atoms of the host matrix, link the solute atoms into magnetically correlated clusters. Two solute atoms belong to the same cluster provided there is an unbroken chain of adjacent solute atoms linking them. At low solute concentrations, clusters are finite in size and the magnetic correlation length, which is restricted by the size of clusters, cannot diverge at $T = 0$, so the system exhibits no spontaneous magnetisation. The average size of the finite clusters $S(p)$ grows with increasing solute fraction p until a critical solute fraction p_c is reached, at which $S(p_c)$ diverges with the appearance of an infinite cluster of macroscopic dimensions. The magnetic correlation length in the infinite cluster diverges below some critical temperature T_c ($T_c = 0$ at $p = p_c$) and long-range magnetic order is established. At higher solute fraction ($p > p_c$) the development of the infinite cluster, as it incorporates more and more finite clusters, is reflected in the rapid increase of the ordering temperature T_c. Correspondingly, the finite clusters become less and less numerous with increasing solute fraction (see fig. 1.4.1).

1.4.1 Early works

In an attempt to understand the behaviour of magnetic systems with dilution several early researchers had proposed improvements of the Bethe-Peierls-Weiss (BPW) method (see Smart, ref. 43, for an introductory survey). The BPW procedure involves taking a small cluster of atoms consisting of an arbitrarily chosen central atom and its first-neighbour shell, then solving exactly the partition function of this small system in the presence of an effective mean-field due to the rest of the atoms in the crystal.

This approach was generalised by Sato et al (44) to take account of dilution in a random substitutional binary alloy by replacing the coordination number z in the original BPW theory by an average coordination number cz (c is the solute concentration). A critical concentration of $c_{CRIT} = 2/z$ was obtained by this average coordination approach, which neglects concentration fluctuations. A more realistic approach in which the distribution of atoms in the entire crystal is taken into account was also proposed. This cluster variation method involved a direct calculation of the entropy of the system (which determines the free energy in this particular case) by summing pairwise contributions (in the pair-approximation). The free energy was minimised with respect to variation of the cluster parameters, and the critical concentration derived by this procedure was $c_{CRIT} = 1/(z-1)$. Smart (43) considered a Heisenberg spin interaction and configurationally averaged the cluster partition function in his adaptation of the BPW method and obtained the same critical concentration as Sato et al had by their cluster variation method. Sato and Kikuchi (45) later published results of their tetrahedral cluster variation calculations of the critical concentrations for both ferromagnetic and antiferromagnetic transitions in BCC and FCC-structured alloys. Percolation in an FCC-structured antiferromagnet was reported to be complicated by the presence of four different sublattices which resulted in the delay of the emergence of long range magnetic order until much greater solute concentrations ($c_{CRIT} \sim 44.5\%$) were reached. De Gennes et al (46) employed a precursory form of the series expansion method of calculating critical concentrations and obtained approximations to the critical values for various cubic lattices. The critical concentrations obtained in these earlier works are summarised together with more recent results for the FCC lattice in table 1.1.

1.4.2 Percolation theory methods of evaluating critical concentrations

Random solid solution alloys are examples of the so-called site problem in

the standard terminology of percolation theory (see introductory reviews by Shante and Kirkpatrick, ref. 47, or more recently by Stauffer, ref. 55). Magnetic solute atoms are randomly substituted with probability p on a host lattice of non-magnetic atoms. There exists a critical threshold probability $p = p_c$ above which the probability $P(p)$ of a particular site being part of an infinite cluster becomes non-vanishing. There are two basic methods of estimating this critical probability; one is an analytical method in which p_c is defined by the radius of convergence of a series expansion of the mean cluster size $S(p)$ in powers of p and the other employs a Monte Carlo method to evaluate numerically the probability $P_r(p)$ of a particular solute atom being part of an r-site cluster as r tends to infinity.

Series expansion method

The series expansion method of estimating p_c was proposed by Sykes and Essam (48). The principle of the method is to establish the radius of convergence of the power series in p for $S(p)$, the mean cluster size, which must diverge at $p = p_c$ with the appearance of the infinite cluster.

$$S(p) = 1 + \sum_{r=1}^{\infty} a_r p^r \qquad 1.18$$

The coefficients a_r of the series expansion are obtained by enumerating the possible configurations of an r-site cluster (a technique similar in principle to the high temperature expansions in statistical mechanics). Sykes and Essam conjectured that the form of the coefficients for 2D and 3D lattices in the asymptotic limit is $a_r \sim r^j p_c^{-r}$, where j is the critical exponent of the divergence of $S(p)$ at $p \sim p_c$, i.e.

$$S(p) \quad 1/(p_c - p)^{j+1} \qquad 1.19$$

The critical probability was obtained from the ratio ρ_r of alternately

successive coefficients in the limit as r tends to infinity.

$$p_c = 1/\rho = \lim_{r \to \infty} 1/\rho_r \qquad 1.20$$

$$\text{where } \rho_r = \sqrt{\frac{a_r}{a_{r-2}}}$$

In 3D lattices the slope of the convergence determined from an extrapolation of plots of $j_r = r(\rho_r - \rho)/\rho$ vs. $1/r$ to the $1/r = 0$ axis, strongly suggested that j was a rational fraction, $j = 11/16$. By employing this value of j the critical probabilities for various 3D lattices were estimated, in the limit of large r, from successive approximations β_r defined as :

$$\beta_r = (1 + j/r)/\rho_r \qquad 1.21$$

Domb and Dalton (51) employed the series expansion method to estimate the critical probabilities for 2D and 3D lattices with longer range interactions (of interest to this present work in which magnetic solute atoms are in a metallic host). They obtained critical probability values of 0.136 and 0.061 for the FCC lattice by considering interactions up to second- and third-neighbour distances respectively. From the trend in these critical probabilities they deduced that the product of the lattice coordination z (which includes all higher order neighbour interactions) and the critical probability was invariant for a given dimensionality (in the site problem). For 3D lattices they obtained :

$$z\, p_c \simeq 2.7 \qquad 1.22$$

Monte Carlo method

Monte Carlo experiments by Frisch et al (49) and Dean and Bird (50) employed finite-sized lattices with between $N = 10^3$ and 10^4 sites. The method employed by

Frisch et al involved estimating the value of $p = p_c$ at which the probability $P(p)$ of a magnetic site chosen at random being part of a spanning cluster (i.e. a cluster which extends to the dimensions of the finite lattice sample) differs infinitesimally from zero. The probability $P(p)$ was approximated by the probability $P_r(p)$ of a site being part of the largest r - site cluster (where r tends to a large number $\sim pN$). Dean and Bird estimated p_c from the value of p at which the largest change was observed in the modified second moment of the cluster distribution μ (defined by 1.2 3) for a given increment Δp.

$$\mu = \frac{1}{(pN)^2} \sum_r \nu_r r^2 \qquad 1.23$$

ν_r is the number of r-site clusters. A plot of both μ and the fraction f of sites in finite clusters is given in figure 1.4.1 from Dean and Bird's results for an FCC lattice.

Reference	Method	Percolation threshold probability p_c
Sato et al (44)	ACN	0.167
	CV (pair approx.)	0.091
Sato and Kikuchi (45)	CV (tetrahedron approx.)	0.156
Smart (43)	Modified BPW	0.167
de Gennes et al (46)	Short series expansion	0.162
Sykes and Essam (48)	Series expansion	0.195 ± 0.005
Frisch et al (49)	Monte Carlo	0.199 ± 0.008
Dean and Bird (50)	Monte Carlo	0.208 ± 0.01

Table 1.1 - Summary of estimates of critical probabilities of a transition to ferromagnetism in an FCC lattice (first neighbour interactions only)

1.4.3 Cluster shape near the percolation threshold

It was suggested by Domb (52) that the shape of the larger finite clusters near the percolation threshold, which would link together at the threshold to form the infinite cluster, would have an important effect on the critical behaviour of the percolating system. These dominant r-site clusters with perimeters $b \sim a r^{\sigma}$ were argued by Domb to have more ramified ($\sigma \sim 1$) than compact ($\sigma \sim 2/3$) spin configurations. The infinite cluster just above the threshold, being highly ramified, would possess many one-dimensional (1D) links. However, Domb pointed out that there would be a sufficient number of cross links to give the cluster a 2-3D character with non-vanishing spontaneous magnetisation at $T = 0$. He added that it would be likely that the weaker spin correlations in the 1D links would lead to a break up of long range magnetic order in the infinite cluster well before short range order due to localised spin correlations in the finite clusters breaks up. In contrast, Stauffer (53) argued that it was the internal perimeters of the larger clusters rather than external perimeters that were more ramified, and since only the latter influence the critical behaviour he did not consider ramification all that important. The controversy is still very active (see for example the introductory comments in Domb and Stoll's paper, ref. 54).

1.4.4 Application of percolation theory

Percolation theory generally considers only first-neighbour direct exchange interactions and neglects all longer range indirect exchange interactions which are certainly present in dilute transition metal - noble metal alloys, and experimental evidence strongly suggests that they are still dominant just below the percolation threshold. If these longer range indirect interactions reinforce the first-neighbour direct interactions they will lead to a lowering of the critical probability p_c, which

in the limit of infinite range interactions leads to a $p_c = 0$. If the converse is the case, they will raise p_c. An oscillatory interaction of the RKKY-type would have a more complex effect on p_c which would depend on the relative strength and phase of the interaction.

Fluctuations of solute concentration and slight deviations from a perfectly random distribution of solute atoms (due to tendencies to form metallurgical solute clusters or short range order of solute atoms) in real alloys may also modify the percolation threshold.

If, to a very rough approximation, only independent, non-interacting magnetically rigid clusters (i.e. at low temperatures compared to the first-neighbour exchange energy) are considered within a percolation theory, the specific heat will be Schottky-like due to the superparamagnetic behaviour of the finite clusters. In general the specific heat will depend in a complex way on the distribution of cluster shapes and sizes. The behaviour of the larger, and possibly more ramified, clusters which form the percolation threshold may be determined by their shape anisotropy. In the absence of any detailed information on the distribution of cluster shapes and sizes and their interactions, it is not possible to make even the most rudimentary predictions about the specific heat behaviour of a system of finite percolation clusters.

REFERENCES

1. De Launay J., 1956, "Theory of specific heat and lattice vibrations", Solid State Phys. 2, ff 219, (eds. Seitz F. and Turnbull D.)
2. Gopal E.S.R., 1966, "Specific heats at low temperatures", Plenum Press, New York
3. Marshall W., 1960, Phys. Rev. 118, 1519
4. Klein M.W. and Brout R., 1963, Phys. Rev. 132, 2412
5. Klein M.W., 1964, Phys. Rev. 136, A1156
6. Klein M.W., 1976, Phys. Letts. 59A, 52
7. Overhauser A.W., 1960, J. Phys. Chem. Solids 13, 71
8. Levin K. and Mills D.L., 1974, Phys. Rev. B9, 2354
9. Soukoulis C.M. and Levin K., 1977, Phys. Rev. Letts. 39, 581
10. Soukoulis C.M. and Levin K., 1978, Phys. Rev. B18, 1439
11. Soukoulis C.M., 1978, Phys. Rev. B18, 3757
12. Riess I., 1977, Commun. on Phys. 2, 37
13. de Jongh L.J., 1978, J. Appl. Phys. 49, 1305
14. Algra H.A., de Jongh L.J. and Reedijk J., 1979, Phys. Rev. Letts. 42, 606
15. Herring C. and Kittel C., 1951, Phys. Rev. 81, 869
16. Wohlfarth E.P., 1965, Phys. Letts. 15, 106
17. Rivier N. and Mensah A.E., 1977, Physica 91B, 85
18. Spalek J. and Rivier N., 1979, J. Phys. (Paris) Letts. 40, L57
19. Kornblit A., Ahlers G. and Buchler E., 1978, Phys. Rev. B17, 282
20. Robinson W.K. and Friedberg S.A., 1960, Phys. Rev. 117, 402
21. Mathon J., 1968, Proc. Roy. Soc. A306, 355
22. Friedel J., 1962, J. Phys. Radium 23, 692
23. Anderson P.W., 1966, Phys. Rev. 124, 41

24. Ruderman M.A. and Kittel C., 1954, Phys. Rev. 96, 99

25. Yosida K., 1957, Phys. Rev. 106, 893

26. Ref. 9, Chapter 2

27. Adkins K. and Rivier N., 1974, J. Phys. (Paris) Colloque 35, C4-237

28. Edwards S.F. and Anderson P.W., 1975, J. Phys. F : Metal Phys. 5, 965

29. Fischer K.H., 1975, Phys. Rev. Letts. 34, 1438

30. Edwards S.F. and Anderson P.W., 1976, J. Phys. F : Metal Phys. 6, 1927

31. Anderson P.W., Halperin B.I. and Varma C.M., 1972, Phil. Mag. 25, 1

32. Sherrington D. and Southern B., 1975, J. Phys. F : Metal Phys. 5, L49

33. Sherrington D. and Kirkpatrick S., 1975, Phys. Rev. Letts. 35, 1792

34. Thouless D.J., Anderson P.W. and Palmer R.G., 1977, Phil. Mag. 35,593

35. Smith D.A., 1974, J. Phys. F : Metal Phys. 4, L266

36. Smith D.A., 1975, J. Phys. F : Metal Phys. 5, 2148

37. Binder K. and Schroder K., 1976, Phys. Rev. B14, 2142

38. Walker L.R. and Walstedt R.E., 1977, Phys. Rev. Letts. 38, 514

39. Rivier N., 1976, Phys. Rev. Letts. 37, 232

40. Anderson P.W. and Pond C.M., 1978, Phys. Rev. Letts. 40, 903

41. Bray A.J. and Moore M.A., 1980, J. Phys. C : Solid State
(to be published)

42. de Gennes P.G., 1976, la Recherche 7.72, 919

43. Smart J.S., 1961, J. Phys. Chem. Solids 16, 169

44. Sato H., Arrott A. and Kikuchi R., 1959, J. Phys. Chem. Solids 10, 19

45. Sato H. and Kikuchi R., 1972, AIP Conf. Proc. 10, 505
1973, AIP Conf. Proc. 18, 605

46. de Gennes P.G., Lafore P. and Millot J.P., 1959, J. Phys. Chem. Solids 11,
105

47. Shante V.K. and Kirkpatrick S., 1971, Advan. Phys. 20, 325

48. Sykes M.F. and Essam J.W., 1964, Phys. Rev. 133, A310

49. Frisch H.L., Sonnenblick E., Vyssotsky V.A. and Hammersley J.M., 1961, Phys. Rev. 124, 1021

50. Dean P. and Bird N.F., 1966, Mathematics division report Ma 61, National Physical Laboratory, Teddington, Middlesex, England

51. Domb C. and Dalton N.W., 1966, Proc. Phys. Soc. 89, 859

52. Domb C., 1974, J. Phys. C : Solid State Phys. 7, 2677

53. Stauffer D., 1975, J. Phys. C : Solid State Phys. 8, L 172

54. Domb C. and Stoll E., 1977, J. Phys. A : Maths. Gen. 10, 1141

55. Stauffer D., 1979, Phys. Rep. 54, 1.

CHAPTER 2

REVIEW OF PREVIOUS EXPERIMENTAL WORK

2.1 General Introduction

The experimental work performed on the AuFe and CuMn alloy systems over the last 20 or more years has been prolific. This has largely been due to their diverse magnetic properties; for example, AuFe has a Kondo regime at the lowest Fe concentrations, with increasing Fe concentration it passes through a spin glass regime to long range ferromagnetism at still higher concentrations.

A large part of the early experimental work on the dilute alloys has been reviewed by Beck (1-3), Cannella and Mydosh (4-6) and Larsen (7). This review is presented in the form of a critical discussion of the principal investigations which have shaped current thinking about the spin glass state. The review is organised under broad headings, each surveying the experimental work pertaining to a particular aspect of spin glass behaviour. It should be added parenthetically that some of the aspects of spin glass behaviour to be discussed are not necessarily considered to be intrinsic, the intention is merely to present as balanced a view as possible of the diverse phenomena associated with spin glasses. As AuFe and CuMn are similar in many of their magnetic properties, they are not treated separately in this review.

Subsequent sections of the review cover the characteristic changes in behaviour associated with the transition from a spin glass dominated regime to a magnetically long range ordered regime of the more concentrated alloys. A final section surveys the specific heat behaviour of a number of other related magnetic systems.

2.2 The Spin Glass Regime

2.2.1 Scaling Laws and Characteristic Temperatures

Much of the early experimental work on noble-transition metal alloys was concerned with the investigation of the Kondo effect in the very dilute alloys ($c \lesssim 500$ at.ppm), see for example the extensive review by Heeger (8). Some of the first indications of spin glass behaviour evolved out of studies of the RKKY interaction effects responsible for deviations from ideal Kondo behaviour. One of the most obvious properties expected of the RKKY interaction between local moments in the dilute alloys ($0.1 < c < 1$ at.%) was the scaling of many phenomena with impurity concentration. This geometrical property originated from the $1/r^3$ dependence of the RKKY interaction strength in the asymptotic limit $r \gg 1/k_F$, k_F is the conduction electron fermi wave vector (see Chapter 1). Mean field arguments proposed by Blandin and Friedel were employed by Marshall, Klein and Brout (see Chapter 1) to account for the concentration independent, low temperature-linear magnetic specific heat (ref. 10-15 to be discussed). Souletie and Tournier (9) generalised this mean field approach and demonstrated the scaling of a number of other magnetic properties when expressed as concentration independent universal functions of reduced temperature T/c. This mean field description of scaling was reasonably successful, although weakly concentration dependent deviations from a purely universal behaviour were evident. These deviations were considered to be due in part to the finite wavelength of the host conduction electron polarisation, and in part to the increasing role of direct interactions between near neighbour moments and the damping effects of shorter conduction electron mean free paths on the RKKY interaction strength in the more concentrated alloys. Larsen (7) modelled this latter effect and qualitatively accounted for the deviations from simple concentration linear scaling of the characteristic temperatures of AuFe, for concentrations $c > 1$ at.%Fe.

Specific heat measurements

An early series of fairly systematic investigations of the low temperature specific heat of a number of dilute ($c < 1$ at.%) noble-transition metal alloys by Zimmerman, Hoare and Crane (10,11), du Chatenier, de Nobel and Dreyfus et al. (see fig. 2.2.1) (12-15) established that the low temperature - linear magnetic specific heat contribution $\Delta C = C_{ALLOY} - C_{HOST}$ was essentially concentration independent. It was common in work on the dilute alloys to extract the magnetic specific heat contribution ΔC by subtraction of the pure host specific heat from the measured alloy specific heat. Such procedures assumed that the electronic and lattice specific heat terms had changed little on alloying. Elastic constant determinations by Waldorf (22) demonstrated that such changes were indeed negligible at low temperatures for Mn concentrations $\lesssim 1$ at.% in dilute Cu Mn alloys.

de Nobel and du Chatenier (12) demonstrated that in modest magnetic fields ($B \sim 1$ T) the peak in $\Delta C/T$ of a Cu 0.13 at.% Mn and other alloy samples was more rounded and shifted to lower temperatures. In a later work, du Chatenier and Miedema (14) extended measurements to below 1 K and demonstrated the presence of a large hyperfine nuclear specific heat contribution $C_N \propto 1/T^2$ from the Mn nuclear moments of dilute Cu Mn alloys. The magnetic specific heat curves were fitted to Schottky curves appropriate to a ground state splitting in the local effective fields experienced by the moments. The Schottky curves were adapted to take account of the quasi-continuous distribution of local effective fields P(B) of Marshall, Klein and Brout's theory (see Chapter 1). The positive deviations from a simple temperature linear specific heat behaviour at very low temperatures were considered to indicate the presence of a minimum in the effective field distribution P(B) at $B = 0$.

A series of more recent measurements by Ho on dilute Cu Mn alloys ($0.06 < c < 3$ at.% Mn) between 0.06 and 1 K were published in an extensive review

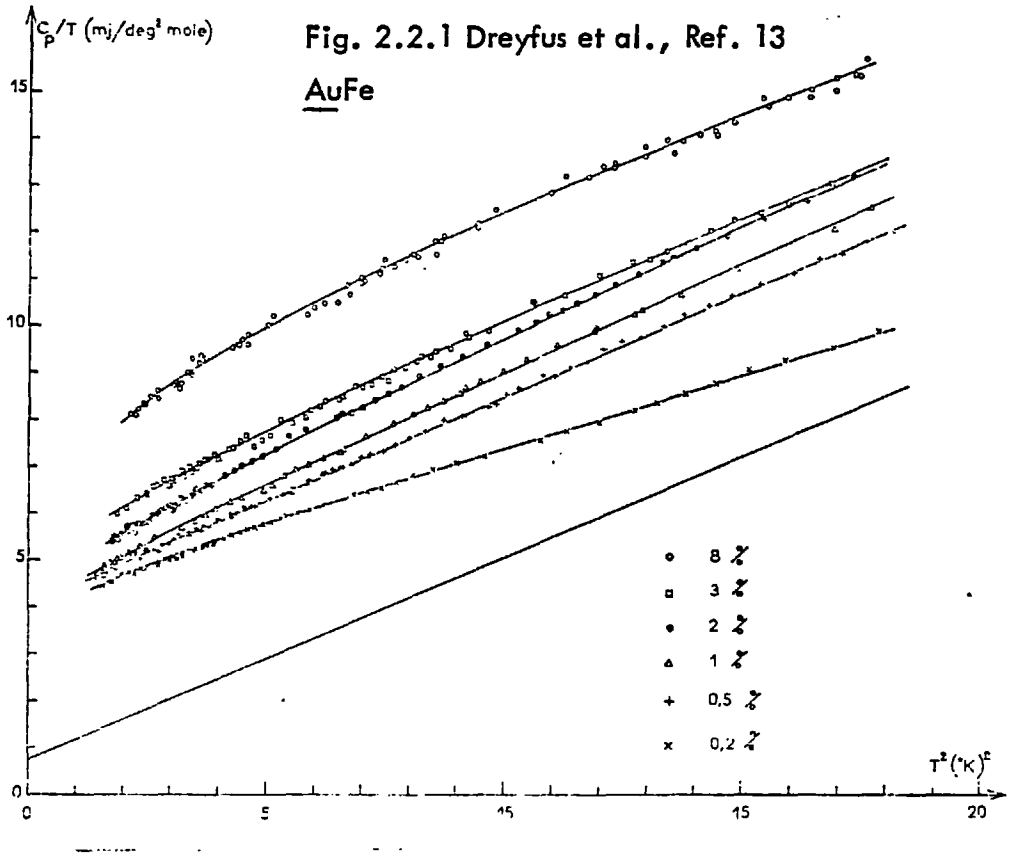

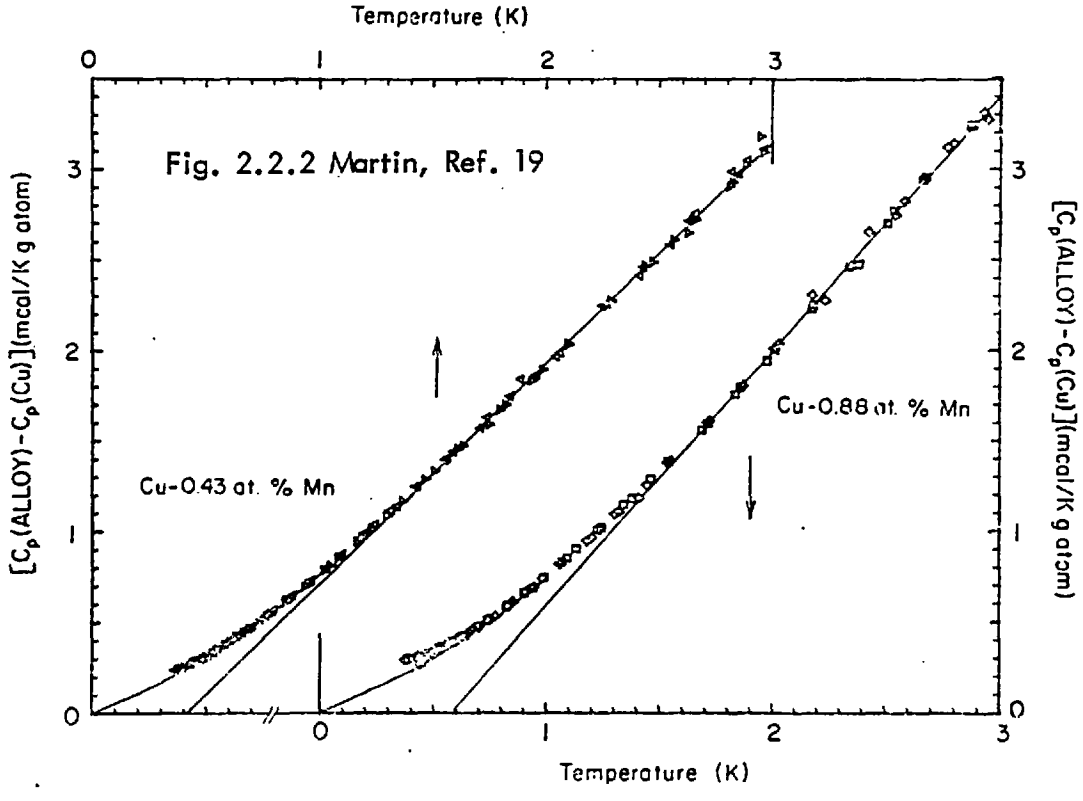

FIG. 4. Specific-heat plots for the two more concentrated alloys. For clarity, the temperature scales are staggered by 1 K. Note the marked linear region of the specific heat and the extrapolation to zero temperature after subtraction of the nuclear specific heat.

of low temperature specific heat of metals by Phillips (16). These were accurate, and showed the earlier measurements of du Chatenier to be in error at the lowest temperatures, although qualitatively correct in indicating deviations from linearity. The results suggested that there were two temperature linear regions of the magnetic specific heat : $\Delta C/T \sim 2.4\ mJK^{-2}mol^{-1}$, $T < 0.3\,K$ and $\Delta C/T \sim 4.5\ mJK^{-2}mol^{-1}$, $T > 2\,K$. These were considered to correspond respectively to a minimum in P(B) at B = 0 and a maximum at B > 0. Fogle et al (17) extended these measurements to more dilute alloys (c ~ 0.01 at.%) the Cu Mn system has a very low Kondo temperature ($T_K \sim 1$ mK) making it ideal for a study over an extensive concentration range.

At the lowest temperatures the magnetic specific heat (see fig. 2.2.2) was found to fit the relationship $\Delta C = AT + BT^2$ with $A \sim 1.8\ mJK^{-2}mol^{-1}$ for all concentrations and $B \sim c^{\frac{1}{2}}$ a weakly concentration dependent function. These results supported Monte Carlo simulations of the dilute spin glass Cu Mn by Walker and Walstedt (see Chapter 1).

A reduced plot of $\Delta C/T$ against log T/C (see fig. 2.2.3) demonstrates deviations from universal behaviour; the peaks in $\Delta C/T$ are observed to occur at $T_o/c \sim 10$ K/at.%. The tail of the anomaly has a $\Delta C/T \propto (T_o/T)^2$ temperature dependence rather than $\propto 1/T^3$, as expected for a simple Schottky anomaly.

Similar measurements by Martin (18,19) on a series of dilute Cu Mn alloys ($0.08 < c < 0.9$ at.% Mn) between 0.35 and 3 K are in good agreement with the results of Fogle et al (see fig. 2.2.4).

Measurements on more concentrated Au Fe and Cu Mn alloys by Wenger and Keesom (20,21) over an extended temperature range were concerned with demonstrating that the rounded specific heat maximum occurred at significantly higher temperatures

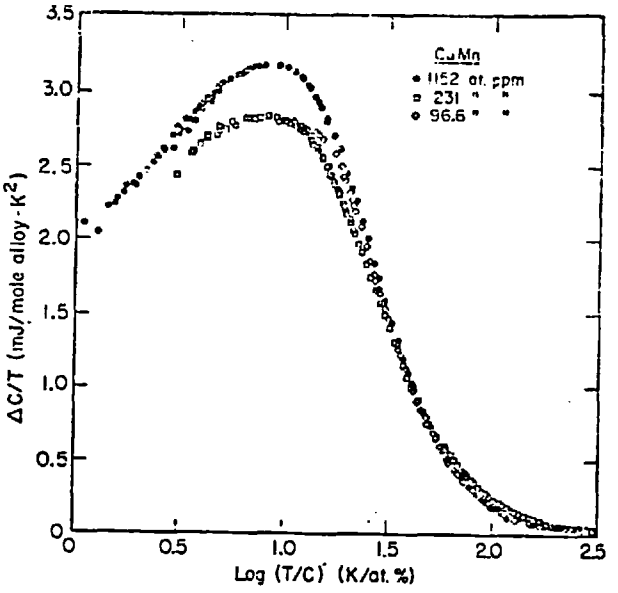

Fig. 2.2.3
Fogle et al.,
Ref. 17

Fig. 2 : The magnetic heat capacity of three dilute Cu Mn alloys, plotted as ΔC/T vs. log (T/concentration)

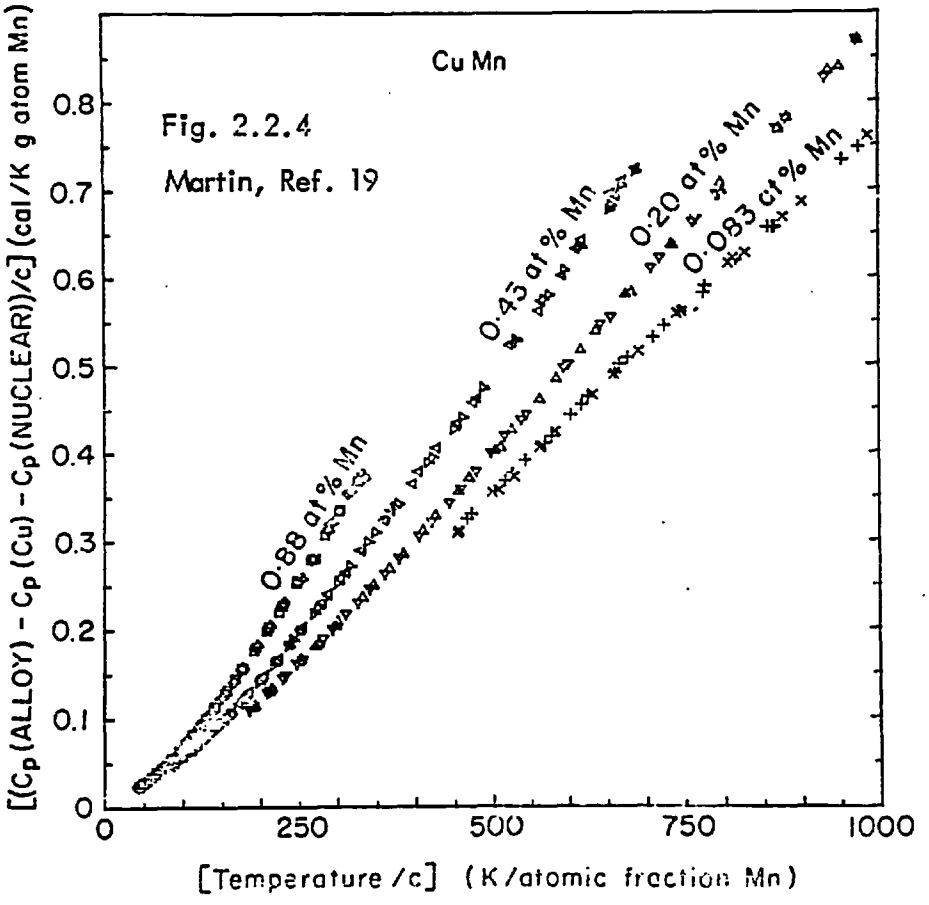

FIG. 6. Plot of scaled spin-glass specific heat against scaled temperature. The concentration c is expressed as an atomic fraction. Higher temperature points for the two most dilute alloys are off scale on this plot.

than the sharp peak of the AC susceptibility (see fig. 2.2.5).

The magnetic specific heat has a characteristically broad peak with an essentially temperature-linear low temperature behaviour and a long tail at high temperatures. The entropy associated with thermal disorder of the moments between $T = 0$ and $T = T_f$ (the temperature of the AC susceptibility peak) was reported to be roughly one third of the $cR \ln(2J+1)$ value. Such results were considered to argue against the occurrence of a sharp phase transition at T_f or temperatures close to it, at least in the conventional sense. The observed specific heat behaviour was very different from the lamda-type anomaly corresponding to the sharp divergence of spin correlations over a narrow critical temperature regime that would generally be associated with a simple long range magnetic ordering process. Very careful consideration is needed as to what does or does not constitute a phase transition before this highly controversial question can be satisfactorily resolved.

Sound velocity measurements by Hawkins et al (23,24) on the same Au 8 at.% Fe alloy that was used by Wenger and Keesom (20) and on a series of Cu Mn alloys with 5, 10 and 15 at.% Mn also showed no sharp anomalies at or near T_f. Velocity changes $\Delta V/V$ measured in a 1.1 T field passed through zero at the same temperature as the susceptibility peak for all the Cu Mn alloys studied. A minimum in the zero field $\Delta V/V$ was observed just below T_f in the Cu 5 at.% Mn alloy. This was an unexpected result since theory would suggest that such a minimum should correspond with a specific heat maximum which usually occurred at temperatures significantly greater than T_f. This result, however, is questionable considering its sensitivity to the subtraction of an adjustable background velocity.

Comparatively recently, there has been a resurgence of interest shown in dilute yttrium- and Scandium- rare earth spin glass alloys. The highly localised 4f electron wavefunctions of the rare earth elements offer a number of advantages

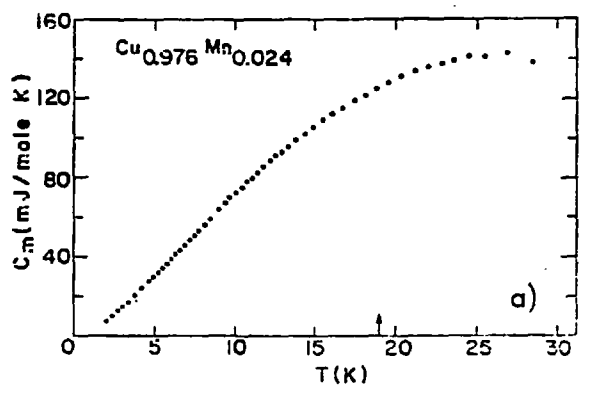

FIG. 4. Magnetic specific heat of $Cu_{0.976}Mn_{0.024}$ in the temperature range 2–30 K. The arrow indicates the ordering temperature T_0.

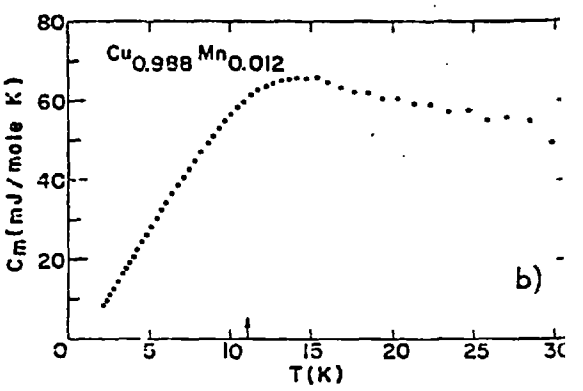

FIG. 3. Magnetic specific heat of $Cu_{0.988}Mn_{0.012}$ in the temperature range 2–30 K. The arrow indicates the ordering temperature T_0.

Fig. 2.2.5 Wenger and Keesom, Ref. 21

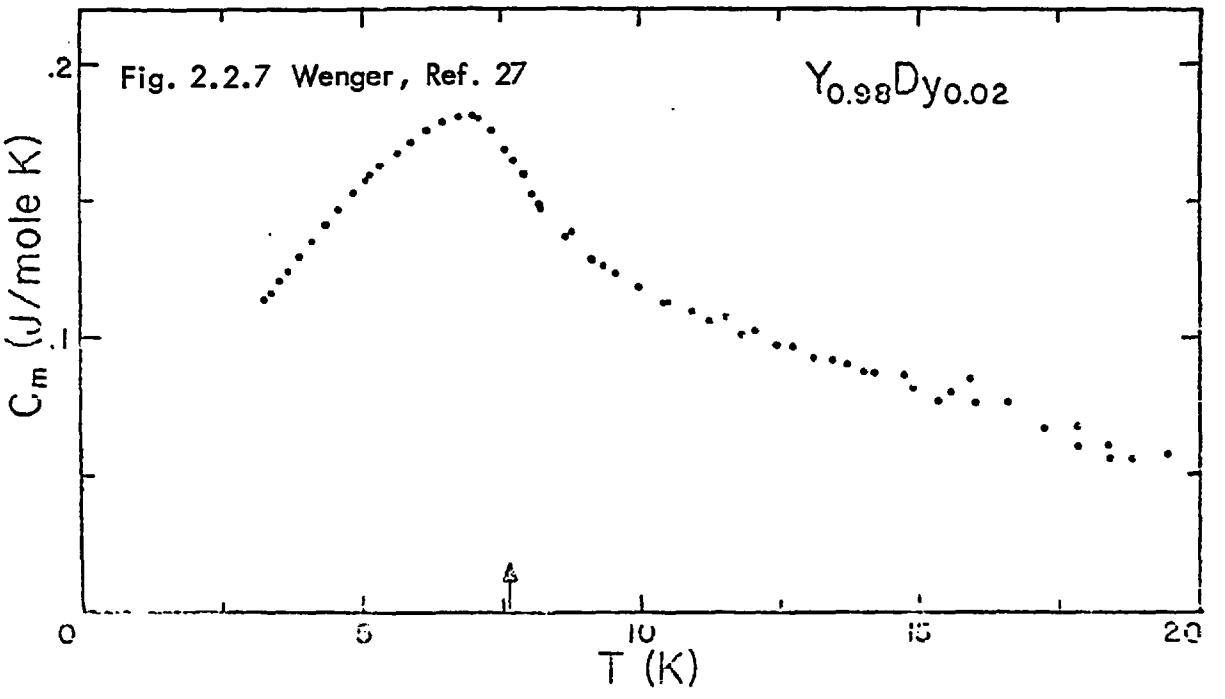

Figure 2. The magnetic specific heat of $Y_{0.98}$ $Dy_{0.02}$ as a function of temperature. The arrow indicates the temperature of its susceptibility peak.

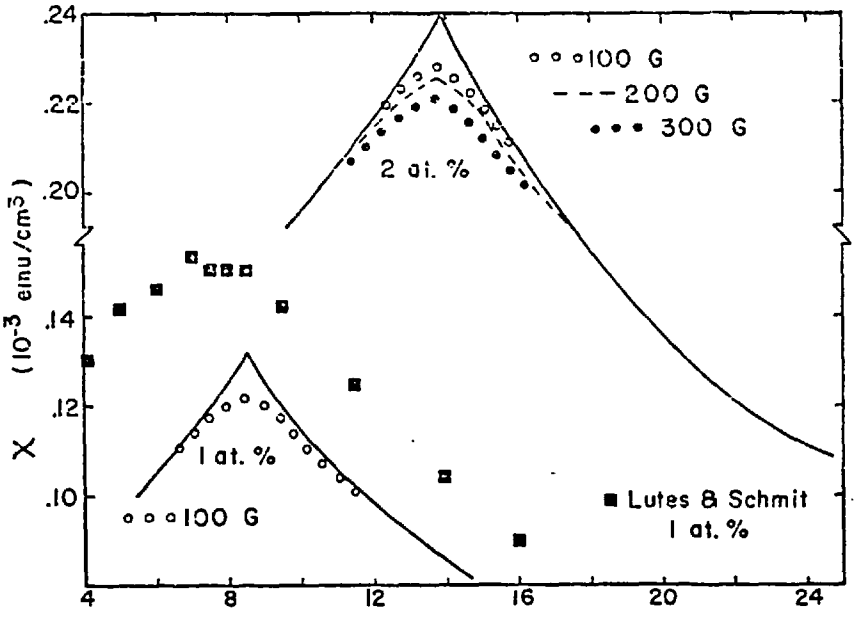

Fig. 2.2.8
Cannella and
Mydosh, Ref. 4

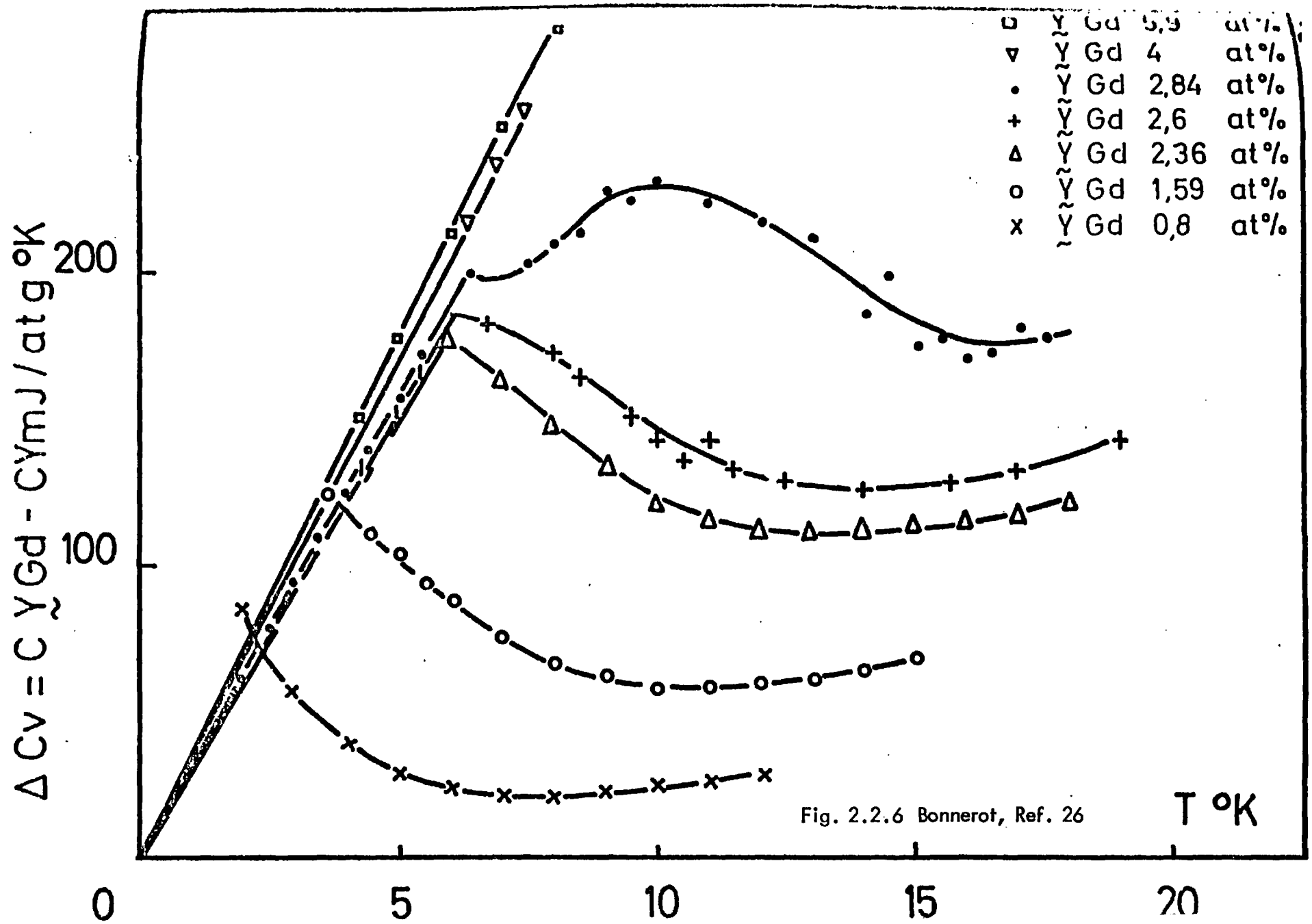

Fig. 2.2.6 Bonnerot, Ref. 26

over the less well localised 3d electron wavefunctions of the transition elements. The RKKY interactions between rare earth ion moments in non-magnetic hosts are uncomplicated by direct f-f exchange and Kondo spin compensation effects. Metallurgical problems are relatively few as they generally form excellent solid solutions over a wide concentration range with hexagonal closepacked or similar compounded structures. The large nuclear hyperfine field and crystal field effects common to a number of rare earth elements can be minimised by careful selection of the constituent elements of alloys to be studied.

Early specific heat measurements were performed on dilute YGd and LaGd by Bonnerot et al (25,26) to investigate the RKKY interaction and the predictions of mean field theories by Marshall, Kelin and Brout. Their measurements on YGd alloys with Gd concentration ranging between 0.8 and 5.9 at.% Gd showed a behaviour characteristically different from that of the dilute noble-transition metal alloys. The low temperature magnetic specific heat was linear in temperature to 1.8 K, their lowest measurement temperature and very weakly concentration dependent. At some characteristic temperature T_o a rather sharp peak was apparently observed (see fig. 2.2.6), although the low precision of their data did not warrant such an inference. The character of the peaks changed to a more rounded form in the 2.8 at.% Gd sample, no peaks were observed in the temperature range of measurement (up to 20 K) for the higher concentration alloys. The temperatures T_o of peaks scaled linearly with Gd-concentration, $T_o/c = 2.3\ K/at.\%$. The magnetic specific heat above T_o was fitted to an expression of the form $\Delta C = T\Delta\gamma + A\,(T_o/T)^2$. A was found to be roughly concentration independent with a value $\sim 0.2\ JK^{-1}mol^{-1}$, whereas $\Delta\gamma/c \sim 2\ mJK^{-1}mol^{-1}at\%^{-1}$ was concentration dependent and rather large for an enhancement term, $\Delta\gamma/\gamma \sim 0.2\ at\%^{-1}Gd$. This latter term was justified by invoking an increase in the density of states at the fermi level due to spin-orbit decoupling of virtual bound

states introduced by the Gd impurities. Below T_o the specific heat fitted the expression $\Delta C/T = \gamma + \Delta\gamma$ where $\gamma \sim 25\ mJK^{-2}mol^{-1}$ was essentially concentration independent.

Relatively new measurements by Levesque et al (28) on dilute Y Gd and Sc Gd alloys were extended to lower temperatures to test scaling laws. The characteristic temperatures of the specific heat and susceptibility maxima of the Y Gd alloys were approximately the same, but both increased faster than the impurity concentration, $T_o \sim c^{3/2}$, no sharp peaks were shown in the specific heat data. Analysis of the Sc Gd data was complicated at the lowest temperatures by uncertainties in the nuclear hyperfine specific heat contribution. Characteristic temperatures of the Sc Gd system scaled more linearly with concentration, but the susceptibility and specific heat maxima followed different concentration dependences of 1.1K at.%$^{-1}$ and 0.4 K at.%$^{-1}$ respectively. At the lowest temperatures the magnetic specific heat of a Sc 3 at.% Gd alloy was found to fit a $T^{1.6}$ power law ($T \gtrsim 30$ mK). This result was again cited as support for the Walker and Walstedt Monte Carlo simulation of the Cu Mn spin glass.

A recent study of the specific heat behaviour of an Y 2 at.% Dy alloy reported by Wenger (27) was in contrast to that of the archetypal noble-metal spin glasses : Au Fe and Cu Mn.

The magnetic specific heat data of the alloy shown in fig. 2.2.7 exhibits a much sharper peak than observed in a Cu 1.2 at.% Mn sample (see fig. 2.2.5a), at a temperature of 7 K, slightly lower than the AC susceptibility peak at 7.64 K (indicated by the arrow in figure 2.2.7). The temperature dependence of the specific heat above the peak was reported to be 1/T, but this was qualified by doubts about the accuracy of the subtraction in this temperature regime. The specific heat below the peak does not appear to go linearly to zero, but further measurements to lower

temperatures are required to clarify this point. The magnetic entropy was calculated to be approximately half the cR ln (2J + 1) value below the peak, assuming $J = 15/2$. Assuming the 1/T dependence of the magnetic specific heat above the peak, the total magnetic entropy associated with the anomaly was calculated to be 90% of the cR ln (2J+ 1) value.

Other measurements

Among other magnetic measurements which have been investigated for scaling properties are magnetisation and resistivity measurements. Souletie and Tournier (9) showed that the initial susceptibility and remanent magnetisation of dilute Cu Mn and AuFe alloys could be plotted as concentration independent universal functions of reduced temperature in the same way as specific heat. It was also demonstrated that concentration independent magnetisation isothermals, plotted for constant T/c, as a function of reduced field B/c, were described approximately by a universal curve.

Resistivity measurements by Laborde and Radhakrishna (29) on very dilute Cu Mn alloys with Mn concentrations ranging from 10 at. ppm to 1 at.% measured between 0.03 and 4 K were shown to fit a universal curve of $\Delta\rho/c$ against log T/c (where $\Delta\rho = \rho_{ALLOY} - \rho_{HOST}$). Measurements reported by Loram, Ford and Whall (30, 31) on very dilute AuFe alloys were also shown to fit a similar universal curve for concentrations between 25 and 5000 at. ppm Fe. At higher Fe concentrations this scaling behaviour was shown to breakdown by Mydosh et al (32), but it was also felt that there was evidence to believe a scaling with T/T_f for concentrations between 0.5 and 8 at.% Fe. The residual resistivity $\Delta\rho_0 = \Delta\rho(T \to 0)$ was linearly dependent on concentration up to $\sim$ 5 at.% Fe, where the concentration dependence becomes slower than linear. An attempt at correlating T_f with T_m, the temperature of the broad maximum in the temperature coefficient of the resistivity $\frac{d(\Delta\rho)}{dT}$, as

predicted to occur at the ordering temperature of a number of materials, met with some success (32,33). There was a reasonably good correlation between 2 and 12 at.% Fe, the lack of correlation above 12 at.% Fe was attributed to the complicated effects of clusters and the sensitivity of the magnetic state of the alloy to heat treatment. However, this excellent correlation between T_f and T_m appeared to be restricted to the Au Fe alloy system where it was argued that the resistivity is particularly sensitive to the cluster freezing due to the large average cluster size compared to the electron mean free path (33). Shoulders in the $\frac{d(\Delta\rho)}{dT}$ curves of other alloy systems were considered to correlate roughly with T_f.

The striking low-field AC susceptibility results of Cannella et al on a range of Au Fe alloys with Fe concentrations between 1 and 22 at.% (34,4) and on Cu Mn alloys with Mn concentrations between 0.2 and 10 at.% (35) sparked off a spate of fervent experimental and theoretical activity. Their results showed relatively sharp, cusp-like peaks at temperatures T_f close to the onset of hyperfine splitting of Mössbauer spectra (36-38), which were highly suggestive of a cooperative phase transition occurring at T_f. The sharpness of the peaks contrasted with the broad maxima observed in the high field DC susceptibility measurements of Lutes and Schmit (39), Tholence and Tournier (40). The shape of these susceptibility curves (see fig. 2.2.8) resembled closely that of a conventional antiferromagnet and were mistakenly thought at first to indicate the onset of long range antiferromagnetic order at T_f.

Rounded susceptibility peaks (see fig. 2.2.8) were obtained when the AC measurements were performed in the presence of DC fields which were considered to simulate the high-field measurements. Guy refuted this interpretation by arguing that such effects were far too large to be due simply to a shift of the measuring point

on the σ vs B curve.

Several theories of spin glass ordering (see Chapter 1) were based on the assumption that the sharp peak in the AC susceptibility represented a cooperative phase transition. They all, however, predict a specific heat cusp at the same temperature as the susceptibility cusp where none has been observed. Alternative descriptions of a spin glass freezing process based on the thermal blocking of spin clusters in local anisotropy fields have been considered; these will be discussed in detail in a later section.

2.2.2 Thermomagnetic history effects

Early investigations of Cu Mn alloys by Street (41) and Owen et al (42,43) reported observing remanence and time dependent effects in their magnetisation measurements which depended strongly on the preceding thermal and magnetic treatment. Similar observations were reported by Lutes and Schmit (39), Tholence and Tournier (40) on Au Fe alloys.

These effects remained poorly characterised until an extensive series of investigations were performed by Kouvel (44,45) of the magnetic hysteresis behaviour of moderately concentrated Cu Mn alloys with between 5 and 30 at.% Mn. The hysteresis loops he had measured at 1.8 K after cooling in a magnetic field ($\sim$ 0.5 - 1 Tesla) were displaced from their symmetrical positions about the origin to negative field values (see fig. 2.2.9).

The thermoremanent magnetisation (TRM) obtained by field-cooling (FC) was unidirectional and parallel to the cooling field direction. In contrast, a zero field-cooled (ZFC) sample exhibited no significant remanence with a magnetisation linearly dependent on field and an effective susceptibility (defined by the slope of the magnetisation line) equal to that of the high field linear region of the field-cooled loop. In the zero field-cooled condition the reversibility of the magnetisation was

disturbed when the applied field appeared to exceed a critical value, and a small time dependent isothermal remanent magnetisation (IRM) was reported to be observed. More careful measurements by Guy (see section 2.2.4) in low DC fields on AuFe alloys showed that in fact the IRM was observed in even the smallest fields, and not just above some critical field value, as suggested by Kouvel. At higher temperatures the loop displacement decreased and hysteresis effects were evident from the opening up of the loops.

Kouvel concluded that no ordinary uniaxial anisotropy of magnetocrystalline or dipolar origin could explain this observed behaviour. He proposed that an exchange anisotropy mechanism, similar to that postulated to explain the behaviour of partially oxidised cobalt particles was probably appropriate. This presupposed exchange anisotropy mechanism was suggested to result from the Mn moment coupling being, as it is widely believed to be, antiferromagnetic at first neighbour and ferromagnetic at second neighbour positions. In a later publication (46) Kouvel gave details of a simple model based on a system of small ensembles of mutually interacting ferromagnetic and antiferromagnetic domains. The anisotropy was considered to result from exchange coupling of the ferromagnetic and antiferromagnetic domains.

Kouvel's model was based on rather elaborate assumptions about the distribution of Mn moments in CuMn alloys. To justify the coexistence of ferromagnetic and antiferromagnetic domains Kouvel assumed that there was substantial inhomogeneity in the form of many small, fairly well defined regions of both atomic short range order and clustering of Mn moments. Whilst there is some evidence of short range order from neutron work (to be discussed later) on moderately concentrated alloys above the low temperature solubility limit of order 10 at.% Mn (see Chapter 4), there seems to be no justification for the degree of inhomogeneity required to account for hysteresis loops in the lower Mn concentration alloys (see also work by Monod and

Prejean, refs. 70, 71). The role of the RKKY oscillatory indirect exchange interaction between moments was largely ignored.

2.2.3 Clusters and Superparamagnetism

The thermoremanent behaviour of Cu Mn and Au Fe spin glass alloys was very difficult to understand without involving clusters and the concepts of superparamagnetism. Some of these attempts to account for thermoremanent behaviour in terms of independent superparamagnetic clusters will be discussed in this and the next section.

A series of investigations by Beck and co-workers (1-3, 47-50) on a set of moderately concentrated Cu Mn alloys revealed thermomagnetic history effects in the high-field magnetisation data. Beck coined the term Mictomagnetism to explain this unusual thermoremanent behaviour. A Mictomagnet was defined as a system of clusters of predominately ferromagnetic spin alignment with large effective moments dispersed in a matrix of individual moments frozen in random orientations.

The evidence for the existence of the clusters came from high-field magnetisation measurements by Mukhopadhyay et al (47,48). The data were interpreted by fitting pairs of isotherms closely adjacent in temperature to an empirical relation involving a Brillouin function to describe the behaviour of the giant cluster moments and a field-independent susceptibility term for individual moments not participating in clusters. It is questionable whether this procedure was applicable to Cu Mn alloys, where long range Mn moment couplings must preclude an interpretation based on independent clusters. For large superparamagnetic giant moments the Brillouin function reduces to a classical Langevin function. Murani (53) pointed out that a fit to a Langevin function is equivalent to fitting the initial susceptibilities to a Curie law relation. Such an interpretation will grossly overestimate the size of the effective cluster moments as it ignores the strong interactions

which must surely be present in these alloys at temperatures not far above T_f. A Curie-Weiss type relation is a more appropriate description of strongly interacting moments. These same remarks also apply to a similar procedure used by de Mayo (51,52) to investigate the effects of annealing heat treatments on cluster sizes in moderately concentrated AuFe alloys.

Further investigations by Tustison and Beck (49,50) were concerned with demonstrating the effects of metallurgical treatment on the size of cluster moments in concentrated Cu Mn alloys. Large AC susceptibility increases occurring on ageing and significant decreases on cold working were interpreted in terms of enhancement and disruption of atomic short range order by these respective metallurgical treatments. It was also suggested that the sharp peak in the AC susceptibility may be due to the short range order. It was argued that in a more random moment distribution, as was considered to have been achieved by cold working, the magnitude of the AC susceptibility peak had been significantly reduced. A similar suggestion has been made more recently by Zibold (54-58) in connection with his work on quench-condensed AuFe films. He argued that his method of evaporating thin AuFe films onto very cold ($\sim$ 14 K) substrates realised more nearly a true random atomic distribution (see Chapter 4 for further comments). However, it remains to be shown that cold working treatments and quench-condensing preparation procedures can produce reasonably defect-free samples commensurate with bulk quenched samples.

Early neutron evidence for the presence of short range order in moderately concentrated Cu Mn alloys was due to Sato et al, Meneghetti and Sidhu (see Chapter 4). Diffuse peaks observed at the $(\frac{1}{2}\ 1\ 0)$ reciprocal lattice positions indicated a Cu_3Au type superlattice with correlation lengths of 2-3 unit cells. Mukhopadhyay et al argued that their data were consistent with magnetic cluster moments of a similar size. However, the assumption that the $(\frac{1}{2}\ 1\ 0)$ diffuse peaks were due entirely to

atomic short range order of the Mn moments was not well founded. This point can only be truly established by a full polarisation analysis of the total diffuse scattering terms. The question of the nature of the spin coupling at first and second neighbour distances, widely believed to be antiferromagnetic and ferromagnetic respectively, is also not so clear cut (57,58).

2.2.4 Relaxation and Magnetic Viscosity

A number of researchers have stressed the analogous thermoremanent behaviour of spin glasses and systems of fine single-domain ferromagnetic particles as theoretically treated by Néel (59) to account for rock magnetic properties. The thermoremanent behaviour of a Au 8at.% Fe alloy was studied by Tournier and Ishikawa (60). They observed a rapid logarithmic decay of an IRM with increasing temperature which was indicative of a thermally-activated relaxation process; limited comparisons were made with Néel's theory.

A later paper published by Tholence and Tournier (61) took the analogy further. Their measurements were restricted to dilute Au Fe alloys ($c \lesssim 1$ at.% Fe) as they considered scaling behaviour to be a criterion of a true spin glass. The IRM and TRM of a Au 0.5 at.% Fe (see fig. 2.2.10) were observed to saturate at the same remanence value but in different field strengths, the TRM saturating in much lower fields than the IRM. No IRM was reported to be observed below a critical field value $B_m/c \sim 100$ mT at.%$^{-1}$. This was refuted more recently by Guy (64) whose low-field DC measurements on Au Fe alloys with concentrations between 0.25 and 7 at.% Fe indicated no critical field.

Tholence and Tournier also made an important distinction between the AC and DC methods of susceptibility measurement. They emphasised that the AC method is only sensitive to that part of the total equilibrium magnetisation which is reversible on the time scale of the experiment, whereas they considered the DC method to sense more

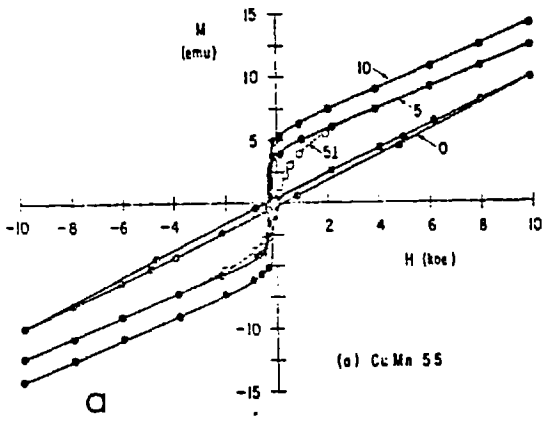

FIG. 3(a)

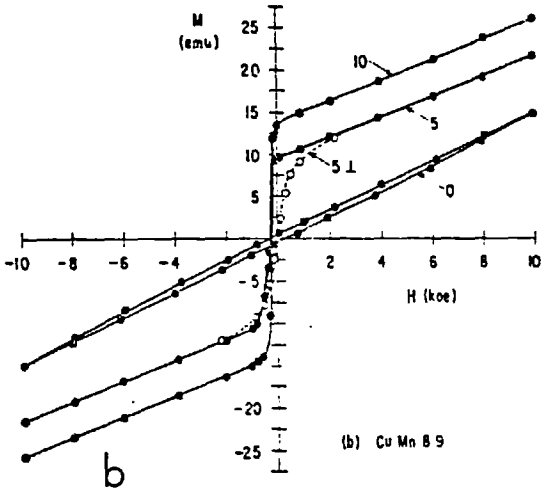

FIG. 3(b)

FIG. 2.2.9

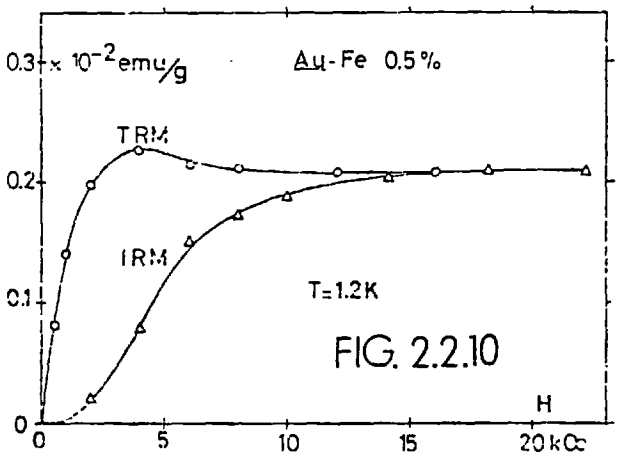

FIG. 2.2.10

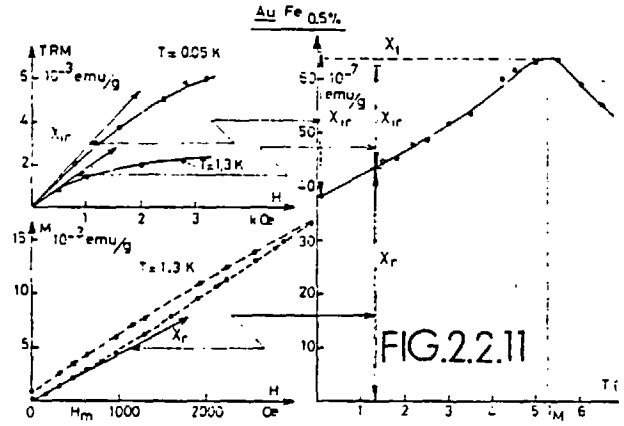

FIG. 5. — Methods to obtain respectively the reversible (χ_r) and the irreversible (χ_{ir}) susceptibilities, and thermal variation of χ_r and of $\chi_t = \chi_r + \chi_{ir}$.

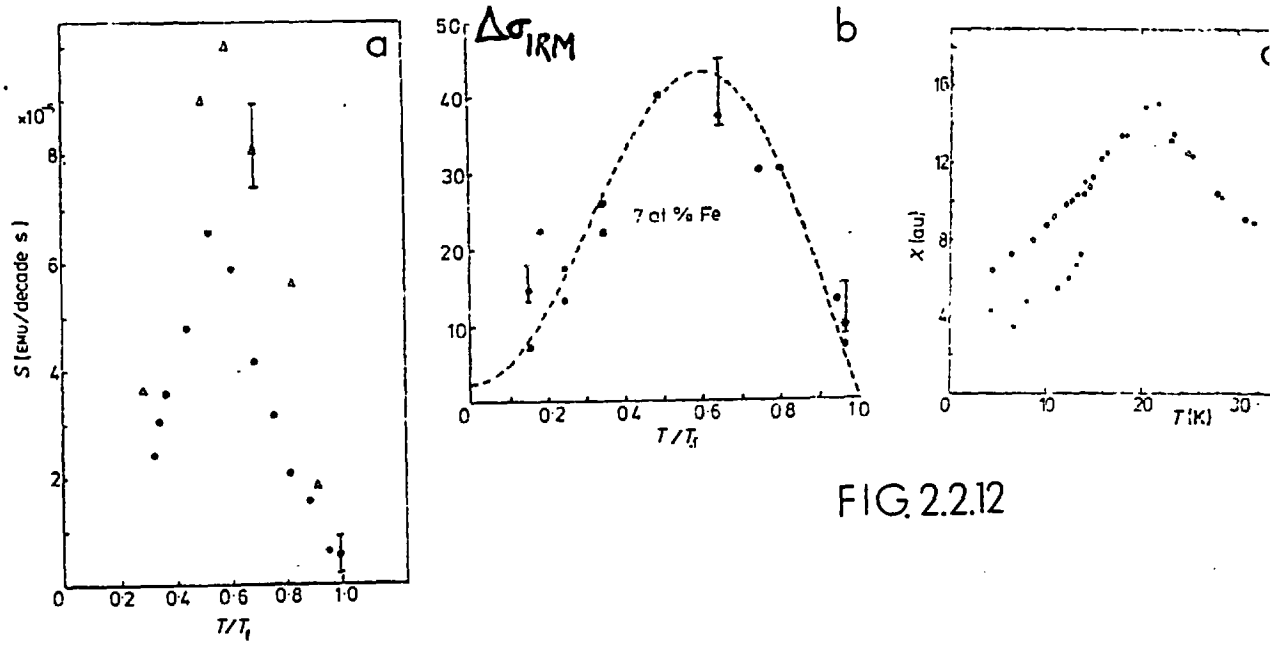

FIG. 2.2.12

nearly the total equilibrium magnetisation when measurements are taken in a continuously applied magnetic field during cooling from temperatures above T_f. This latter method results in an almost temperature independent susceptibility below T_f (see fig. 2.2.11). Recent transverse AC susceptibility measurements seem to indicate that time dependence and remanence may be observed by this method (Sarkissian B.V.B., private communication).

Tholence and Tournier developed a model in which individual moments μ, randomly distributed on an Ising lattice, were considered to have spontaneously divided into N clustered, local regions of n moments in the presence of a random, local anisotropy. By assuming Gaussian statistics, incomplete compensation of all the moments with each region results in a net average moment $\langle M \rangle \sim \sqrt{n}\ \mu$ which corresponds to a saturation remanence of $\sigma_{RS} = \frac{1}{2} N \langle M \rangle$. The giant net moments were considered to be responsible for the irreversible properties, whereas individual moments gave the reversible properties. Values of $n \sim 3 - 500$ for Cu Mn and Au Fe alloys ($0.1 < c < 1$ at.%) were estimated from the ratio of the experimentally determined values of the saturation magnetisation and remanences. For these dilute alloys n was found to be roughly concentration independent whereas the temperature dependence of the saturation remanence scaled with concentration. These observations were interpreted as implying that the anisotropy assumed in their model originated from an interaction with a $1/r^3$ dependence; an anisotropy of the RKKY interaction or of a dipolar origin were speculatively suggested.

Guy (62) reported susceptibility measurements in low DC fields ($\lesssim$ 2 mT) obtained by a Foner-type vibrating sample magnetometer (VSM) on a Au 4 at.% Fe alloy. His measurements demonstrated that contrary to the findings of Tholence and Tournier (61) a zero-field cooled sample develops an IRM slowly $\Delta\sigma_{IRM} \propto \ln t$ ($t \gtrsim 10$s) in even the smallest fields, $B \lesssim 1$ mT. Furthermore, the IRM eventually saturates after

a long time at the TRM value obtained by cooling to the same temperature in the presence of the same field B from a temperature above T_f.

In further publications Guy (63-65) extended the work of Tholence and Tournier on a series of alloys : AuFe 0.25-7 at.% Fe and a Cu 2 at.% Mn to lower DC fields and drew some more detailed parallels with Néel's single-domain particle theory. Guy attributed the sharp peak in the AC susceptibility to a strong temperature dependence at T_f of the cluster moment relaxation time. This was in analogy with the Hopkinson peak which occurs in some ferromagnets at a temperature $T < T_c$, where the anisotropy is very strongly temperature dependent.

Among several other features reported were the concentration scaling of the ratios $\frac{\sigma(T)}{\sigma(T_f)}$ and $\frac{\sigma_{TRM}(T)}{\sigma(T_f)}$ indicating that both $\sigma(T)$ and $\sigma_{TRM}(T)$ were determined by $\sigma(T_f)$. The characteristic occurrences (see fig. 2.2.12) of a shoulder in $\chi_R(T)$, the reversible susceptibility component, a peak in $\Delta\sigma_{IRM}(T)$ the incremental IRM (obtained by applying a 2mT field for 2 min. after ZFC) and in S(T) the logarithmic decay coefficient at $T \sim 0.6T_f$ are all suggested to have a common origin.

For $T < 0.8\ T_f$ the magnetic viscosity coefficient $V = S/\sigma_o$ (σ_o the initial value of the remanence at $t = 0$) of the IRM and TRM follow different temperature dependencies. V_{IRM} is roughly temperature independent whereas V_{TRM} is approximately linear in temperature (see fig. 2.2.13). Such results were interpreted in terms of a simple thermal activation model for independent particles (see ref. 65 for details). For $T < 0.8\ T_f$ observed sharp changes in both viscosity coefficients due to the very rapid increase in relaxation rates close to T_f may, it was suggested, result from the cooperative freezing at T_f of the part of the system responsible for anisotropy below T_f.

The frequency dependence of the temperature of the AC susceptibility peak predicted by the Néel model has recently been the subject of controversy. The theory predicts that a cluster with moment μ in anisotropy energy well E relaxes with time

constant $\tau = \tau_o \exp(E/kT)$. Therefore, at temperature T_b a cluster will be blocked to a measurement probe with characteristic measurement time $\tau_m \lesssim \tau = \tau_o \exp(E/kT_b)$. The largest clusters with the highest blocking temperatures T_b have the longest characteristic relaxation time. Thus, with decreasing measurement time τ_m, or correspondingly with increasing measurement frequency ν_m, a characteristic temperature like T_f would be expected to shift to higher temperatures, $1/T_b \propto \ln \nu_m$.

Such frequency dependent shifts of T_f have indeed been observed in Au Fe (55) and the tertiary spin glass systems (La Gd)Al_2 (66) and (Sr Eu) S (67). However, observations over a fairly extensive range of frequencies have failed to detect any significant frequency dependence of T_f in susceptibility measurements on Cu Mn (48, 68) and Ag Mn (69). It is difficult in general to make detailed comparisons between such experiments because of the widely different conditions under which these experiments were performed. The temperature differences are often rather small, and it is not clear from the published experimental details what precautions, if any, were taken to avoid eddy current heating effects or what part of the complex susceptibility response $\chi = \chi' + i\chi''$ was being measured.

Unusual magnetisation "jumps" in dilute Cu Mn ($<$ 2 at.% Mn) alloys have been the subject of current research by Monod and Prejean (70,71). Very rapid magnetisation reversals in times less than 100 ms have been observed in hysteresis loop measurements on a 0.5 at.% Mn sample cooled from 4.2 to 1.35K in a 0.32T field. The jumps seem to occur spontaneously, not only at reproducible threshold field values of 15 mT reverse and 3 mT forward, but also at slightly smaller fields after a few minutes. An intermediate zero magnetisation state was also observed on certain occasions. These results were, in the view of the authors, considered to be evidence of macroscopic magnetic domains ; the magnetisation reversal perhaps resulting from the propagation of a domain

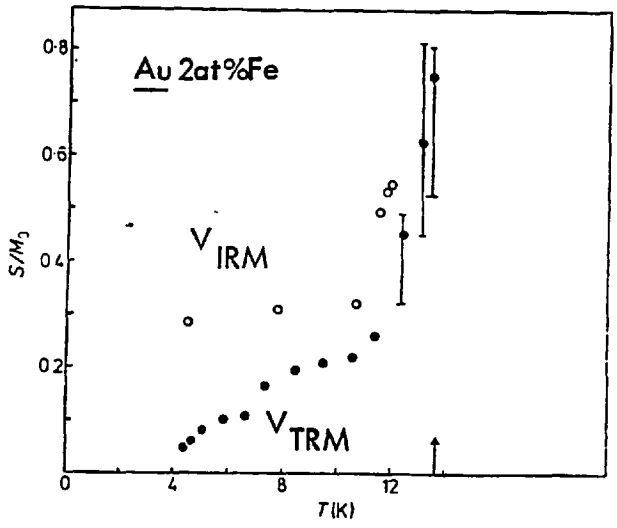

Fig. 2.2.13
Guy, Ref.65

a) Murani, Ref. 74

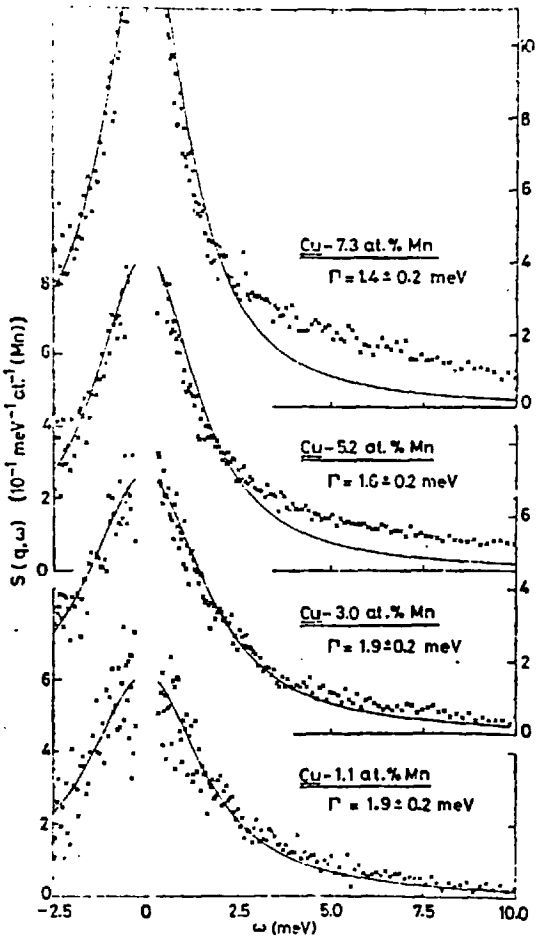

FIG. 1. $S(q,\omega)$, in units of meV^{-1} per Mn atom, vs ω for $q = 0.08$ Å^{-1} at $T = 300$ K, for Cu-Mn alloys with Mn concentrations as indicated in the diagram. The data points for elastic scattering are not shown in the diagram. The continuous curves represent the best fits to the data using the Lorentzian form for the spectral function $f(q,\omega)$. Note the progressive narrowing of the spectra accompanied by increasing deviation from the fits in the high-energy wings with increasing concentration.

Fig. 2.2.14

b) Murani, Ref. 75

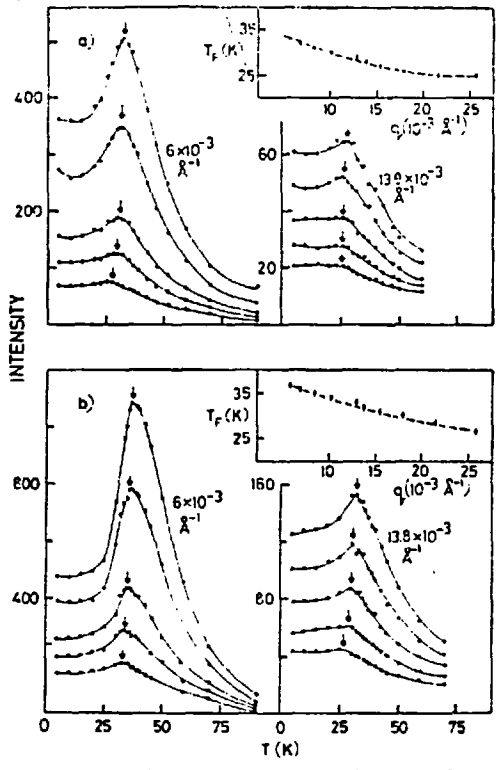

FIG. 1. Forward scattering intensity as a function of temperature for a series of q values for $AuFe$ alloys containing (a) 10 at.% Fe and (b) 13 at.% Fe. The arrows mark the temperatures T_F of the discontinuities in the scattering. These are shown plotted versus q in the insets.

wall throughout the sample. The occurrence of magnetisation jumps in AuFe alloys is not so well established, Tournier and Ishikawa (60) briefly reported observing a jump in the magnetisation of a Au 8 at.% Fe alloy, but did not investigate further.

2.2.5 Spin dynamics

Murani (72) recently reviewed a number of experimental investigations of the temperature dependence of the spin dynamics of AuFe and CuMn spin glass alloys. By probing the spin dynamics around T_f with neutrons, ESR, NMR, Muon precession and Mossbauer it was hoped that a better understanding of the spin freezing process could be gained.

High temperature ($T \sim 300$ K) low angle diffuse neutron scattering data reported by Murani and Tholence (73,74) on a range of dilute CuMn alloys (1-7 at.% Mn) were analysed by constant q spectral function fits $S(q,\omega)$. The low $q \sim 0.8$ nm^{-1} quasi-elastic spectra were fitted over a wide energy range ($0.5 < \omega < 10$ meV) by relatively narrow Lorentzian line forms (halfwidth $\Gamma \sim 2$ meV), the best fits were obtained at the lowest solute concentrations (see fig. 2.2.14a).

The weak q-dependence of the line width of the most dilute alloy was consistent with a Korringa relaxation mechanism whereby isolated spins indirectly dissipate their energy to the lattice via the host conduction electrons. A narrowing of the line width and deviations from a true Lorentzian line shape due to additional high energy quasi-elastic scattering in the wings of the spectra were reported to occur with increasing solute concentration. These deviations and the increasing q-dependence of the line width of the more concentrated alloys were argued to be evidence of exchange narrowing resulting from the increasing importance of RKKY exchange couplings between solute spins in these alloys. Note that in such concentrated alloys direct solute-solute near neighbour couplings would also be expected to contribute to the exchange narrowing.

Magnetic diffuse scattering cross sections evaluated from earlier neutron data (73) on a Cu 8 at.% Mn alloy showed no evidence of the critical fluctuations at $T \sim T_f$ normally associated with a cooperative phase transition. Simultaneous deviations of the elastic and quasi-elastic cross sections occurred below a temperature well above T_f as a result of the limited instrumental energy resolution of the spectrometer, $\Delta E \sim 0.2$ meV. This resolution limitation effect is due to slowly relaxing paramagnetic spins or groups of correlated spins with relaxation times $\tau \gtrsim \tau_m$ where $\tau \sim \hbar/\Gamma$. These appear to be frozen on the neutron time scale and thus contribute to the apparent elastic cross section.

Earlier low angle diffuse neutron scattering (75) from a pair of AuFe alloys (10 and 13 at.% Fe) were not resolution limited, and distinct critical scattering peaks were observed in the data (see fig. 2.2.14b). A q dependence of the critical scattering peak temperatures was observed for a series of q values between 0.05 and 0.3 nm^{-1}. The q dependence of the isothermal total integrated scattering intensity deviated significantly from a simple Ornstein-Zernike form. These peaks were considered to be due to the continuous freezing of superparamagnetic finite-sized clusters (resulting from concentration fluctuations) with decreasing temperature. For a given q it was argued that the freezing process would be dominated by clusters of size $\sim 1/q$. Thus, in terms of Neel's model, the freezing of the larger clusters at higher temperatures correlates well with the increase of the critical scattering peak temperatures at lower q values.

Very recent measurements by Alloul (76,77) of ^{63}Cu NMR in finely divided dilute Cu Mn samples (0.4 - 4.7 at.% Mn) have demonstrated the presence of strong spin correlations in the spin glass state at temperatures ($T \lesssim T_f/4$) where the zero-field NMR was observable. A large RF field enhancement was observed, which depended strongly on the sample's magnetic history. This behaviour was said to be

typical of single domain ferromagnet and was interpreted as evidence of the coherent rotation of a macroscopic magnetisation resulting from the collective interactions of the majority of the sample's Mn moments. The absence of any detectable RF field enhancement of the zero-field NMR in a ZFC sample argued against the presence of "domains" in such a state, since they would be coupled by an interaction of the same magnitude as the exchange interaction and would therefore be indistinguishable. However, the sense in which Alloul used the term "domain" was not made clear in his paper.

A magnetic field B_i induced an irreversible remanent magnetisation which, due to strong spin correlations, behaved as a macroscopic "domain". An undirectional anisotropy energy B_d, speculated to be due to spins not participating in the strongly correlated "domain" and a uniaxial anisotropy B_{ax}, were both considered to be induced by the field B_i and to determine the magnetostatic behaviour of the remanent magnetisation. The anisotropy energies associated with B_d and B_{ax} were both observed to be essentially independent of magnetic history; a similar observation was made by Kouvel (45) with regard to his magnetic hysteresis loop measurements. The existence of a unique macroscopic anisotropy, well defined in magnitude, with its axis parallel to the cooling field, wos inferred from the external field B_o dependence of the RF field enhancement factor $\eta(B_o)$. This evidence was considered to argue against the microscopically distributed random anisotropy usually assumed to account for the temperature and frequency dependence of the AC susceptibility in terms of a "blocking" of independent domains. Alloul concluded that "domains" were not present, a priori, in a spin glass, but were induced, together with their associated anisotropy, by externally applied fields. He stated further that he considered the latter conclusion to argue against the sharp peak in the low-field susceptibility being due to the blocking of independent "domains".

The occurrence of abrupt magnetisation reversals under the specific condition $|B_o + B_d| < B_{ax}$ as observed in the magnetisation loop measurements by Monod (70, 71) imply a more complex phenomenon. Alloul thought, like Monod, this could perhaps involve the nucleation and propagation of a "domain-wall" rather than a simple magnetostatic interaction of the domain magnetisation with its anisotropy. Alloul concluded finally that the concepts of the independent "domain" theory need not be abandoned. He considered it conceivable, even in the presence of strong correlations, for part of the "domain" magnetisation to respond to sufficiently large applied fields B_i and relax in an Arrhenius thermally-activated fashion on suppressing B_i.

ESR measurements of the spin dynamics of dilute Cu Mn alloys (42,78,79) and Y 2 at.% Gd (81) show a "bottlenecking" effect due to the long spin-lattice relaxation times of the Korringa mechanism compared to the characteristic spin precession period $\tau_m \sim 10^{-7}$ s. Below T_f the linewidths ΔB and g-shifts are large, with increasing temperature they decrease continuously with no anomalous behaviour at T_f, until at some temperature well above T_f a minimum linewidth is observed as ΔB begins to increase linearly with T in Korringa fashion and g opproaches 2. In dilute Au Fe alloys ($\lesssim$ 10 at.% Fe) the ESR line widths are too large to be observed due to the very rapid relaxation of individual non S-state Fe ions strongly coupled to the lattice via their orbital moments (80). At higher Fe concentrations many Fe atoms are in strongly correlated finite-sized near-neighbour clusters with correspondingly slower relaxation times. The temperature dependence of the resonance linewidth of these more concentrated alloys is complicated by the presence of both the Korringa and the finite cluster relaxation channels. The ESR line width behaviour modifed by "bottleneck" effects is very similar to the linewidth behaviour of resolution limited quasi-elastic neutron scattering spectra.

In conclusion these various probes of the spin dynamics seem to indicate that the development of spin correlations begins at temperatures well above T_f, as is evidenced by the substantial amount of entropy ($\sim$ 70% cR ln (2 J + 1)) associated with the long tail of the magnetic specific heat to temperatures well above T_f (20,21).

2.2.6 Concluding Remarks

The terms "clusters", "clouds" and "domains" are frequently used in the literature in connection with descriptions of remanent behaviour. It is not often made clear by the authors what exactly is meant by the particular term they have chosen to use. However, from the context of their use the following general definitions may be offered.

The term "clusters" appears more frequently to be used when referring to metallurgically inhomogeneous regions of predominately ferromagnetic moment couplings. These regions may be due to atomic clustering of moments with ferromagnetic first-neighbour couplings (e.g. as in aged dilute Cu Co) or short range order of moments with ferromagnetic second-neighbour couplings (e.g. as in aged, moderately concentrated Cu Mn). Also included in this definition are regions, usually termed "finite-clusters", of ferromagnetically coupled first-neighbour moments resulting from statistical concentration fluctuations of purely random Fe atomic distributions in, for example, moderately concentrated Au Fe alloys. Clusters as defined above may be regarded as rigid, independent entities if the intra-cluster exchange coupling experienced by a moment within the cluster is much stronger than the inter-cluster coupling of the same moment with all other moments not included in clusters through long range RKKY interactions, or with other clusters through dipolar interactions of their giant moments. These clusters behave superparamagnetically at temperatures above T_f which are low enough for the clusters to be rigid entities with well-defined giant moments (see the magnetic

phase diagram of Au Fe, fig. 2.3.1).

The term "clouds" has become loosely associated with the Tholence and Tournier model (see section 2.2.4) of local microscopic regions of predominately antiferromagnetic spin alignment (on an Ising lattice) with a net moment resulting from incomplete compensation. "Domain" is a term frequently employed by Alloul and Monod in connection with their NMR work. They use the term to refer to regions of macroscopic magnetisation resulting from the partial alignment of otherwise randomly orientated, strongly correlated spins.

Thermoremanent behaviour is not easy to understand without invoking models based on magnetic clusters (used in a general sense) blocked by local anisotropy. The analogy with Neel's theory of single-domain ferromagnetic particles has certainly proved to be useful in relating some of the diverse phenomena associated with spin glasses. To justify the presence of independent magnetic clusters thermally fluctuating against local anisotropy energy barriers as assumed in the Neel theory is not so easy. However, the presence of strong cluster correlations may not be as serious an objection to a Neel model as first thought. Consider, for example, how spin correlations are taken care of in the Curie-Weiss law by simply transforming the temperature dependence of a Curie law from T to $T-\theta$ where θ is a characteristic temperature of the spin correlations.

The foregoing discussion was centred on rigid, independent clusters which can be well described by the theory of superparamagnetism. In real alloys, intra-cluster exchange may not be strong compared to inter-cluster interactions; account must be taken of internal spin dynamics of clusters in such cases. The theoretical attempts of Smith and Soukoulis (see Chapter 1) on this problem could well point the way to more fruitful approaches to spin glass theory.

There is currently a resurgence of experimental interest in the spin glass state with many results of work performed in the early 1970's being brought into question by new data from more carefully planned experiments. The revival of interest was very evident at two recent meetings : the joint Intermag - MMM conference in New York (July 1979) and ICM-79 in Munich (September 1979). Some of the major topics of interest included the behaviour of the susceptibility close to its peak, magnetisation jumps and the nature of the remanence. Guy has been looking more closely at the magnetisation components close to T_f and has experimental evidence which questions the simple separation of the total magnetisation into reversible and irreversible components, as originally suggested by Tholence and Tournier. Tholence has been considering the frequency dependence of the susceptibility peak temperature and stressed the importance of the RKKY interaction strength in determining the magnitude of the observed frequency dependent shifts of T_f. Alloul, Monod and Prejean have been extending their study of magnetisation jumps and spin dynamics in dilute Cu Mn alloys.

At the time of writing many of the ideas about the spin glass state are in flux. It would appear that there are signs of recognition by many researchers of the importance of both cluster (again, used in the general sense) and phase transition concepts of spin glass phenomenology, rather than the sharp polarisation of opinion that had existed previously on these subjects.

2.3 The Transition to Long-Range Magnetic Order

2.3.1 Introduction

In very dilute alloys the randomly distributed magnetic solute atoms are well dispersed throughout the host matrix; statistically, the number of clusters of two or more first-neighbour solute atoms is insignificant. As the solute concentration is increased the number and average size of solute clusters increases until at a critical concentration a cluster with the dimensions of the sample termed the "infinite cluster" forms. This is the picture of the percolation process by which the short-range direct exchange interactions between first-neighbour solute atoms establish long-range magnetic order. In real alloys long-range interactions between solute moments modify this simplistic picture. Some of the experimental evidence discussed in this section on Au Fe and Cu Mn will give some clues as to how the emergence of long-range magnetic order is affected by the persistence of extensive short-range order in the form of finite clusters not part of the infinite cluster but interacting with it by indirect RKKY exchange couplings (87). In such large cluster regions the local moment picture will no longer be suitable as the d-electrons of the solute atoms become increasingly itinerant in character with the development of an electronic 3d-band structure as the areas of overlapping atomic d-orbitals become more extensive.

The long-range magnetic order which emerges in concentrated Au Fe alloys is ferromagnetic in nature and differs from the antiferromagnetism of concentrated Cu Mn alloys. For this reason the experiments on these alloys will be discussed separately in the following sections.

2.3.2 Emergence of ferromagnetism in concentrated Au Fe alloys

Magnetisation and susceptibility

One of the most notable early experimental investigations of the emergence

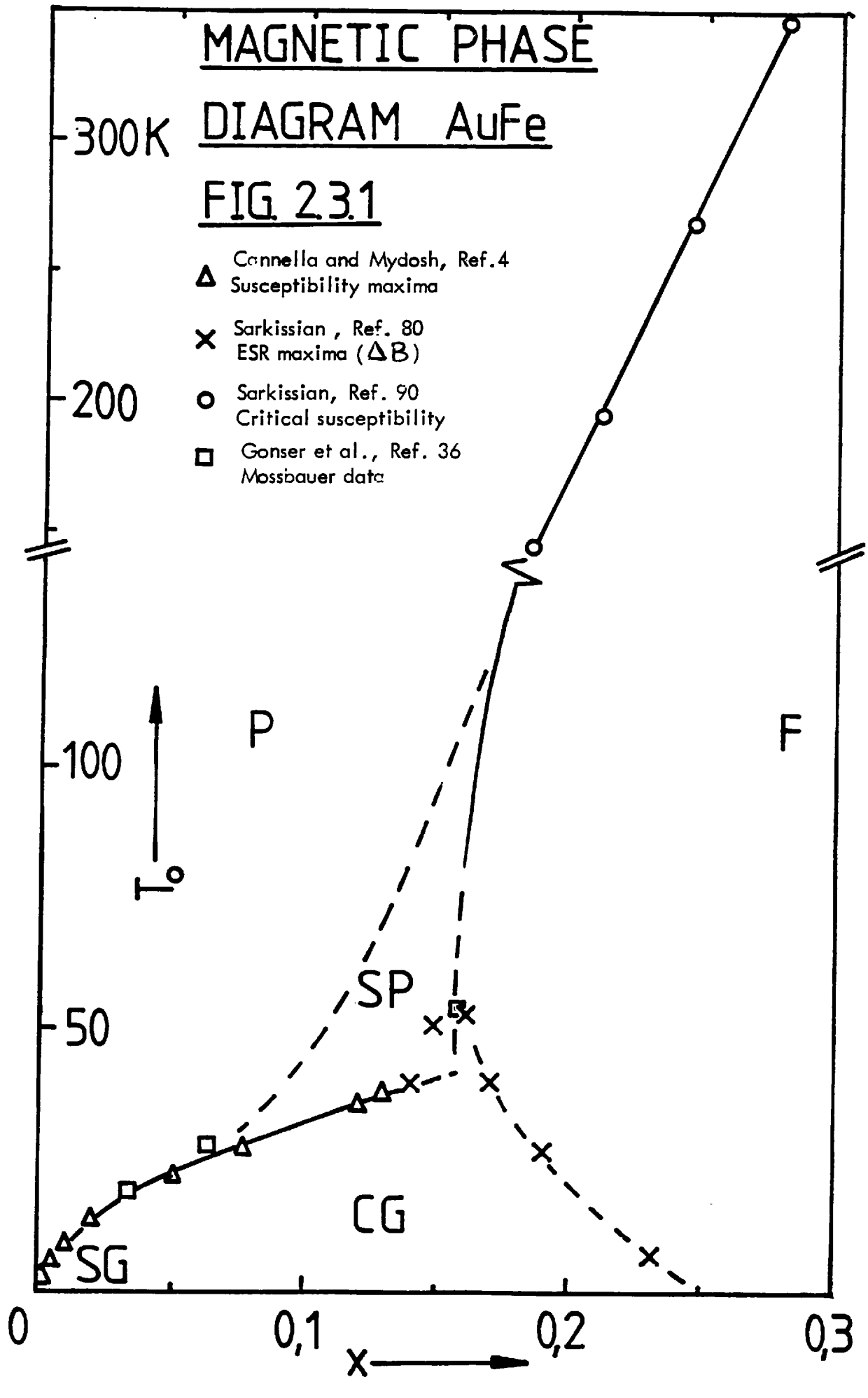
MAGNETIC PHASE
DIAGRAM AuFe
FIG 2.3.1
Cannella and Mydosh, Ref.4
Susceptibility maxima
Sarkissian , Ref. 80
ESR maxima (ΔB)
Sarkissian, Ref. 90
Critical susceptibility
Gonser et al., Ref. 36
Mossbauer data
300K
200
100
50
P
F
SP
CG
SG
0
0,1
0,2
0,3
x

of ferromagnetism in Au Fe were the high-field magnetisation measurements of Crangle and Scott (82). They analysed their data with Arrott type plots of B/σ vs. σ^2 isotherms which gave the Curie temperature as the temperature at which the B/σ ($\sigma^2 = 0$) intercept values interpolated to zero. Finite Curie temperatures were found for alloys with $c \geqslant 14.9$ at.% Fe but not for $c \leqslant 11.1$ at.% Fe. Mossbauer measurements of Gonser et al (36) on 15.7, 19.5 and 24.7 at.% Fe alloys and Borg (83) on an 18 at.% Fe alloy were also reported but no marked changes were observed in the character of the spectra of these alloys from those of the lower Fe concentration alloys. Gonser et al attempted to interpret the transition temperatures they had deduced from their measurements in terms of some of the early percolation theories and concluded that their results fitted Sato et al's average coordination number scheme which predicted a critical concentration of 16.7 at.% Fe (see Chapter 1). In the light of recent percolation theory calculations of critical concentrations it seems most likely that any such agreement with this earlier result was fortuitous. Magnetic hysteresis loop measurements on a 15 at.% Fe alloy by Murani (84) and on a 19 at.% Fe alloy by Coles et al (85) showed no hysteresis effects or remanence at $\sim$77 K. The magnetisation loop obtained at 4.2 K for the 15% alloy exhibited a time-dependent remanence typical of the lower concentration spin glass alloys, but any loop displacement of the kind observed by Kouvel was too small to be observed. A stable hysteresis loop typical of a normal bulk ferromagnet was obtained for the 19% alloy at 4.2 K. Further low-field magnetisation measurements by Murani (84) on the 15% alloy showed thermomagnetic history effects typical of spin glass alloys.

Low-field AC susceptibility data reported by Cannella et al (4,34) on 17 and 22 at.% Fe alloys were significantly different from those of their lower Fe

concentration alloys. A sharp divergence of the susceptibility was observed as the temperature decreased through the Curie temperature. Below the Curie temperature the susceptibility remained constant, limited by the demagnetisation fields induced by the sample shape (ellipsoidal).

More recent low-field susceptibility measurements reported by Coles et al (87) were performed on a range of alloys with Fe concentrations between 15.1 and 26 at.%. The interesting feature of these measurements was the fall in the low-temperature AC and DC susceptibility at a characteristic temperature T_f which decreased with increasing Fe concentration from $T_f \sim 45$ K at 16% to $T_f < 2$ K at 26%.

Maartense and Williams (89) measured the critical AC susceptibility of a 22 at.% Fe sample (a thin sliver of 40 μm foil) in various DC bias fields B. The Curie temperature (T_c = 213 K) of the sample was determined from the temperature at which a point of inflection was observed in the high-temperature side of the critical susceptibility curve (at zero DC bias field). The principal maxima observed at zero bias field became increasingly rounded and shifted to lower temperatures whilst a secondary peak which evolved close to T_c shifted slightly to higher temperatures as the applied bias field was increased. This secondary peak was considered to be the true critical peak for which the critical exponents (defined by 2.1 and 2.2) $\delta \sim 3.5$ and $\gamma \sim 1.5$ were determined.

$$\chi(B,T_c) \propto B^{-\nu}, \qquad \nu = 1 - 1/\delta \qquad 2.1$$

$$\chi(0,T) \propto \epsilon^{\gamma}, \qquad \epsilon = T/T_c - 1 \qquad 2.2$$

The good linearity of a log-log plot of the $\chi(0,T)$ vs. ϵ data in the range $10^{-2} < \epsilon < 5 \times 10^{-1}$ was considered to argue against the presence of superparamagnetic

metallurgical precipitates in their alloy. No significant change in this behaviour was observed after a low-temperature ($< 100^{\circ}C$) annealing treatment of the alloy. However, the striking sensitivity of the Curie temperature of this quenched alloy to such treatments was considered to be due to a large concentration of lattice vacancies aiding the diffusion of Fe atoms into a less random distribution.

Verbeek and Mydosh (88) reported low-field AC susceptibility measurements on 17 and 18 at.% Fe samples (spheres) in DC bias fields up to 150 mT. They considered the DC bias fields to suppress the strong ferromagnetic response of the infinite cluster in these post-percolation alloys. In fields greater than 100 mT a second susceptibility peak became evident at lower temperatures which was ascribed to the independent freezing of the finite clusters.

Some very recent, extremely low-field (< 0.1 nT RMS) AC susceptibility measurements were briefly reported by Sarkissian (90) at ICM-79. Needle-shaped samples were employed to avoid the large demagnetising fields in spherical-shaped samples which mask the long-range critical fluctuations that occur close to T_c. Sketches of $\chi'(\omega)$, the real part of the complex susceptibility response, obtained for the 14, 17, 21 and 28% alloys are given in figure 2.3.2. A single rounded susceptibility peak in alloys with concentrations of 15% or less changes into a sharp, critical peak which shifts rapidly to higher temperatures, leaving a "shoulder" at low temperatures, in alloys with concentrations greater than 16%. The characteristic temperature T_f at which the susceptibility associated with the "shoulder" falls to zero decreases from $\sim$25 K in the 18% alloy to $\sim$5 K in the 24.5%, no decrease was observed in the 28% alloy down to 2 K. These decreases of the susceptibility associated with the "shoulder" were very gradual, there was certainly no evidence of peaks with the degree of sharpness observed by Verbeek and Mydosh (88).

Similar low temperature susceptibility decreases or shallow peaks have been

Critical dynamics of AuFe

FIG. 2.3.2

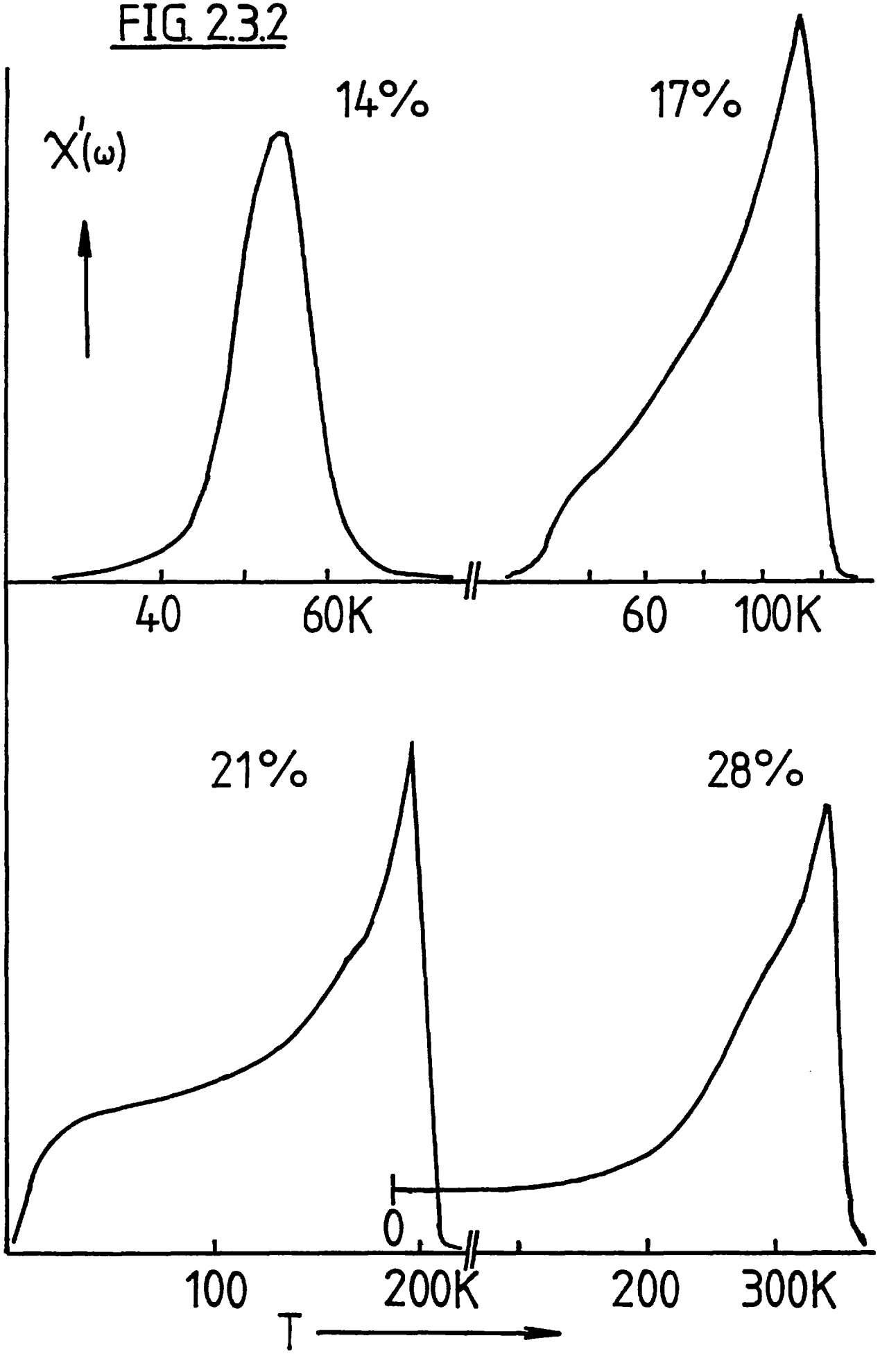

observed in a number of other dilute ferromagnetic or antiferromagnetic alloys just above the critical concentration. Nieuwenhuys et al (91) recently reviewed some of the evidence for such effects in Fe Al, Cr Fe, PdFe, Pd Mn and PdFe Mn. Meschede et al (93) also reported observing a decrease of the low-temperature susceptibility of a weakly ferromagnetic $Eu_{0.54}Sr_{0.46}S$ sample.

Neutron scattering

Small-angle diffuse neutron scattering measurements on a range of alloys between 10 and 23 at.% Fe were reported by Murani et al (92). These were quite difficult experiments to perform, even with the high flux reactor at ILL Grenoble. Long periods were involved in obtaining sufficiently high counts due to the strong neutron absorption cross section of Au.

No critical scattering peaks were observed in alloys with concentrations of 15% or less down to the lowest $q \sim 0.5\ nm^{-1}$. However, for alloy concentrations of 17% or more, clear critical peaks were observed with $q \sim 1\ nm^{-1}$, at temperatures increasing from ~ 150 K for the 17% alloy to ~270 K for the 23% alloy. This was the first direct evidence of a critical concentration for AuFe alloys of ~ 16 at.% Fe. Another interesting feature of these results to be remarked on by the authors was the continuing increase of the low-angle diffuse scattering at temperatures below ~50 K. It was suggested that this rise of the diffuse scattering at low temperatures may be due to the growing strength of spin correlations in finite clusters.

Other measurements

Low-temperature resistance data of Coles et al (85) on a range of alloys between 18 and 30 at.% Fe showed a large increase in the resistance increment $\Delta\rho_o = \rho_{4.2} - \rho_{1.5}$ around the critical concentration. The resistance increment $\Delta\rho_o$ developed in the cluster-glass regime of concentrations between 10 and 16 at.%; at the critical concentration a fairly sharp knee was observed as $\Delta\rho_o$ continued to increase more

slowly up to 22% before beginning to fall again to a pre-percolation value at ~30%. This behaviour was considered to reflect the development up to the critical concentration and subsequent persistence above the critical concentration of finite clusters. A double "shoulder" was observed in the $\Delta\rho = \rho_{ALLOY} - \rho_{HOST}$ data for the 17 and 22% alloys of a series studied by Mydosh et al (32).

The general features of the temperature dependence of the ESR line-width have previously been discussed under the heading of spin dynamics (section 2.2.5). In the post-percolation alloys a rapid increase of line-width is observed at temperatures just below the Curie temperature of the infinite cluster. The line-width peaks at a temperature close to the T_f values taken from the low-field susceptibility data before beginning to decrease at still lower temperatures. This effect decreased markedly with increasing Fe concentration and was certainly absent in a 28% alloy. Such behaviour was suggested to be the result of a relaxation process involving the very rapidly relaxing finite clusters through which the slowly relaxing infinite cluster transfers its energy to the lattice. The finite cluster relaxation channel was thought to become blocked at lower temperatures due to the freezing of the finite clusters.

K.A. Mirza and J.W. Loram (private communication 1978) reported an early result of their extensive specific heat investigations of concentrated AuFe alloys. The measurements on an 18% alloy exhibited a well-defined critical ordering peak at $T_c = 165$ K agreeing fairly well with $T_c = 148$ K for an 18.5% alloy obtained from low-field AC susceptibility data (70). No sharp anomaly was evident in the data at or close to T_f.

Concluding remarks

In the preceding review of experiments on concentrated AuFe alloys many references were made to the role of finite clusters close to and just above the percolation limit. Percolation theory (discussed in Chapter 1) certainly indicates

that a substantial fraction of the moments may be expected to be in finite clusters just above the critical concentration and that this fraction remains significant up to ~30 at.% Fe. The changes in magnetic behaviour evident below ~50 K in a variety of magnetic properties of alloys just above the percolation limit was strongly suggestive of an independent freezing of finite clusters. The decrease of the low-temperature susceptibility of these dilute ferromagnetic alloys could be ascribed to coercivity in the infinite cluster. However, it was pointed out by Coles et al (87) that the absence of any such effect in the 28% alloy argues against this interpretation. A further interpretation was suggested by Verbeek and Mydosh (88) in which the infinite cluster breaks up into many finite clusters below T_f, due to the increasing strength of some randomly orientated local anisotropy or shape anisotropy associated with the infinite cluster.

At this present stage the understanding of the AuFe system may be summarised in a magnetic phase diagram (fig. 2.3.1). From the lowest concentrations a low temperature spin-glass regime evolves slowly with increasing concentration into a cluster-glass regime above ~8-10% characterised by finite clusters which behave superparamagnetically above T_f and freeze at T_f in a spin-glass fashion. At a critical concentration of ~16% a weak ferromagnetic regime emerges with a more rapid increase of transition temperature with increasing concentration. At lower temperatures in this regime a finite cluster freezing is considered to occur at characteristic temperatures continuing on from the freezing temperatures of the cluster-glass regime just below the percolation limit. The characteristic finite cluster freezing temperatures gradually fall to zero at ~28%, where the number of finite clusters is insignificant and the alloys begin to behave as good ferromagnets.

The nature of the low-temperature magnetic state of alloys in this weak ferromagnetic regime is far from clear. There is certainly a need for further work to

elucidate the character of the finite cluster freezing and the low-temperature excitations to determine the similarities in the behaviour of these alloys to that of those just below the percolation limit.

2.3.3 Emergence of antiferromagnetism in concentrated Cu Mn alloys

The delay of the emergence of long-range antiferromagnetic order in the Cu Mn alloy system until a concentration of ~ 72 at.% Mn is reached (97) can at least in part be ascribed to the more complex percolation criterion in these FCC structured alloys. The critical concentration of ~45% calculated by Sato et al (see Chapter 1) is far short of the experimentally determined value and indicates that other factors must be involved. Increasing metallurgical problems and the FCC-FCT structural phase transition of the long-range magnetically ordered alloys at the Neel temperature further complicate the study of concentrated Cu Mn alloys. These metallurgical and structural changes are discussed in more detail in Chapter 4.

Concentrated Cu Mn alloys have been studied most extensively by neutron scattering experiments; these works will be discussed first as their conclusions form the basis of interpretations of the other experimental investigations.

Neutron scattering

The main features of the concentrated Cu Mn alloys were established by the early neutron scattering experiments of Meneghetti and Sidhu (94) and Bacon et al (95). The diffraction patterns (see fig. 2.3.3) obtained for these alloys (50-95 at.% Mn) are characterised by nuclear Bragg peaks at the (111), (200) and (002) positions. Magnetic reflections appear in the diffraction patterns of alloys with more than ~72% Mn at the (110) and (201) positions. These reflections are characteristic of a simple type-1 antiferromagnetic layer structure (see fig. 2.3.4). A broad, diffuse peak is observed closer to the (100) position in these concentrated alloys rather than the $(1\frac{1}{2}\,0)$ position in diffraction patterns of the quenched dilute alloys with less than

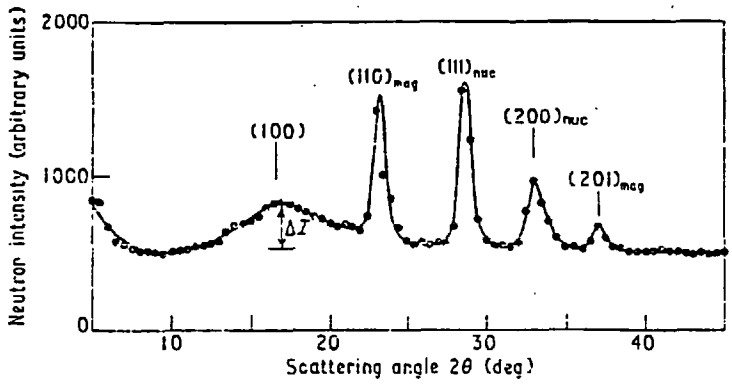

Figure 1. Neutron diffraction patterns of 82 at.% γ-MnCu alloy at 290 K. Sample rotating, experimental background subtracted. ΔI is a measure of the intensity of the diffuse peak.

Fig. 2.3.3 Vance et al., Ref.96

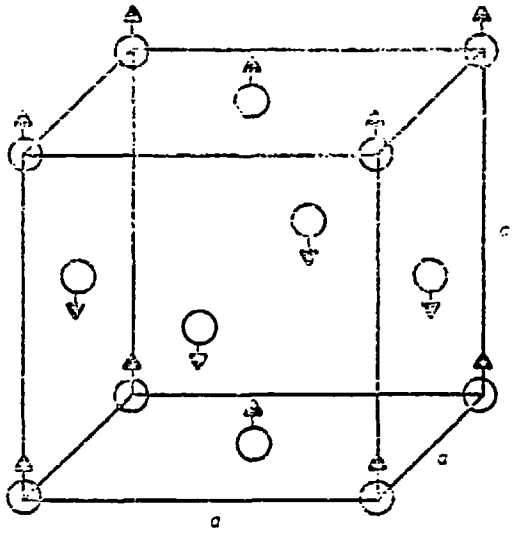

Figure 1. The magnetic structure of antiferromagnetic γ-Mn.

Fig. 2.3. 4 Meneghetti and Sidhu, Ref. 94

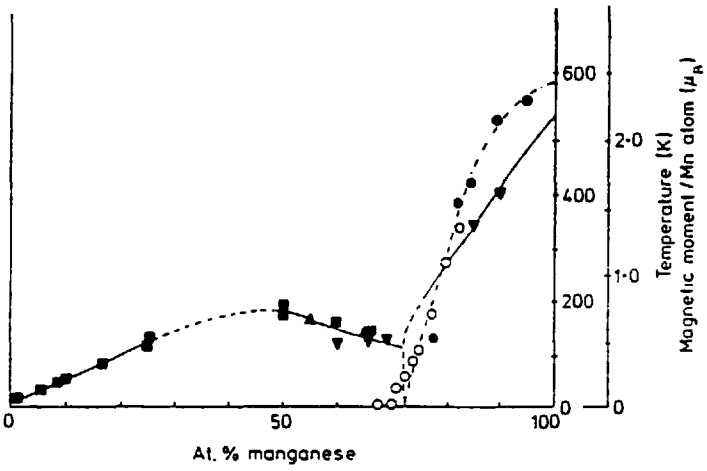

Figure 1. The variation of magnetic moment per manganese atom with composition; ● Bacon *et al* (1957), ○ present measurements, shown together with the variation of Néel temperature T_N, and spin freezing temperature T_F with composition; ▼ Smith (1960), ▲ Coles (1976), ■ Tustison and Beck (1976). The full line for T_N is derived from the measurements of Basinski and Christian (1951) and Bacon *et al* (1957).

Fig. 2.3.5 Cowlam et al., Ref.97

72% Mn.

The intensity of the Bragg peak at the (111) position approaches zero at a composition of ~68% where coherent scattering from Cu and Mn nuclei cancel due to the opposite sign of their respective scattering lengths. This convenient feature enabled very sensitive measurements of the compositional changes which occur during ageing heat treatments of an alloy of this composition (so called "null-matrix" composition) by Vance et al (96). However, the weakening of the nuclear Bragg peaks in this composition regime prevents reliable neutron measurements of the small tetragonal distortion ($c/a < 1$) which occurs below the Neel temperature. The intensities of the magnetic (110) and (201) reflections are strongly temperature dependent and tend to zero above the Neel temperature. Cowlam et al (97) derived the composition dependence of the magnetic moment per Mn atom from comparisons of the relative intensities of the magnetic superlattice and fundamental Bragg reflections (see fig. 2.3.5). Cowlam et al (98) discussed the compositional variation of the Mn moment in a number of other γ-Mn alloys in connection with band theory calculations.

The nature of the diffuse peak close to the (100) position in the diffraction patterns of the concentrated quenched alloys has attracted much interest and speculation since it was first observed in the early works. The absence of polarisation analysis techniques in these early works prevented reliable determination of the scattering processes responsible for the diffuse peak. The temperature dependence of the peak suggested that it was due to magnetic SRO. Vance et al (96) concluded that the peak was due to static or quasi-static magnetic SRO. The intensities of (100) diffuse peaks of a series of alloys (~75-90%) were observed to peak at the respective alloy's Neel temperature, whereas the width of the peaks were essentially independent of composition and temperature. The large increase of the low-angle diffuse background

of these concentrated alloys was attributed to extensive atomic clustering but no evidence of second phase precipitation was found. The temperature dependence of the diffuse peak suggests that magnon scattering could also be responsible for it. Vance et al showed that the scattering was predominately elastic or quasi-elastic in nature and therefore could not involve magnon creation or annihilation.

Metallurgical difficulties prevent the preparation of single-phase, single crystal samples in this high Mn concentration regime. A technique first demonstrated by Bacon et al (95) to partially overcome this problem involves applying pressure to the FCT structured alloys (i.e. $>$ 80% Mn at room temperature) to orientate the anisotropy axis of the moments, i.e. the c-axis of the crystallites. Campbell and Wells (99,100) used this technique of stress orientation to aid their study of a pair of alloys close to the critical concentration. Bacon et al had demonstrated that a pressure of $\sim$450 MPa irreversibly orientated the c-axes of the crystallites parallel to the axis of compression. This was verified by showing that the magnetic reflections were enhanced when the scattering vector $\underline{K}$ was perpendicular to the stress vector $\underline{\sigma}$ and diminished in the parallel geometry. A high degree of alignment, evidenced by the large ratio of intensities of the (200) and (002) nuclear peaks, was achieved by this technique; the degree of orientation was not fully qualified, however. Campbell and Wells, in their work on a stressed 72% alloy, observed a cusp-like peak at the (001) position of the diffraction pattern obtained in the $\underline{K} \parallel \underline{\sigma}$ geometry which they attributed to magnon scattering. A broad peak observed close to the $(1\,\frac{1}{2}0)$ position of the diffraction pattern obtained in the $\underline{K} \perp \underline{\sigma}$ geometry was attributed to magnetic defect scattering. This latter type of scattering results from static spatial fluctuations of moment alignment or moment size in an ordered magnetic structure. A recent polarisation analysis on a stressed 90% alloy by Campbell et al (001) was considered to confirm the earlier interpretation that magnon

scattering was responsible for the diffuse (001) peak. Cywinski et al (101), however, point out that at 4.2 K the presence of an expected gap of ~ 3 meV in the magnon spectra implied that, in their experiment, the ~ 6 meV incident neutron energy would not excite many spin waves. The intensity of this (001) magnetic diffuse peak was observed to be greater at 4.2 K than at room temperature. These results made the magnon scattering interpretation of the (001) peak doubtful. A very careful energy analysis of the neutron scattering would be required to resolve this question.

Other measurements

Other experimental investigations of concentrated Cu Mn alloys are sparse, although a lot of interest was shown in the metallurgical and mechanical properties of these alloys on account of their high vibrational damping capacities. Low temperature specific heat measurements by Zimmerman and Sato (102) (see Chapter 4) were discussed in connection with ideas about the electronic band structure of γ-phase transition metal elements. The low extrapolated electronic specific of γ-Mn was suggested to indicate a broader d-band in this phase. The authors further speculated that the similar electronic specific heats of other close packed transition metals suggests that the crystal structure may play a more important role than density of states at the fermi level in determining electronic specific heat.

Bacon et al (95) and Street (103) reported observing kinks at the Neel temperature in the otherwise monotomic increase of their resistivity and susceptibility data. Tustison and Beck (50) measured the low-field AC susceptibility of 50, 60 and 66 at.% Mn alloys. Peaks were observed in the susceptibility data, the 50% alloy exhibiting the highest peak temperature. In general the magnitude and temperature dependence of the susceptibility was much weaker than observed in the lower concentration alloys. The large, temperature independent component of the susceptibility and the decreasing temperature of the susceptibility peak in alloys

with $\geq$ 50% Mn were associated with the extensive short-ranged antiferromagnetic order considered to prevail in these pre-percolation alloys.

Coles (105) reported low-field ($\sim$ 4 mT) magnetisation and resistivity measurements on a number of Cu Mn alloys with concentrations between 20 and 75 at.% Mn. Alloys with more than $\sim$ 45% Mn exhibited minima in their resistivity at $\sim$ 20 K. Plots of ($\rho_{min} - \rho_{1.5\,K}$) and ($\rho_{200\,K} - \rho_{20\,K}$) show sharp changes close to the critical concentration. Mossbauer data obtained by Window (104) indicate spin freezing at temperatures close to the susceptibility maxima of alloys with 50% Mn or more.

Coles suggested that a CPA-like Mn d-band had formed by near neighbour d-orbital overlap in alloys with $\sim$ 40% Mn. He believed that the increasing width of this d-band with increasing Mn concentration competed with the localisation of moments at solute sites to produce the observed fall in T_f between 50 and 70% Mn. The relatively small, weakly temperature dependent susceptibility of the higher concentration alloys resembled the high temperature exchange-enhanced Pauli paramagnetism of other d-band itinerant antiferromagnets.

Very recently Coles (106) suggested that Cu Mn alloys with Mn concentrations between 45 and 65% were good examples of Stoner spin glasses (107, 108). A Stoner spin glass was defined as a frozen spin structure, in which the 3d electrons providing moments form a d-band. In the particular case of Cu Mn alloys the Mn is of sufficient concentration to provide a 3d band of CPA character. Antiferromagnetic first neighbour couplings between the Mn moments in FCC structured Cu Mn result in frustration effects, which hinder the onset of long-range itinerant antiferromagnetism, responsible for the Stoner glass character. A re-interpretation of neutron data on alloys in the Stoner glass regime may help to clarify ideas about the degree of localisation of moments.

2.4 Specific heat of alloys near the critical concentration

2.4.1 Introduction

Studies of the concentration dependence of the low-temperature specific heat af a number af allays undergaing transitians ta lang-range magnetic arder have exhibited the comman feature of a peak in the apparent electranic specific heat caefficient close ta the critical concentration. Since this feature was first recognized there have been several attempts ta account for it, some af which have been in terms of superparamagnetic particles (109 - 12), spin fluctuations (113 - 5), band splitting (116 - 7) and critical fluctuations (118).

Many af the allays, natably anes in which the magnetic solute atams do nat possess local moments in the dilute regime, exhibit fairly sharp up-turns in their law-temperature specific heat, with the strongest deviatians accurring close to the critical concentration. In the following sectians a critical discussion will be presented of the attempts to account far these features.

2.4.2 Superparamagnetic particles

The arigin af the departures fram linearity af the low-temperature specific heat of alloys like Ti Fe, V Fe and Cu Ni clase ta their critical concentratians had been the subject of considerable speculation. Early attempts ta account for this apparently anomalous behaviour were in terms of the thermal fluctuations of superparamagnetic clusters of solute atoms suppasedly resulting from metallurgical inhamogeneity of the alloys. Livingston and Bean (109) and Schroder (110) applied classical statistical mechanics to calculate the specific heat of a system af superparamagnetic particles, each with tatal spin J, interacting with an effective uniaxial internal field B. In the limit of large J the partition functian sum over discrete energy levels could be replaced by a cantinuous integral. The specific heat so derived was Einstein-like at law temperatures comprising af a temperature independent specific heat cantribution af k

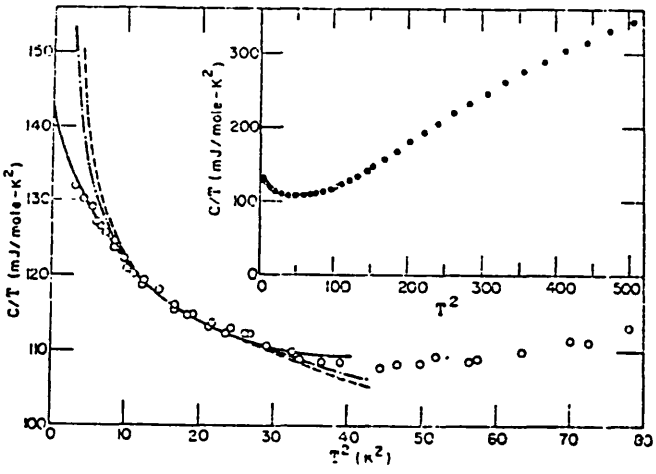

C/T versus T^2 for UAl_2. Fits using $C = AT + BT^3 + Df(T)$ are shown, where $f(T) = 1/T^2$ (dashed curve), $1/T$ (dashed-dot), and $T^3 \log T$ (solid curve). The inset shows the same data over a larger temperature range (MSD Negative 60450).

d. UAl_2 from ref. 126

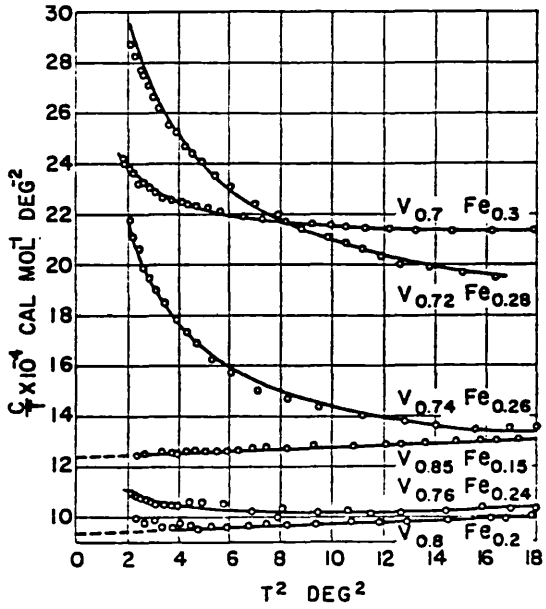

a. V Fe from ref. 119

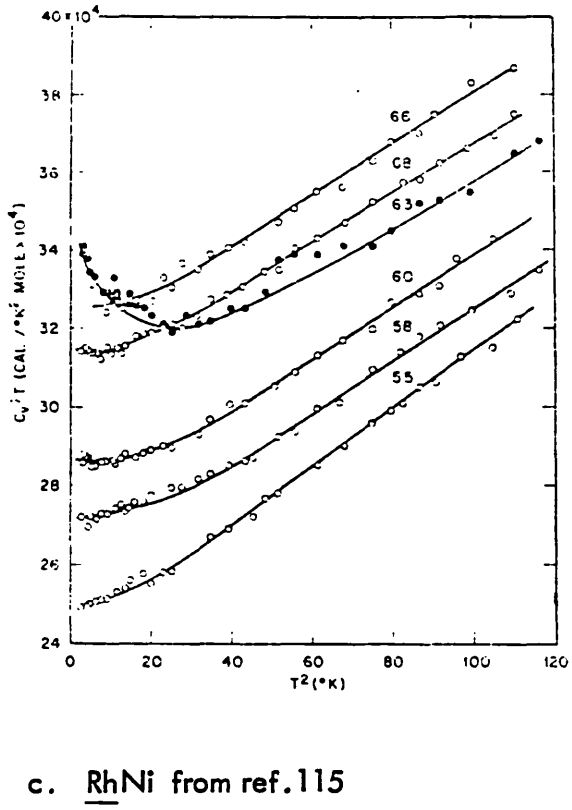

c. RhNi from ref. 115

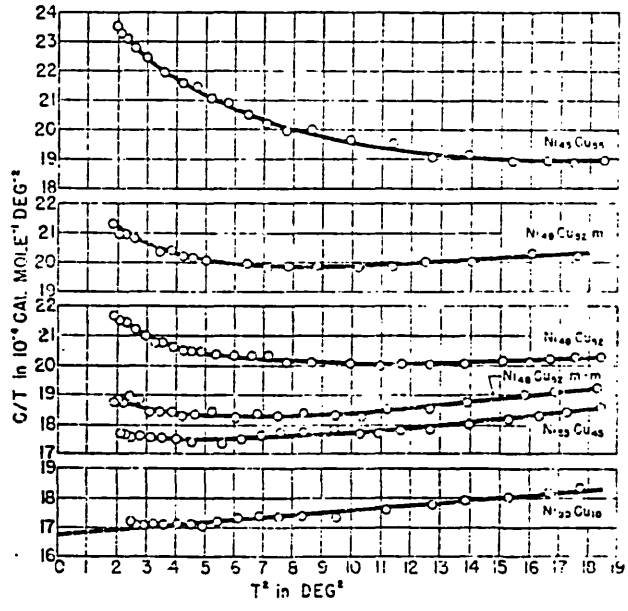

. Low-temperature specific heat of Ni-Cu solid solution alloys. For alloy $Ni_{0.48}Cu_{0.52}$, data were obtained both without magnetic cooling and after magnetic cooling from room temperature to 4.2°K with the magnetic field turned on during the measurements (m) and after magnetic cooling with the magnetic field on during the measurements (m-m).

b. CuNi from ref. 120

Figure 2.4.1

(Boltzman constant) per particle falling exponentially to zero below a characteristic temperature $T_E = g\mu_B B/k$ due to the finite separation of the lower energy levels. Above a higher characteristic temperature related to the total anisotropy energy of a particle, $T_m \sim g\mu_B JB/k$, the specific heat falls roughly as $1/T^2$.

Some fits to previously obtained data on Cu Ni and V Fe using the expression $C = A + \gamma T + \beta T^3$ were shown to be reasonably successful in the restricted range of temperatures between 1.4 and 4.2 K (see fig. 2.4.1a and b). Hahn and Wohlfarth (112) attempted a similar interpretation of the data obtained by Bucher et al (114) for some Rh Ni alloys (see fig. 2.4.1c). The superparamagnetic cluster approach was compared with the spin fluctuation model adopted by Benneman (113) for Cu Ni alloys (120 - 1). Hahn and Wohlfarth estimate that for the above mentioned alloys the range of measurement temperatures lies between T_E and T_m where the supposed paramagnetic clusters are expected to contribute a temperature-independent term to the specific heat. However they stressed that this over-simplified model cannot be taken too seriously, a more realistic approach must take account of variations of anisotropy, cluster shape and size, and their interactions. By a more general approach to the anisotropy, Hahn and Wohlfarth derived a further term, linear in temperature, which accounts for an apparent enhancement of the electronic specific heat $\Delta\gamma = \alpha\ k/T_m$ per particle ($\alpha \sim 1$ a numerical constant depending on the type of anisotropy).

Hayes et al (111) interpreted the specific heat of an aged Cu 0.7% Co alloy in terms of the development of superparamagnetic clusters. The results indicated a larger single particle anisotropy than the mean value deduced from torque measurements. Lanchester et al (122) investigated the effect of magnetic fields up to 6.5T on the low-temperature specific heat of Cu Ni alloys with compositions between 40 and 44 at.% Ni, close to the critical concentration ~43%. The specific heat anomaly was suppressed by the externally applied magnetic field in a way that at least qualitatively could be

understood as an augmentation of intrinsic internal fields leading to an increase of T_E and a corresponding broadening and shift to higher temperatures of an Einstein-like specific heat anomoly. In detail the fit to a simple Einstein function was less than satisfactory, even in the narrow range of temperatures considered ($0.3 < T < 4K$) and after allowing for variation of the cluster concentration in the fits. No allowance was made for an effective enhancement of the temperature linear specific heat term as predicted by Hahn and Wohlfarth, yet the presence of such a term, strongly dependent on field, was apparent in their data.

It is easy to obtain fairly good fits over a limited temperature range to a superparamagnetic cluster specific heat function which has a sufficient number of adjustable parameters, but it is more difficult to justify the physical significance of the fit parameters. A far better procedure to fix parameters such as cluster size and anisotropy field was adopted by Levin and Mills (see Chapter 1) in their cluster mean-field approach. In this latter model a Schottky-like cluster specific heat was obtained even for clusters as large as 50 spins; the internal spin dynamics of clusters was also considered, but this is not so important at the low temperatures considered here.

The solute atoms in the dilute regime of alloys like V Fe, Cu Ni and Rh Fe carry no local moments, these only appear at much higher solute concentrations. Realistic models of such alloys should also take into account localised spin fluctuations.

2.4.3 Spin fluctuations

The notion of persistent spin fluctuations (paramagnons) in nearly ferromagnetic fermi liquids was first discussed by Doniach and Engelsberg (124) in connection with the exchange enhanced paramagnetic susceptibility of pure palladium and by Berk and Schrieffer (125) in connection with the absence of a transition to superconductivity in He^3.

In the case of palladium the strong spin correlations of the d-band holes were

treated as a renormalisation of their self-energies due to the emission and reabsorption of long-lived spin fluctuation (paramagnons). On approaching the ferromagnetic instability from the paramagnetic side, the temporal persistance of the spin fluctuations increases as the Stoner enhancement factor increases. Calculations based on this model lead to a low-temperature electronic specific heat term corrected by paramagnons (i.e. electron-paramagnon interactions) of the form :

$$C_E/T = \gamma m^*/m + \alpha\gamma(T/T_{SF})^2 \ln(T/T_{SF}) \qquad 2.3$$

$$\alpha \sim U_o^2 n^2 (E_F) S$$

where T_{SF} is the characteristic spin fluctuation temperature, U_o is the spin correlation energy, $n(E_F)$ is the density of states at the fermi level and S is the Stoner exchange enhancement factor. The above specific heat expression is valid for temperatures $T < T_{SF}$. Although no evidence of spin fluctuation contributions to the specific heat of pure palladium have been observed, there is widely accepted evidence that such effects are responsible for the low-temperature deviations observed in the specific heat of UAl_2 (126, 127) and other intermetallic narrow 5f-band compounds (see fig. 2.4.1d).

Bucher et al (114) attempted to account for the low-temperature specific heat deviations of a Rh 63 at.% Ni alloy on the basis of the spin fluctuation model. These deviations were evident in the low-temperature specific heat data of alloys with Ni concentrations between 55 and 70% around the critical concentration for ferromagnetism $\sim$63%. A plot of the total specific heat at 1.4K peaks asymmetrically at the critical concentration whereas the coefficient of the temperature-linear term appears to peak at a slightly higher concentration ($\sim$ 66%). This latter discrepancy was considered to be due to the continuing increase of the density of states $n_{\uparrow}(E_F)$ of the majority-spin d-band, as the fermi level rises with increasing nickel concentration, until a maximum

in $n_{\uparrow}$ (E_F) is reached just inside the ferromagnetic regime.

The specific heat anomaly (a broad minimum in C/T as given by expression 2.3) is only expected to be observed at low temperatures $T \sim T_{SF}$. In alloys where the solute atoms are non-magnetic in the dilute regime ($T_{SF} \gg T$) no anomaly is expected; it is only as the ferromagnetic instability is approached, where T_{SF} tends to zero, that anomalous behaviour is found. It is expected that in this temperature range, moderately large magnetic fields ($B \sim$ few Tesla) with characteristic interaction energies $\mu_B B \sim k T_{SF}$ are likely to have a significant influence on the specific heat anomalies. Triplett and Phillips (123) demonstrated that an external field $B \sim 4T$ was sufficient to suppress the specific heat anomalies of these Rh Ni alloys. By contrast, Brodsky and Trainor (127) showed that an external field $B \sim 4.3T$ had an insignificant effect on the specific heat of UAl_2 as predicted by the spin fluctuation expression $\frac{\Delta C}{C} \sim \left(\frac{\mu_B B}{k T_{SF}}\right)^2$ for $T_{SF} \sim 25K$. The magnetic field dependence of the specific heat must therefore be interpreted with care when seeking to establish the validity of a spin fluctuation or some alternative model.

Lederer and Mills (128) have stressed the need to consider a localised rather than uniform exchange enhancement in their discussion of the Pd Ni system. They remark that the electronic specific heat close to the critical concentration for ferromagnetism ~3 at.% Ni is corrected by a term of the form $(T/T_{SF})^3$ rather than $(T/T_{SF})^3 \ln (T/T_{SF})$ as in the case of uniform enhancement. Further discourse on this subject by Barnea (129) and Fulde and Luther (130) have made plausible an account of localised spin fluctuations in terms of the framework of the uniform enhancement model by postulating a shift of T_{SF} to higher temperatures. From the theoretical standpoint the spin fluctuation concept requires further development, it should therefore be invoked with care in interpreting experimental phenomena.

2.4.4 Alternative schemes

Two further interpretations have been proposed in the literature to explain the anomalous specific heat behaviour close to the critical concentration. One is an adaptation of Miedema's (116) band splitting scheme proposed by Wohlfarth (117), the other is an interpretation in terms of critical fluctuations of the order parameter by Ododo (118).

Miedema developed an empirical scheme to calculate the electronic specific heat coefficient of non-magnetic binary transition metal alloys. It was proposed that the elements of the alloy contribute individually to the total electronic specific heat of the alloy in proportion to their concentration. A correction term accounting for the charge transfer occurring on alloying is estimated from the electronegativity difference of the two constituent elements.

Wohlfarth adapted Miedema's scheme to account for the anomalous specific heat behaviour of Pt Ni close to the critical concentration. From data in the paramagnetic regime an appropriate value for the paramagnetic electronic specific heat coefficient of Ni γ^{P}_{Ni} was deduced such that :

$$\gamma_{PtNi}(x) = \gamma_{Pt}(1-x) + \gamma^{P}_{Ni}x \qquad 2.4$$

At the ferromagnetic instability the Ni d-band was supposed to split and reduce the contribution to the electronic specific heat coefficient of the alloy from the Ni atoms by $\Delta\gamma$. Wohlfarth deduced from his theory of weak itinerant ferromagnetism that $\Delta\gamma \sim \gamma^{P}_{Ni}(|x-x_c|)$, where x_c is the critical concentration. This semi-empirical expression failed to predict the correct concentration dependence of $\gamma_{Pt\,Ni}$. The expression obtained for $\gamma_{Pt\,Ni}$ peaked well into the ferromagnetic regime, and beyond the peak varied quadratically with concentration, whereas an

almost linear dependence was observed experimentally.

Ododo (118) reviewed a number of schemes proposed in the literature to account for the anomalous specific heat close to the critical concentration. He compiled experimental results on the concentration dependence of the low-temperature specific heat of various alloys to show that the peaking of the temperature-linear specific heat coefficient at the critical concentration was not restricted to a ferromagnetic transition, but had also been observed for an antiferromagnetic transition e.g. CrFe. Invoking the theory developed by Mathon (see section 1.2.6), he argued that critical fluctuations of the order parameter were responsible for the anomalous concentration dependence of the specific heat near a critical concentration. Although the theory was not strictly applicable to alloy systems in which localised moments undergo long range ordering (as the magnetisation may be non-uniform) he suggested that damping of the critical fluctuations, due to the presence of a disordered spin glass regime preceding the emergence of long range order in such systems, may result in a broadening of the specific heat peak.

REFERENCES

1. Beck P.A., 1971, Metals Trans. 2, 2015
2. Beck P.A., 1972, J. Less Common Metals 28, 193
3. Beck P.A., 1978, Prog. Mater. Sci. 23, 1
4. Cannella V. and Mydosh J.A., 1972, Phys. Rev. B6, 4220
5. Cannella V., 1973, Amorphous Magnetism, eds. Hooper H.O. and de Graaf A.M., Plenum N.Y., 195
6. Mydosh J.A., 1974, AIP Conf. Proc. 24, 131
7. Larsen U., 1978, Phys. Rev. B18, 5014
8. Heeger A.J., 1969, Solid State Physics 23, 283, eds. Seitz F., Turnbull D. and Ehrenreich H., Acad. Press, N.Y.
9. Souletie J. and Tournier R., 1969, J. Low Temp. Phys. 1, 95
10. Zimmerman J.E. and Hoare F.E., 1960, J. Phys. Chem. Solids 17, 52
11. Crane L.T. and Zimmerman J.E., 1961, J. Phys. Chem. Solids 21, 310
12. de Nobel J. and du Chatenier F.J., 1959, Physica 25, 969
13. Dreyfus B., Souletie J., Tournier R. and Weil L., 1964, Compt. Rend. Acad. Sci. (Paris) 259, 4266
14. du Chatenier F.J. and Miedema A.R., 1966, Physica 32, 403
15. du Chatenier F.J., de Nobel J. and Boerstoel B.M., 1966, Physica 32, 561
16. Phillips N.E., 1971, Crit. Rev. Solid State Sci. 2, 467
17. Fogle W.H., Ho J.C. and Phillips N.E., 1978, J. Phys. (Paris) Colloque 39, C6-901
18. Martin D.L., 1978, J. Phys. (Paris) Colloque 39, C6-903
19. Martin D.L., 1979, Phys. Rev. B20, 368
20. Wenger L.E. and Keesom P.H., 1975, Phys. Rev. B11, 3497
21. Wenger L.E. and Keesom P.H., 1976, Phys. Rev. B13, 4053

22. Waldorf D.L., 1960, J. Phys. Chem. Solids 16, 90

23. Hawkins G.F., Moran T.J. and Thomas R.L., 1975, AIP Conf. Proc. 29, 235

24. Hawkins G.F. and Thomas R.L., 1978, J. Appl. Phys. 49, 1627

25. Bonnerot J., Caroli B. and Coqblin B., 1966, Ann. Acad. Sci. Fennicae AVI 210, 120

26. Bonnerot, 1966, Ph.D. Thesis, Orsay

27. Wenger L.E., 1978, J. Appl. Phys. 49, 1630

28. Levesque B., Caudron B. and Costa P., 1979, J. Phys. (Paris) Colloque 40, C5-266

29. Laborde O. and Radhakrishna P., 1973, J. Phys. F : Metal Phys. 3, 1731

30. Loram J.W., Whall T.E. and Ford P.J., 1970, Phys. Rev. B2, 857

31. Ford P.J., Whall T.E. and Loram J.W., 1970, Phys. Rev. B2, 1547

32. Mydosh J.A., Ford P.J., Kawatra M.P. and Whall T.E., 1974, Phys. Rev. B10, 2845

33. Ford P.J. and Mydosh J.A., 1976, Phys. Rev. B14, 2057

34. Cannella V., Mydosh J.A. and Budnick J.I., 1971, J. Appl. Phys. 42, 1689

35. Cannella V. and Mydosh J.A., 1973, AIP Conf. Proc. 18, 651

36. Gonser U., Grant R.W., Meecham C.J., Muir A.H. and Wiedersich H., 1965, J. Appl. Phys. 36, 2124

37. Violet C.E. and Borg R.J., 1966, Phys. Rev. 149, 540

38. Window B., 1970, J. Phys. C : Solid State Phys. 3, 922

39. Lutes O.S. and Schmit J.L., 1964, Phys. Rev. 134, A676

40. Tholence J.L. and Tournier R., 1971, J. Phys. (Paris) Colloque 32, C1-211

41. Street R., 1960, J. Appl. Phys. 31, 310S

42. Owen J., Browne M.E., Arp V. and Kip A.F., 1957, J. Phys. Chem. Solids 2, 85

43. Owen J., Browne M.E., Knight W.D. and Kittel C., 1956, Phys. Rev. 102, 1501

44. Kouvel J.S., 1960, J. Appl. Phys. 31, 142S

45. Kouvel J.S., 1961, J. Phys. Chem. Solids 21, 57

46. Kouvel J.S., 1963, J. Phys. Chem. Solids 24, 795

47. Mukhopadhyay A. and Beck P.A., 1975, Solid State Commun. 16, 1067

48. Mukhopadhyay A.K., Shull R.D. and Beck P.A., 1975, J. Less Common Metals 43, 69

49. Tustison R.W., 1976, Solid State Commun. 19, 1075

50. Tustison R.W. and Beck P.A., 1976, Solid State Commun. 20, 841

51. de Mayo B., 1972, AIP Conf. Proc. 5, 492

52. de Mayo B., 1974, J. Phys. Chem. Solids 35, 1525

53. Murani A.P., 1974, J. Phys. F : Metal Phys. 4, 757

54. Zibold G., 1978, J. Phys. (Paris) Colloque 39, C6-896

55. Zibold G., 1978, J. Phys. F : Metal Phys. 8, L229

56. Zibold G., 1979, J. Phys. F : Metal Phys. 9, 917

57. Davis J.R. and Hicks T.J., 1979, J. Phys. F : Metal Phys. 9, 753

58. Davis J.R., Burke S.K. and Rainford B.D., 1979, Proc. ICM 79, Munich, Germany (to be published)

59. Neel L., 1955, Adv. Phys. 4, 191

60. Tournier R. and Ishikawa Y., 1964, Phys. Letts. 11, 280

61. Tholence J.L. and Tournier R., 1974, J. Phys. (Paris) Colloque 35, C4-229

62. Guy C.N., 1975, J. Phys. F : Metal Phys. 5, L242

63. Guy C.N., 1976, Physica 86-88B, 877

64. Guy C.N., 1977, J. Phys. F : Metal Phys. 7, 1505

65. Guy C.N., 1978, J. Phys. F : Metal Phys. 8, 1309

66. von Lohneysen H., Tholence J.L. and Tournier R., 1978, J. Phys. (Paris) Colloque 39, C6 - 922

67. Eiselt G., Kotzler J., Maletta H., Stauffer D. and Binder K., 1979, Phys. Rev. B 19, 2664

68. Gray E.M., 1979, J. Phys. F : Metal Phys. 9, L167

69. Dahlberg E.D., Hardiman M. and Souletie J., 1978, J. Phys. (Paris) Letts. 39, L389

70. Monod P. and Prejean J.J., 1978, J. Phys. (Paris) Colloque 39, C6-910

71. Monod P., 1979, Proc. Joint Intermag - MMM Conf., New York (J. Appl. Phys. 50 - to be published)

72. Murani A.P., 1978, J. Phys. (Paris) Colloque 39, C6 - 1507

73. Murani A.P. and Tholence J.L., 1977, Solid State Commun. 22, 25

74. Murani A.P., 1978, Phys. Rev. Letts. 41, 1406

75. Murani A.P., 1976, Phys. Rev. Letts. 37, 450

76. Alloul H., 1979, Phys. Rev. Letts. 42, 603

77. Alloul H., 1979, Proc. Joint Intermag - MMM Conf., New York (J. Appl. Phys. 50 - to be published)

78. Griffiths D., 1967, Proc. Phys. Soc. 90, 707

79. Salamon M.B. and Herman R.M., 1978, Phys. Rev. Letts. 41, 1506

80. Sarkissian B.V.B., 1979, Phil. Mag. B 39, 413

81. Male S.E., 1976, Ph.D. thesis, London

82. Crangle J. and Scott W.R., 1965, J. Appl. Phys. 36, 921

83. Borg R.J., 1970, Phys. Rev. B 1, 349

84. Murani A.P., 1974, J. Phys. F : Metal Phys. 4, 757

85. Coles B.R., Taylor R.H., Sarkissian B.V.B., Khan J.A. and Bennett M.H., 1977, Physica 86 - 88B, 275

86. Coles B.R. and Sarkissian B.V.B., 1978, Inst. Phys. Conf. Ser. 39.6, 466

87. Coles B.R., Sarkissian B.V.B. and Taylor R.H., 1978, Phil. Mag. B37, 489

88. Verbeek B.H. and Mydosh J.A., 1978, J. Phys. F : Metal Phys. 8, L109

89. Maartense I. and Williams G., 1978, Phys. Rev. B17, 377

90. Sarkissian B.V.B., 1979, Proc. ICM-79, Munich, Germany (to be published)

91. Nieuwenhuys G.J., Verbeek B.H. and Mydosh J.A., 1979, J. Appl. Phys. 50, 1685

92. Murani A.P., Roth S., Radhakrishna P., Rainford B.D., Coles B.R., Ibel K., Goeltz G. and Mezei F., 1976, J. Phys. F : Metal Phys. 6, 425

93. Meschede D., Steglich F., Felsh W., Maletta H. and Zinn W., 1980, Phys. Rev. Letts. 44, 102

94. Meneghetti D. and Sidhu S.S., 1957, Phys. Rev. 105, 130

95. Bacon G.E., Dunmur I.W., Smith J.H. and Street R., 1957, Proc. Phys. Soc. 241A, 223

96. Vance E.R., Smith J.H. and Sabine T.M., 1970, J. Phys. C : Metal Phys. Suppl. 1, S34

97. Cowlam N., Gillott L. and Shamah A.M., 1978, Inst. Phys. Conf. Ser. 39, 619

98. Cowlam N., Bacon G.E., Gillott L., Harmer G.R. and Self A.G., 1979, J. Phys. F : Metal Phys. 9, 1387

99. Campbell S.J. and Wells P., 1978, J. Phys. F : Metal Phys. 8, 2593

100. Campbell S.J., Cywinski R., Hicks T.J. and Wells P., 1979, Proc. ICM satellite conf. on Neutron Scattering, Julich, Germany (to be published in J. Magn. & Magn. Mater.)

101. Cywinski R., Wells P., Campbell S.J. and Hicks T.J., 1979, Proc. Int. Conf. on Neutron Scattering, Warsaw, Poland (to be published in Nukleonics)

102. Zimmerman J.E. and Sato H., 1961, J. Phys. Chem. Solids 21, 71

103. Street R., 1960, J. Appl. Phys. Suppl. 31, S310

104. Window B., 1969, J. Phys. C : Solid State Phys. 2, 2380

105. Coles B.R., 1977, Physica 91B, 167

106. Coles B.R., 1979, Proc. ICM-79, Munich, Germany (to be published)

107. Hertz J.A., 1979, Phys. Rev. B19, 4796

108. Mathon J., 1978, J. Phys. F : Metal Phys. 8, 1783

109. Livingston J.D. and Bean C.P., 1961, J. Appl. Phys. 32, 1964

110. Schroder K., 1961, J. Appl. Phys. 32, 880

111. Hayes E.J., Hahn A. and Wohlfarth E.P., 1972, J. Phys. F : Metal Phys.2, 351

112. Hahn A. and Wohlfarth E.P., 1968, Helv. Phys. Acta. 41, 857

113. Bennemann K.H., 1967, Phys. Letts. 25A, 233

114. Bucher E., Brinkman W.F., Maita J.P. and Williams H.J., 1967, Phys. Rev. Letts. 18, 1125

115. Brinkman W.F., Bucher E., Williams H.J. and Maita J.P., 1968, J. Appl. Phys. 39, 547

116. Miedema A.R., 1973, J. Phys. F : Metal Phys. 3, 1803

117. Wohlfarth E.P., 1974, Phys. Letts. 47A, 125

118. Ododo J.C., 1978, J. Phys. Chem. Solids 37, 727

119. Cheng C.H., Wei C.T. and Beck P.A., 1960, Phys. Rev. 120, 426

120. Gupta K.P., Cheng C.H. and Beck P.A., 1964, Phys. Rev. 133, A203

121. Guthrie G.L., Friedberg S.A. and Goldman J.E., 1959, Phys. Rev. 113, 45

122. Lanchester P.C., Whitehead N.F. and Wells P., 1977, Physica 86-88B, 825

123. Triplett B.B. and Phillips N.E., 1971, Phys. Letts. 37A, 443

124. Doniach S. and Engelsberg S., 1966, Phys. Rev. Letts. 17, 750

125. Berk N.F. and Schrieffer J.R., 1966, Phys. Rev. Letts. 17, 750

126. Trainor R.J., Brodsky M.B. and Isaacs L.L., 1974, AIP Conf. Proc. 24, 220

127. Brodsky M.B. and Trainor R.J., 1977, Physica 91B, 271

128. Lederer P. and Mills D.L., 1968, Phys. Rev. Letts. 20, 1036

129. Barnea G., 1975, J. Phys. C : Solid State Phys. 8, L216

130. Fulde P. and Luther A., 1968, Phys. Rev. 170, 570.

CHAPTER 3

EXPERIMENTAL LOW TEMPERATURE CALORIMETRY

3.1 Introduction to Calorimetry Methods

3.1.1 Adiabatic Methods

The first significant low temperature heat capacity measurements to be performed were the work of Nernst in 1910. His original adiabatic calorimeter design has since undergone many changes; however, its basic principle of operation remains the same. The salient feature of the adiabatic calorimeter is the thermal isolation of the sample from its environment, allowing the heat content of the sample to be conserved. The heat capacity of a sample in such a calorimeter is determined from the changes of sample temperature in response to small discrete increments of its heat content.

A typical adiabatic calorimeter design consists of a sample suspended in an evacuated chamber by fine, thermally insulating threads. A small thermometer and electrical heater element are attached to the sample to monitor its temperature and provide it with heat. The typical experimental procedure would be to precool the sample initially, then to start raising its temperature slowly, by increments, and to take temperature measurements at each increment. A small change in sample temperature ΔT corresponding to a small measured increment of sample heat content ΔQ is related to the sample heat capacity C by the expression 3.1.

$$C = \lim_{\Delta T \to 0} \frac{\Delta Q}{\Delta T} \qquad 3.1$$

The sample is precooled by establishing thermal contact between it and the surrounding heat bath provided by immersion of the sample chamber in a cryogenic fluid. In early designs the thermal contact was provided by the brief introduction

of helium exchange gas into the evacuated sample chamber. The problem with this method was that helium, which is strongly adsorbed by very cold surfaces, could not be completely removed on re-evacuating the sample chamber. The subsequent desorption from the sample surface at higher temperatures led to unpredictable heat losses and large errors in results. This method was superseded in the early 1950's by mechanical heat switches. These consist simply of a clamp in good thermal contact with the heat bath, which grips the sample holder to complete the thermal path from the sample to the heat bath. Mechanical switches are now a standard feature of modern adiabatic calorimeter designs (1) (2) (3).

The measurement accuracy of an adiabatic calorimeter is dependent on the level of stray heat losses from the sample. Most calorimeters were designed to accept large samples in the 20 - 200 gram range. Heat losses would then be negligible in comparison to the total heat content of the sample. However, the use of large samples has created problems of its own. Thermal gradients in large samples are likely to be more significant than in small samples. It is also more difficult to ensure good homogeneity of composition throughout a large alloy sample. Recent calorimeter designs trade off sample size for an acceptable level of thermal drift, correcting for the drift in the subsequent analysis of measurements.

Provided adequate steps are taken in the construction of the calorimeter to minimise heat losses the accuracy of the results can be high, limited only by the precision of the thermometry. With the advent of Germanium resistance thermometers total errors in measurements could be reduced below $\pm$ 0.5%.

Calorimetry has the well deserved reputation of being laborious, experimentally time consuming, and involving much tedious data analysis to obtain good results. It is perhaps not too surprising that there have been a number of schemes published in the literature to partially automate the operation of calorimeters (4) (5) (6). The use of

computers for data analysis has also gone a long way to reducing the work load in this area.

3.1.2 Relaxation Methods

Relaxation calorimetry offers an alternative approach to the adiabatic method which dispenses with the stringent sample isolation requirement and the complex engineering schemes to precool the sample. The relaxation technique utilizes a permanent weak thermal link between the sample and a constant heat bath.

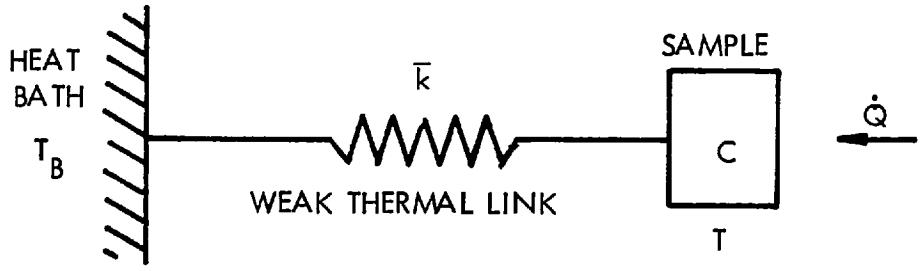

Fig. 3.1.1

In figure 3.1.1 $\bar{k}$ is the average thermal conductance of the weak link. If the link is a strip of length l and cross section area A cut from a material of thermal conductivity K(T) at temperature T, then its average thermal conductance $\bar{k}$ with one end at temperature T_B, the other at T, is given by the conductivity integral 3.2.

$$\bar{k} = \frac{A}{l(T - T_B)} \int_{T_B}^{T} K(T)\,dT \qquad 3.2$$

If, as in figure 3.1.1, a constant thermal power $\dot{Q}$ is supplied to the sample at equilibrium, it will remain at temperature T such that the thermal power loss from the sample, down the temperature gradient across the weak thermal link, balances that supplied to it.

$$\dot{Q} = \bar{k}\,(T - T_B) \qquad 3.3$$

DC Method

The DC step method is the simplest technique of relaxation calorimetry. Consider the sample having reached equilibrium at temperature T with thermal power $\dot{Q}$ supplied to it. If the thermal power is stepped abruptly to $\dot{Q}'$ by a small amount $\Delta\dot{Q}$, then the sample temperature will relax exponentially by an amount ΔT to a new equilibrium value T'.

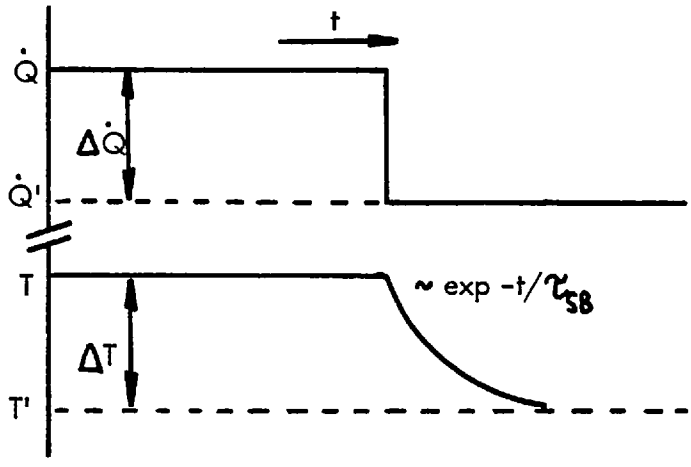

fig. 3.1.2

A fundamental relationship of thermal conduction from which the conductivity integral 3.2 is derived is given in 3.4.

$$k = \frac{A\,K(T)}{l} = \frac{d\dot{Q}}{dT} \qquad 3.4$$

where A, K(T) and l are as previously defined, and k is the thermal conductance of the weak link. For small $\Delta\dot{Q}$ and ΔT 3.4 becomes :

$$k = \frac{\Delta\dot{Q}}{\Delta T} \qquad 3.5$$

Taking the original definition of heat capacity, given by equation 3.1, ΔQ may be eliminated from 3.5 to yield :

$$\Delta\dot{T} = \frac{k}{C}\,\Delta T$$

Solving this differential equation gives :

$$T - T' = \Delta T \exp -\frac{kt}{C}$$

The exponential temperature relaxation time constant τ_{SB} is then given by :

$$\tau_{SB} = C/k \qquad 3.6$$

Combining relationships 3.5 and 3.6 results in 3.7.

$$C = \tau_{SB} \frac{\Delta \dot{Q}}{\Delta T} \qquad 3.7$$

This expression is the working formula used for calculating heat capacity measured by the DC step technique. Other DC methods exist which involve different methods of changing the thermal power to the sample, i.e. the pulse and sweep methods (7).

All DC methods are measurements of the transient response of the sample temperature to changes in ther thermal power supplied to it. As such they are susceptible to drifts in the heat bath temperature. Employment of signal averaging techniques reduces the effect of this source of noise; these techniques require a repetitive or AC heating method.

AC Method

Sullivan and Seidel (8) were the first to propose an AC method of relaxation calorimetry ; Bachmann et al. (7) extended the method to a small sample calorimeter.

A sinusoidally changing voltage of amplitude V_H, frequency ω, applied across a heater element resistance R_H will generate an AC thermal power $\dot{Q}$ changing at frequency 2ω .

$$\dot{Q} = \frac{V_H^2 \sin^2 \omega t}{R_H} = \frac{V_H^2}{2R_H}(1 + \cos 2\omega t) \qquad 3.8$$

The DC term in expression 3.8 $\dot{Q}_o = V_H^2/2R_H$ maintains the sample at an average temperature T_o given by 3.3.

$$\dot{Q}_o = \frac{V_H^2}{2R} = \bar{k}(T_o - T_B)$$

Whilst the AC term $\dot{Q}_o \cos 2\omega t$, causes the sample temperature to oscillate at frequency 2ω, with amplitude T_2 about the average temperature T_o.

In their paper Sullivan and Siedel considered a more realistic model of an AC calorimeter system which included the effects of finite thermal resistance in the path from the heater, through the sample, to the thermometer.

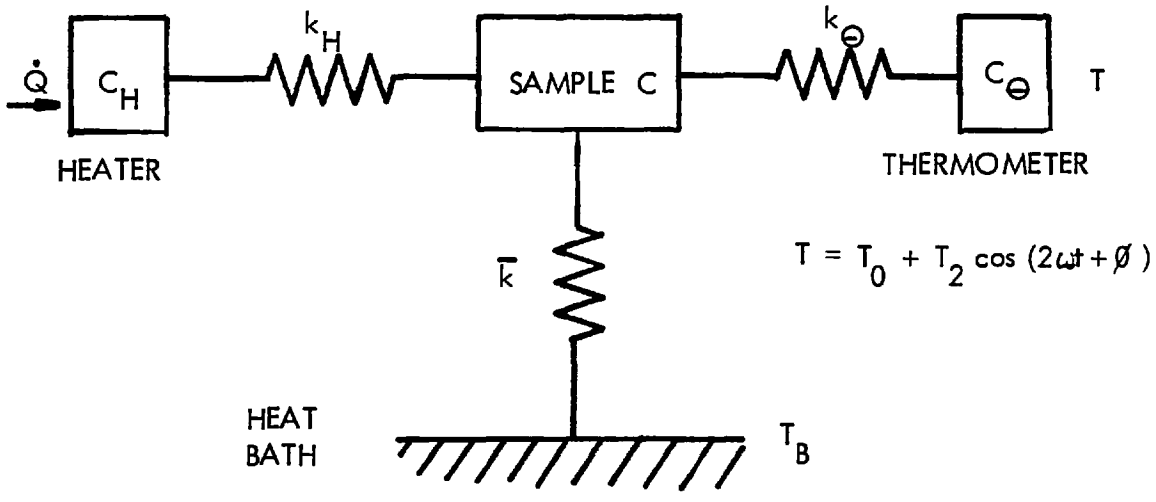

fig. 3.1.3

They derived a complex expression for the temperature oscillation amplitude T_2 which, to a first order approximation, is given in 3.9.

$$T_2 = \frac{\dot{Q}_o}{2\omega C}\left[1 + \frac{1}{4\omega^2\tau_{SB}^2} + 4\omega^2\tau_{INT}^2\right]^{-1/2} \qquad 3.9$$

where $\sin\phi = \left[1 + \left(\frac{1}{\omega}\tau_{SB} - \omega\tau_{INT}\right)^2\right]^{-1/2}$ and $\tau_{INT} \ll \frac{1}{\omega} \ll \tau_{SB}$

τ_{INT} was defined as a composite internal thermal relaxation time constant which includes the relaxation time constants $\tau_H = \frac{C_H}{k_H}$ and $\tau_\theta = \frac{C_\theta}{k_\theta}$ associated with thermal paths from the sample to the heater and thermometer, and a time constant associated with thermal diffusion through the sample τ_D.

$$\tau_{INT}^2 = \tau_H^2 + \tau_\theta^2 + \tau_D^2 \qquad 3.10$$

Where $\tau_D = \frac{l^2}{\sqrt{90}\,D}$, l is the sample thickness in the direction of heat flow and $D = K/C\rho$ is the thermal diffusivity of the sample.

A further approximation reduced expression 3.9 to

$$T_2 \simeq \frac{\dot{Q}_0}{2\omega C} \qquad 3.11$$

This expression is valid to 1% accuracy, provided the frequency ω of the heater voltage is limited to the range :

$$10/2\,\tau_{INT} < \frac{1}{\omega} < \frac{\sqrt{2}}{5}\,\tau_{SB} \qquad 3.12$$

Expression 3.11 can be inverted to give the basic formula for calculating heat capacity measured by the AC method.

$$C = \frac{V_H^2}{4\omega T_2 R_H} \qquad 3.13$$

3.1.3 Frequency Limits

The frequency limits expressed in 3.12 can be understood intuitively to imply that ω should not be so large that internal relaxation times become significant, hence generating temperature inhomogeneity in the sample. Frequency ω should also not be so small as to create temperature oscillations too large in amplitude and thus lose the

temperature resolution of the measurements.

In the following sections the frequency limits expressed in 3.12 will be related to measurable characteristic time constants.

Lower Frequency Limit

Consider the full expression for T_2 (see equation 3.9).

In the lower frequency limit where internal relaxation effects may be neglected it reduces to :

$$T_2 \simeq \frac{\dot{Q}_o}{2\omega C}\left[1+\frac{1}{4\omega^2\tau_{SB}^2}\right]^{-1/2} \qquad 3.14$$

where

$$\dot{Q}_o = \frac{V_H^2}{2R_H} = \int_{T_B}^{T_0} k(T)dT$$

For metals at low temperatures, the thermal conductance k (T) can be approximated by :

$$k(T) \simeq \xi T$$

i.e. $$\dot{Q}_o = \tfrac{1}{2}\xi(T_0^2 - T_B^2)$$

but $$\tau_{SB} = \frac{C(T)}{k(T)} = \frac{C(T)}{\xi T}$$

now for $\frac{1}{\omega} \lesssim \sqrt{\frac{2}{5}}\,\tau_{SB}$ i.e. $\tau \lesssim 2\tau_{SB}$ expression 3.14 reduces to :

$$\frac{T_2}{T} \simeq \frac{\dot{Q}_o}{2\omega C T_0} = \frac{1}{4\omega\tau_{SB}}\left[1-\left(\frac{T_B}{T_o}\right)^2\right]$$

For good temperature resolution T_2/T_o should be 5% or less. Thus :

$$\omega\tau_{SB} \gtrsim 5\left[1-\left(\frac{T_B}{T_o}\right)^2\right]$$

$$\tau \approx \frac{2\pi}{5}\left[1-\left(\frac{T_B}{T_o}\right)^2\right]^{-1}\tau_{SB}$$

i.e.

$$\begin{aligned} T_o > 3T_B \quad & \tau \lesssim 1{\cdot}2\,\tau_{SB} \\ 3T_B > T_o > 1{\cdot}5T_B \quad & \tau \lesssim 1{\cdot}5\,\tau_{SB} \\ T_o < 1{\cdot}5T_B \quad & \tau \lesssim 2\,\tau_{SB} \end{aligned} \qquad 3.15$$

Higher Frequency Limit

At higher frequencies the internal thermal relaxation time of the sample becomes important. The effect is manifest as a non-linear change of the T_2-amplitude with increasing frequency. The internal thermal relaxation time constant τ_{INT} characterises this effect, and therefore an upper frequency limit may be defined from it.

The technique used to measure this second order effect of the internal relaxation time involves compensating for the first order linear frequency dependence of the T_2-amplitude by an opposing frequency dependence in the AC heater voltage.

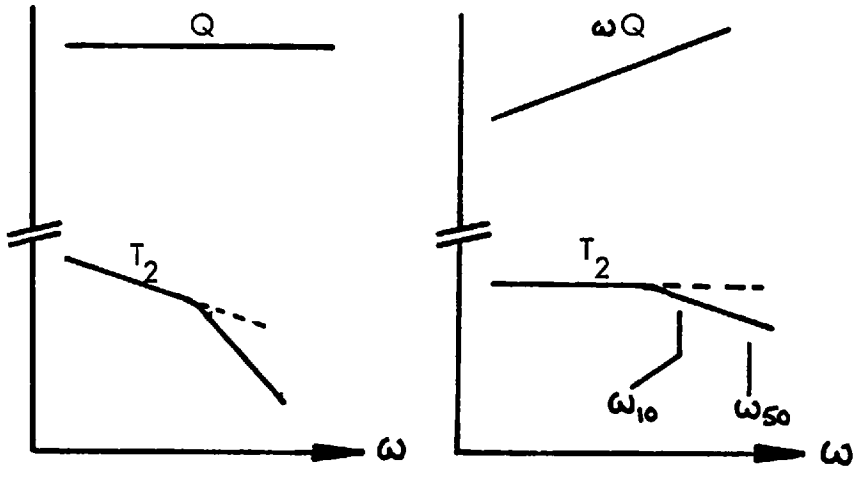

fig. 3.1.4

The frequency dependent AC heater voltage is superimposed on a large DC component to minimise the shift in average sample temperature T_o, with changes in the amplitude of the AC component. A consequence of using a heater voltage composed of a large DC plus a small AC signal is that the temperature oscillates at the same

frequency as the AC component rather than at twice this frequency, as is the case for a pure AC heater voltage. Consider :

$$V_H^2 = (a + b\sin\omega t)^2$$

$$= a^2 + 2ab\sin\omega t + b^2\sin^2\omega t$$

For $a \gg b$ $$\simeq a^2 + 2ab\sin\omega t$$

The ω-component will be dominant in the limit $a \gg b$.

Returning to the derivation of the upper frequency limit, consider expression 3.9 in the high frequency limit for a frequency dependent heater voltage amplitude,

$$\dot{Q}_o = \dot{Q}_o'\omega$$

i.e. $$(1 + \omega_{50}^2\tau_{INT}^2)^{-\frac{1}{2}} = \frac{1}{2}$$

$$\therefore \omega_{50}\tau_{INT} = \sqrt{3}$$

From the inequality 3.12

$$\frac{1}{\omega} > 10\sqrt{2}\,\tau_{INT}$$

eliminating τ_{INT} from the above expressions yields :

$$\omega < \frac{\omega_{50}}{10\sqrt{6}}$$

i.e. $$\tau \gtrsim 25\,\tau_{50} \qquad 3.16$$

Similarly for a 10% reductian in T_2-amplitude at

$$\omega < \frac{9\,\omega_{10}}{10\sqrt{38}}$$

i.e. $$\tau \gtrsim 7\tau_{10} \qquad 3.17$$

In summary, the heat capacity may be calculated from expression 3.13 to 1% accuracy, provided that :

$$\tau_{SB} > \tau > 25\tau_{50} \text{ or } 7\tau_{10}. \qquad 3.18$$

The lower frequency limit is retained at the τ_{SB} value for all temperatures owing to increasing non-linearity in the thermometry at lower temperatures. It is therefore desirable to keep the T_2/T_o ratio below 5% (e.g. 3% at 2 K) to minimise the effect of the non-linearity. This point is discussed further in a later section on the measurement errors.

3.2 Calorimeter Design

As the AC relaxation calorimetric method is fairly novel it is worthwhile describing the apparatus and its operation in some detail. The calorimeter was designed and constructed by Dr. Kay Nicholson (9) during the course of a research studentship in this laboratory. Whilst the original design concepts remain unchanged the calorimeter has undergone a number of modifications to simplify its operation.

3.2.1 Cryostat Design

The cryostat used in the experiment was a metal cryostat of a fairly standard design. It consisted of an inner stainless steel helium dewar surrounded by a liquid nitrogen cooled copper shield thermally isolated by a vacuum interspace. The liquid nitrogen jacket occupied the upper half of the cryostat. A copper ring near the neck of the cryostat made thermal contact between the nitrogen jacket and the helium dewar, this reduced the thermal gradient in the wall of the latter. The helium boil-off rate was generally found to be about 1 litre of gas per minute. A 3 litre charge of liquid helium gave a useful run time of over 12 hours.

3.2.2 Sample Platform

The sample platform consisted of a copper foil tray (see figure 3.2.1). The weak thermal link in the form of a thin brass strip was silver soldered to the tray. The thermometer, a standard Allen Bradley carbon resistor, was attached to the sample platform by wrapping it in one of the tabs cut out of the copper foil tray. To improve

thermal contact the enamel of the resistor's outer case was sanded thin before cementing it in place with a smear of thinned GE 7031 varnish. The thermometer leads were cropped short and 32 SWG enamelled copper wires were soldered to them. These leads were heat sunk to the sample platform by being wrapped around and varnished in place on a further pair of tabs on the copper foil tray. A thin piece of paper was used to insulate the wires as a precaution against an electrical short circuit to the platform through the varnish rotting the enamel insulation on the wires. The heater element was a thin film metal oxide resistor of nominal resistance 1 KΩ, and a specified temperature coefficient of less than 6 ppm. In the temperature range 1.5 - 20 K the element's resistance was measured to be 997 $\pm$ 0.3Ω. For extra support the element was cemented to a piece of copper foil with a smear of thinned varnish.

The sample, usually in the form of a button with approximately parallel flats polished on the upper and lower surfaces, was sandwiched between the heater plate and the sample platform. A 10 mg smear of RS heat sink compound was used to improve thermal contact at the interfaces.

The whole sample platform assembly was suspended by the thermal link from a thick copper rod (see figure 3.2.2). The copper rod itself was screwed into the brass sample chamber flange with heat sink compound packed into the threads to improve thermal contact.

Short electrical connections were made with fine cotton covered manganin wire from the thermometer, and heater leads to 32 SWG enamelled copper wires wrapped around and varnished to a copper rod heat sinking post screwed into the brass flange. These leads were connected to 30 SWG cotton-covered manganin wires on a thermally heat sunk pin board. The manganin wires were wrapped around and varnished to an aluminium ring seated under the flange, providing the first heat sink stage for these wires.

SAMPLE PLATFORM

Fig. 3.2.1

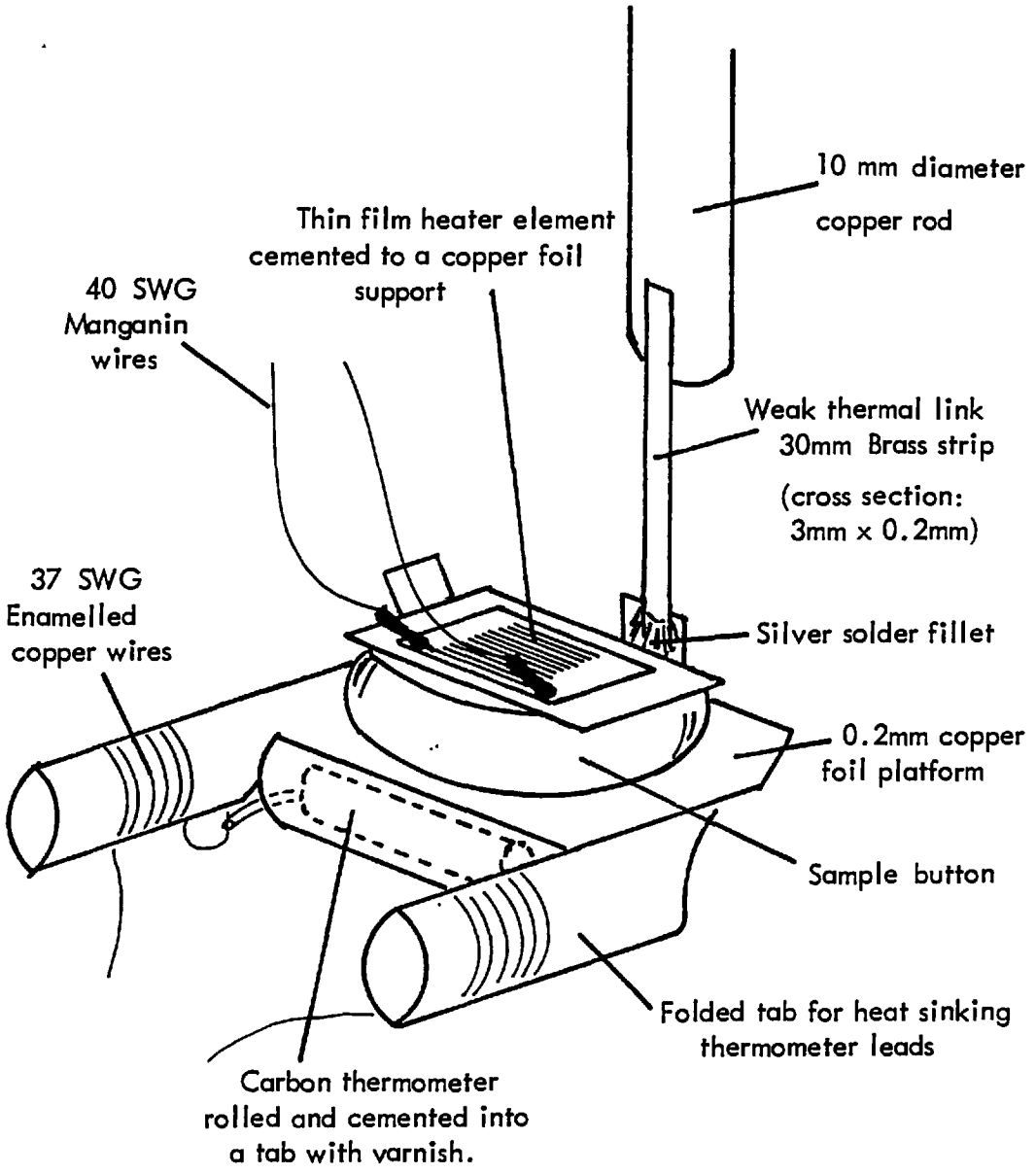

SAMPLE CHAMBER

Fig. 3.2.2

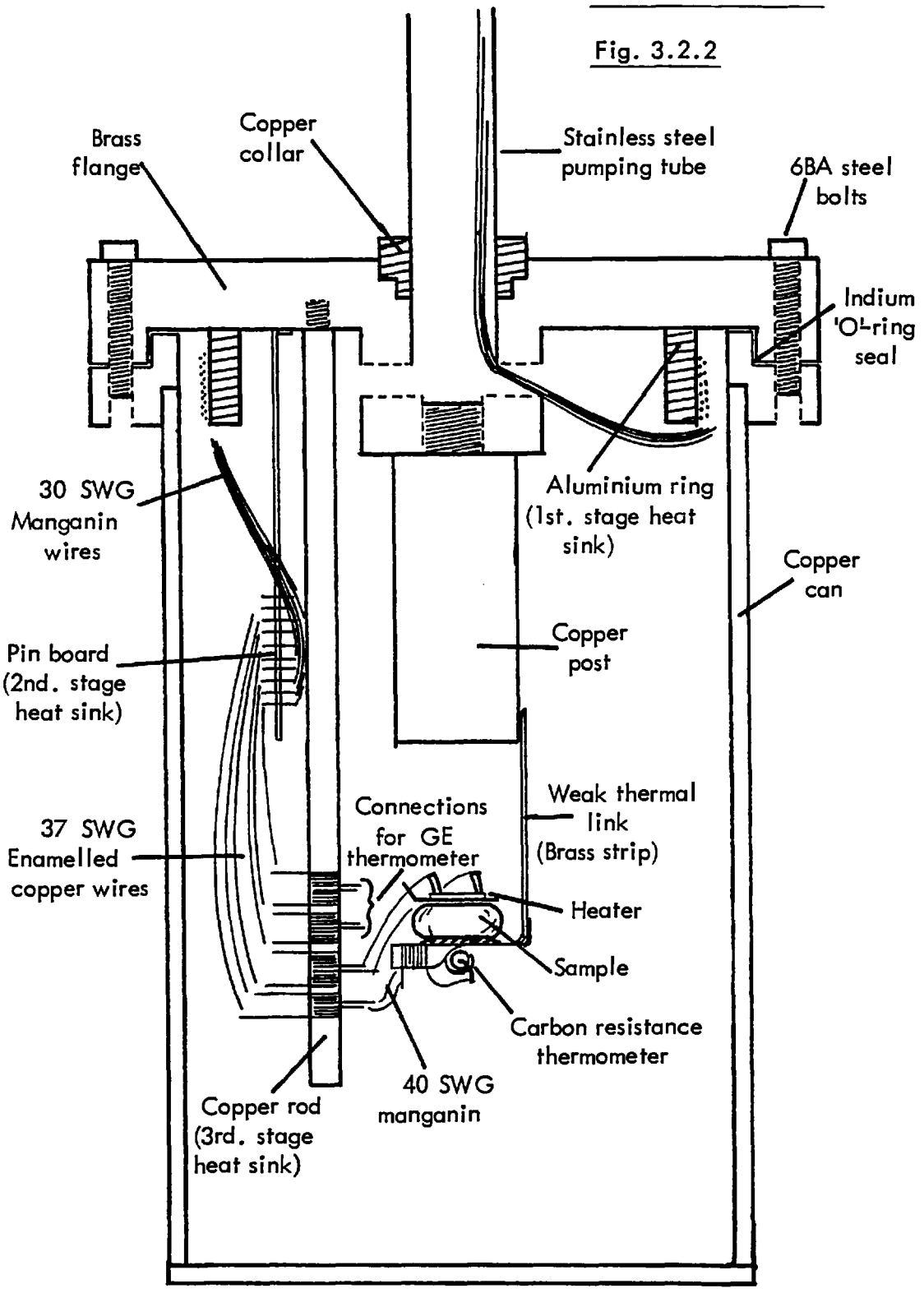

3.2.3 Superconducting Solenoid

A 0.3 Teslo superconducting coil (see figure 3.2.3) wos wound os o solenoid around the outside of the sample chomber. The coil consisted of about 1700 turns in 5 layers of close wound enomelled 34 SWG Niomox superconducting wire. The field per unit current wos colibroted ot low currents ($<$80 mA) using o Holl probe gauss-meter, with o longitudinol probe ploced ot the opproximote position of the somple, i.e. the centre of the solenoid. The colibrated field per unit current was 141 $mT\,A^{-1}$.

Six 32 SWG enomelled copper wires, in two sets of three stronds, were used as leads from the coil to the vocuum tight feed-through connectors on the cryostot flonge. This orrongement improved the cooling efficiency of the leads by increasing the surface oreo of the wires exposed to the cold helium gas stream.

The current for the coil wos supplied by o BOC 60A superconducting mognet controller. The coil wos found to be copable of toking o 20A current for prolonged periods without generating too much heot in the copper leods. For periods shorter than 10 minutes, currents up to 30A could be token. These currents were well below criticol volues quoted for the Niomax wire used to wind the coil.

The use of the coil wos found to shorten the run time substontiolly, especiolly when pumping on the helium spoce to achieve lower bath temperoture. A 4 litre chorge of liquid helium would lost no more thon 6 hours. For heot capacity meosurement runs in o magnetic field the somple plotform wos bent through 90° to reduce the cross section oreo of the somple perpendiculor to the field direction. This orrongement reduced the demognetizing fields induced in the somple by its shape.

The mognetoresistonce of on Allen Bradley carbon resistor wos shown by Clement ond Quinnell (11) to be well described by the relotionship :

$$\frac{\Delta R}{R} \propto H^2 T^{-3/2} \qquad 3.19$$

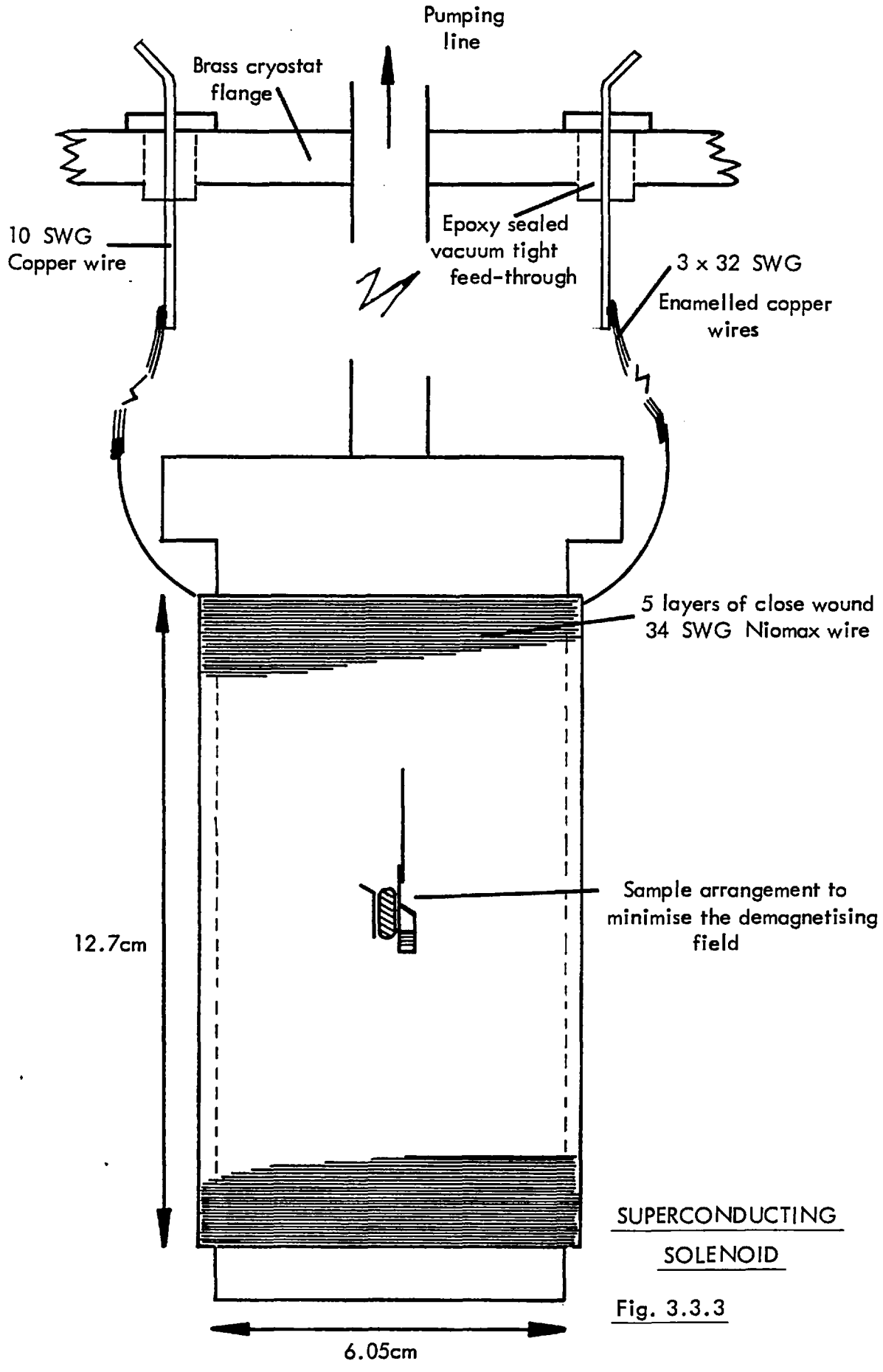

SUPERCONDUCTING SOLENOID

Fig. 3.3.3

At 4.2 K for a field of 0.5 Tesla they found $\Delta R/R$ was less than 0.05%. Magnetoresistance effects were expected to be negligible for the range of fields generated by the solenoid. A preliminary experimental run with the solenoid verified this conclusion.

3.2.4 Electronic Systems

The electronic systems of the calorimeter (see figure 3.2.4) include a bridge network to detect and amplify a small change in resistance of the thermometer. An amplifier to mix AC and DC voltage components and to drive the heater. A means of measuring the time period and amplitude of the AC voltage supplied to the heater. Finally, a current supply for the germanium resistance thermometer.

The bridge circuit (see figure 3.2.5) consisted of the carbon resistance thermometer in one arm and a Dekastat 12 KΩ precision switched decade resistor plus dummy lead resistance formed the fixed arms of the bridge network. Bridge excitation currents in the range 0.7 to 100 μA could be selected to minimise self-heating effects in the thermometer by switching the appropriate resistor in series with a 1.35V mallory cell used to power the bridge. Small deviations in the thermometer resistance from the value set on the Dekastat variable resistor resulted in an off-balance voltage proportional to the resistance deviation. This off-balance voltage was amplified (see figure 3.2.6) by a factor of about 10^4 using a low-drift chopper stabilised operational amplifier module (ANCOM type 15C-3) and displayed on a chart recorder. To reduce noise the amplifier was band limited to pass frequencies below a value set by a capacitor-resistor pair in the amplifier's feedback network.

The heater power supply (see figure 3.2.7) used a high impedance FET input operational amplifier to mix the AC and DC voltage components. The AC signal was provided by a Brookdeal 471 low-frequency sinewave generator. The input from the

BLOCK DIAGRAM OF CALORIMETER ELECTRONIC SYSTEMS

FIG. 3.2.4

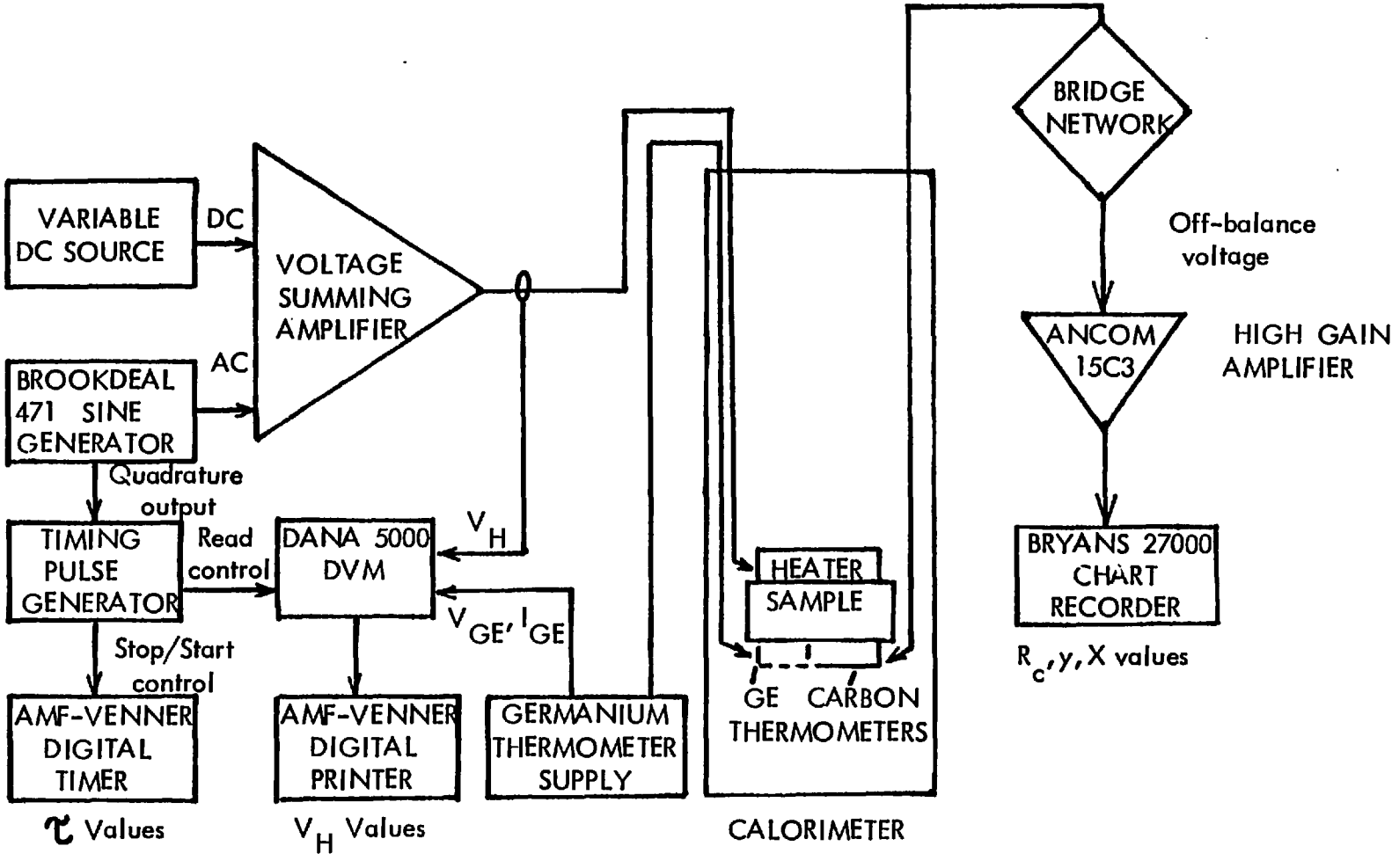

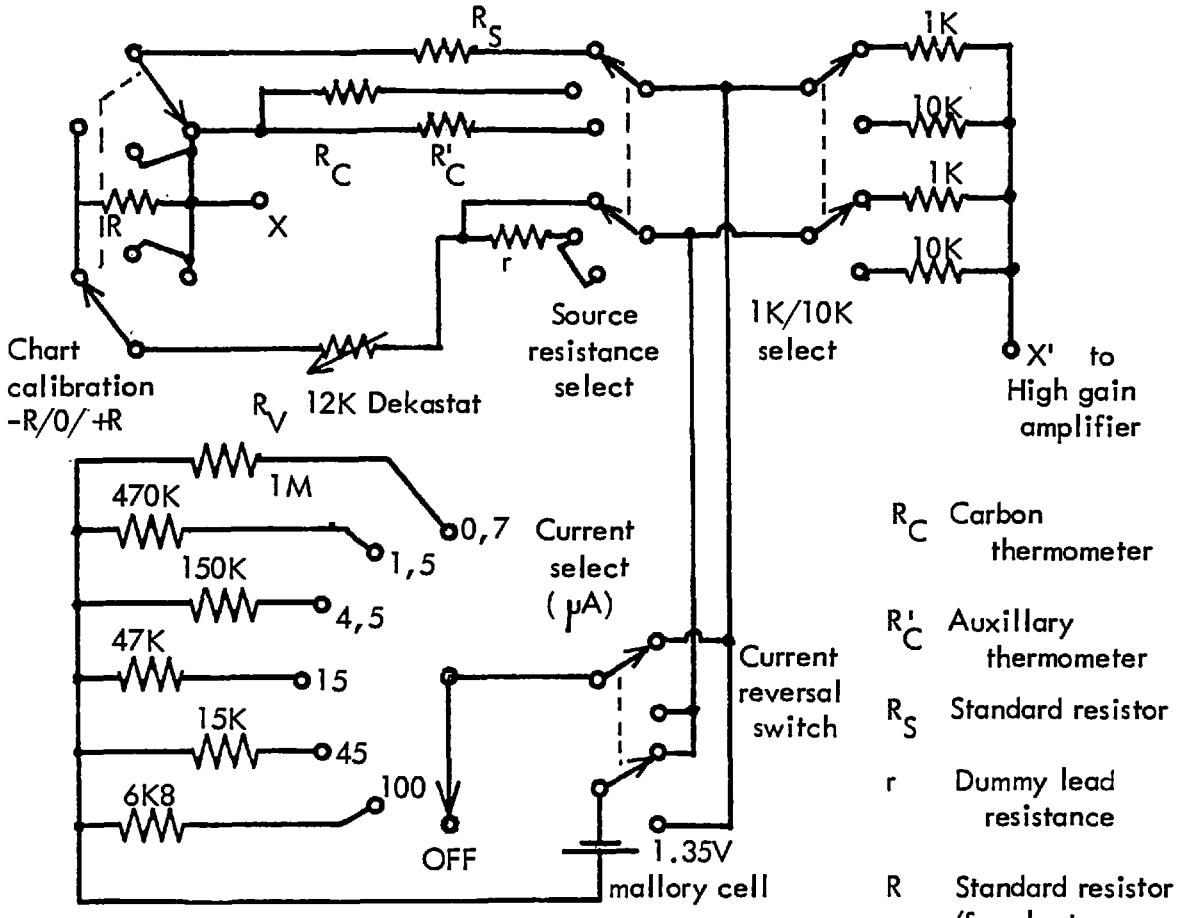

BRIDGE CIRCUIT Fig. 3.2.5

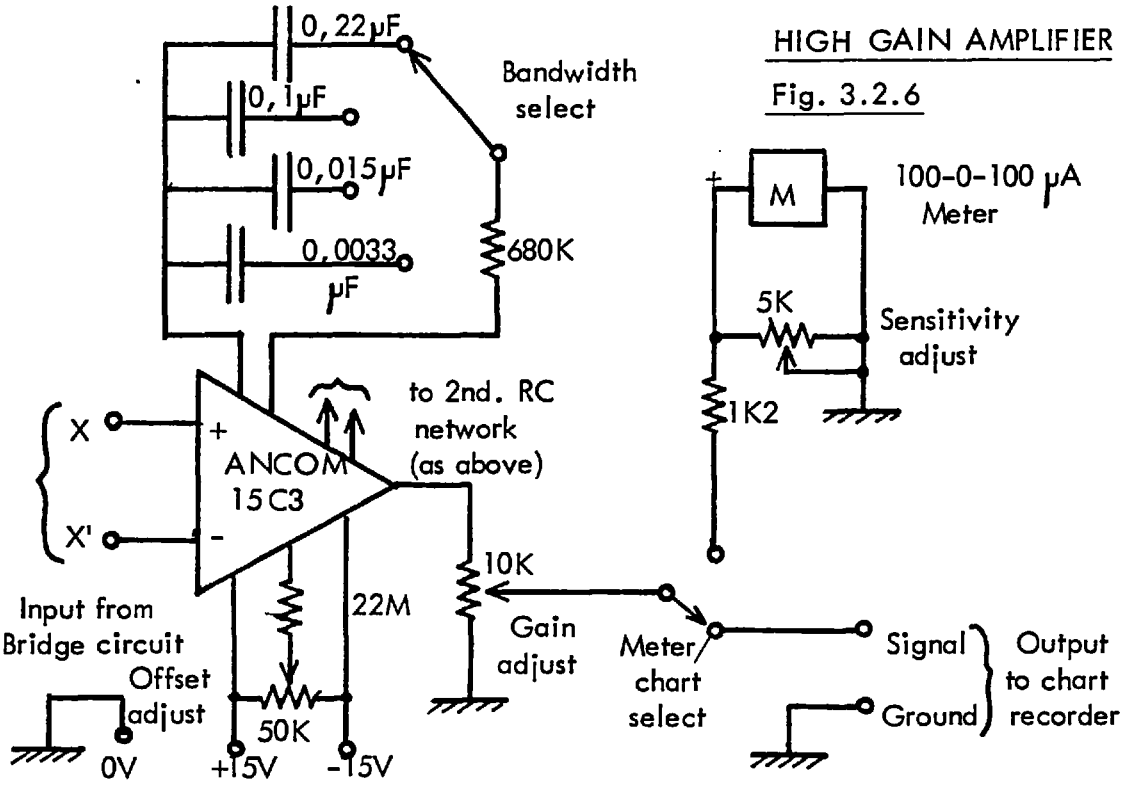

HIGH GAIN AMPLIFIER

Fig. 3.2.6

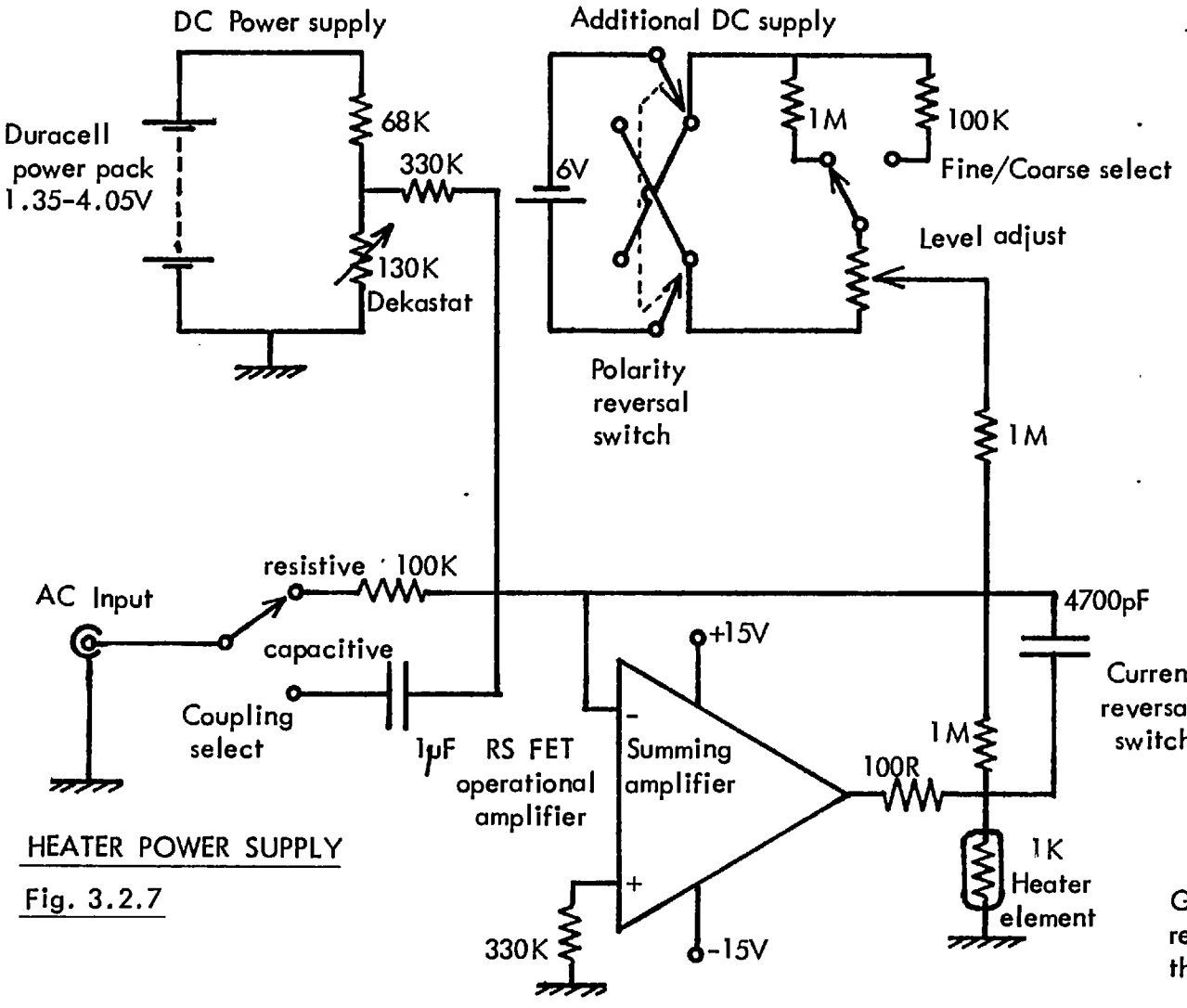

HEATER POWER SUPPLY

Fig. 3.2.7

GERMANIUM THERMOMETER POWER SUPPLY

Fig. 3.2.8

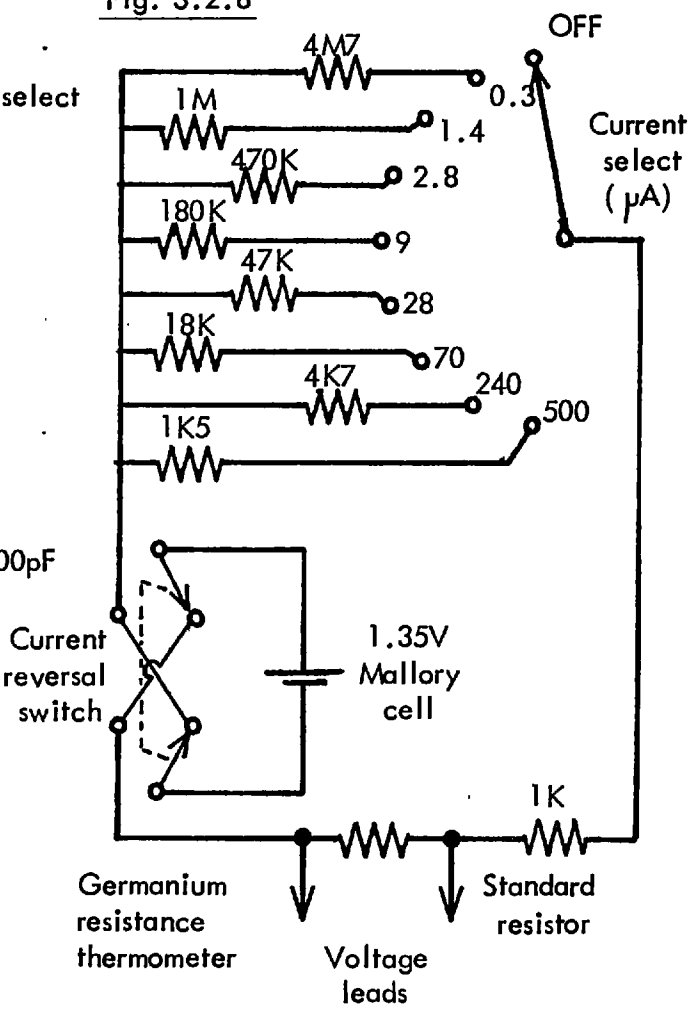

sinewave generator could be coupled to the mixing amplifier either resistively or capacitively to give the amplitude a linear frequency dependence. Another 130 KΩ Dekastat resistor was used to vary the DC voltage component. An additional DC source was provided to give small positive or negative increments for trimming the heater voltage.

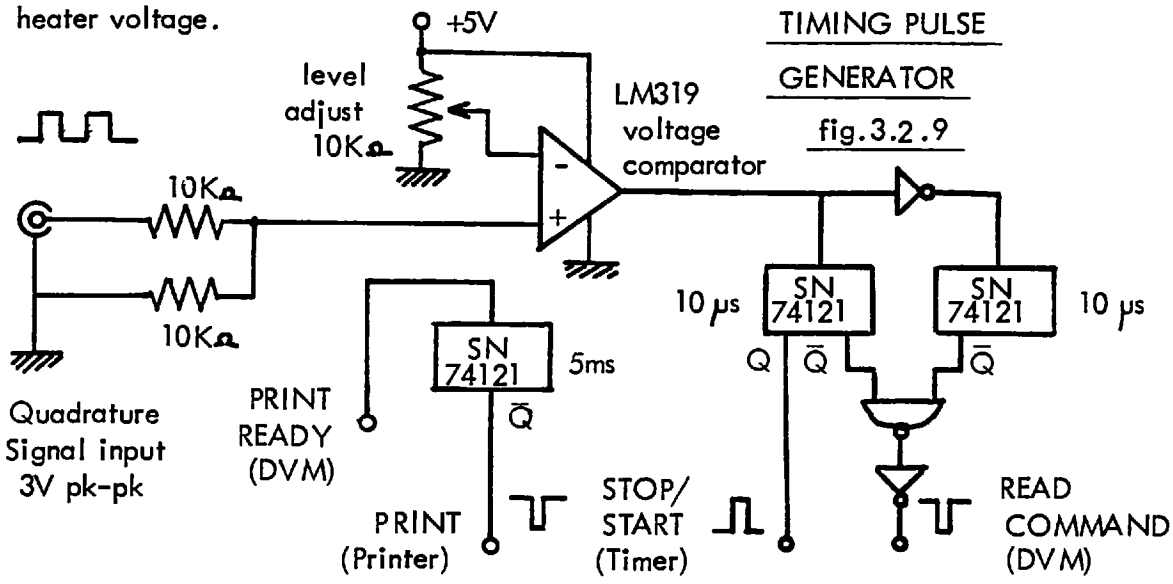

The square wave quadrature output from the sinewave generator (see figure 3.2.9) was used to trigger an AMF-Venner electronic digital timer to measure the time period τ and a Dana 5000 6-figure digital voltmeter to measure the successive positive and negative peaks of the heater voltage. The digital voltmeter required 50 ms to read a voltage, during this time the voltage close to a peak would have changed by 0.03% for τ = 10 s. In practice it was found that taking readings at $\tau \sim 30$ s gave the most consistent results, scatter in data for V_H due to noise was never more than $\pm 0.2\%$. A check of the stability of the heater voltage to changes in frequency showed no significant dependence. Successive heater voltage peak readings were printed out by an AMF-Venner digital printer.

3.3 Thermometry

3.3.1 Choice of Thermometer

The measurement of temperature is of central importance to calorimetry. The

quality of specific heat measurements depends critically on the accuracy and reproducibility of the thermometry. This is especially true of AC relaxation calorimetry since this method depends not only on temperature measurement but also on the temperature sensitivity of the thermometer.

A carbon resistance thermometer was selected for its high temperature sensitivity (see figure 3.3.3) and low heat capacity (hence fast response) over the temperature range of interest, 1.5 - 20 K. The thermometer was an 1/8th watt Allen Bradley carbon resistor of 100Ω nominal room temperature resistance. The carbon thermometer was calibrated against a standard germanium resistance thermometer (serial no. GE 881) above 4.5 K. This germanium thermometer was commercially calibrated to ± 0.1% accuracy over the range 4.5 - 100 K by CryoCal Inc., Riviera Beach, Florida, U.S.A. in December 1967. The calibration was checked up to 7 K against a more recently calibrated thermometer and found to be within 10 mK of the original calibration. No other calibrated thermometer was available at the time to check beyond 7 K. Below 4.2 K the carbon thermometer was calibrated against the T_{58} helium vapour pressure scale.

3.3.2 Thermometer Reproducibility

Lindenfeld (10) in a review on carbon thermometry reported that ± 0.1% reproducibility in T had been observed for a hermetically sealed carbon thermometer protected from thermal and mechanical shock. The thermometer used in the calorimeter, although not encased in a perfect hermetic seal, was isolated from thermal shock by the weak thermal link and from helium by the evacuated sample chamber. It was therefore not expected to show appreciable calibration hysteresis on repeated thermal cyclings between room and liquid helium temperatures.

In the original arrangement of the calorimeter the germanium thermometer was permanently fixed to the sample platform to allow calibration of the carbon thermometer

every run. The calibration data from a number of consecutive runs performed over a two month period, with the calorimeter in this earlier configuration, are plotted chronologically (A, B ... and A', B' ...) in figures 3.3.1 a and b as percentage temperature deviations $\epsilon_T = (T - T')/T'$ from temperatures T' derived from a three span fit (see section 3.3.3) to one of the calibrations (underlined in the figures). The observed deviations were not greater than $\pm$ 0.5% for 1.5 - 4.2 K and $\pm$ 0.3% for 4.5 - 20 K. These deviations were of the same order as the systematic error introduced through the use of the three span interpolation fits in the former calibration procedure. Thus by improving the quality and number of calibration points and using five span interpolation fits it was considered that a single calibration was sufficient for a number of subsequent runs. The reduction of systematic fit errors would offset the calibration hysteresis errors incurred by this procedure. The simplification of the run procedure and of the subsequent analysis afforded by the adoption of this new calibration procedure allowed more experimental data points to be taken in a given run without significant loss of the original thermometry precision.

The addenda heat capacity was reduced to nearly half of its original value (see section 3.5.1) by removing the germanium thermometer. Sample sizes and time constants were also reduced correspondingly.

3.3.2 Thermometer Calibration Procedure

The germanium thermometer was inserted in a copper block of approximately 6 g mass. RS heat sink compound was used to improve thermal contact with the block which was mounted as a sample would be in the calorimeter. Short ($\sim$ 2 cm) electrical connections were made from the thermometer to the appropriate leads on the heat sinking post (see figure 3.2.1) using fine 40 SWG cotton covered manganin wires.

Calibration temperatures were set by applying an appropriate DC voltage to the heater. The germanium thermometer resistance was determined by a four terminal

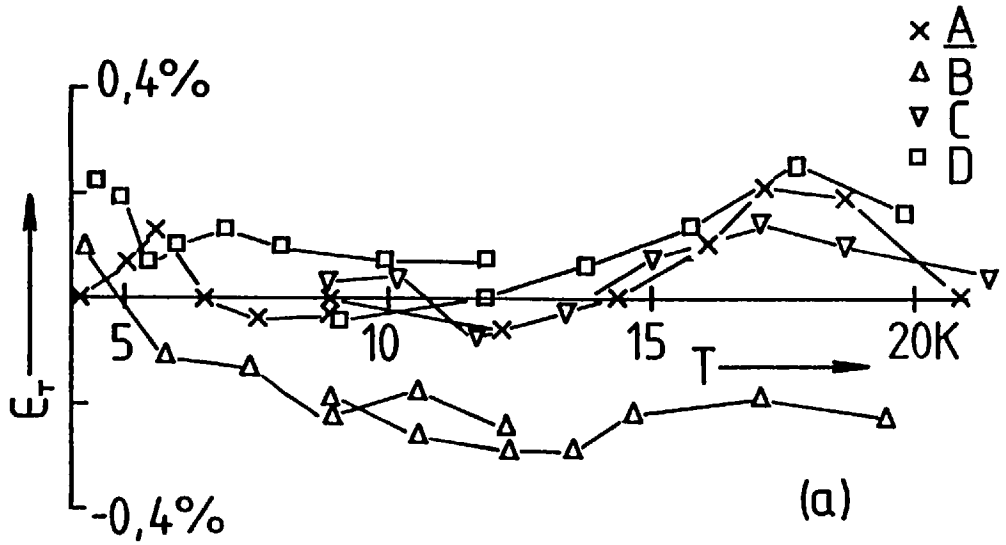
A
B
C
D
0,4%
-0,4%
5
10
15
20K
T
ε_r
(a)

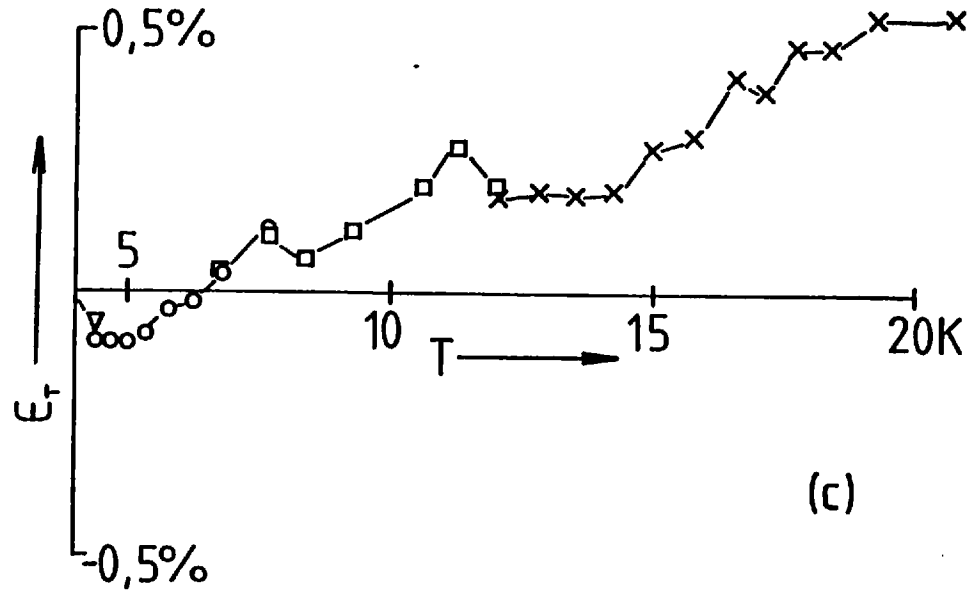
0,5%
-0,5%
5
10
15
20K
T
ε_r
(c)

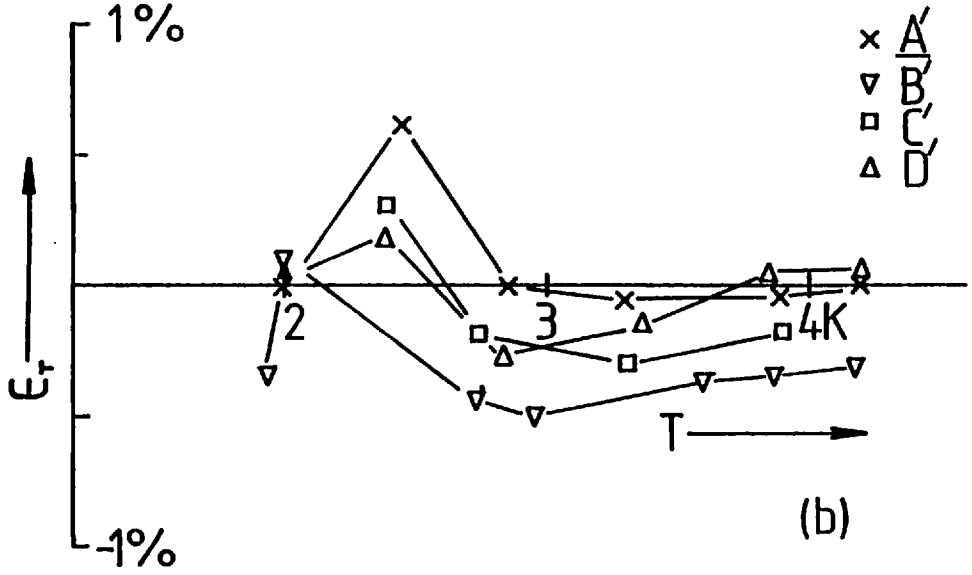
A'
B'
C'
D'
1%
-1%
2
3
4K
T
ε_r
(b)

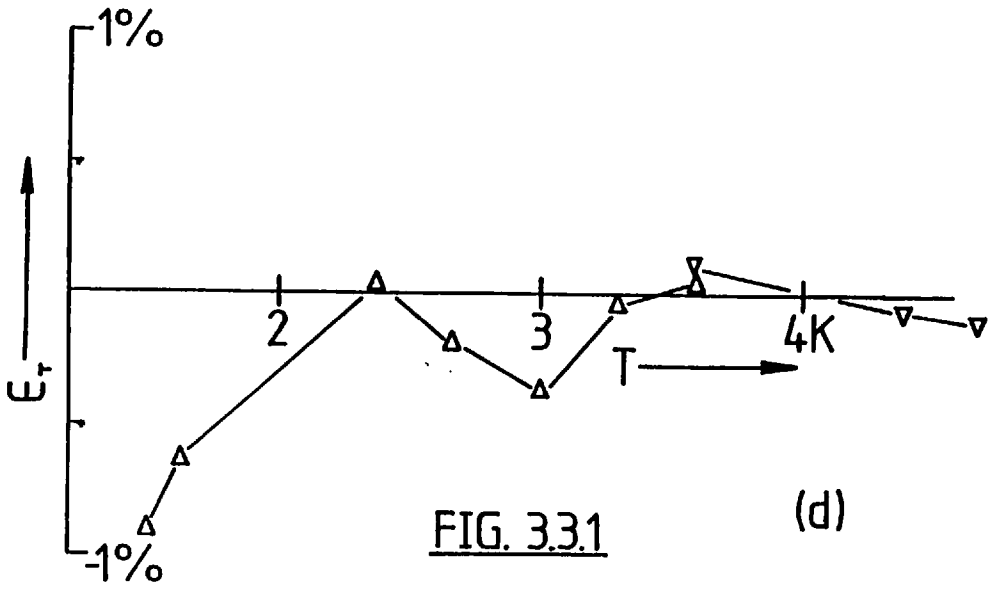
1%
-1%
2
3
4K
T
ε_r
(d)

FIG. 3.3.1

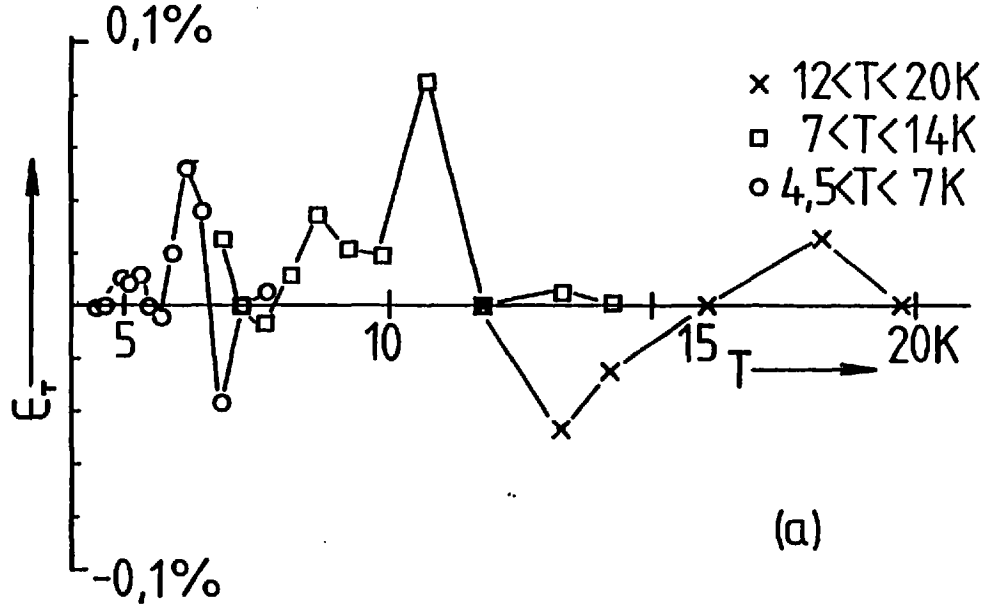
0,1%
× 12<T<20K
□ 7<T<14K
○ 4,5<T< 7K
5
10
15
T
20K
ε_T
-0,1%
(a)

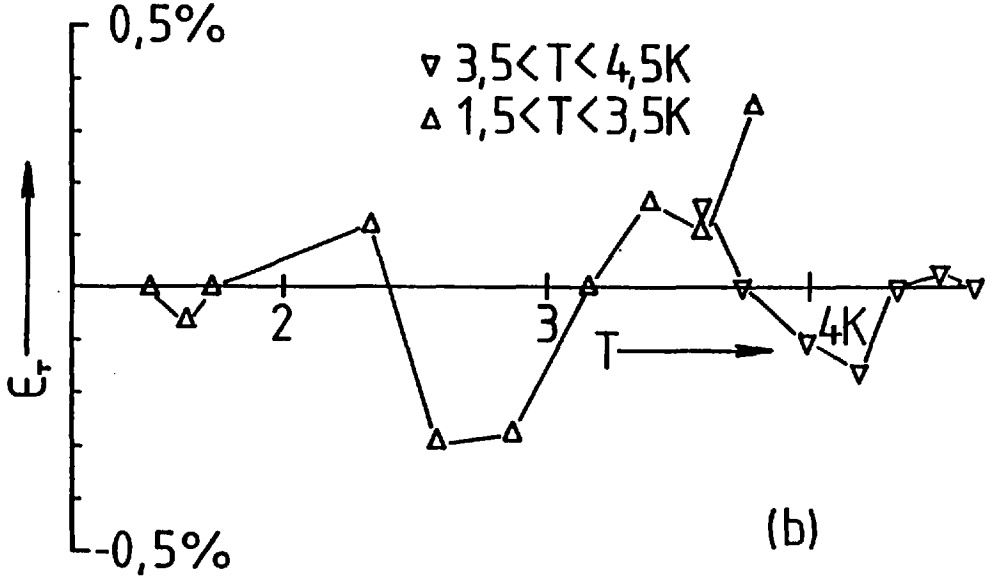
0,5%
▽ 3,5<T<4,5K
△ 1,5<T<3,5K
2
3
T
4K
ε_T
-0,5%
(b)

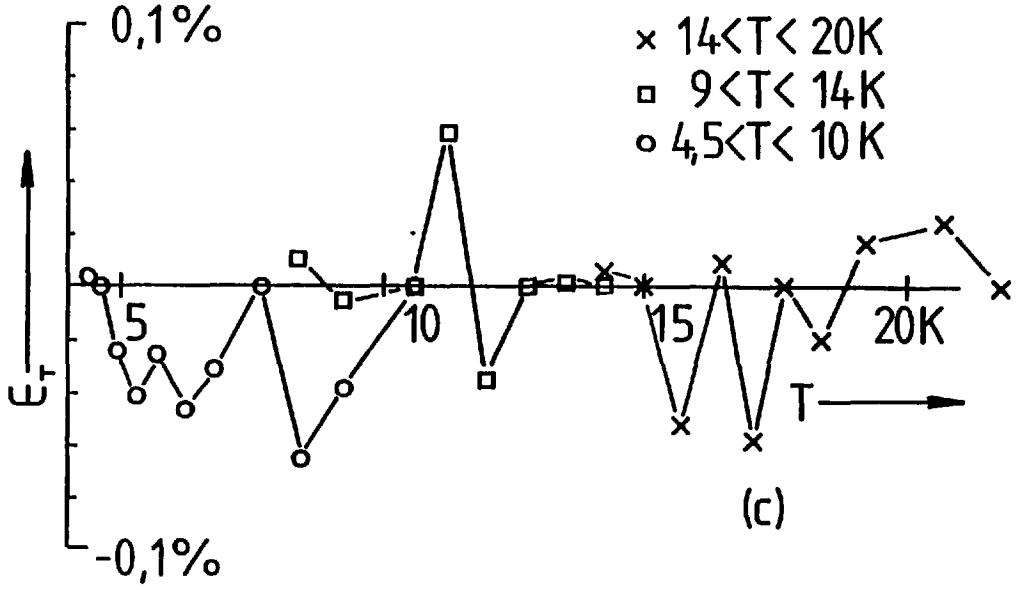
0,1%
× 14<T< 20K
□ 9<T< 14K
○ 4,5<T< 10 K
5
10
15
20K
T
ε_T
-0,1%
(c)

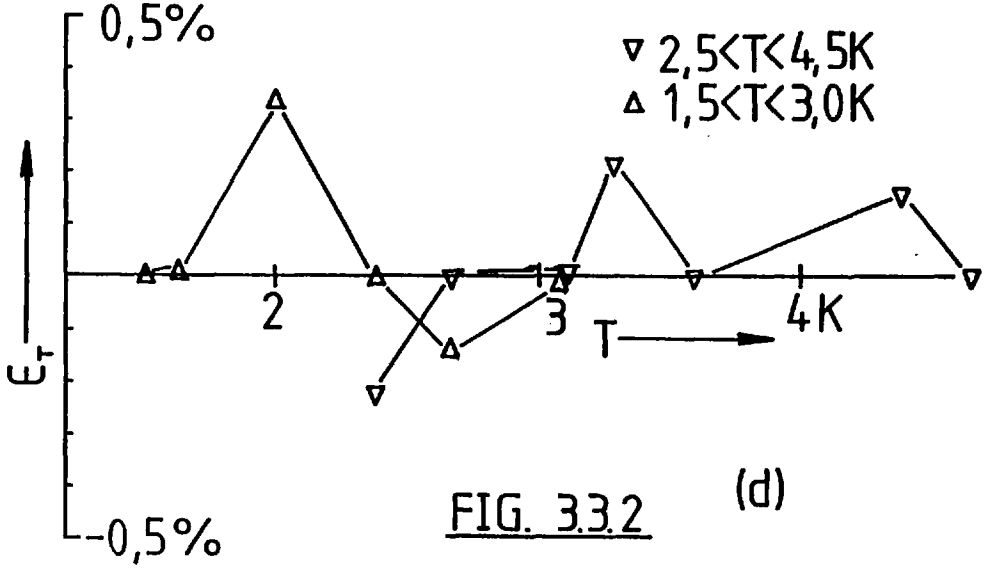
0,5%
▽ 2,5<T<4,5K
△ 1,5<T<3,0K
2
3
T
4K
ε_T
-0,5%
(d)

FIG. 3.3.2

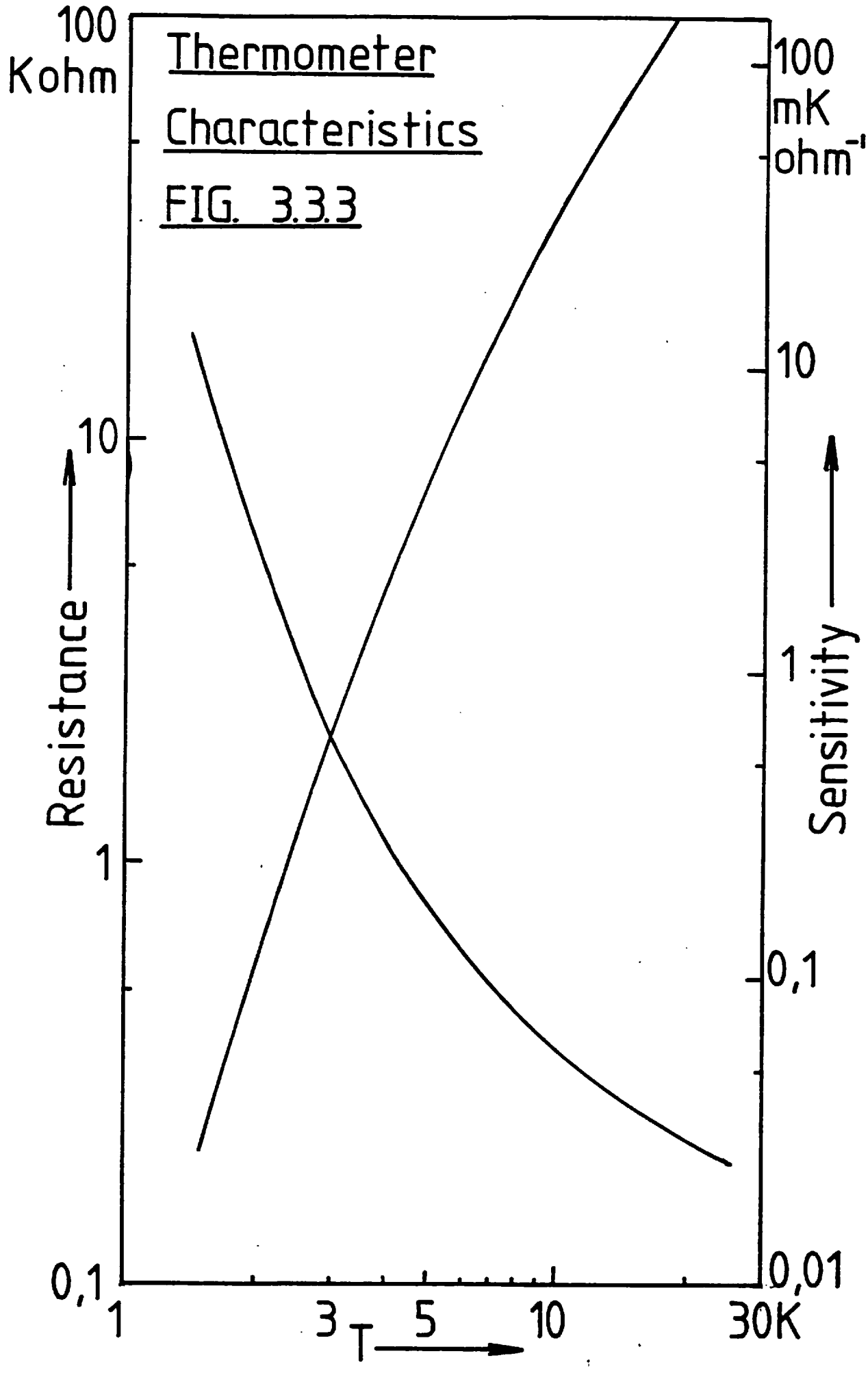
Thermometer
Characteristics
FIG. 3.3.3
100
Kohm
10
1
0,1
Resistance
100
mK
ohm⁻¹
10
1
0,1
0,01
Sensitivity
1
3
5
10
30K
T

technique (see figure 3.2.8). The thermometer's excitation current was derived from the voltage dropped across a 1 KΩ precision standard resistor in series with the thermometer. All voltage measurements were made with a 6-figure Digital voltmeter. The carbon thermometer resistance was read from the scale on the Dekastat variable resistor at the bridge balance point for forward and reverse directions of the bridge excitation current. The calibration temperatures were obtained from a smoothed cubic spline interpolation table of the germanium thermometer's calibration data. The interpolation data was estimated to be accurate to $\pm$ 0.2% in temperature by comparing the original calibration temperatures with those predicted by the interpolation table.

By progressively reducing the vapour pressure above the liquid helium bath the sample temperature was stabilised at selected calibration points below 4.2 K. Vapour pressure fluctuations during calibration were reduced to less than 0.5 torr by regulation of the pumping speed to match the helium gas boil-off rate. The helium vapour pressure was measured by a pair of Wallace and Tiernan dial manometer gauges calibrated with the T_{58} vapour pressure scale to read temperature directly. The low pressure gauge was kept evacuated when not in use. Temperature scale reading errors in the low pressure gauge were less than $\pm$0.3% in the range 1.5 - 1.95 K. Errors on the high pressure guage were less than $\pm$ 0.2% in the range 3 - 4.2 K and $\pm$ 0.5% in the range 2.5 - 3 K, increasing to $\pm$ 1% close to the λ-point in the range 2 - 2.5 K, where the scale becomes significantly non-linear. Due to the indirect nature of the calibration procedure temperature and pressure gradients are likely to be significant, thus low temperature thermometry errors of $\pm$0.5% ($\pm$ 1% close to the λ-point) could be more realistic.

3.3.4 Interpolation of the Calibration Data

The Clement and Quinnell (12) formula (equation 3.20) was used as the basic

interpolation formula for the carbon thermometer calibration data.

$$A/T = 1 - B\log R + C/\log R \qquad 3.20$$

A, B and C are constants determined by simultaneous solution of the set of equations obtained by substitution in equation 3.20 of resistance and temperature data from three calibration points. It was not found to be possible to fit the entire temperature range 1.5 - 20 K adequately with a single fit. Multi span fits were tried; the results for a three and five span fit are shown in figures 3.3.1 and 3.3.2 respectively. The deviations of the calibration data points from a five span fit can be seen to be far less systematic than those of a three span fit.

Two extensive calibrations were performed during the latter series of experiments, one six months after the other. These were labelled calibrations A and B, their fit deviations are plotted in figures 3.3.2a, b and c,d respectively. Figure 3.3.1 c and d show deviations of calibration data for B from the fit to the calibration data for A. These fit deviations indicate the maximum temperature errors that could be expected for the experiments performed between these two calibrations. The maximum errors could be up to 1% in the range 1.5 - 3 K, $\pm$ 0.3% in the range 3 - 10 K and up to 0.6% in the range 10 - 20 K.

The temperature sensitivity of the thermometer was derived by differentiation of equation 3.20 with respect to R.

$$\frac{dT}{dR} = \frac{T^2 \log e}{AR}\left[B + C/\log^2 R\right] \qquad 3.21$$

Figure 3.3.3 is a plot of the typical thermometer characteristics and indicates the problems entailed in attempting to obtain an adequate fit to the Clement and Quinnell formula.

3.3.5 Discussion of Thermometry Errors

The thermometry errors are dominated by the small calibration shifts occurring at each thermal cycling of the thermometer between room and helium temperatures. During a two month interval, over which the thermometer was thermally cycled several times, the calibration shift errors were observed to be no greater than $\pm 0.5\%$ in the range 1.5 - 4.2 K and $\pm 0.3\%$ in the range 4.2 - 20 K. These errors were observed to double over a six month period at the extremities of the calibration range, i.e. 1.5 - 3 K and 15 - 20 K, but at intermediate temperatures the calibration was relatively insensitive to thermal cycling. Since most of the experiments were performed within three months of one of the calibrations, A or B, the temperature errors were expected to be no worse than $\pm 0.5\%$ in the range 1.5 - 3 K, $\pm 0.3\%$ in the range 10 - 20 K.

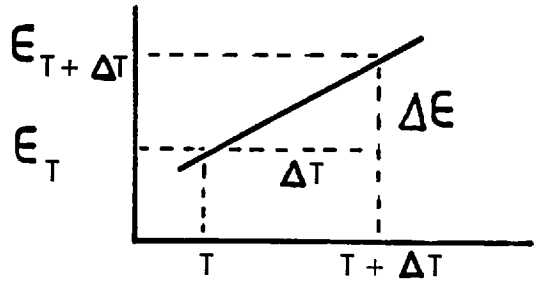

Fig. 3.3.4

The errors in the temperature sensitivity may be estimated from the slope of the temperature deviation plots. Consider two calibration points $[R, T]$ and $[R + \Delta R, T + \Delta T]$ in figure 3.3.4, where ΔR and ΔT are small quantities; an interpolation fit would predict temperatures T' and T' + ΔT' from thermometer resistance values R and R + ΔR respectively. The corresponding fit deviations at these temperatures are ϵ_T and $\epsilon_{T+\Delta T}$ as defined below :

$$\epsilon_T = \frac{(T-T')}{T'}$$

$$\epsilon_{T+\Delta T} = \frac{T+\Delta T-(T'+\Delta T')}{T'+\Delta T'}$$

$$\Delta\epsilon = \epsilon_{T+\Delta T} - \epsilon_T \simeq \frac{\Delta T - \Delta T'}{T'}$$

The error in temperature sensitivity ϵ_S is then given by :

$$\epsilon_S = \left(\frac{dT}{dR} - \frac{dT'}{dR}\right) \Big/ \frac{dT'}{dR} = \frac{\Delta T - \Delta T'}{\Delta T'}$$

$$\therefore \epsilon_S = T' \frac{\Delta \epsilon}{\Delta T'} \qquad 3.22$$

Thus by considering the general trends in the fit deviations plotted in figures 3.3.1c and d the temperature sensitivity errors are expected to be no worse than $\pm$ 1% in the range 1.5 - 3 K, $\pm$ 0.5% in the range 3 - 10 K and $\pm$ 1% in the range 10 - 20 K.

3.4 Experimental Measurements

3.4.1 Estimation of Time Constants

With every new sample it is necessary to estimate the time constants τ_{SB} and τ_{INT} to calculate the operating frequency limits. It is also important to consider the time constants associated with the electronic systems. RC filter networks in the bridge and heater summing amplifiers reduce noise but will also tend to introduce unwanted frequency dependences.

Sample Related Time Constants

The procedure for measuring τ_{SB} has already been described in section 3.1.2 on the DC method of relaxation calorimetry.

Measurement of τ_{INT} is more involved as was suggested in section 3.1.3 on the higher frequency limit. A frequency dependent AC heater voltage is obtained by capacitively coupling the AC voltage component to the summing amplifier. Starting from an AC frequency value low enough for the T_2- amplitude to be frequency independent (usually $\tau \sim$10 or 20s) the AC frequency is gradually increased. The

additional DC source is used to trim the DC voltage component to compensate for an increase of the AC component and so maintain a constant average temperature. The value τ_{50} is read from the digital timer at the point when the T_2-amplitude has fallen to half its frequency independent value. If it is apparent that τ_{50} is going to be so small that it exceeds the frequency limits of the chart recorder (i.e. $\tau_{50} < 1s$) then τ_{10} corresponding to a 10% reduction of its frequency independent value is read instead. The lower frequency limits are then calculated from τ_{50} and τ_{10} using expressions 3.16 and 3.17 respectively. The frequency limits are usually measured at about five representative temperatures throughout the temperature range of interest.

System Related Time Constants

The frequency limitations of the electronic systems is mainly due to the finite response time of the chart recorder and the bandwidth of the two amplifiers, i.e. the heater summing and the bridge high gain amplifiers. The chart recorder response was limited by the maximum velocity of the pen (v_{max} = 38 cms^{-1}). This implies that for a given amplitude of displayed wave form there is a cut-off frequency above which the wave form becomes distorted. The cut-off frequency is higher for the smaller amplitude waveforms, it varied between 0.5 - 5 Hz for waveforms of peak-to-peak amplitude 20 - 2 cm. The heater summing and bridge high gain amplifiers separately have cut-off frequencies of 3.5 and 70 Hz respectively. The combined effect of the above frequency limits puts an overall frequency limit on the system of about 0.5 Hz for up to 20 cm amplitude waveforms and 1 Hz for up to 10 cm amplitude waveforms.

3.4.2 Experimental Procedure

At the start of any experimental run the sample would be mounted on the platform using 10 mg of heat sink compound. The sample chamber would be sealed, evacuated and left to precool in liquid nitrogen overnight. The following morning the liquid

nitrogen was expelled to be replaced by a charge of liquid helium. The cryostat was then left for a couple of hours to reach a state of adequate thermal stability. For a new sample the frequency limits were estimated first, as described in section 3.3.4. The heat capacity measurements were commenced usually from the high temperature end of the range of interest where residual thermal gradients following the helium transfer affect the measurements least.

The resistance value corresponding to the required temperature was set on the Dekastat variable resistor in the bridge network. The sample was brought approximately to the required temperature by gradually increasing the amplitude of a high frequency ($f \sim 1$ Hz) resistively coupled pure AC heater voltage. After allowing the sample to reach equilibrium at its new temperature, the thermometer resistance was read from the Dekastat resistor at the bridge balance point for both directions of the bridge current. The AC frequency was then decreased slowly to the lower limit set by τ_{SB}.

As explained in section 3.1.2 on the AC method, the frequency of the temperature oscillations is predominantly at twice the frequency of the applied AC heater voltage. However, there was usually a residual DC component in the heater voltage which would give rise to distorted temperature oscillations. The unwanted DC component was trimmed out, using the additional DC source. The digital printer was set to record ten or so successive peak heater voltage amplitudes from which an average value for V_H was calculated. A few cycles of the temperature oscillations were traced out on the chart recorder whilst the time period τ of the waveform was measured on digital timer.

The frequency was progressively lowered in about five steps to the upper limit, taking recordings of the trace amplitude and waveform time period at each step. The chart trace was calibrated by replacing the carbon thermometer with a standard decade resistance box set equal to its resistance value. A deflection recorded on the chart

trace from a known resistance increment gave the chart calibration factor X (Ω cm^{-1}). The above procedure was repeated at various temperature points throughout the range of interest.

When measurements were made at temperatures below 4.2 K the run was interrupted for 1 - 2 hours whilst the bath temperature was lowered by pumping on the helium. Time was allowed for adequate thermal stability to be established before taking further measurements. The lowest bath temperature achieved was about 1.3 K, though 1.5 K was more typical.

3.4.3 Analysis of Measurements

The first part of the analysis was the processing of results recorded on the chart trace. The peak-to-peak amplitude values y of the temperature oscillation traces were measured and plotted against the corresponding time periods τ. These results usually gave straight line plots with gradient α (cm s^{-1}) passing through the origin. Occasionally deviations from linearity were observed in these plots at smaller τ values. This was attributable to the crossing of the higher frequency limit when τ_{INT} values were small and therefore very difficult to measure with adequate precision for some samples at these higher frequencies. The chart calibrations gave values for X (Ω cm^{-1}), the resistance deviation of the thermometer required to give unit deflection on the chart trace. The product of these values for α and X, together with the temperature sensitivity $\frac{dT}{dR}$ calculated from thermometer resistance using the expression 3.21, gave a value for the term ωT_2 in expression 3.13.

$$\omega T_2 = \frac{2\pi T_2}{\tau} = \pi \alpha X \frac{dT}{dR}$$

Substituting for ωT_2 in expression 3.13 gives :

$$C = \frac{V_H^2}{4\pi \alpha X R_H \frac{dT}{dR}} \qquad 3.23$$

The heat capacity calculated by expression 3.23 is the total value composed of contributions from the sample and the addenda. The addenda represents total contributions from the sample platform, thermometer, heater, wires and grease, etc. The addenda heat capacity was measured in a separate calibration run, the results for this are presented later in section 3.5.1. The sample heat capacity obtained after subtracting the addenda contribution was normalised to give its molar value.

$$\frac{C}{T} = \frac{A}{m_s}\left[\left(\frac{C}{T}\right)_{TOTAL} - \left(\frac{C}{T}\right)_{ADDENDA}\right] \qquad 3.24$$

where m_s is the sample mass and A is the mass of one formula unit of the sample material. Expressions 3.23 and 3.24 were evaluated in the same computer program used to calculate the T and dT/dR values.

3.4.4 Discussion on Errors in Heat Capacity Measurements

Uncertainty of the total measured heat capacity is considered as two categories of errors, random and systematic in nature.

Random Errors

Purely random errors in the total measured heat capacity, resulting from the imprecision of the measurement techniques, amount approximately to $\pm 1.5\%$. The quantities V_H, y, X are the most significant contributors to this random error component. An error of $\pm 0.2\%$ in V_H contributes $\pm 0.4\%$ to the uncertainty of the heat capacity since it enters the calculations of the heat capacity as V_H^2. Both y and X contribute a further $\pm$ 0.5% each.

Systematic Errors

The approximation which resulted in the simplification of expression 3.9 to 3.13, the basic expression for calculating heat capacity measured by the AC relaxation method, has by definition introduced a systematic error of up to 1%. Calibration shifts in the thermometry lead to further systematic errors; the magnitude of this contribution has

already been discussed in section 3.3.5. Non-linearity in the thermometry, arising partly from the limitations of the bridge circuit, may also make a significant contribution.

Percentage errors ϵ_{TN} and ϵ_{BN}, corresponding to non-linearity in the thermometry and the bridge circuit respectively, depend on the amplitude of the temperature oscillations, T_2.

$$\epsilon_{TN} = \frac{T_2 - T_2'}{T_2'} \qquad \text{where} \quad T_2' = \Delta R \left(\frac{dT}{dR}\right)_{T_o} \qquad 3.25$$

$$\epsilon_{BN} = \frac{Y - Y'}{Y'} \qquad \text{where} \quad Y' = 2X\Delta R \qquad 3.26$$

$$\Delta R = \tfrac{1}{2}\left[R(T_0 + T_2) - R(T_0 - T_2)\right] \qquad 3.27$$

Figures 3.4.1a and b illustrate these non-linearity errors. Both the thermometer and the bridge show asymmetry in their non-linearity errors. The nature of this asymmetry is such that the deviations of positive and negative temperature excursions about T_o compensate for each other and the total peak-to-peak amplitude of the displayed chart trace is to first order insensitive to such non-linearity effects. A value for ΔR may be derived by Taylor series expansion of $R(T_0 + T_2)$ and $R(T_0 - T_2)$.

$$\Delta R = T_2 R'(T_0) + \frac{T_2^3}{6} R'''(T_0) \qquad 3.28$$

where $R'(T_0)$ and $R'''(T_0)$ correspond respectively to the first and third temperature derivatives of the thermometer's resistance characteristic at temperature T_0. The thermometer non-linearity error then simplifies to expression 3.29.

$$\epsilon_{TN} = -\frac{T_2^2}{6}\frac{R'''(T_0)}{R'(T_0)} \qquad 3.29$$

A full consideration of the non-linearity in the bridge led to the estimate for

FIG. 3.4.1

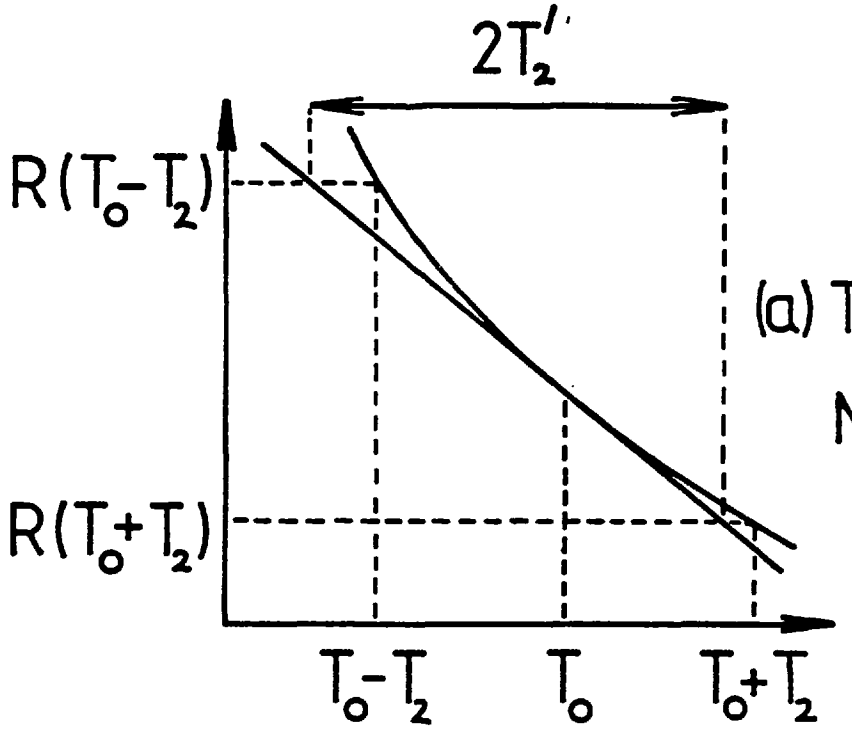

(a) Thermometer Non-linearity

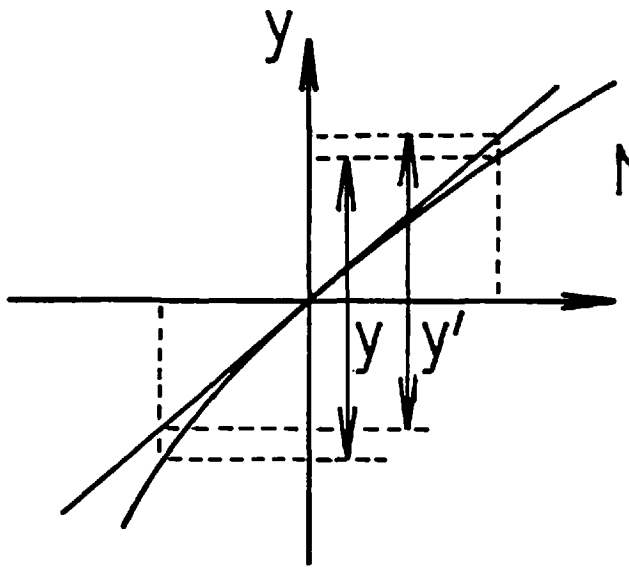

(b) Bridge Non-linearity

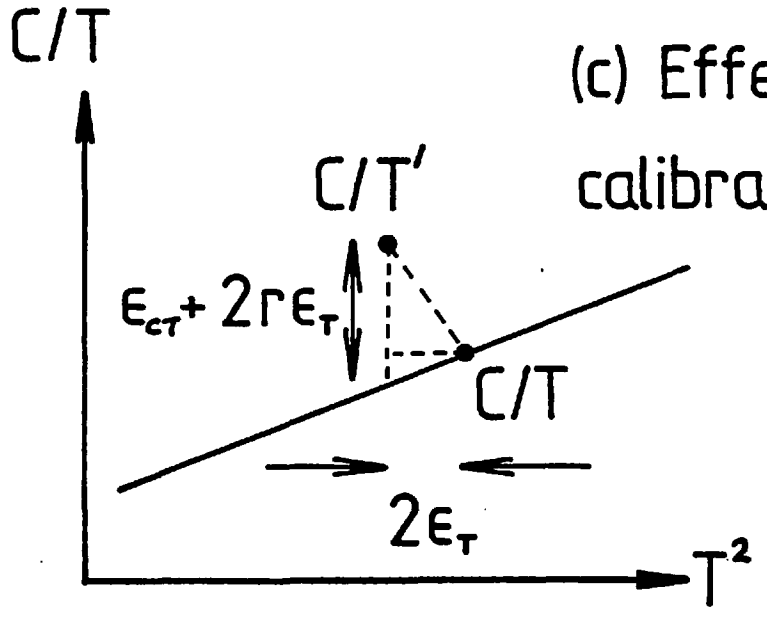

(c) Effect of calibration error

ϵ_{BN} given below.

$$\epsilon_{BN} \simeq -\frac{1}{8}\left[\frac{\Delta R}{R + R_x}\right]^2 \qquad 3.30$$

where R is the thermometer resistance at T_0 and R_X the resistance of one of the fixed arms of the bridge circuit (i.e. 1 KΩ or 10 KΩ depending on the value of R).

Both ϵ_{TN} and ϵ_{BN} are second order effects amounting to less than 0.5% at 2 K, and 0.3% at 20 K for T_2/T_0 ratios of 5% or less. The degree of linearity of plots of y against τ verify that these second order effects are indeed negligible. However, the non-linearity is readily observable as a distortion of the chart trace waveform resulting in an apparent shift of the chart trace centre to lower temperatures. This effect becomes more accentuated at lower temperatures.

To estimate the effects of thermometer calibration error on the calculated heat capacity values, consider expression 3.23 for C/T. The denominator of expression 3.23 contains the product T dT/dR, thus the error in C/T, ϵ_{CT} is the sum of the respective errors in T and dT/dR.

$$\epsilon_{CT} = -\epsilon_T - \epsilon_S \qquad 3.31$$

As C/T values are usually plotted against T^2, then the shift in T^2 value and the effect of the gradient of the plot should also be taken into account (see figure 3.4.1c). The net observed heat capacity error in plots of C/T against T^2 arising from thermometer calibration error is given below.

$$\epsilon_{CT} = -\epsilon_S - \epsilon_T (2r + 1) \qquad 3.32$$

where $r = \beta T^2/(\gamma + \beta T^2)$

The effects of the most significant systematic errors are summarised in the table below. A blanket value of 0.5% has been included to account for non-linearity and

formula approximation errors, the latter varies from sample to sample, being small for a large working frequency interval between the upper and lower limits.

T	1.5 - 3K	3 - 10K	10 - 20K
ϵ_T	0.5	0.3	0.5
ϵ_S	1.0	0.5	1.0
ϵ_{CT}	2.0	1.5	3.0

The subtraction of the addenda heat capacity will magnify these errors by a factor $(1 + 2\, C_A/C_S)$ where C_A and C_S are respectively the addenda and sample heat capacities. For most of the samples considered in the series of experiments reported in this thesis the ratio C_A/C_S varied from 0.2 - 0.4 over the temperature range 2 - 20 K.

Total systematic errors in C/T are estimated to vary from 3 - 5% over the temperature range 2 - 20 K. Additionally there is the random error C/T of $\pm$ 2 - 3% over the range 2 - 20 K.

3.5 Results and Conclusions

The preliminary results obtained with the calorimeter are reported in this section. The results include measurements of the addenda heat capacity and a check of the calorimeter's calibration and accuracy using a pure copper sample, comparing results obtained with data published by Holste et al (13).

3.5.1 Addenda Heat Capacity

The addenda heat capacity constitutes the collective heat capacities of the sample platform, thermometer, heater, heat sink compound and any contribution from the electrical leads and thermal link. This component of the total measured heat capacity must be subtracted from the data to yield the sample heat capacity.

The addenda contribution was measured in a separate experiment with the heater

adhered directly to the sample platform by a 10 mg smear of RS heat sink compound. The heat sink compound was weighed to the nearest milligram to ensure consistency as it has ten times the heat capacity of its weight equivalent of copper (see reference 7) and accounts for about 5% of the addenda heat capacity. The addenda was measured shortly after calibration A was performed, hence fits to that calibration were used in the analysis. The present addenda results, together with the original addenda (i.e. germanium thermometer attached) and 1.7 g copper are plotted in figures 3.5.1 and 2. The line through the addenda data points represent fits to the expression $C/T = A + BT^2$ over three temperature ranges.

RANGE	$A(\mu JK^{-2})$	$B(\mu JK^{-4})$
$2 < T^2 < 10K^2$	12.5	1.53
$10 < T^2 < 70K^2$	11.0	1.71
$70 < T^2 < 400K^2$	25.0	1.50

These fit parameters were used to calculate the addenda contribution to be subtracted from the total measured heat capacity values. The majority of the data points lie within $\pm$ 2.5% of these fits.

3.5.2 Copper Heat Capacity Data

A sample of approximately 3.5 g mass was prepared from Johnson Matthey Specpure (5N) copper. The sample was annealed in vacuum at 200°C for 2 hours to relieve any strain induced whilst melting the source material into a button shape. Flat surfaces were arc-planed on the top and bottom of the sample button and finished with fine carborundum paper. The sample was measured shortly after calibration B was performed. The results are plotted in figures 3.5.3, 4 and 5, together with data published by Holste et al (13).

The first remark to make about these results is the significant systematic error in the data above 10 K. This error is larger than estimated in the previous section, and

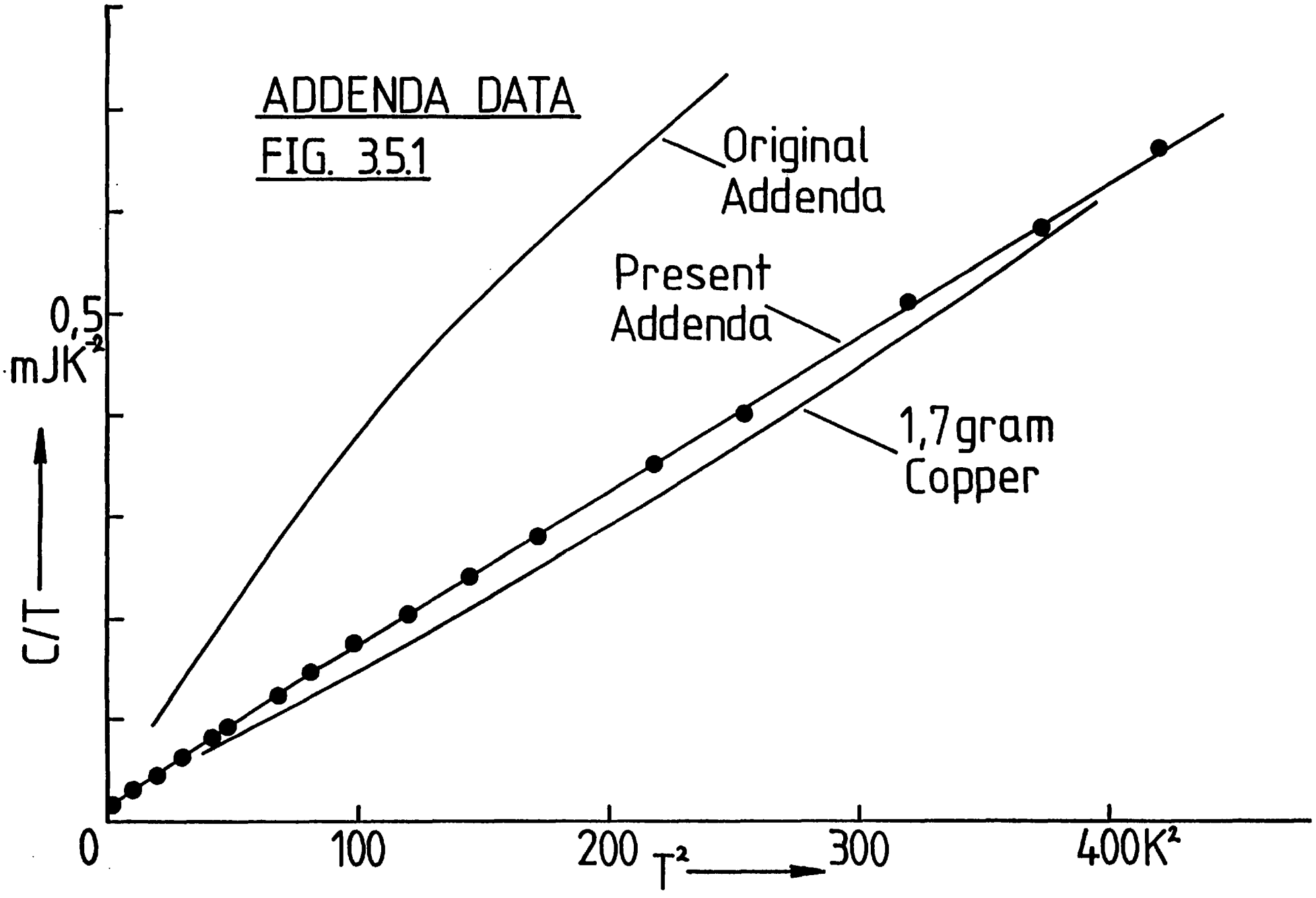
ADDENDA DATA
FIG. 3.5.1
Original
Addenda
Present
Addenda
1,7 gram
Copper
0,5
mJK⁻²
C/T
0
100
200
300
400K²
T²

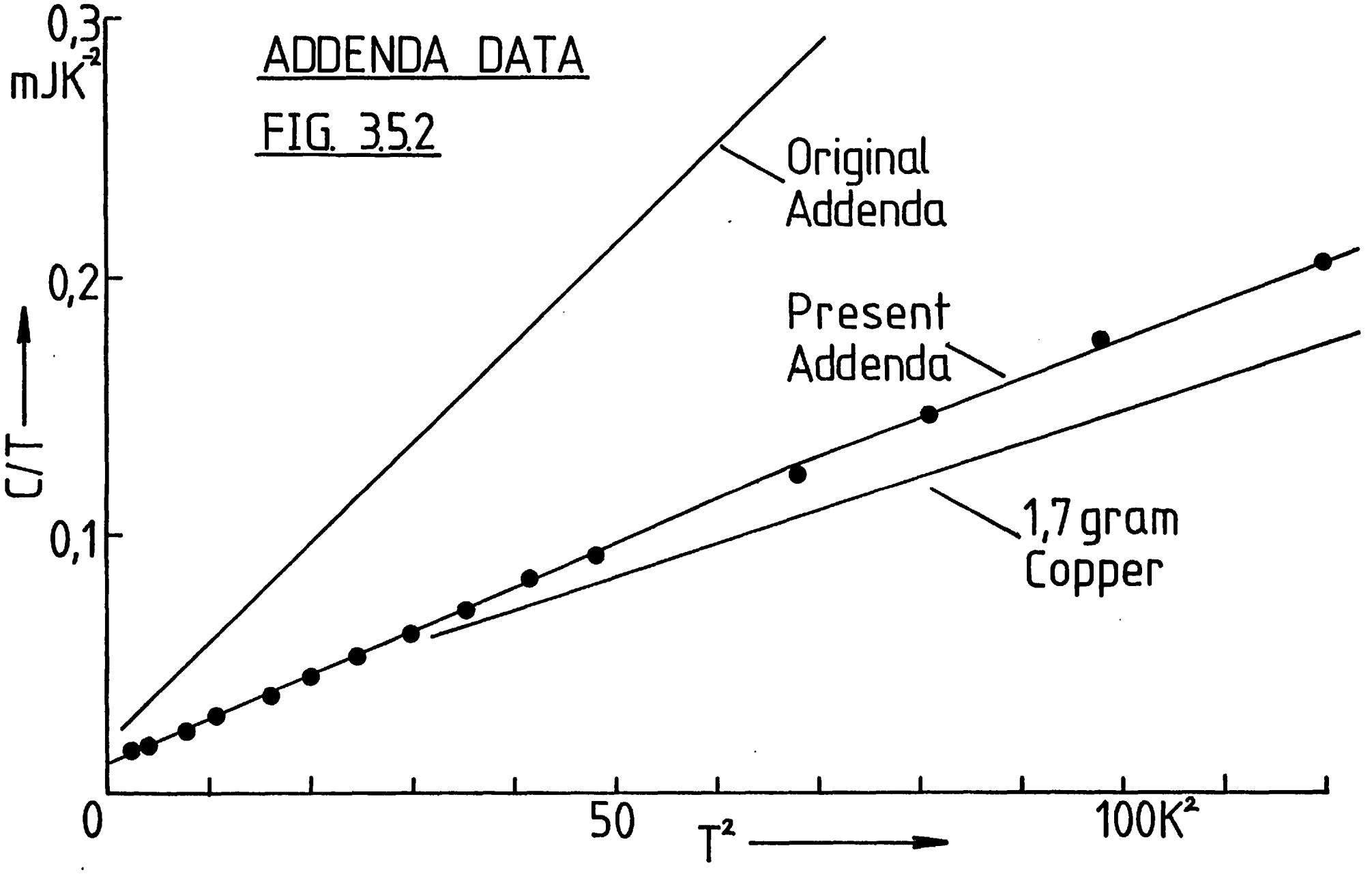
ADDENDA DATA
FIG. 3.5.2
0,3
mJK⁻²
0,2
0,1
C/T
0
50
T²
100K²
Original
Addenda
Present
Addenda
1,7 gram
Copper

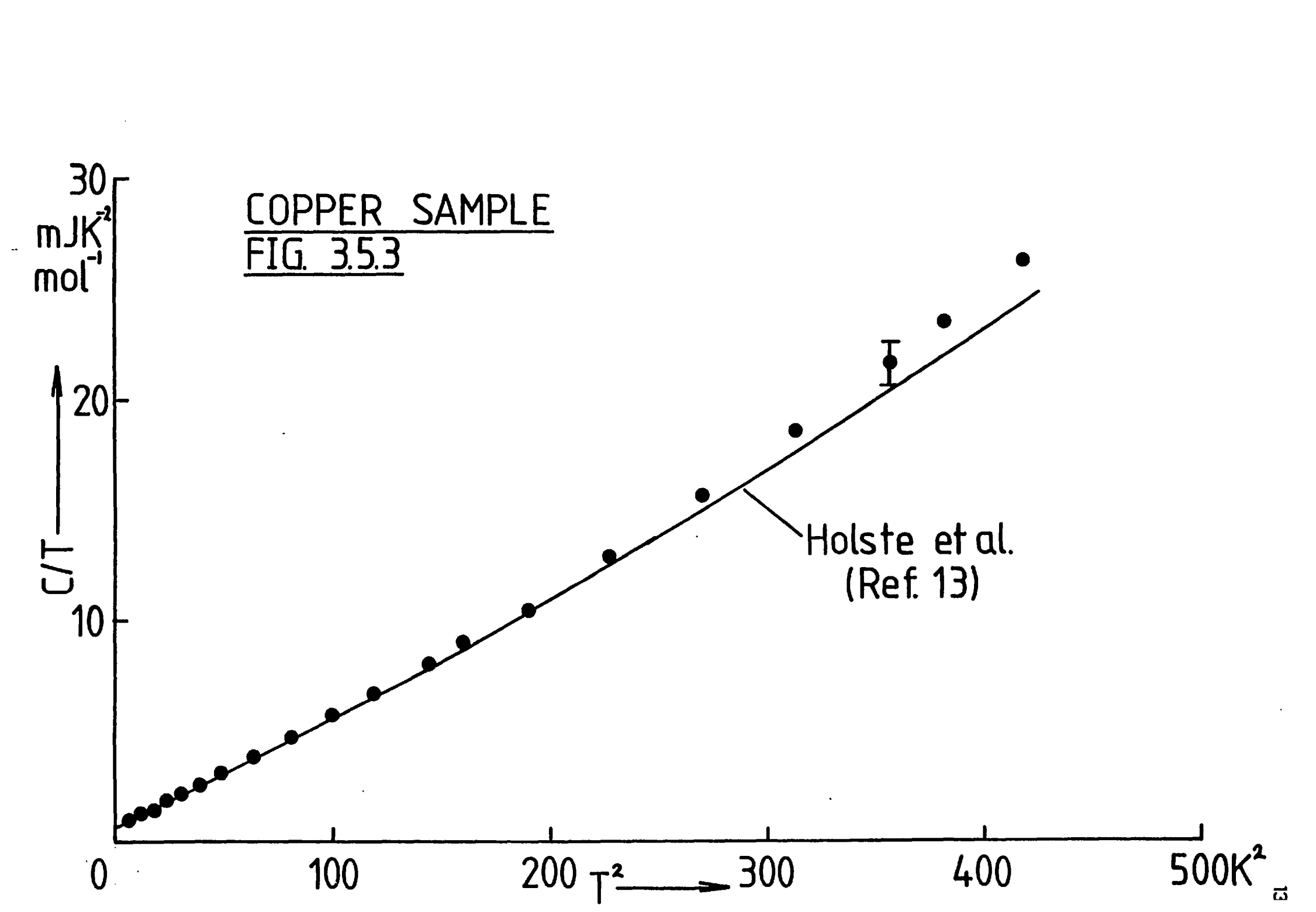
COPPER SAMPLE
FIG. 3.5.3
30
mJK⁻² mol⁻¹
20
10
C/T
0
100
200
T²
300
400
500K²
Holste et al.
(Ref. 13)

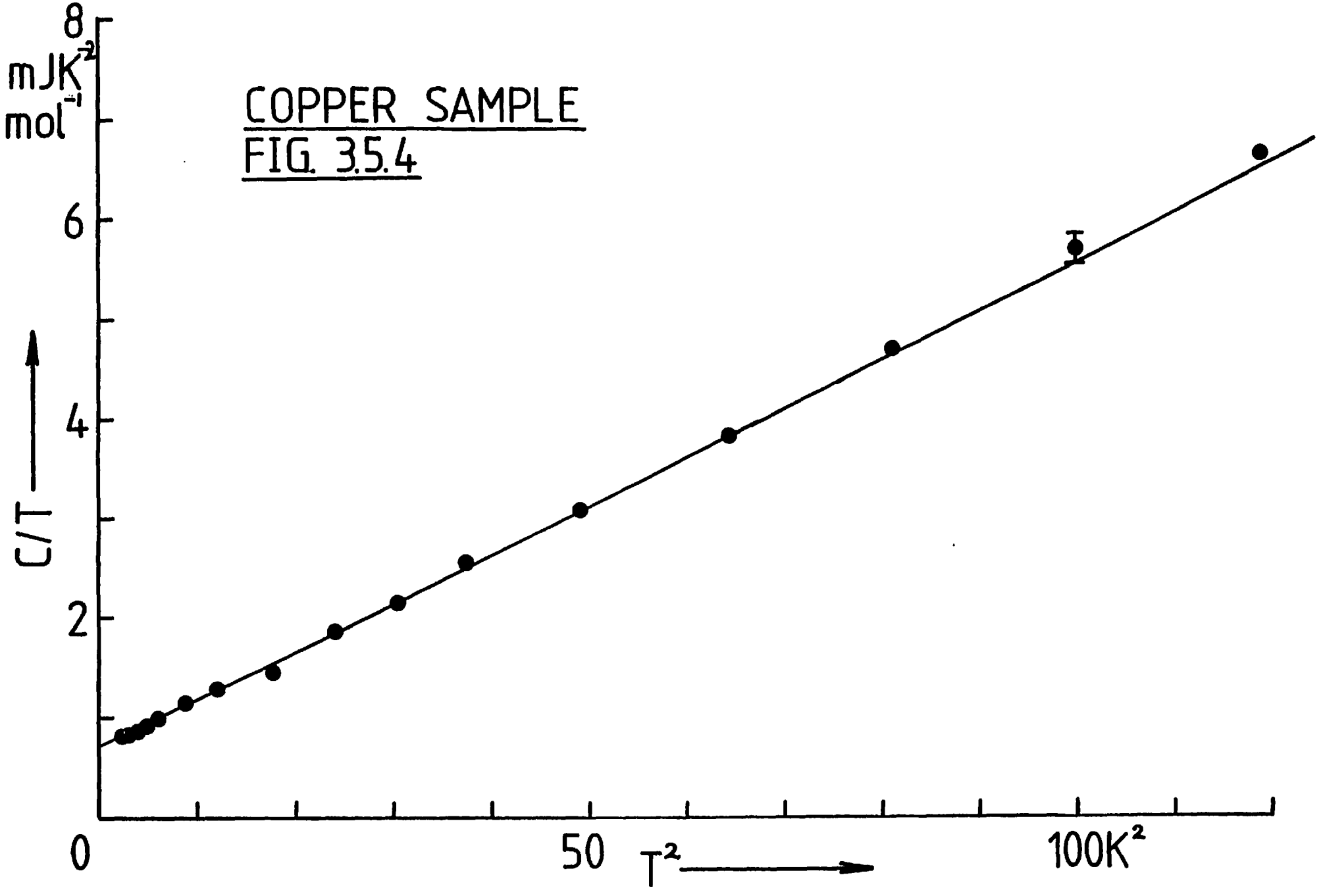
COPPER SAMPLE
FIG. 3.5.4
8
6
4
2
0
mJK⁻²mol⁻¹
C/T
50
T²
100K²

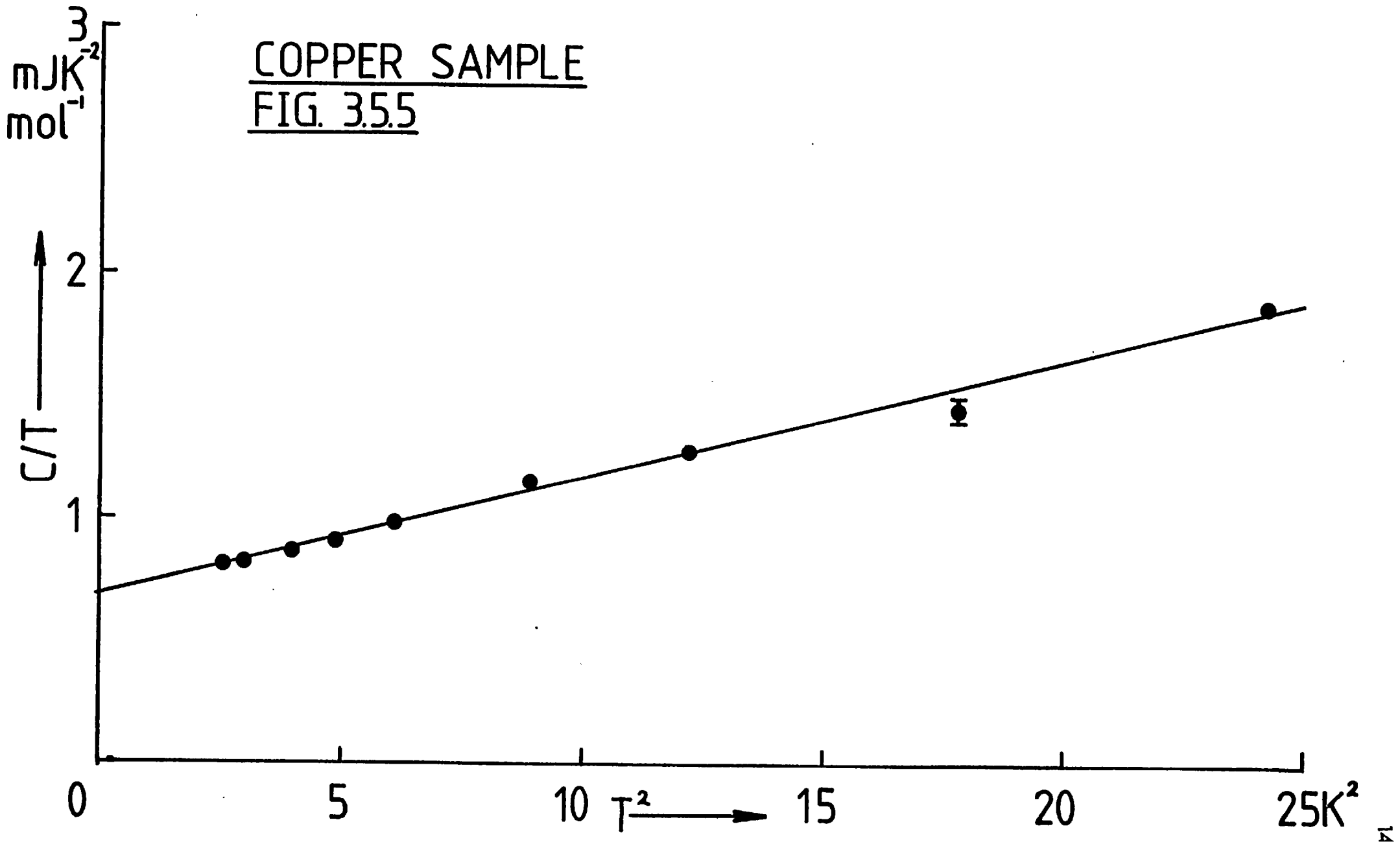
COPPER SAMPLE
FIG. 3.5.5
3
mJK⁻² mol⁻¹
2
1
C/T
0
5
10
T²
15
20
25K²

shows a distinct temperature dependence which can best be seen in the plot (fig. 3.5.6) of percentage deviations ϵ_{CT} of the heat capacity data from Holste et al's data.

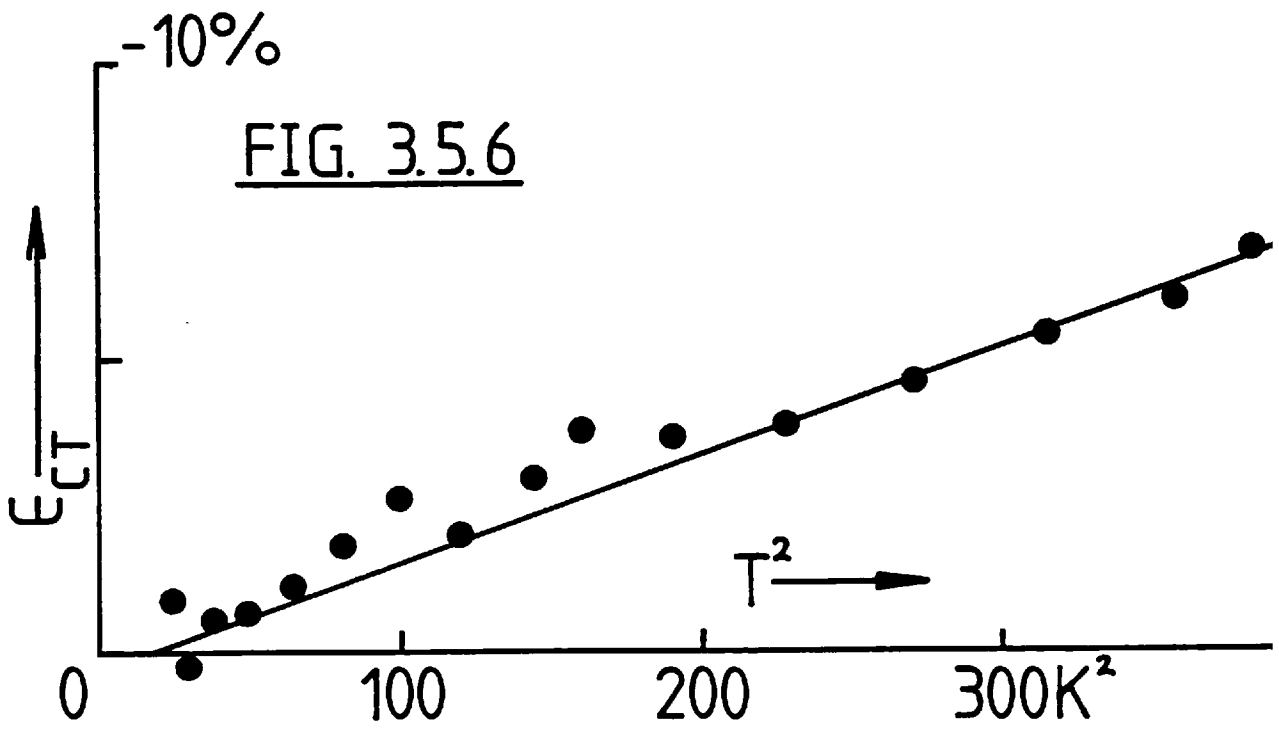

FIG. 3.5.6

The deviations ϵ_{CT} appear to be linearly dependent on T^2

$$\epsilon_{CT} = \frac{\Delta C/T}{C/T} = \frac{C/T_{HOLSTE} - C/T}{C/T} = \zeta T^2 \qquad 3.32$$

i.e. $\Delta C \propto T^4$ for $\beta T^2 \gg \gamma$

It is plausible that the source of such error is through unaccounted radiation losses from the sample, this would fit the observed T^4 dependence of the error. However, even the most generous estimate of a possible radiation loss of 0.2% of total thermal power applied to the sample at 20 K falls short of the value required to account for the observed deviations.

A further possibility is that the problem originates in the thermometer calibration through inadequate thermal sinking of the germanium thermometer leads. The effect is modelled below in figure 3.5.7.

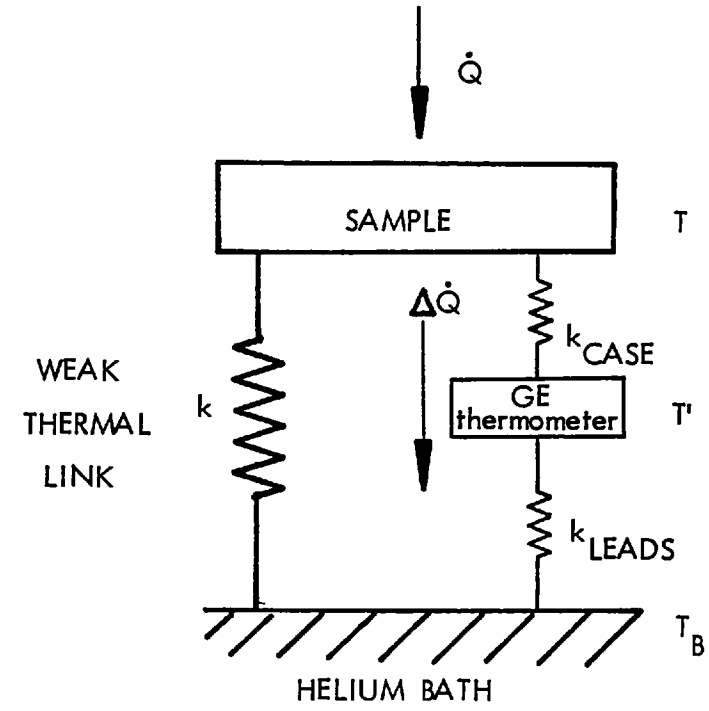

fig. 3.2.7

If the sample and carbon resistor were at temperature T, a small, finite thermal current $\Delta\dot{Q}$ could flow along a path from the sample through the thermometer casing to the germanium crystal sensing element, then along the manganin thermometer leads to a copper heat sinking post at temperature T_B. The resulting thermal gradient between the carbon and germanium thermometers would result in erroneously low calibration temperatures T' .

$$\epsilon_T = \frac{T - T'}{T'} \simeq \frac{k_{CASE}}{k_{LEADS}} \frac{T' - T_B}{T'} \qquad 3.33$$

$$\text{since } k_{CASE} \ll k_{LEADS}$$

The thermal conductance of the thermometer's encasing material k_{CASE}, which is predominately epoxy and helium gas, would be expected to exhibit a T^3 dependence, whereas the metallic manganin leads will have a mean thermal conductance k_{LEADS} proportional to $(T' - T_B)$. Therefore ϵ_T would be expected from expression 3.33 to be proportional to T^2 and resulting errors in C/T would also exhibit this temperature dependence. The thermometry error required to produce the C/T deviations plotted in

fig. 3.5.6 is estimated to be ϵ_T = 1 - 2% from expression 3.32.

For temperatures below 4.2 K the majority of the data points scattered randomly in an error band of $\pm$ 2% about Holste et al's result, well within the expected accuracy of the calorimeter in this temperature range.

3.5.3 Concluding Remarks

An AC relaxation calorimeter for measuring specific heat capacity of small samples has been described in the previous sections. Although in absolute terms its accuracy cannot match that achievable by adiabatic methods, it does have a notable advantage over the adiabatic type of calorimeter. When measuring small relative changes in heat capacity, such as close to a λ-type anomaly or with the sample in an external magnetic field, the steady state method is most appropriate.

The experimental errors have been reviewed in some detail, with particular attention being directed to systematic thermometry errors. The alternative calibration procedure adopted to reduce the addenda heat capacity and simplify experimental procedure was shown to have an insignificant effect on the experimental accuracy achieved with the original calorimeter arrangement. The new experimental procedure allowed sufficient data to be taken during a single run. This was considered an important advantage when making measurements on an alloy sample that could have aged significantly during the time between two experimental runs.

During the course of this work many experimental runs were performed and the calorimeter was considered to be sufficiently well understood to omit a calibration check immediately after the modifications were performed on the sample platform. It was not until towards the end of the latter series of experiments, when a run on a copper calibration sample was included for completeness, that the problem of insufficient thermal sinking of the thermometer leads was realised. Fortunately the systematic error in most of the later results over the temperature range 10 - 20 K does not critically affect the conclusions of this work which concentrate mainly on the low temperature data.

REFERENCES

1. Martin D.L., 1966, Phys. Rev. 141, 576
2. Boerstoel B.M., 1970, Ph.D. thesis, Leiden
3. Moody D.E. and Rhodes P., 1963, Cryogenics 3, 77
4. Schwall R.E., Howard R.E. and Stewart G.R., 1975, Rev. Sci. Instrum. 46, 1054
5. Martin D.L., Bradley L.L.T., Cazemier W.J. and Snowdon R.L., 1973, Rev. Sci. Instrum. 44, 675
6. Joseph O., Moody D.E. and Whitehead J.P., 1976, J. Phys. E : Sci. Instrum., 595
7. Bachmann R., Di Salvo F.J., Geballe T.H., Greene R.L., Howard R.E., King C.N., Kirsch H.C., Lee K.N., Schwall R.E., Thomas H-U and Zubeck R.B., 1972, Rev. Sci. Instrum. 43, 205
8. Sullivan P.F. and Seidel G., 1968, Phys. Rev. 173, 679
9. Nicolson L.K., 1976, Ph.D. thesis, London
10. Lindenfeld P., 1962, Temperature, Reinhold, New York, 3, 399
11. Clement J.R. and Quinnell E.H., 1950, Phys. Rev. 79, 1028
12. Clement J.R. and Quinnell E.H., 1952, Rev. Sci. Instrum. 23, 213
13. Holste J.C., Cetas T.C. and Swenson C.A., 1972, Rev. Sci. Instrum. 43, 670

CHAPTER 4

EXPERIMENTAL RESULTS

INTRODUCTION

The specific heat measurements made on a number of solid solution alloys of the Y Gd, Au Fe and Cu Mn systems are presented in this chapter. The alloys were carefully prepared with reasonable homogeneity of composition. Metallurgical problems particular to any of the alloy systems concerned are discussed in the following section.

4.1 Metallurgical Considerations

4.1.1 The Y Gd Alloys

Two dilute Y Gd alloys with compositions of 2.0 and 3.4 at% Gd were investigated in this work. The high miscibility of the two rare earth elements enabled good, homogeneous solid solution alloys to be easily prepared. The hexagonal closepacked (HCP) phase of the dilute Y Gd alloys is stable below 1100°C, and no precipitation or ordering effects are expected at low temperatures from the alloy's phase diagram (1). These alloys were consequently given no solution treatment during preparation.

Considering the dilute nature of these alloys, it is worth commenting on the purity of the yttrium supplied by Rare Earth Products Ltd. As is common for most of their rare earth elements, they quote a purity of 99.9% for yttrium. It is evident from the variations in low-temperature specific heat data of yttrium and scandium (2,3) reported in the literature that magnetic impurities are far from insignificant. This has prompted Wells et al (4) and Tsang et al (5) to employ solid state electron-transport refinement techniques (6,7) to improve purity of their yttrium and scandium specific heat samples. The yttrium sample used by Wells et al contained ~ 480 at. ppm oxygen, ~ 200 at. ppm nitrogen, ~ 25 at. ppm total lanthanide content and ~ 10 at. ppm other contaminants. Their specific data is reproduced in figures 4.3.7 and 4.3.8 and discussed

in section 4.3.4 on the Y Gd alloys.

4.1.2 The Au Fe Alloys

Seven Au Fe alloys in the intermediate composition range 14 - 28 at% Fe, around the critical concentration ~16 at% Fe, were prepared for this work. The phase diagram for the Au Fe system is reproduced (from ref. 1) in fig. 4.1.1b. The FCC-structured gamma-phase of the Au Fe solid solution alloys in the composition range of interest is only stable at elevated temperatures. As - cast alloys were solution treated at a suitably chosen temperature (~ 900°C) not far below the solidus curve. A rapid quench to room temperature following the solution treatment was considered to retain the high temperature gamma-phase with good homogeneity. Electron microprobe (~1 μm probe resolution) analyses of some of these alloys revealed no evidence of Fe-rich precipitates. All alloys required storage under liquid nitrogen to prevent ageing of the metastable gamma-phase which would have occurred if they were kept at room temperature.

4.1.3 The Cu Mn Alloys

Four Cu Mn alloys were investigated, their nominal compositions ranged from 30 - 70 at% Mn in the concentration regime approaching the critical concentration (~72 at% Mn) for the onset of long range antiferromagnetic order. The phase diagram for the Cu Mn alloy system is reproduced (from ref. 1) in fig. 4.1.1a. The gamma-phase of these alloys, as it is for the Au Fe alloys, is only stable at elevated temperatures. A similar solution treatment (at 800 - 850°C) followed by a rapid water quench of the as-cast alloys was required to retain the gamma-phase at lower temperatures.

There is an indication in the phase diagram of possible superlattices at the Cu_3Mn and Cu_5Mn stoichiometric compositions. Their presence implies the strong tendency of alloys in this composition range to develop atomic short range order.

The metallurgy of alloys with more than ~72 at% Mn becomes complicated by a

Phase Diagrams FIG. 4.1.1

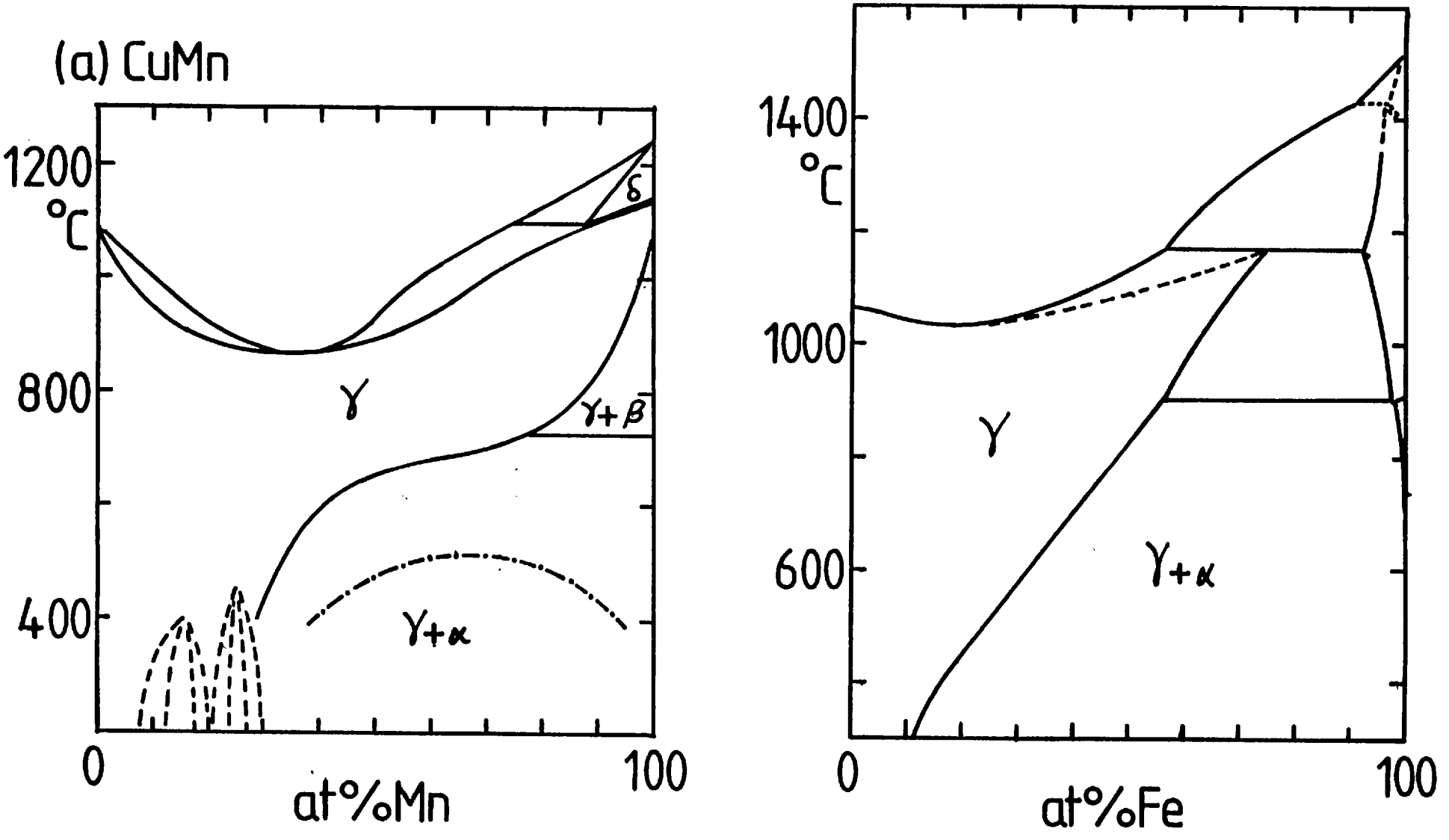

Martensitic-like structural transformation accompanying the antiferromagnetic phase transition. At the Néel point a tetragonal distortion ($c/a < 1$) of the lattice from an FCC- to FCT-structure occurs. Yeomans and McCormick (8) report that the tetragonal lattice distortion, which occurs in quenched alloys with more than $\sim$ 80 at% Mn (i.e. magnetically long-range ordered at room temperatures), is relieved by the formation of microtwins in the FCT-domain structures (observed as banding in polished sections of these alloys). The high damping capacity observed by Butler and Kelly (9) in these alloys is thought to be due to the movement of these microtwin boundaries.

It is interesting at this point to review further the findings of Yeomans and McCormick on their 38, 48 and 58 at% Mn samples. They observed in electron micrographs of polished sections of the as-quenched 88% and aged (5 hr. at 500°C) 38% alloys a mottled, tweed-like structure. Dark field microscopy of satellite spots in the electron diffraction patterns revealed a dense array of small ($d \sim 100$ Å) spherically-symmetric particles. These were observed to grow in size according to classical laws of competitive particle growth (i.e. $d \sim t^{\frac{1}{3}}$), on annealing at 500°C. Annealing of the 58% sample for 50 hr. at 400°C resulted in the appearance of a banding in the tweed structure. This was taken to be the signature of the highly-twinned FCT-domains associated with the presence of antiferromagnetic order in this aged alloy.

Gross heterogeneity resulting from the precipitation of coarse alpha-manganese particles at grain boundaries and depletion of a wide intra-granular precipitate-free zone did not occur until after very long ageing times.

Vintaykin et al (10, 11)* in a study of antiferromagnetic order in heterogeneous MnCu alloys have also observed a transitional phase preceding gross alpha-manganese precipitation. They attribute this zonal segregation phase to a metastable miscibility gap in the (gamma + alpha) - manganese region of the phase diagram (marked by the chain line in fig. 4.1.1a). It should be added parenthetically that it is questionable

* See also Vitek and Warlimont, ref. 40

whether a metastable phase boundary has a place on an equilibrium phase diagram. They deduced, from their neutron diffraction data on samples aged for 20 hr. at 400°C, that these two phases have manganese concentrations of 37 and 95 at% irrespective of the average manganese concentration of the samples (~ 45 - 95 at% Mn). They further report observing in their neutron data that antiferromagnetic order is always accompanied by the Martensitic transformation and that the magnetic order is not just confined to the manganese-rich regions, but is continuous throughout the sample. A model is postulated by them to explain the observed continuity of the magnetic order based on the structural changes occurring in the Martensitic transformation.

The state of the system is determined by competition between magnetic and structural factors of the total system free energy. At temperatures above the Néel temperature the magnetic free energy due to weak spin correlations is small; the lower free energy of a cubic lattice symmetry therefore determines the structural state of the system. As the temperature falls towards the Néel temperature the magnetic free energy increases as the spin correlations strengthen. A point is reached, at a temperature lower still, where the reduction of magnetic free energy afforded by a tetragonal distortion of the lattice symmetry more than compensates the resulting increase in structural free energy (which is relieved by the formation of microtwins as previously mentioned). This is also the Néel point, as the tetragonal distortion results in a divergence of the spin correlations marking the onset of long range antiferromagnetic order.

The above ordering process was postulated to occur in homogeneous Cu Mn alloys with greater than 72 at% Mn and in the manganese-rich regions of their heterogeneous alloys. They explain the observation that magnetic correlation lengths were at least an order of magnitude greater than the size of the manganese-rich regions by arguing that magnetic order has spread to the manganese-depleted regions. The strong coherence of

the zonal segregation phase results in the spread of the tetragonal distortion from the manganese-rich to the manganese-depleted regions of the alloy. Where, in their opinion, the induced tetragonal distortion enables the manganese-depleted regions to order antiferromagnetically and complete the continuity of the magnetic state.

Their model also enabled them to understand the lower ordering temperatures observed for the $\sim$ 50 - 60 at% Mn alloys. At lower manganese concentrations ($\sim$ 50 - 60 at% Mn) there is a lower volume fraction of the manganese-rich regions resulting in a lower total magnetic free energy. Consequently, lower temperatures are required before it becomes energetically favourable for the Martensitic transformation and the onset of long range magnetic order to occur. Vintaykin et al (12) also report reversible shape memory effects occurring (on thermally cycling above the Néel temperature) in alloys which have been plastically deformed in the Martensitic state. These effects can also be explained by the close interplay of the magnetic and structural systems of these alloys.

The preference for tetragonal symmetry in the antiferromagnetically ordered state is a feature common to a number of FCC systems. The conflicting nature of the coupling between first and second neighbour moments no doubt results in the instability of the cubic structural symmetry. This is a point that will be returned to in the next chapter.

4.1.4 Real vs. Ideal Solid Solution Alloys : the Question of Homogeneity

Ever since the commencement of studies on solid solution alloys the question of homogeneity has been the subject of controversy. The central question seems to have been to what extent are the observed magnetic properties of such alloys an artifact of inhomogeneity.

Some of the early work by Beck and co-workers (reviewed previously, Chapter 2) on the changes of magnetic properties resulting from differing metallurgical treatments

was a step towards the resolution of this controversy. The work, however, did not satisfactorily demonstrate the presence of inhomogeneity in rapidly quenched solid solution alloys. It sufficed to show that effects in magnetic properties like the susceptibility cusp and Curie-Weiss-like behaviour of the high temperature susceptibility were attributable to inhomogeneity, which was enhanced by annealing and diminished by cold working treatments of their alloys.

The first direct evidence to answer this question awaited the development of X-ray and Neutron diffuse scattering techniques. The early X-ray diffraction work of Warren and Averbach (13) and Cowley (14, 15) on the subject of order-disorder transitions in binary solid solution alloys formed the basis for analysis of diffuse scattering data. The degree of inhomogeneity could be expressed in terms of a Warren-Cowley atomic correlation parameter, α_i, defined in 4.1.

$$\alpha_i = 1 - \frac{p_i}{x} \qquad 4.1$$

where p_i is the probability of finding an A atom in the i-th neighbour shell surrounding a B-atom and x is average atomic fraction of B atoms in the binary alloy. A positive value of α_1(the first neighbour shell atomic correlation parameter) indicates a preference for like neighbours usually termed : clustering, and the converse indicates a preference for unlike neighbours usually termed : short range order (SRO). The correlation parameters are obtained by fourier analysis of the diffuse scattering intensity in reciprocal space.

Sundahl et al (16) used the X-ray diffuse scattering technique to study the effects of local atomic order on the magnetic properties of a Au-25at% Fe alloy. The alloy, which had been quenched in silicone oil after a $\frac{1}{2}$ hr. solution treatment at 900°C, showed some SRO with an $\alpha_1 = -0.061$. After an anneal at 75°C for 70 days, the alloy showed less SRO with an $\alpha_1 = -0.024$, indicating that some clustering had

occurred. Resistivity measurements on a thin foil sample receiving the same heat treatment showed a 25 K increase of its Curie temperature in the quenched state (T_c = 283 ± 5 K) when it was annealed. A study by Sundahl et al (17) of a range of quenched Au Fe alloys showed similar freezing or Curie temperature increases after ageing treatment, with the largest increases occurring around ~17 at% Fe.

Borg and Dienes (18) reported observing clustering in Au Fe alloys which had been produced by 14 MeV neutron radiation-enhanced diffusion. More recently Zibold (19) reported susceptibility measurements on low-temperature (T ~ 14 K) quench-condensed Au Fe films with 2-12 at% Fe. The cusps in susceptibility measurements on these films were more rounded and occurred at significantly lower temperatures than for the equivalent bulk quenched alloys. These effects were attributed by Zibold to the more ideally random nature of the atomic distributions in his films. However, such cold-substrate vapour condensation techniques are used to produce amorphous films (see, for example, Raeburn and Aldridge, ref. 20). A comparison of properties of these films to those of bulk polycrystalline alloys may therefore be unreasonable.

The X-ray atomic scattering factors of copper and manganese are insufficiently different to allow adequate resolution of atomic correlations in Cu Mn alloys. However the early neutron work on copper-rich Cu Mn alloys by Meneghetti and Sidhu (21) and Arrott (22) reported the presence of a broad peak in the diffuse scattering at the ($\frac{1}{2}$ 1 0) position. Arrott attributed the diffuse peak to atomic SRO in his well annealed single-crystal 5-15 at% Mn alloys. In contrast, Meneghetti and Sidhu interpreted the temperature dependence of the neutron scattering form factors of their alloys as evidence for magnetic SRO being responsible for the diffuse peak. Sato et al (23) concluded that atomic and magnetic SRO were probably both responsible for the diffuse peak, but reliable separation of these terms would have to await polarisation analysis. Sato et al also deduced from the width of the diffuse peak a correlation length for the SRO of 2-3

FCC unit cell lengths in 10 - 25 at% Mn alloys. They showed that the SRO was not suppressed by rapid quenching and its correlation length was not very different in their aged alloys.

More recently Davis et al (24,25) have used polarisation analysis of their diffuse neutron scattering data to examine the spin correlations in a range of Cu Mn alloys. Quenched, polycrystalline Cu Mn samples showed atomic SRO for concentrations below $\sim$ 60 at% Mn, peaking around 45 at% Mn with $\alpha_1 \sim -0.09$, changing over to clustering above $\sim$ 60 at% Mn with $\alpha_1 \sim 0.04$ at 75 at% Mn.

In conclusion, a small degree of inhomogeneity has been observed in rapidly quenched Au Fe and Cu Mn alloys of compositions similar to those studied in this work. It was noted in an earlier chapter that purely statistical concentration fluctuations in an ideal random alloy, arising as a consequence of its discrete nature, result in inhomogeneity. Metallurgical treatment of solid solution alloys appears only to have a quantitative effect on their magnetic properties, i.e. changes in the size of, and temperature at which the cusp in the low-field susceptibility occurs in copper-rich Cu Mn and gold-rich Au Fe alloys. Qualitatively, the details of the magnetic ordering are unlikely to have been significantly changed by the presence of the degree of inhomogeneity observed in quenched solid solution alloys.

4.2 Sample Preparation and Treatment

Samples were prepared from appropriate amounts of high purity elements to have heat capacities of at least 2 - 3 times the addenda heat capacity over the range of temperatures under investigation. The source and purity of the elements used in all samples are as listed below :

Y, Gd	Rare Earth Products	3N
Au, Cu	Johnson Matthey 'Specpure'	5N
Fe, Ni, Mn	" " "	4N5

Exceptions to these are the Cu - 60 at% Mn alloy whose manganese (4N5 purity) was obtained from Koch Light and the Au - 22 at% Fe alloy whose gold content was supplemented by 2g of 3N purity material supplied by Johnson Matthey.

The elements of each sample were arc-melted together on a water cooled copper hearth under a pure argon atmosphere. The button-shaped samples were inverted and remelted several times to improve homogeneity. The weight losses incurred during melting were $<0.1\%$ for the Y Gd alloys, typically 0.5% for the Au Fe alloys and 1% for the Cu Mn alloys. In the case of the Cu Mn alloys the high volatility of the manganese was probably responsible for the higher losses, although precautions were taken to avoid excessive Mn vaporisation. No significant tarnish of the titanium getter button was observed during the preparation of these samples.

At this stage the Au Fe and Cu Mn alloys were lightly cold-worked into the required shape. Approximately parallel flats on the top and bottom surfaces of the buttons were finished by spark planing. The Au Fe and Cu Mn alloys were sealed in evacuated quartz capsules for the following solution treatments :

Cu - 30 at% Mn	24 hr. at 750°C
Cu - 60 at% Mn	48 hr. at 800°C
Cu - 65 at% Mn	72 hr. at 800°C
Cu - 70 at% Mn	72 hr. at 850°C
Au Fe : all alloys	$>$ 60 hr. at 900°C

All alloys were rapidly quenched by plunging them directly from the hot furnace into cold water after solution treatments. A short solution treatment of not less than 2 hr. at the appropriate temperature followed by water quenching was given to some

of these alloys prior to repeat determinations of their specific heat.

An electron microprobe analysis (~ 1 μm resolution) of the as-cast Au-22 at% Ni alloy revealed no significant segregation into Au- and Ni- rich phases as might have been expected from the presence of a miscibility gap in the phase diagram of this alloy (1). However, the small separation of the liquidus and solidus lines indicated that the composition variation of the as-cast alloy was likely to be small; consequently, the Au - 22 at% Ni alloy received no heat treatment.

Any surface oxide contamination which had developed on the Cu Mn and Y Gd alloys was removed by a brief etch in aqua regia diluted by an equal volume of water. The top and bottom surfaces of all samples were given a final polish with fine wet carborundum paper. The Au Fe, Au Ni and Cu Mn alloys were then stored until required under liquid nitrogen.

Average mole formula weight, A, and atomic fraction of the i-th element, x_i, were calculated using 4.2 and 4.3

$$1/A = \sum_i {}^{w_i}/_{A_i} \qquad \text{where} \qquad \sum_i w_i = 1 \qquad 4.2$$

$$x_i = \frac{{}^{w_i}/_{A_i}}{\sum_j {}^{w_j}/_{A_j}} = \frac{A}{A_i} \cdot w_i \qquad 4.3$$

A_i, A_j and w_i, w_j refer to the atomic weight, and weight fraction of the i-th and j-th elements respectively.

The compositions of the Y Gd and Cu Mn alloys were determined by chemical analysis; nominal compositions were taken for the Au Fe alloys. Compositional accuracies were estimated to be ± 0.02 at% for the Y Gd, ± 0.1 at% for the Au Fe and ± 0.1 - 0.2 at% for the Cu Mn alloys.

4.3 Presentation of Specific Heat Results

4.3.1 General Remarks

The specific heat results obtained on the three alloy systems are presented as plots of C/T against T^2. All results for the Au Fe and Cu Mn (except the 30 at% Mn alloy) were calculated using fits to thermometer calibration B. These results may therefore show the same systematic errors above T ~ 10 K as were observed in the copper calibration results calculated using the same thermometer fits. Error bars indicated in the plots are ± 3% below T ~ 10 K and ± 5% above.

Earlier measurements on the Au - 20 - 24 at% Fe and Cu - 60 at% Mn alloys agreed, within the estimated experimental accuracy, with the more recent measurements. The agreement of the two Cu - 60 at% Mn determinations was so good that it cast some doubt on the explanation given earlier to account for the large systematic error observed above T ~ 10 K in measurements on the copper calibration sample. However, the agreement is more likely to be fortuitous as systematic shifts were often observed in the high temperature data of these earlier measurements.

The low temperature data in the range $2.45 < T < 3.6$ K of all samples, calculated using fits to thermometer calibration B, showed similar systematic deviations. Difficulties with thermometer calibration in this temperature range were evidently responsible for this systematic error. The problem was likely to be partly due to the poor resolution of the helium vapour pressure gauge and partly due to significant thermal gradients in this temperature range. The systematic deviations of the as-plotted data in this temperature interval were smoothed out using a procedure which assumed a calibration error of ϵ_T = 1% at T ~ 2.5 and 3.5 K and 2% at T ~ 3 K. The corrections were performed on the molar specific heat data using the factors illustrated in fig. 3.4.1 (c).

4.3.2 The Au Fe Alloys

The specific heat data obtained for the seven Au Fe alloys and a Au - 22 at% Ni

alloy are presented in fig. 4.3.1. A separate plot (fig. 4.3.2) of the low temperature ($T < 4.5$ K) data also includes the results of Dreyfus et al (26) for an 8 at% Fe alloy. The low temperature data for the 16 at% Fe alloy were insufficient to warrant plotting fig. 4.3.2 but an estimated value of C/T at $T^2 = 5$ (in K^2) was included in fig. 4.3.3 with an appropriately larger error bar of $\pm 5\%$.

The high temperature data in fig. 4.3.1 show no marked change of character over the composition range 14 - 28 at% Fe. The specific heat of all the alloys increases monotonically with temperature and resembles the data obtained on the behaviour of the Au Ni alloy. No anomalies of any significance are observed, similar behaviour was reported by Wenger and Keesom (27) on their 1 and 8 at% Fe alloys.

The low temperature data in fig. 4.3.2 show small but definite deviations from a simple $\gamma T + \beta T^3$ relationship. For this reason it was considered inappropriate to fit a straight line to the data in an attempt to extract effective values of γ and θ_D. Such approaches can obscure the interpretation of the data by analysing them in the framework of an unrealistic model and attaching more significance than perhaps should be to the effective γ and θ_D values thus obtained.

The total specific heat is a complex mixture of contributions from excitations of the electron, phonon and spin systems of the alloy and their interactions. Whilst a separation of electron and phonon terms of the specific heat of a simple, pure, non-transitional metal may be possible it would be inappropriate to attempt such an analysis of the Au Fe specific heat data. It was therefore considered best to plot the total specific heat at a fixed temperature low enough for the likely phonon contribution to be small and vary insignificantly with composition.

The composition dependence of the total specifc heat of the Au Fe alloys considered in this work and those of Dreyfus et al (26) are plotted as C/T at the

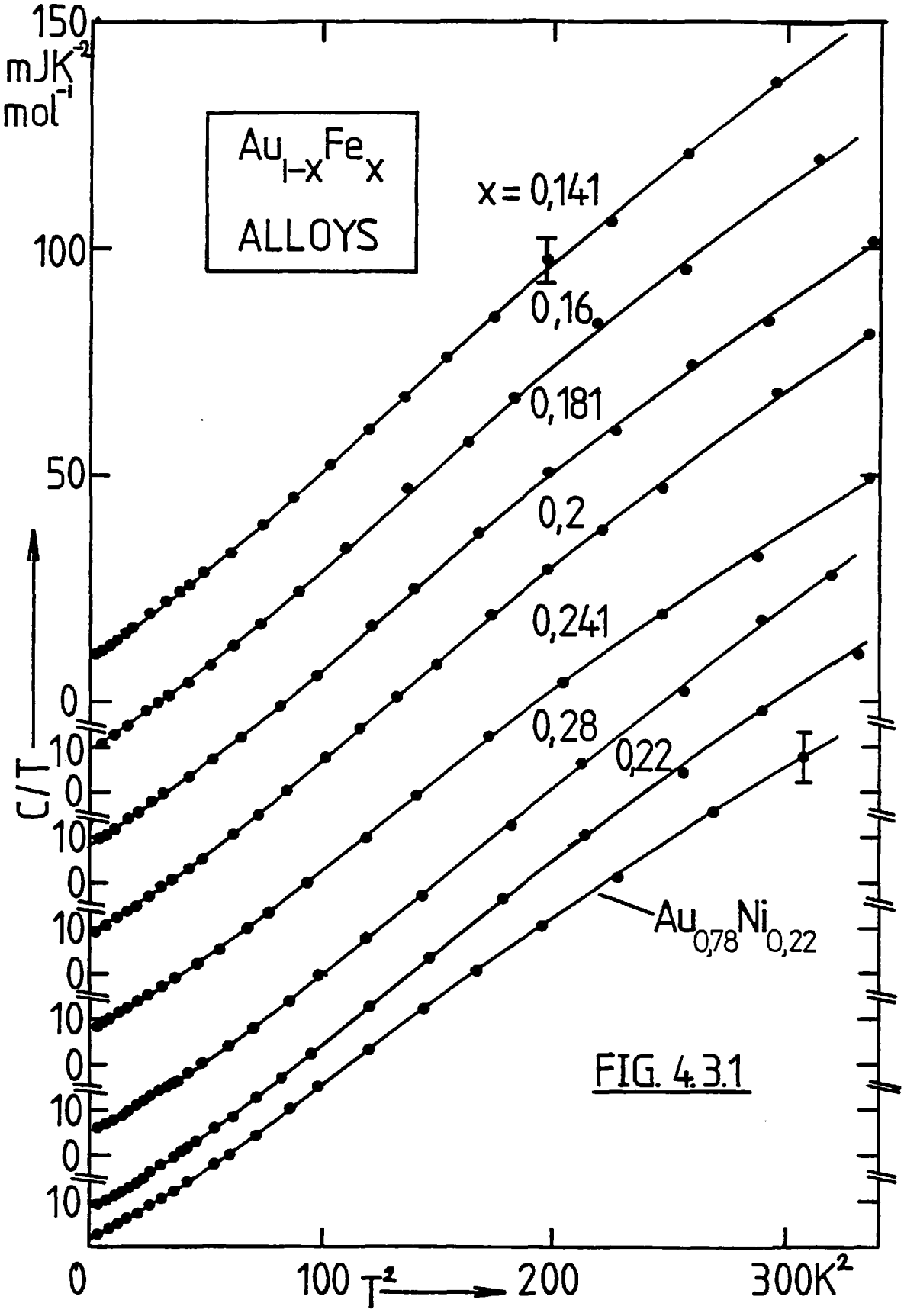
150
mJK⁻²
mol⁻¹
100
50
0
10
0
10
0
10
0
10
0
10
0
10
C/T
Au1-xFex
ALLOYS
x = 0,141
0,16
0,181
0,2
0,241
0,28
0,22
Au0,78Ni0,22
0
100 T² ⟶ 200
300K²

FIG. 4.3.1

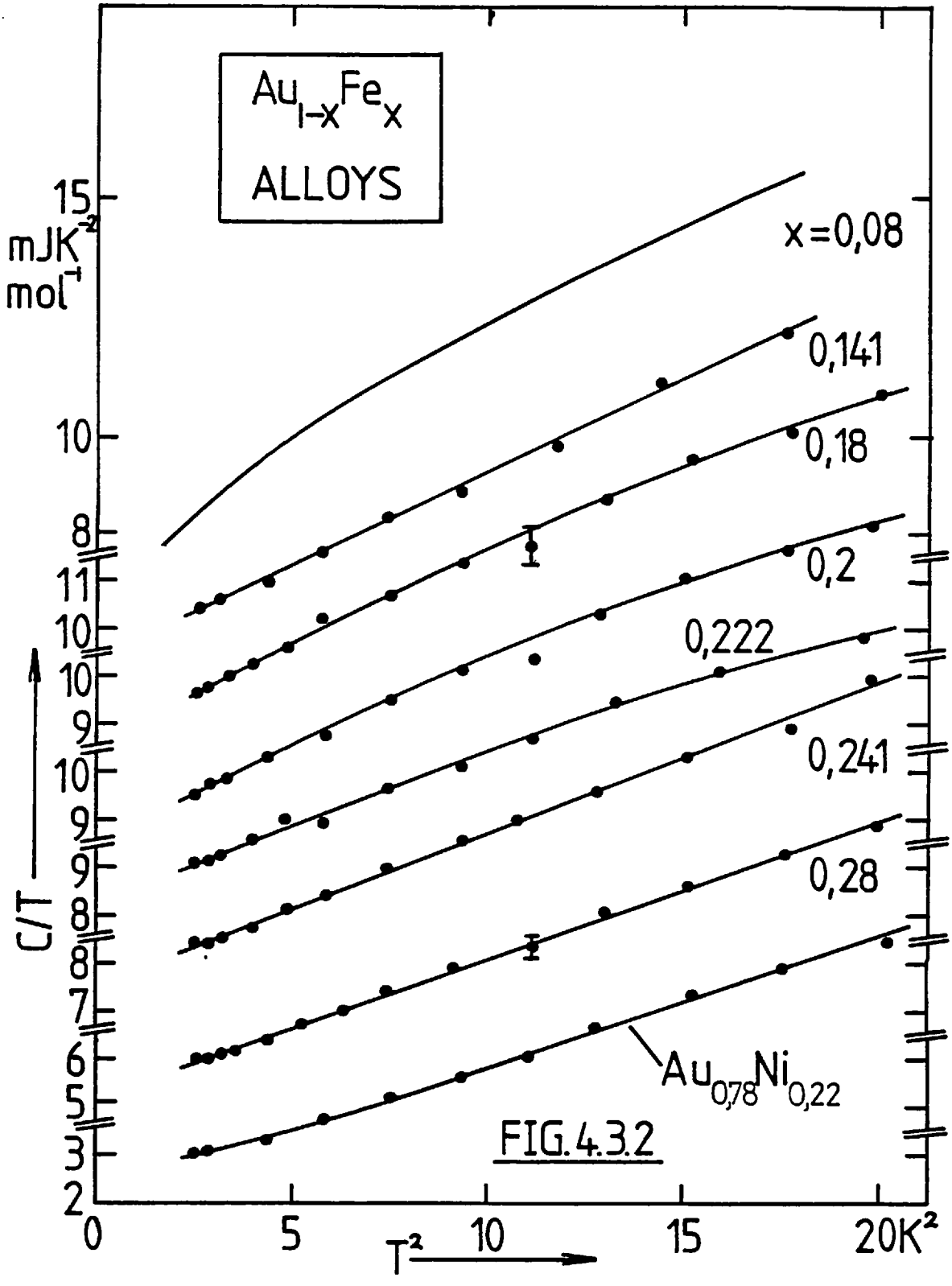
Au1-xFex
ALLOYS
x=0,08
0,141
0,18
0,2
0,222
0,241
0,28
Au0,78Ni0,22
C/T
mJK-2 mol-1
T2
0
5
10
15
20K2
15
10
8
11
10
10
9
10
9
9
8
8
7
6
5
3
2

FIG. 4.3.2

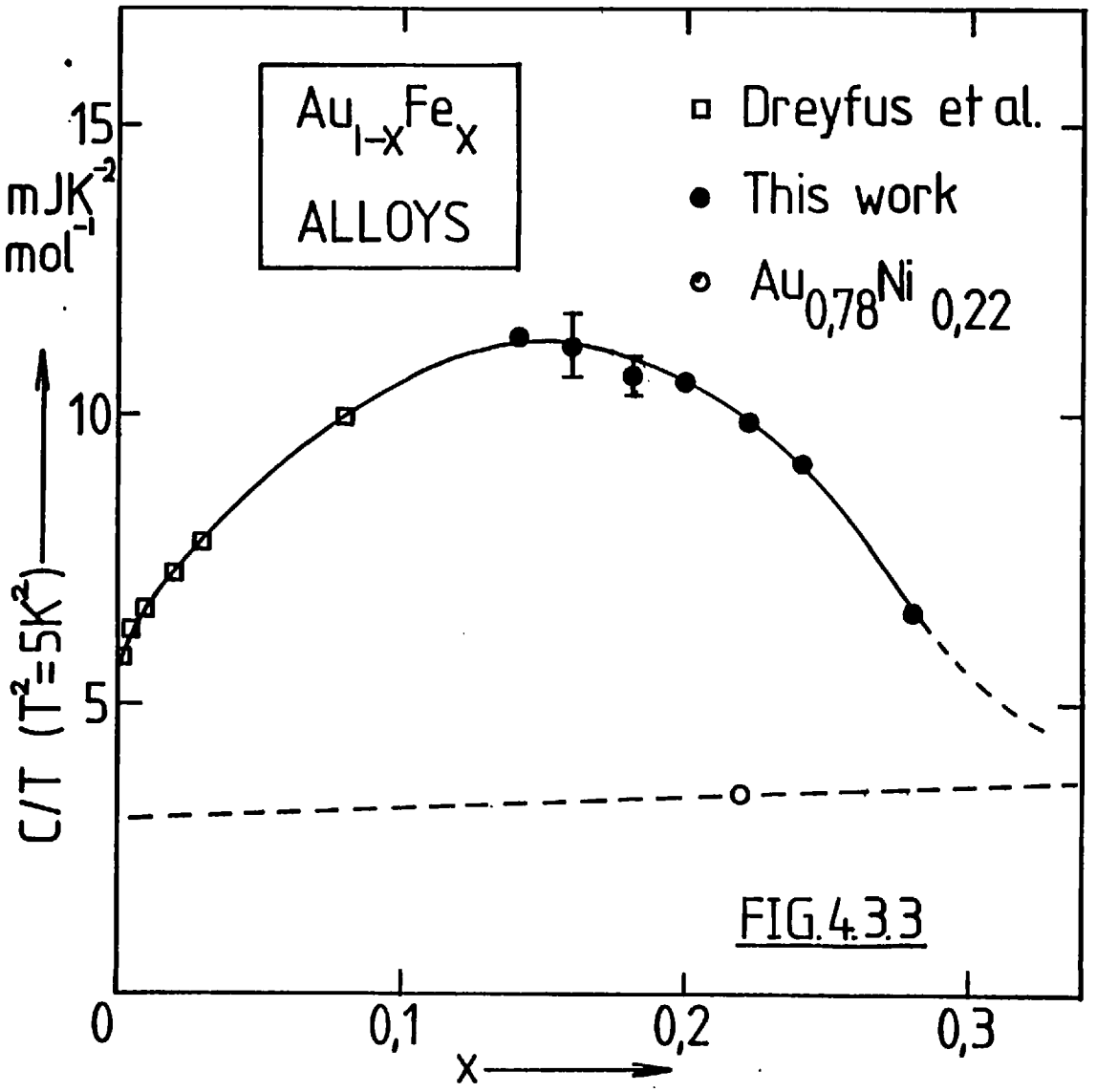
$Au_{1-x}Fe_x$
ALLOYS
Dreyfus et al.
This work
$Au_{0,78}Ni_{0,22}$
15
10
5
0
0,1
0,2
0,3
x
C/T (T^2=5K^2)
mJK^{-2} mol^{-1}

FIG. 4.3.3

fixed temperature of T^2 = 5 (in K^2) in fig. 4.3.3. The agreement with data obtained on alloys in the composition range 14 - 26 at% Fe by Whitehurst and Crangle (28) is reasonably good considering the $\pm$ 8% scatter in their low temperature data. The total specific heat at T^2 = 5 (in K^2) is observed to rise gradually from the low concentration spin glass regime to a shallow peak around the critical concentration ($\sim$ 16 at% Fe) for long range ferromagnetic order. The total specific heat then falls gradually, almost as a quadratic function of concentration, until $\sim$ 28 at% Fe when it appears to begin to level off at a value comparable with the expected total lattice and electronic specific heat.

The Au Ni Alloy

The Au - 22 at% Ni alloy was expected to be comparable in lattice character to the Au Fe alloys but should have no local moments. The broken line in fig. 4.3.3 indicates the likely electronic and lattice contributions to the total specific heat.

Kuentzler and Kapper (29) quoted a $\gamma = 1.64$ mJ $K^{-2}mol^{-1}$ and $\theta_D = 185.2K$ obtained by extrapolation of their measurements in the temperature range $6.5 < T < 10.5K$ on a Au - 20 at% Ni alloy. These results correspond to a value for C/T at T^2 = 5 (in K^2) of 3.17 mJ K^{-2} mol^{-1} which is 9% lower than the value obtained for the Au Ni alloy of this work. However, an earlier publication by Kuentzler (30) clearly showed the data for a Au - 20 at% Ni alloy to deviate from linearity below T $\sim$ 5 K unlike the later publication, where the data is shown to be linear up to T $\sim$ 12 K. In view of this confusion and their procedure of extrapolating the higher temperature data to obtain γ and θ_D values, it is not too surprising that there is such a discrepancy between the values of C/T at T^2 = 5 (in K^2).

An attempt was made to extract the magnetic contribution to the specific heat of the Au - 22 at% Fe alloy by subtracting of the total specific heat of the Au - 22 at% Ni alloy. The Debye temperatures of nickel and iron in their BCC forms are 473 K and

477 K respectively. If this similarity remains on alloying with gold in an FCC structure, then the specific heat of a Au Ni alloy should be a reasonable measure of the lattice contribution to the total specific heat of a Au Fe alloy of equivalent composition.

The resulting specific heat difference, $\Delta C = C_{Au\,Fe} - C_{Au\,Ni}$, was essentially linear in T with $\Delta C/T = 6.45 \pm 0.25\ mJ\,K^{-2}\,mol^{-1}$ up to $T \sim 6\,K$, then showing a higher order T dependence above $T \sim 6\,K$. However, a glance at the specific heat curves for these two alloys in fig. 4.3.1 indicates that the apparent divergence of the two curves above $T \sim 6\,K$ is likely to be the result of larger subtraction errors. Extrapolation of the linear term to very low temperatures indicates that there may be a power law dependence on T below $T \sim 0.2\,K$.

An estimate of the total entropy associated with the magnetic specific heat, assuming a continuation of the linear dependence at higher temperatures, would imply that all the moments do not become fully disordered until $T \gtrsim 300\,K$. The remaining entropy below $T \sim 4\,K$ is equivalent to $\sim 1\%$ of the total $cR\ln(2J+1)$ value (assuming $J = 1.5$ for an alloy of this Fe concentration).

Measurements in a Magnetic Field

Relative changes in specific heat can be measured to a much greater degree of accuracy by steady state relaxation calorimetry, a resolution of 1% should have been easily obtainable. This feature of relaxation calorimetry makes it particularly amenable to measurement of specific heat in a magnetic field.

Preliminary specific heat measurements were made on the 16 and 22 at% Fe alloys in magnetic fields up to $B \sim 0.4$ Tesla. The measurements were made in one of two possible modes : (a) cooling from $T \sim 60\,K$ (highest obtainable temperature) and measuring in a continuous field of $B = 0.14$ Tesla, (b) cooling in zero-field and measuring in fields up to $B \sim 0.4$ Tesla. Results of measurements in the temperature

range 2 - 10 K on the 22 at% Fe alloy, taken after field cooling (mode : a), were indistinguishable from measurements made in zero-field. Similarly, no field dependence was observed in measurements made in the temperature range 5 - 15 K on either of the alloys after zero-field cooling (mode : b). Since the magnetic fields employed were rather small (with an interaction energy equivalent to the thermal energy at $T \sim 0.5$ K) the insensitivity of the specific heat is perhaps not surprising.

Nieuwenhuys and Mydosh (31) reported observing at $T \sim 2$ K no significant change of specific heat of a Au - 4 at% Fe alloy in fields up to 2 Tesla. However, they observed that the thermal relaxation rate of the sample at temperatures in the range 1.3 - 3.9 K, after the application or removal of a 2 Tesla magnetic field, exhibited an inverse time dependence (i.e. $Q \propto 1/t$) in apparent agreement with Monte Carlo simulations of dynamical spin glass behaviour.

4.3.3 The Cu Mn Alloys

The results of specific heat measurements made on the four Cu Mn alloys are presented in fig. 4.3.4. A separate plot of the low temperature ($T < 4.5$ K) data is given in fig. 4.3.5. The compositional dependence of the total specific heat at $T^2 = 5$ (in K^2) is plotted together with the data of Zimmerman, Hoare and Sato (32, 33) in fig. 4.2.6. The arrow indicates the critical concentration of ~72% manganese established by the neutron work of Cowlam et al. (34).

The measurements for the 30 at% Mn alloy were made with the calorimeter in its original configuration. The results are a combination of two experimental determinations, one above and one below $T \sim 4.2$ K. The rest of the alloys were measured with the calorimeter in its present configuration analysed using fits to thermometer calibration B.

The high temperature results (fig. 4.3.4) again show a monotonic increase with

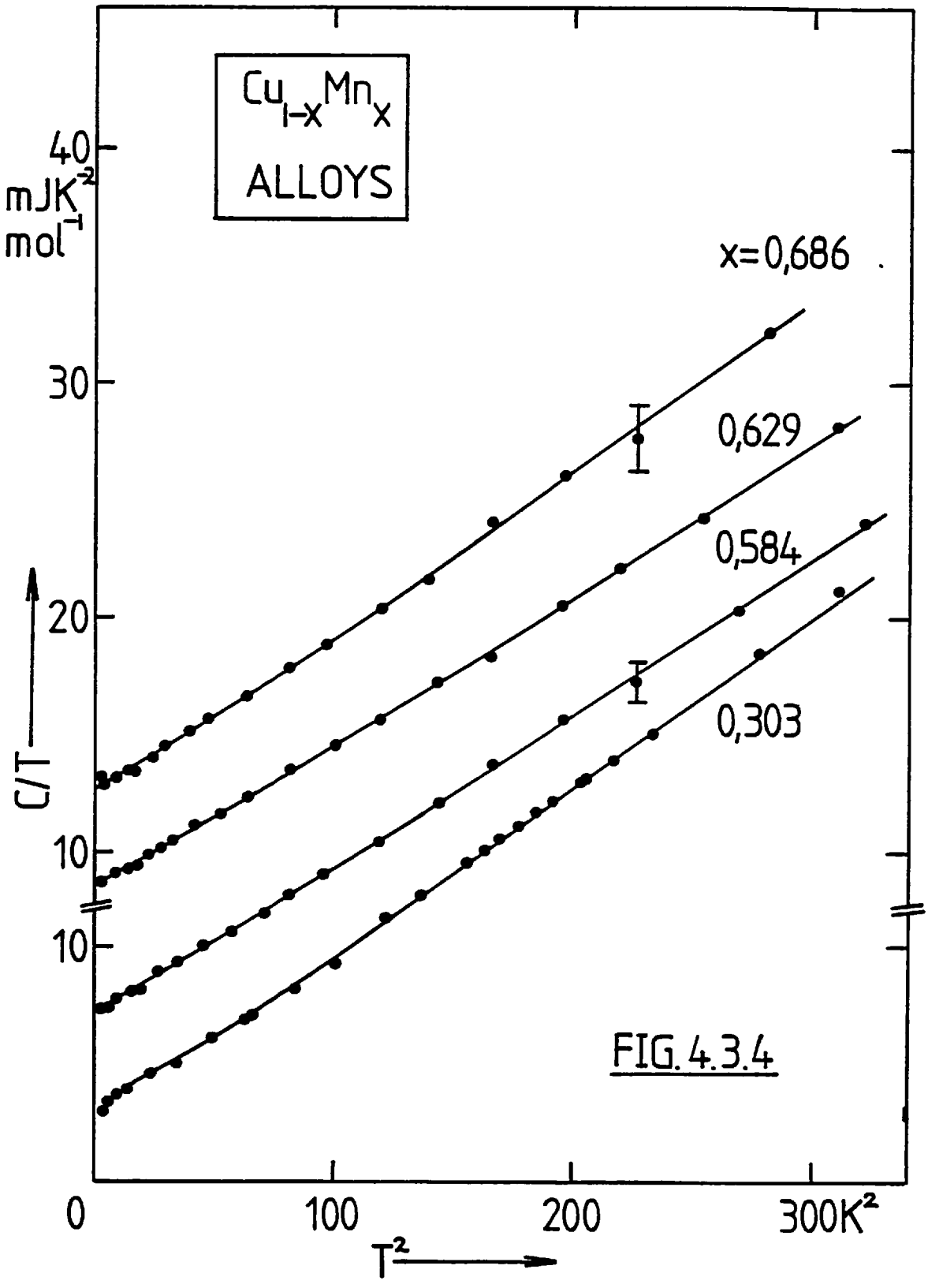
$Cu_{1-x}Mn_x$
ALLOYS
x=0,686
0,629
0,584
0,303
40
30
20
10
10
C/T
mJK^{-2}
mol^{-1}
0
100
200
300K²
T^2

FIG. 4.3.4

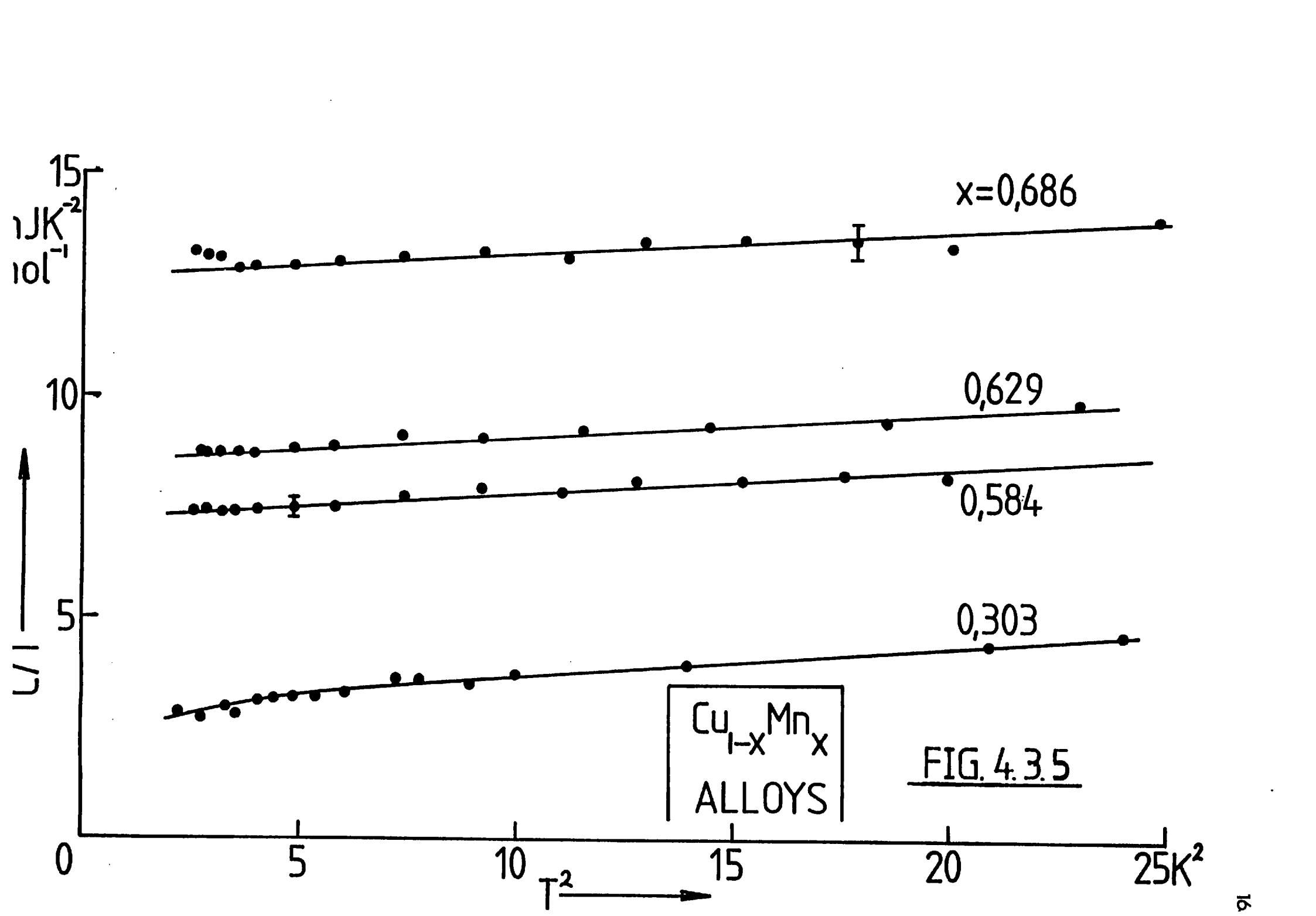

FIG. 4.3.5

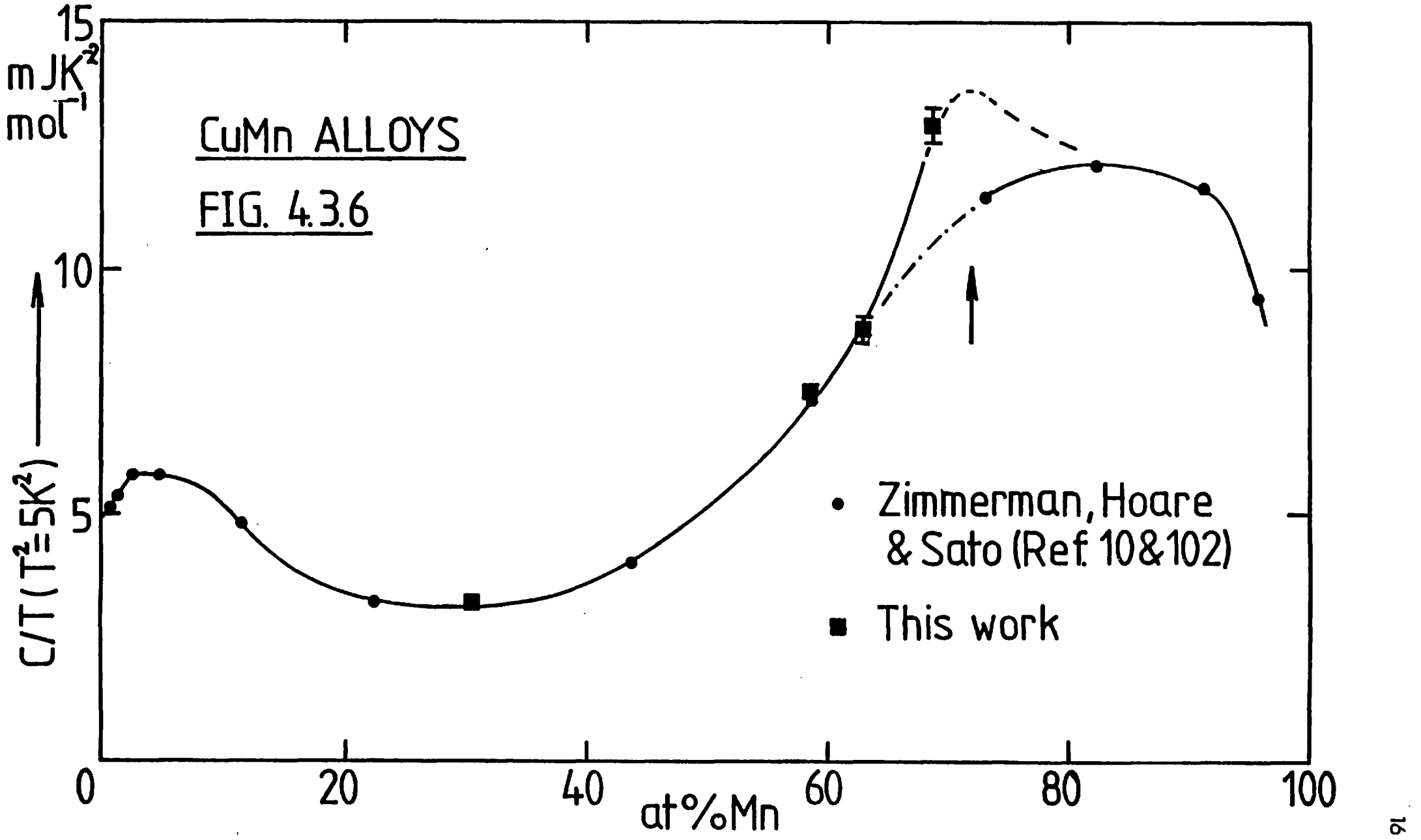
CuMn ALLOYS
FIG. 4.3.6
15
10
5
0
20
40
60
80
100
at%Mn
mJK⁻²mol⁻¹
C/T (T²=5K²)
Zimmerman, Hoare & Sato (Ref. 10&102)
This work

temperature and no indications of any significant anomalies. Although the data of the 30 at% Mn alloy seems to exhibit a small, broad anomaly below $T \sim 9$ K. Extrapolating the high temperature data for this alloy to low temperatures and subtracting it from the actual low temperature data reveals an anomaly peaking at $T \sim 3$ K with associated entropy $\Delta S \sim 5$ mJ K^{-1} mol^{-1} which is approximately 0.1% of the theoretical $cR \ln (2J + 1)$ value (assuming $J = 2$). However, it is unlikely that it represents a real effect in view of the uncertainty in the high temperature data and the questionable assumption that an extrapolation to lower temperatures of this data gives the non-magnetic specific heat.

The low temperature results (fig. 4.3.5) are again very similar in nature to those of the AuFe alloys, except perhaps for their more linear character. The slight turn-up of the data below $T \sim 2$ K for the 70 at% Mn alloy is perhaps noteworthy, even though it is not significantly greater than the estimated experimental error. It may be associated with the proximity of the critical concentration, since all the Cu Mn alloys with greater than 73 at% Mn of the Zimmerman and Sato work (32) exhibited similar turn-ups.

The total specific heat at $T^2 = 5$ (in K^2) plotted as a function of manganese concentration in fig. 4.2.6 exhibits a small maximum in the spin glass regime ($C \lesssim 10$ at% Mn). It then falls to a shallow minimum around 25 at% Mn before rising sharply to a second; larger maximum around the critical concentration of ~ 72 at% Mn (marked by the arrow in the figure) for long range antiferromagnetic order. The total specific heat then remains largely unchanged until beyond ~ 90 at% Mn before beginning to fall again. The peaking of the total specific heat around the critical concentration is again observed as in the case of the AuFe alloys.

4.3.4 The YGd Alloys

Specific heat measurements were made on the two YGd alloys with compositions

of 2 and 3.4 at% Gd. The full results are presented in fig. 4.3.7, together with the data of Wells et al. (4) for pure yttrium. An enlargement of the lower temperature data is shown in fig. 4.3.8, the peaks of the anomalies are indicated by arrows at the temperatures 6.4 ± 0.15 K and 12.8 ± 0.6 K for the 2 and 3.4 at% Gd alloys respectively.

These measurements were made with the calorimeter in its earlier configuration. The small low-temperature thermal diffusivity of these alloys was responsible for unfavourably large internal thermal relaxation time-constants and unfortunately prevented measurements being taken below 4.2 K.

The differential specific heat ΔC, defined by 4.4, is scaled by the Gd-concentration c (in at%) and plotted as a function of the scaled temperature T/c in fig. 4.3.9.

$$\Delta C = C_{ALLOY} - C_{PURE\ YTTRIUM} \qquad 4.4$$

The arrow in fig. 4.3.9 indicates the position of the anomaly peak of $\Delta C/c = 90\ mJ\ K^{-1}\ mol.\%^{-1}$ at $T/c = 3.2\ K\%^{-1}$ for the 2 at% Gd alloy.

A plot of $\Delta C/T$ against T is given in fig. 4.3.10 for the 2 at% Gd alloy. Assuming ΔC is the magnetic specific heat, then $\Delta C/T$ should be equivalent to the temperature derivative magnetic entropy $\partial S/\partial T|_H$. An integration of $\Delta C/T$ over the temperature range of the anomaly therefore gave the total magnetic entropy associated with it.

$$S_m = \int_0^\infty \frac{\Delta C}{T} dT \qquad 4.5$$

Suitable extrapolations of the $\Delta C/T$ data to low and high temperatures were made to obtain an estimate of S_m; these are marked by broken lines in fig. 4.3.10.

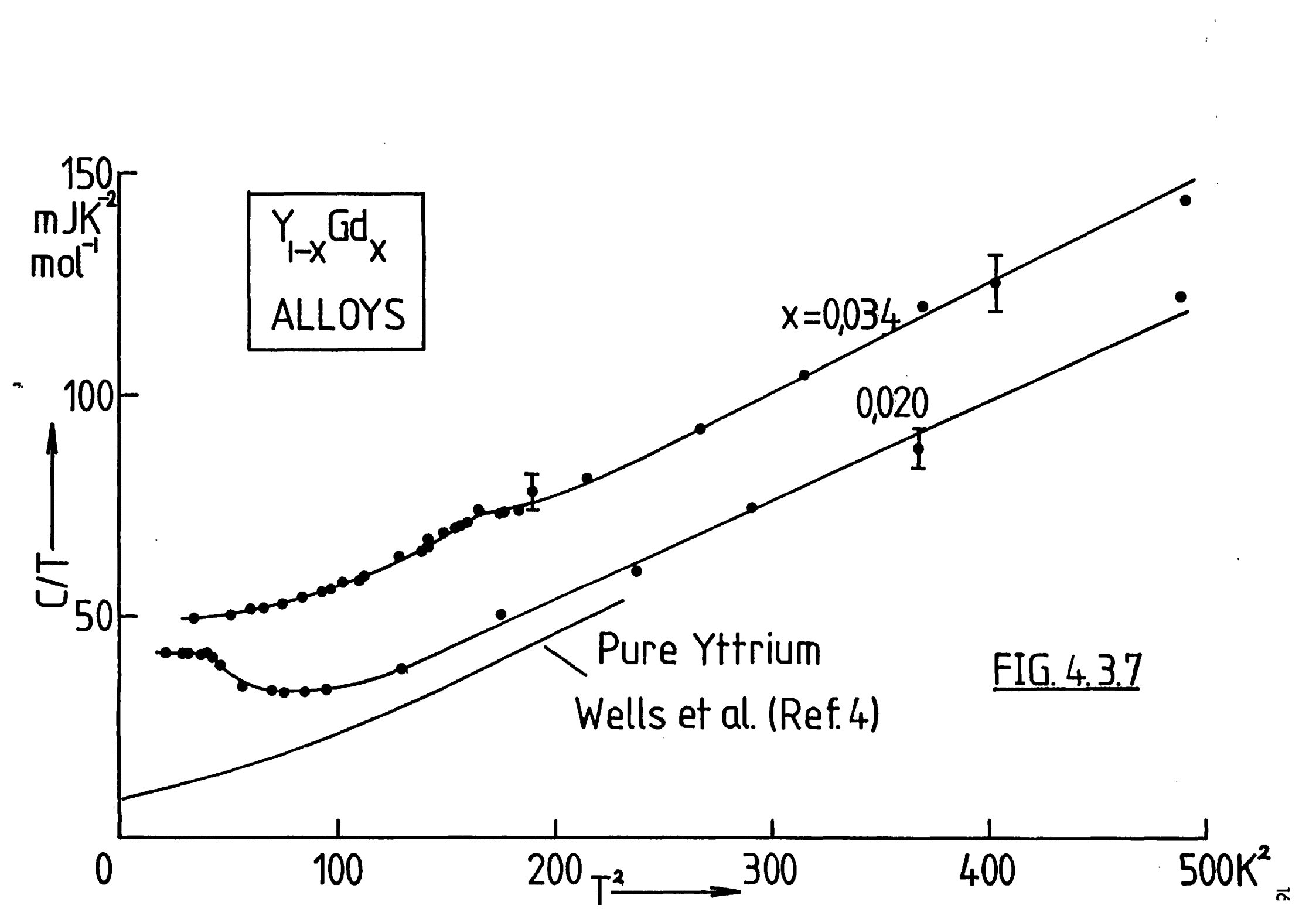
150
mJK⁻²
mol⁻¹
100
50
C/T
Y1-xGdx
ALLOYS
x=0,034
0,020
Pure Yttrium
Wells et al. (Ref. 4)
0
100
200
300
400
500K²
T²

FIG. 4.3.7

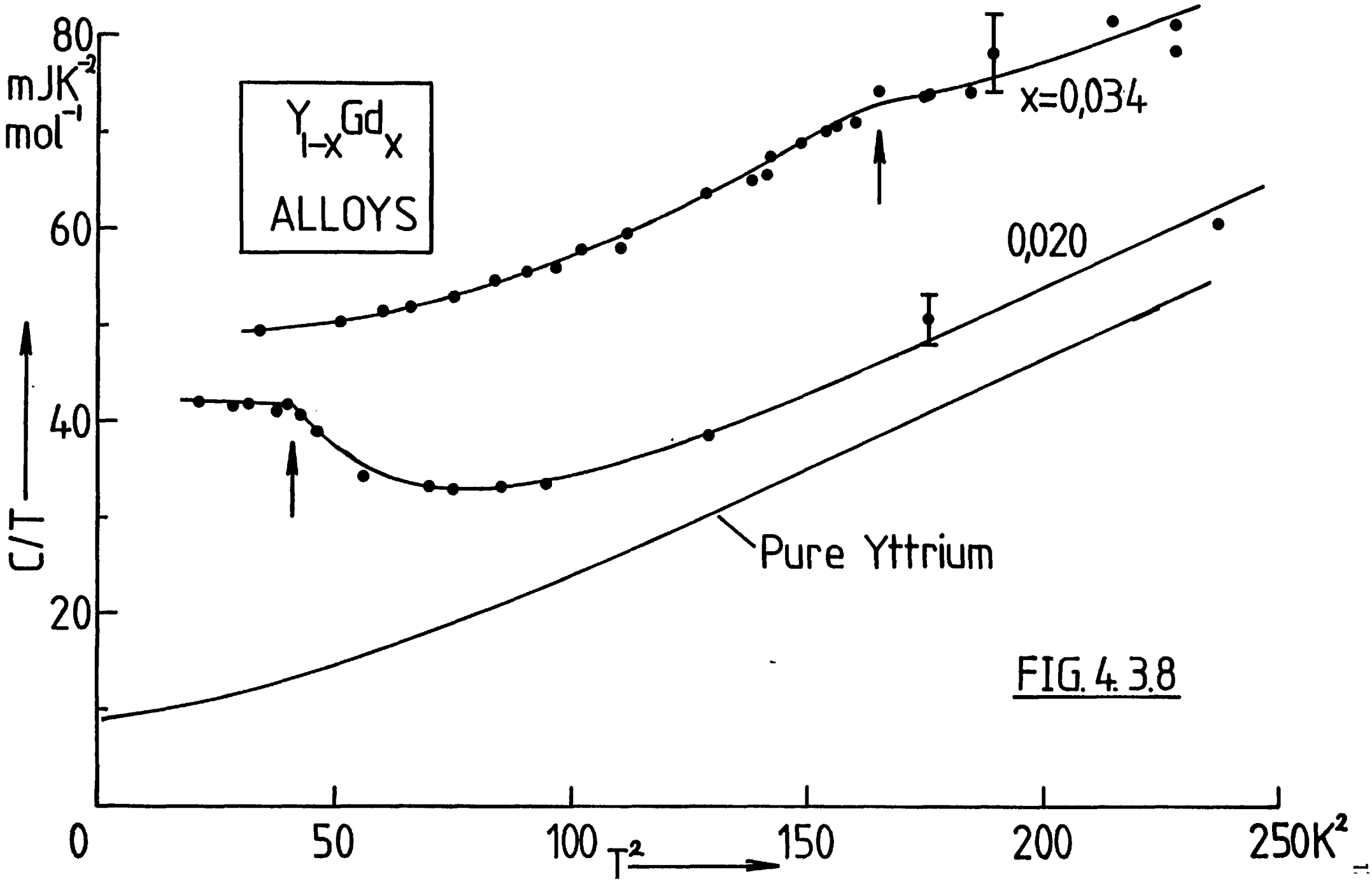
80
mJK⁻²
mol⁻¹
60
40
20
C/T
Y1-xGdx
ALLOYS
x=0,034
0,020
Pure Yttrium
0
50
100
150
200
250K²
T²

FIG. 4.3.8

The tail of the anomaly in $\Delta C/T$ was found to fit the simple power law, given in expression 4.6, over the temperature range $6.5 < T < 15K$

$$\Delta C/T = A_0 + A_1 (T_0/T)^3 \qquad 4.6$$

$T_o = 6.4K$ is the temperature of the anomaly peak, $A_o/c = 1.9\,mJ\,K^{-2}mol^{-1}at.\%^{-1}$ and $A_1 T_o = 0.16\,J\,K^{-1}mol^{-1}$. The former result is in good agreement with the Bonnerot (35,36) data, whereas the latter result and the value of T_o differ significantly. Although the more recent data of Levesque et al (37) ($T_o \sim 5.4K$) suggest that the discrepancy is not so great. The configurational entropy associated with the anomaly tail, obtained by integrating expression 4.6 (without the A_o term) between the temperature limits $T_o < T < \infty$ was $\sim$23% of the $cR \ln (2J + 1)$ assuming $J = 7/2$ (the Gd^{3+} free ion value). A further configurational entropy change of $\sim$ 53% of $cR \ln (2J + 1)$ was estimated to occur below the anomaly peak by making a suitable extrapolation of the data. The total measured configurational entropy amounts to only $\sim$ 76% of $cR \ln (2J + 1)$. If the tail of the specific heat anomaly has a temperature dependence of $\sim 1/T$ as suggested by Wenger for a $\underline{Y}Dy$ alloy (see Chapter 2) rather than a Schottky-like $1/T^2$ dependence then all the configurational entropy can be accounted for. The results are not sufficiently accurate at high temperatures to resolve this speculation. The value of T_o for the Y 3.4 at.% Gd alloy is reasonably consistent with the susceptibility and resistivity data of Sarkissian and Coles (38,39).

The measurement problems which restricted the results to temperatures above 4.2K may have been partly responsible for the peak in the data for the 2% alloy occurring at a significantly higher temperature than observed by other researchers. No further conclusions will therefore be drawn from these early measurements due to the uncertainty of the data.

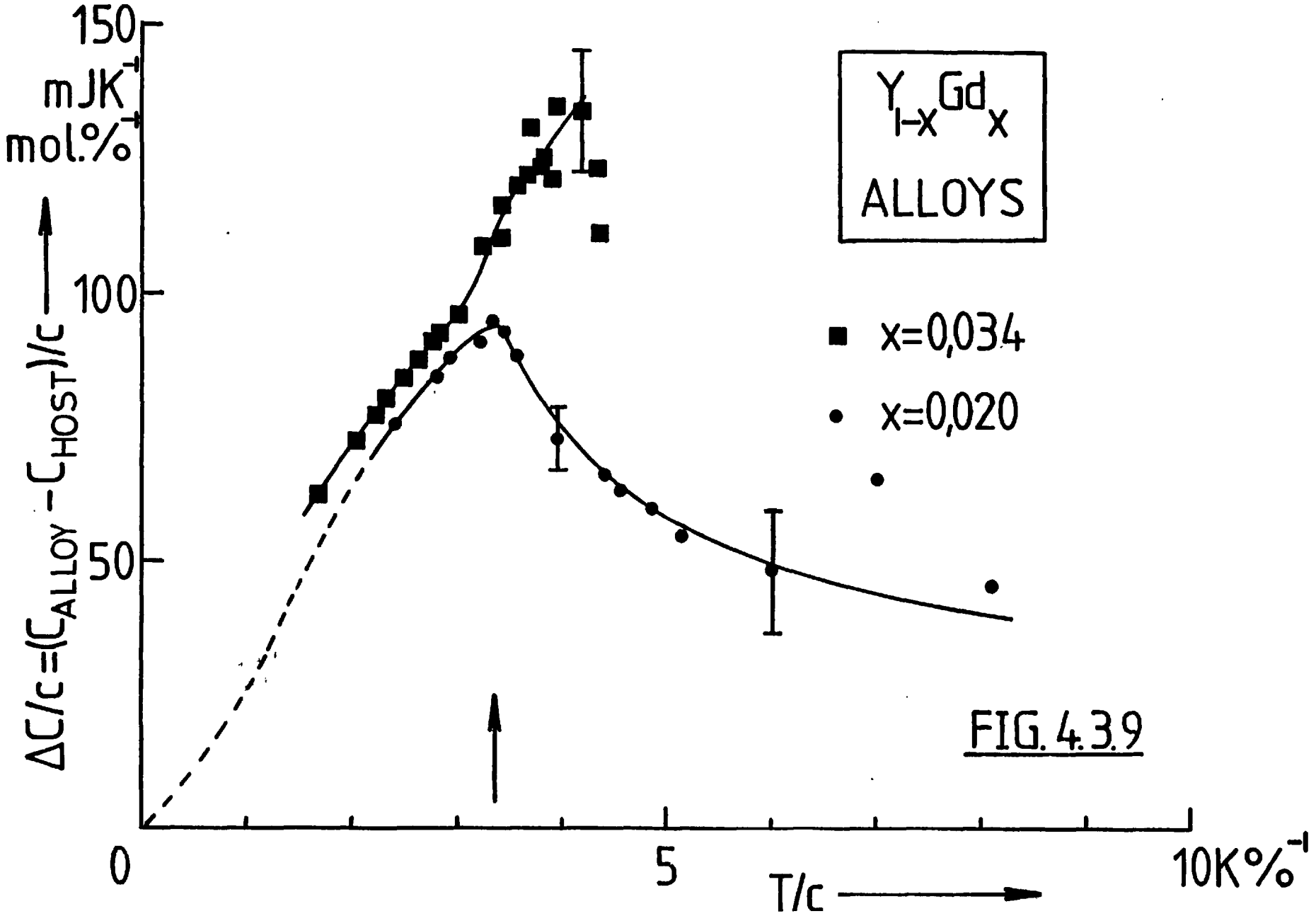
150
mJK⁻¹
mol.%⁻¹
100
50
0
5
10K%⁻¹
T/c
ΔC/c=(C_ALLOY − C_HOST)/c
Y1-xGdx
ALLOYS
x=0,034
x=0,020

FIG. 4.3.9

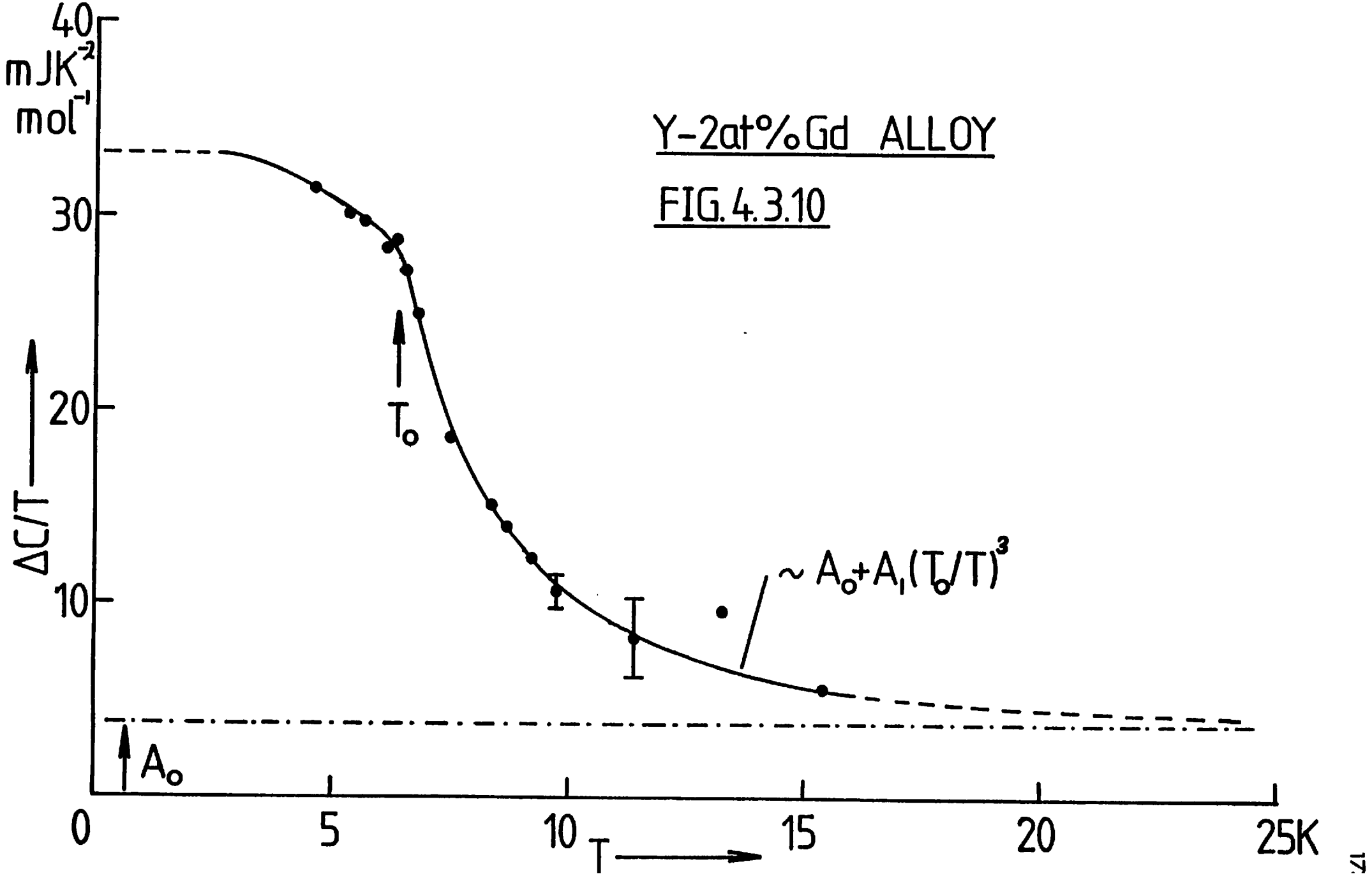

Y-2at%Gd ALLOY

FIG. 4.3.10

REFERENCES

1. Hansen M. and Anderko K. (eds.), 1958, Constitution of Binary Alloys, McGraw-Hill, New York. Supplements edited by Elliott R.P. (1965) and Shunk F.A. (1969)
2. Cetas T.C., Holste J.C. and Swenson C.A., 1969, Phys. Rev. 182, 679
3. Isaacs L.L., 1973, Phys. Rev. B8, 3301
4. Wells P., Lanchester P.C., Jones D.W. and Jordan R.G., 1976, J. Phys. F : Metal Phys. 6
5. Tsang T.-W.E., Gschneider K.A. Jr. and Schmidt F.A., 1976, Solid State Commun. 20, 737
6. Jordan R.G. and Jones D.W., 1973, J. Less Common Metals 31, 125
7. Jordan R.G., Jones D.W. and Hems V.J., 1975, J. Less Common Metals 42, 101
8. Yeomans S.R. and McCormick P.G., 1978, Mat. Sci. & Eng. 34, 101
9. Butler E.P. and Kelly P.M., 1968, Trans. Metall. Soc. AIME 242, 2099 and 2107
10. Vintaykin Ye.Z., Dmitriyev V.B. and Udovenko V.A., 1979, Phys. Met. Metall. 44(5), 107
11. Vintaykin Ye.Z., Litvin D.F. and Udovenko V.A., 1974, Phys. Met. Metall. 37 (6), 92
12. Vintaykin Ye.Z., Udovenko V.A., Makushev S. Yu. and Litvin D.F., 1979, Phys. Met. Metall. 45 (4), 139
13. Warren B.E. and Averbach B.L., 1953, Modern Research Techniques in Physical Metallurgy, Amer. Soc. Metal., Cleveland, Ohio, 95-130

    Warren B.E., 1969, X-Ray Diffraction, Addison-Wesley, Reading, Mass.
14. Cowley J.M., 1950, J. Appl. Phys. 21, 24

15. Cowley J.M., 1950, Phys. Rev. 77, 667

16. Sundahl R., Silvertsen J., Chen T., 1965, J. Appl. Phys. 36, 1223

17. Sundahl R., Chen T., Silvertsen J. and Sato Y., 1966, J. Appl. Phys. 37, 1024

18. Borg R.J. and Dienes G.J., 1975, J. Appl. Phys. 46, 99

19. Ref. 56, Ch.2

20. Raeburn S.J. and Aldridge R.V., 1978, J. Phys. F : Metal Phys. 8, 1917

21. Ref. 44, Ch. 2

22. Arrott A., 1965, J. Appl. Phys. 36, 1093

23. Sato H., Werner S.A. and Yessik M., 1971, AIP Conf. Proc. 5, 508

24. Ref. 57, Ch. 2

25. Ref. 58, Ch. 2

26. Ref. 13, Ch. 2

27. Ref. 20, Ch. 2

28. Whitehurst A. and Crangle J., 1976, private communication

29. Kuentzler R. and Kapper J.P., 1979, J. Phys. F : Metal Phys. 9, 195

30. Kuentzler R., 1978, Inst. Phys. Conf. Ser. 39, 426

31. Nieuwenhuys G.J. and Mydosh J.A., 1977, Physica 86-88 B, 880

32. Ref. 102, Ch. 2

33. Ref. 10, Ch. 2

34. Ref. 97, Ch. 2

35. Ref. 26, Ch. 2

36. Ref. 25, Ch. 2

37. Ref. 28, Ch. 2

38. Sarkissian B.V.B. and Coles B.R., 1976, Commun. on Phys. 1, 17

39. Sarkissian B.V.B., 1975, Ph.D. thesis, London

40. Vitek J.M. and Warlimont H., 1976, Metal Sci. J. 10, 7.

CHAPTER 5

FINAL DISCUSSION AND CONCLUSIONS

5.1 Discussion of the AuFe data

The low-temperature specific heat data for the AuFe alloys presented in the previous chapter exhibited an almost featureless monotonic temperature dependence. In plots of C/T vs. T^2 slight downward deviations from linearity (although not much greater than the experimental uncertainty) were apparent at the lowest temperatures in the data obtained on some of the alloys, the 18, 20 and 22% in particular. There was certainly no evidence of the low-temperature up-turns observed in the plots of C/T vs. T^2 which have sometimes in the past been ascribed in an adhoc fashion to the presence of superparamagnetic clusters (see discussion in section 2.4.2).

No anomalous behaviour was evident in the specific heat data at the characteristic temperatures of the low temperature deviations observed in the susceptibility and ESR data of the post-percolation alloys previously ascribed by Coles et al (ref. 87, Chapter 2) to the independent freezing of the finite clusters. Such insensitivity was also apparent at the spin glass freezing temperature in the specific heat measurements by Wenger and Keesom (see section 2.3.1) on dilute pre-percolation alloys. It is interesting to remark at this point on the similar specific heat observations by Meschede et al (ref. 93, Chapter 2) on $Eu_xSr_{1-x}S$ compounds around the critical concentration for ferromagnetism ($x_{CRIT} \sim 0.51$) which failed to reveal any anomalies at characteristic finite-cluster freezing temperatures T_f indicated by AC susceptibility and small-angle neutron data. The spin glass ordering in these non-metallic compounds was ascribed to competing ferromagnetic first-neighbour and antiferromagnetic second-neighbour interactions. Neutron data by Maletta and Convert (1) exhibited a broadening of magnetic Bragg peaks and an increase in small-angle diffuse scattering below the

characteristic temperatures T_f, which were in contrast to Au Fe, ascribed to a break-up of the infinite cluster into smaller finite clusters. The break-up of the infinite cluster was argued to have been driven by the freezing of the finite-clusters at the temperatures T_f which extrapolated back to the pre-percolation values of the spin glass freezing temperatures (see fig. 5.1.1), as was observed in Au Fe by Coles et al (ref. 87, Chapter 2) (compare corresponding magnetic phase diagram, fig. 2.3.1).

The concentration dependence of the total specific heat at constant temperature exhibited a very broad peak centred approximately at the critical concentration. This characteristic behaviour is typical of many systems undergoing transitions to long-range magnetic order (see discussion of subject in section 2.4). The very broad shape of the peak in the total specific heat and its almost quadratic dependence on Fe concentration is different from the notably sharper and roughly linear concentration dependence of some other alloys (e.g. Rh Ni, Cu Ni and V Fe, see fig. 5.1.2). Au Fe is uniquely different from these other alloys in that the Fe atoms appear to possess good local moments up to and just above the percolation threshold which can interact both directly through first-neighbour exchange and indirectly through the conduction electrons of the host matrix. However, d-electrons are likely to be more itinerant in character as d-bands form through atomic d-orbital overlap in the extensive regions of the infinite cluster which incorporates almost all spins above $\sim$ 30 at% Fe (see comments by Coles, ref. 105, Chapter 2).

The ferromagnetism of iron and its alloys in particular has been controversial for a number of years, and is at the very centre of the long-standing itinerant vs. local moment debate. The large exchange splitting ($\sim$ 2 eV) of the d-bands of pure BCC-structured iron is incompatible with its Curie temperature in a Stoner model of d-band ferromagnetism. Edwards (2), extending the ideas of Mott and Hubbard, proposed a model of the band structure of transition metals which takes into account the strong

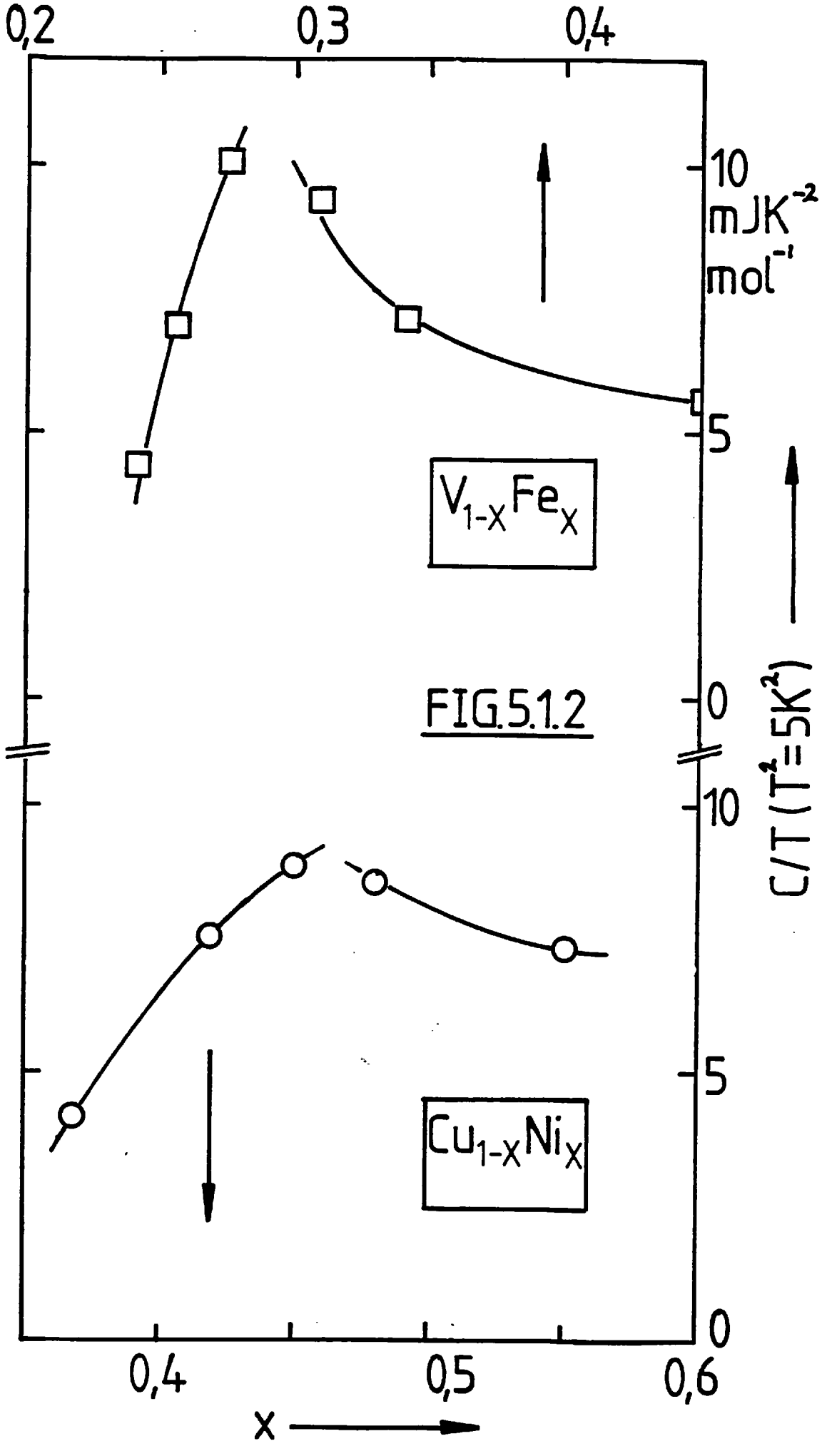

FIG.5.1.2

3d-electron correlations. In pure BCC-structured iron it was proposed that a Hubbard splitting of the d-band results in an upper and lower band consisting of 2 localised hole states (S = 1) and 0.9 itinerant hole states per Fe atom respectively.

Abraham et al (3) have experimentally investigated the properties of FCC-structured microcrystalline iron particles in a copper matrix. They proposed from their findings that it is weakly antiferromagnetic with a spin structure similar to γ - Mn, a low Néel temperature and a saturation moment of $\sim 0.7\ \mu_B$ per Fe atom. The beginnings of a trend to antiferromagnetism is apparent in the concentration dependence of the saturation moment of Au Fe alloys which, after levelling out at $3\ \mu_B$ per Fe atom near 30 at% Fe, begins to fall from this value just beyond $\sim$ 50 at% Fe with increasing concentration (see evidence reviewed by Coles et al, ref. 85, Chapter 2).

The local moment description is perhaps most appropriate to the concentration regime studied in this present work. At the low temperatures of these present measurements the spins in all clusters will be highly correlated, and the spin system will possess very few degrees of freedom. These remaining degrees of freedom may be partly due to the interactions of the clusters (through indirect interactions of individual moments in different clusters) and partly due to the locally weaker spin correlations in the highly ramified branch-like regions of the infinite cluster just above the percolation threshold (see section 1.4). The weak links in the infinite cluster are probably largely responsible for the suppression of the onset of long-range magnetic order until fairly low temperatures are reached well below the temperatures at which the majority of spin correlations in the infinite cluster have formed. The weak links will be very few in number just above the percolation threshold and will not contribute significantly to a critical ordering anomaly. With increasing concentration the strengthening of the weak links leads initially to a very rapid rise of ordering temperature and the development of a fluctuation-broadened

critical ordering anomaly. Thus it would seem unlikely that the low-temperature specific heat would be affected by the appearance of the infinite cluster and would instead remain dominated by the finite-cluster system.

There is ample experimental evidence for the independent freezing of finite-clusters above the percolation concentration in Au Fe alloys (see Coles et al, ref. 87, Chapter 2). It seems reasonable to assume that the low temperature specific heat data presented here represents the beginnings of an ordering anomaly associated with the freezing of finite-clusters in some cluster glass-like configuration similar to that which occurs below the percolation threshold. It is also fairly reasonable to suppose that whatever form the finite cluster freezing specific heat anomaly may take, its leading low temperature term ($T \ll T_f$ characteristic finite-cluster glass freezing temperature) is likely to be some simple power law, if not linear in temperature. Experimentally, an approximately linear temperature dependence was observed. The coefficient of this linear term may roughly reflect the fraction of spins in finite-clusters. It seems very significant that the low constant-temperature total specific heat is projected to have reached the non-magnetic level (as indicated by the Au Ni alloy data) by $\sim$30 at% Fe. This is the concentration where Monte Carlo simulations of percolation in FCC-structured alloys by Dean and Bird (see section 1.4) indicated that the fraction of spins remaining in finite-clusters was less than 5% of the total. Closely similar results were observed by Coles et al (ref. 85, Chapter 2) in the concentration dependence of the "excitation"-resistivity $\Delta\rho = \rho_{4.2} - \rho_{1.5}$ which developed to anomalously large proportions in the concentration regime leading up to the percolation threshold, where it remained relatively constant until $\sim$24 at% Fe before falling fairly rapidly to pre-percolation values just beyond $\sim$30 at% Fe. No significant specific heat contribution was expected from spin wave - like excitations of the infinite cluster at the low temperatures ($T \ll T_c$) considered in this present work.

More extensive specific heat measurements to much higher temperatures have been performed recently by K.A. Mirza and J.W. Loram on several Au Fe alloys with concentrations ranging between 2 and 23 at% Fe. Preliminary results confirm speculations about the form of the finite-cluster freezing anomaly and the development of the critical long-range ordering anomaly in the post-percolation alloys.

The resistivity, susceptibility and ESR measurements performed on Au Fe alloys are fairly extensive and further work in this area would be unlikely to reveal new information (excepting studies of critical spin dynamics). However, there seems to be plenty of scope for further neutron measurements to characterise the low-temperature regime of the post-percolation alloys.

5.2 Discussion of the Cu Mn data

In this section the main features of the temperature and concentration dependence of the specific heat data for the Cu Mn alloys presented in the previous chapter are summarised and discussed.

In plots of C/T vs. T^2 the data for all the Cu Mn alloys were predominately linear up to $\sim$18K with a slight positive curvature at the uppermost temperatures. No significant anomalies were observed in the present range of measurements. The 58.4, 62.9 and 68.5 at% Mn alloys exhibited quasi-Debye temperatures (i.e. extracted from the average gradient of C/T vs. T^2 curves at $\sim$7K) of 320, 320 and 310 ± 5 K respectively. The low-temperature data for these three more concentrated alloys differed only in the highest concentration alloy which exhibited a slightly shallower temperature dependence with a quasi-Debye temperature of 330 ± 5K (evaluated at $\sim$ 3K), and a small but noticeable up-turn below 2K. In contrast, the data for the 30.3 at% Mn alloy exhibited a noticeable down-turn below 2K, and a quasi-Debye temperature of 300 ± 5K (evaluated at $\sim$ 14K). The measured

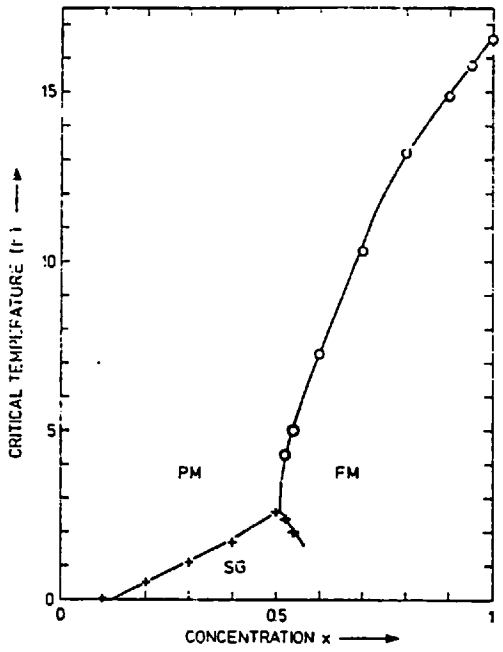

FIG. 3. Magnetic phase diagram of $Eu_xSr_{1-x}S$: PM paramagnetic; FM, ferromagnetic; SG, spin-glass phase. The freezing temperatures for $x \leq 0.50$ and t Curie temperatures for $x \geq 0.60$ are taken from Ref. The double transitions for $x = 0.52$ and 0.54 are resul from the present work.

Fig. 5.1.1
Maletta and Convert,
Ref. 1

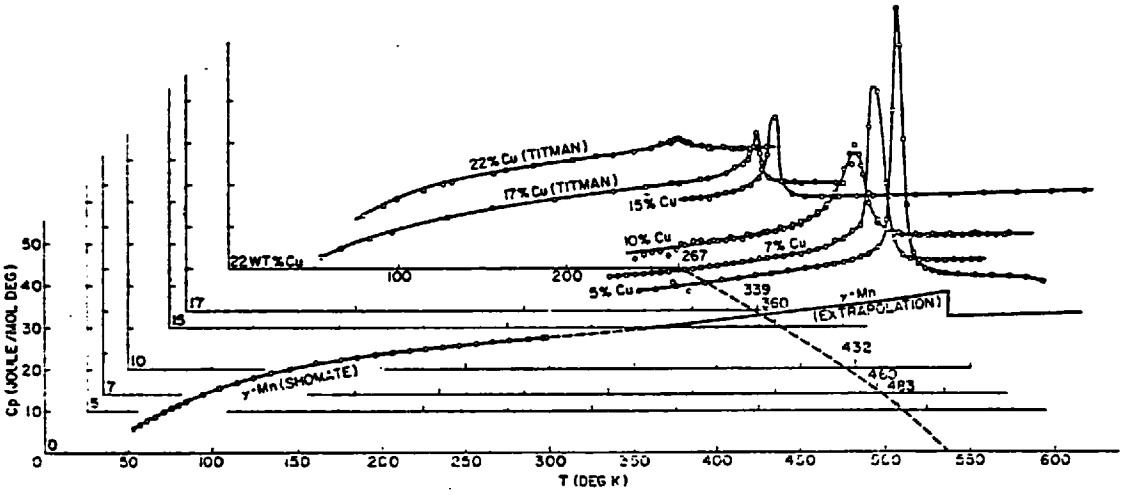

FIG. 1. Specific heat of MnCu alloys as a function of temperature and composition.

Fig. 5.2.1 Zimmerman et al., Ref. 4

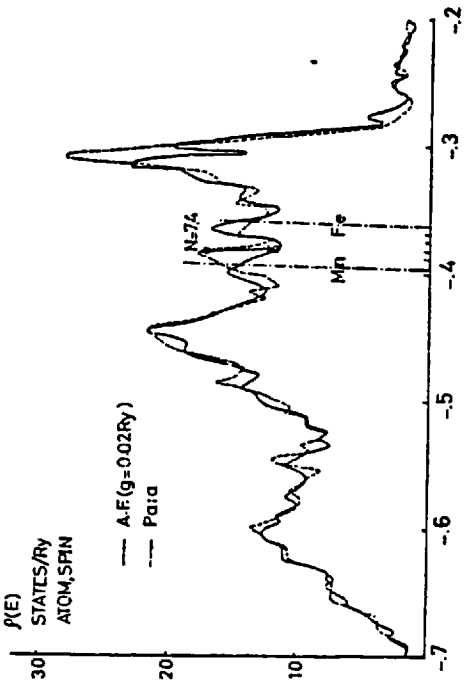

a) Total density of states

Fig. 5.2.2 Asano and Yamashita, Ref. 9

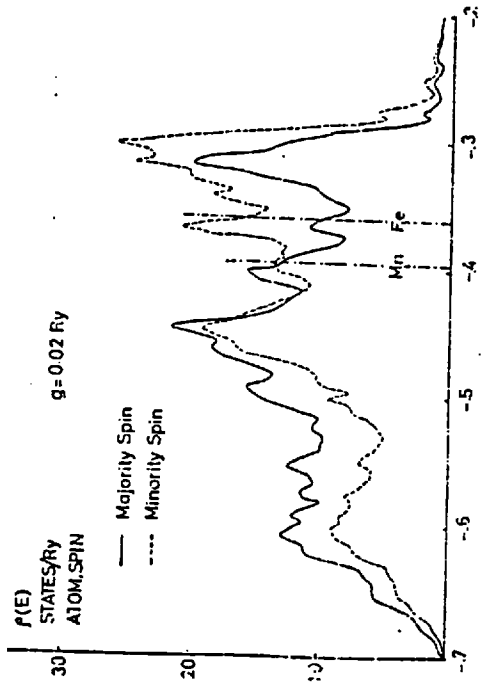

b) Local density of states

quasi-Debye temperatures are slightly lower than the corresponding values for pure copper and manganese (electrolytic γ- Mn see reference in Zimmerman et al, ref. 4) of 345 and 366K respectively. These figures suggest the possible presence of some specific heat contributions from excitations with a small T^3 dependence, which seem to be most significant in the 68.5% alloy.

Other high temperature specific heat measurements on Cu Mn were reported by Zimmerman et al (4) for a series of four Cu Mn alloys with between 87 and 95.5 at% Mn, and also by Titman (5) on a further four alloys between 65 and 85 at% Mn. These measurements exhibited critical ordering anomalies at temperatures ranging from 267K in the 80% alloy to 483 K in the 95.5% alloy, which developed from a shallow cusp-like peak to a sharp γ-type singularity over this same concentration range (see fig. 5.2.1). The 65 and 69% alloys of Titman's investigation exhibited closely similar specific heat data with no anomalies which were fitted to a $C_p = \gamma T + \beta T^3$ relationship between 100 and 300K (with no more than 1% deviation) where γ = 15.6 m J $K^{-2} mol^{-1}$ and Θ_D = 338 K. The fit to the 65% alloy data was used as a measure of the non-magnetic background specific heat to extract the total change in entropy associated with the critical ordering anomalies in the 80 and 85% alloys. The total entropy change determined in this way was only $\sim$ 10 - 20% of the total configurational entropy (assuming J = 2), and was taken to imply that the local moment forming d-electrons were to some extent itinerant in character. However, the assumption that the specific heat data for the 65% alloy can be used as a measure of the non-magnetic background is rather doubtful in the light of the considerable experimental evidence of the presence of extensive magnetic SRO in alloys below the critical concentration $\sim$ 72%.

As a function of Mn concentration the low constant-temperature total specific

heat data exhibits a shallow minimum around ~ 25 - 30% from which it climbs gradually at first, then rather more steeply as it approaches the critical concentration. The data of this present work shows that the low constant-temperature total specific heat for the 68.5% alloy is larger than the just antiferromagnetic 73% alloy of Zimmerman and Sato's investigation (ref. 102, Chapter 2). Again the peaking of the low constant- temperature total specific heat close to the critical concentration resembles the behaviour of many alloys undergoing transitions to long-range order, but is notably different from the weaker concentration dependent behaviour of the Au Fe data in its corresponding critical regime.

The critical concentration ~ 72% is substantially larger than the 45% predicted by Sato and Kikuchi (see section 1.4). This discrepancy reflects in part the inherent problems of establishing long-range antiferromagnetic order in an FCC lattice, where the cubic symmetry results in frustration of spins on (111) planes. It is no coincidence that a tetragonal distortion of the lattice occurs in the magnetically long-range ordered alloys at the Neel temperature. The high spin correlation energy resulting from extensive magnetic SRO (see neutron evidence discussed in section 2.3.3) which favours a transition to a lower free energy long-range ordered state will tend to "drive" the lattice into a lower symmetry structure. It is interesting to mention at this point the isotropic spin structure proposed for antiferromagnetic γ - Fe Mn alloys (intermediate compositions), which retains the cubic symmetry of the lattice by aligning spins along different $\langle 111 \rangle$ directions to minimise the free energy (see Endoh and Ishikawa, ref. 6). It is not possible to differentiate clearly between this isotropic spin structure and the colinear type AF-1 structure in the neutron data; the nature of the spin structure can only be inferred from the symmetry

of the lattice, specifically in the presence or absence of tetragonal distortion. In this respect the neutron evidence of Frolov et al (7), which demonstrates the presence of tetragonal distortion across the entire composition range of the γ-Fe Mn alloy system, contests the proposed isotropic spin structure for the intermediate composition range of this alloy.

The close interplay of the metallurgy and physics of the Cu Mn system was apparent in many investigations. The work of Vintaykin et al (refs. 10 and 11, Chapter 4) on heterogeneous alloys discussed previously in Chapter 4 is a good example of the interactions of these aspects. Vintaykin et al had interpreted the observed increase in the Neel temperature of moderately aged Cu Mn alloys (above 50 at% Mn) in terms of a free energy model in which long-range magnetic order could only be realised in a lattice with tetragonal symmetry. In the aged alloys the locally Mn-rich regions with higher magnetic free energy were considered to act as nucleation sites for the whole lattice. The ordering temperature of these aged alloys was supposed to depend on the relative volume fractions of the Mn-depleted and Mn-rich regions. However, if their model is taken seriously, it would imply that it should be possible to obtain long-range magnetic order in the intermediate concentration range alloys simply by applying sufficient pressure to induce the required degree of tetragonal distortion.

In interpreting the properties of the aged alloys, it is important to consider the decomposition mechanism in some detail. The work of Yeomans and McCormick (ref. 8, Chapter 4) established the nature of a zonal segregation phase which was thought to be due to a metastable miscibility gap (see Cu Mn phase diagram, fig. 4.1.1). They showed that the zonal segregation phase involved the growth of coherent Mn-rich particles which were rather diffusely integrated into a Mn-depleted matrix by fairly shallow interfacial concentration gradients. It was these rather

diffuse boundaries to the Mn-rich particles which were considered responsible for the mechanical strength of the moderately aged Cu Mn alloys. Furthermore, J.R. Davis (private communication) has suggested that the shallow interfacial concentration gradients may also be important in establishing the continuity of the magnetic order of the moderately aged alloys, as was observed in the neutron measurements by Vintaykin et al. In this respect it is probably significant that the composition (~ 45 at% Mn) at which long-range magnetic order abruptly disappears in the moderately aged alloys is at the limit of the coherent spinoidal decomposition regime where short range ordering becomes important.

Experiments on the aged alloys may lead to an improved understanding of the nature of the magnetic order in the quenched alloys, at least in one respect they already seem to stress the importance of the local character, in determining the magnetic order, even in the concentrated alloys.

Turning now to consider the possible band characteristics of concentrated Cu Mn alloys. It is reasonable to expect that by ~ 45 at% Mn there is a sufficient concentration of first-neighbour Mn d-orbital overlap for the Mn d-electrons to be no longer wholly localised, as indeed they are in the dilute alloys, so that they form a CPA-like d-band (CPA-like in the sense that it is appropriate to a disordered substitutional alloy in which local environment effects are not important in determining the magnetic state of a solute atom as they are in e.g. Cu Ni). (See Coles, ref. 105, Chapter 2). Evidence to support this proposition may be found from the indications of d-electron itineracy in the non-Curie-Weiss-like behaviour of the susceptibility above its peak temperature (see Coles, ref. 105, Chapter 2 - N.B. magnetic SRO may also be partly responsible), the non-integral value of the sublattice moment per Mn atom (see Cowlam et al, ref. 98, Chapter 2) and the small entropy change associated with the loss of the long-range magnetic order in alloys with

concentrations greater than ~72%. The large low constant-temperature total specific heat which develops between 40-70 at% Mn may also, in part, be due to the broadening of the d-band as it develops with increasing Mn concentration.

Whilst no band structure calculations have been published in the literature for concentrated Cu Mn alloys, there have been two calculations of the band structure of γ - Mn by Fletcher (8), Asano and Yamashita (9). The main features of the γ - Mn band structure are shown by the local density of states curves in fig. 5.2.2. In the antiferromagnetic state spin dependent effective potential $J_{eff} \sim 0.06$ Ryd produces a complexly k-dependent energy gap ~ 0.13 - 0.16 Ryd ($<$ 0.4 Ryd for the d-bandwidth) between pairs of energy bands. Majority spin band states, with large wavefunction amplitude at atomic sites of the same spin, occupy the lower half of the energy bands. The fermi level is in the middle of the bands and the lower band is occupied, resulting in an induced moment on each sublattice (the net polarisation and corresponding local effective potential self-consistently stabilises the spin polarised state). Whilst a drastic change of the local density of states occurs in passing from the paramagnetic to antiferromagnetic states, the total density of states remains constant.

It is very difficult in these concentrated alloys to differentiate between the presence of magnetic SRO and the itineracy of d-electrons, both of which could conceivably explain the concentration dependence of the sublattice moment or the Néel temperature. Without doubt both magnetic SRO and itinerant Mn d-electrons must be present in the alloys. An example of the difficulty is evidenced by the observed fall in susceptibility peak temperatures of alloys in the concentration range 50 - 65% which could be ascribed to a competition between local on-site moment formation and the increasing broadening of a CPA-like Mn d-band, i.e. a Stoner

glass (see Coles, ref. 105, 106, Chapter 2). Conversely, bearing in mind the change in the character of the decomposition of alloys above ~45%, this decrease in peak temperature could be ascribed to the increasing antiferromagnetic SRO resulting from the tendency of Mn atoms to cluster, in comparison to the more ferromagnetic SRO character which seems to result from the tendency of Mn atoms to give atomic SRO in the more dilute alloys (see Tustison and Beck, ref. 50, Chapter 2, and Davis et al, ref. 58, Chapter 2). In either case the specific heat may be expected to increase in this concentration regime.

There seems to be no obvious experiment that can be performed to clearly resolve these different aspects of the magnetic properties of concentrated Cu Mn alloys. Resistivity, susceptibility, neutron and specific heat measurements are fairly extensive, although it would be useful to re-investigate the specific heat at higher temperatures to link up with the low-temperature data. At this stage it may be best to attempt to draw parallels with other γ-Mn alloy systems (e.g. γ-Fe Mn, see ref. 6).

REFERENCES

1. Maletta H. and Convert P., 1979, Phys. Rev. Letts. 42, 108
2. Edwards D.M., 1970, Phys. Letts. 33A, 183
3. Abrahams S.C., Guttman L. and Kasper J.S., 1962, Phys. Rev. 127, 2052
4. Zimmerman J.E., Arrott A., Sato H. and Shinozaki S., 1964, J. Appl. Phys. 35, 942
5. Titman J.M., 1961, Proc. Phys. Soc. 77, 807
6. Endoh Y. and Ishikawa Y., 1971, J. Phys. Soc. Japan 30, 1614
7. Frolov T.L., Kibal'nik D. and Bogachev I.N., 1977, Sov. Phys. Dokl. 21, 530
8. Fletcher G.C., 1971, J. Phys. F : Metal Physics 1, 177
9. Asano S. and Yamashita J., 1971, J. Phys. Soc. Japan 31, 1000.